Technische Universität München
Fakultät für Physik

Dissertation

Search for long-lived particles decaying to oppositely charged lepton pairs with the ATLAS experiment at $\sqrt{s} = 13$ TeV

Dominik Krauss

Max-Planck-Institut für Physik
(Werner-Heisenberg-Institut)

Fakultät für Physik der Technischen Universität München

Max-Planck-Institut für Physik
(Werner-Heisenberg-Institut)

Search for long-lived particles decaying to oppositely charged lepton pairs with the ATLAS experiment at $\sqrt{s} = 13$ TeV

Dominik Krauss

Vollständiger Abdruck der von der Fakultät für Physik der Technischen Universität München zur Erlangung des akademischen Grades eines

Doktors der Naturwissenschaften (Dr. rer. nat.)

genehmigten Dissertation.

Vorsitzender:		Prof. Dr. Alejandro Ibarra
Prüfer der Dissertation:		
	1.	apl. Prof. Dr. Hubert Kroha
	2.	Prof. Dr. Stephan Paul

Die Dissertation wurde am 19. Juni 2019 bei der Technischen Universität München eingereicht und durch die Fakultät für Physik am 19. Juli 2019 angenommen.

Abstract

In this thesis, a search for new long-lived, massive particles decaying into oppositely charged ee, $e\mu$ or $\mu\mu$ pairs with the ATLAS experiment at the Large Hadron Collider is presented. The search is based on data of proton–proton collisions at a centre-of-mass energy of 13 TeV recorded in 2016, corresponding to an integrated luminosity of 32.8 fb^{-1}. The lepton pairs are required to form a common vertex within the inner tracking volume of the ATLAS detector, which is displaced from the primary collision vertex. The signal selection criteria suppress the background produced in collisions to a negligible level. High-energy cosmic-ray muons are the dominant source of the remaining background, which is estimated from the data to be 0.27 ± 0.17 events. No vertices with invariant mass greater than 12 GeV are observed, in agreement with the background expectation. The result is interpreted in a simplified supersymmetric model in which the lightest neutralino produced via squark-antisquark production is long-lived and decays to $\ell^+\ell'^-\nu$ ($\ell = e, \mu$) via R-parity violating couplings. Upper limits on the signal cross-section are derived for specific squark and neutralino masses and for neutralino lifetimes ($c\tau$) between 1 mm and 10 m.

Danksagungen

Zunächst möchte ich Hubert Kroha und dem Max-Planck-Institut für Physik dafür danken, dass sie diese Doktorarbeit ermöglicht haben. Während meiner vierjährigen Zeit als Doktorand konnte ich viele interessante Sommerkurse, Workshops und Konferenzen besuchen. Dies ermöglichte es mir, in viele Länder zu reisen und fremde Kulturen kennenzulernen. All diese Erfahrungen haben viel Spaß gemacht und ich werde in meinem zukünftigen Leben sehr davon profitieren.

Als nächstes möchte ich Mike danken, der im ersten Jahr mein Betreuer war. Auch nachdem er die Wissenschaft verlassen hatte, half er mir stets bei schwierigen Problemen. Seine Kommentare zu meiner Doktorarbeit waren sehr hilfreich und haben sie deutlich verbessert.

Ich möchte auch Max danken, der die Analyse vor mir gemacht hat. Er konnte mir oft mit seinen schnellen und detaillierten Antworten helfen.

Darüber hinaus möchte ich mich bei meinen Kollegen von ATLAS-MDT, Andi, Bini, Johannes, Katha, Marian, Nico, Philipp, Rainer, Stefan und Verena bedanken, die mir oft bei Problemen aller Art helfen konnten. Die täglichen Mittagspausen und die gemeinsamen Aktivitäten auf Konferenzen haben immer viel Spaß gemacht.

Besonderer Dank gilt meinem Freund Raphael von der GERDA-Gruppe, mit dem ich mich schon immer gerne über verschiedene Themen der Physik ausgetauscht habe.

Abschließend möchte ich meiner Mutter Doris und meiner Tante Inge für ihre tolle Unterstützung während meines ganzen Lebens danken.

Contents

Chapter 1

Introduction

The Standard Model of particle physics describes the known elementary particles and their interactions except gravity. It was developed in the 20th century as a consequence of many ground-breaking experimental and theoretical discoveries and is based on the principles of quantum field theory. Its predictions have been verified in numerous experiments over the past decades. The most recent success was the discovery of the Higgs boson by the ATLAS [1] and CMS [2] experiments at the Large Hadron Collider in 2012, almost 50 years after its postulation. There are, however, observations that are not explained by the Standard Model, such as dark matter and dark energy, which together constitute about 95% [3] of the energy content of the universe. In addition, the Standard Model cannot explain why there is so much more matter in the universe than antimatter, although both should have been produced in equal amounts in the Big Bang.

An extension of the Standard Model that addresses many of the open questions in particle physics is supersymmetry, which introduces a superpartner for each particle of the Standard Model whose spin differs by a half-integer. Since the start of operation of the Large Hadron Collider in 2010, the ATLAS and CMS experiments have performed numerous searches for supersymmetry, all of which have not been successful so far. It is therefore essential to consider also less conventional signatures when searching for supersymmetry. Certain supersymmetric models predict the existence of long-lived particles decaying into pairs of oppositely charged leptons. If the long-lived particle has a lifetime in the range of pico- to nano-seconds, its decay may be detected as a displaced vertex in the inner tracking volume of the ATLAS detector.

In this thesis, a search for displaced dilepton vertices from the decays of new long-lived particles with masses larger than 12 GeV into oppositely charged ee, $e\mu$ or $\mu\mu$ pairs is presented. The search is based on data of proton–proton collisions at a centre-of-mass energy of 13 TeV recorded by the ATLAS experiment in 2016, corresponding to an integrated luminosity of 32.8 fb^{-1}. The sensitivity of the ATLAS detector to such long-lived particles is studied with a supersymmetric model where the lightest neutralino produced via squark-antisquark production is long-lived and decays into two charged leptons and a neutrino via R-parity violating couplings.

The principles of the Standard Model and supersymmetry are explained in Chapters 2 and 3, respectively, followed by an introduction to the Large Hadron Collider and the ATLAS experiment in Chapter 4. The search for displaced dilepton vertices is discussed in Chapter 5. The conclusions are presented in Chapter 6.

Chapter 2

The Standard Model

The Standard Model of particle physics (SM)[1] is the current fundamental theory that describes the known elementary particles and their interactions. It was developed in the middle of the 20th century based on the principles of gauge-invariant quantum field theories [5]. It consists of two parts, the Glashow-Weinberg-Salam theory [6–8], which is a unified description of the electromagnetic and weak interactions, and quantum chromodynamics [9, 10], which is the quantum field theory of the strong interaction. The remaining fourth fundamental interaction, gravity, is not part of the Standard Model and described by general relativity [11] on macroscopic scales. A quantum field theory of gravity has not been found yet, which is one of the unsolved problems in particle physics.

More details on the theoretical principles of the Standard Model, the interactions and the particles involved are discussed in the following sections.

2.1 Gauge-invariant quantum field theories

The elementary particles of the Standard Model are classified into two types. Fermions have half-integer spin and form the visible matter in the universe. They are further subdivided into quarks and leptons, which differ in their interactions. Bosons are particles with integer spin and mediators of the interactions, except the Higgs boson, which is a consequence of the spontaneous electroweak symmetry breaking as discussed in Section 2.4.

The particles and their interactions are described by quantum field theories. Fermions are represented by spinor fields and bosons by vector fields. In the following, the two-

[1] A detailed introduction to the general principles of the Standard Model can be found in reference [4].

component Weyl notation is used for fermions since it is needed later on for the discussion of supersymmetry.

The field equations describing the propagation and interactions of fields are obtained via Hamilton's principle and are the well-known Euler-Lagrange equations

$$\partial_\mu \frac{\partial \mathcal{L}}{\partial(\partial_\mu \Phi)} - \frac{\partial \mathcal{L}}{\partial \Phi} = 0 \tag{2.1}$$

with the Lagrangian density $\mathcal{L}(\Phi, \partial_\mu \Phi)$. For a free and massless fermion, denoted by a Weyl spinor χ, the Lagrangian density is given by

$$\mathcal{L} = i\chi^\dagger \bar{\sigma}^\mu \partial_\mu \chi, \tag{2.2}$$

where $\bar{\sigma}^\mu = (\mathbb{1}, -\vec{\sigma})$ and $\vec{\sigma}$ are the Pauli matrices. Interactions between fermions are introduced by requiring that the Lagrangian density is invariant under local gauge transformations, which correspond to local phase transformations of the fermion fields

$$(\chi_1, \ldots \chi_M)^\mathrm{T} \to e^{i\alpha^1(x^\mu)T_1 + \ldots + i\alpha^N(x^\mu)T_N} (\chi_1, \ldots \chi_M)^\mathrm{T}, \tag{2.3}$$

where T_a are the generators of the Lie group of the gauge symmetry, $\alpha^i(x^\mu)$ are space-time dependent scalar phases and $(\chi_1, \ldots \chi_M)^\mathrm{T}$ is a multiplet of fermion fields in the fundamental representation of the Lie group. The generators T_a are the Hermitian charge operators of the interaction fulfilling the commutation relation of the associated Lie algebra,

$$[T_a, T_b] = i f_{abc} T_c, \tag{2.4}$$

with the structure constants f_{abc}. To ensure the gauge-invariance of the Lagrangian density, the derivative in Equation (2.2) has to be substituted by the gauge covariant derivative,

$$\partial_\mu \to D_\mu = \partial_\mu - igT_a W_\mu^a, \tag{2.5}$$

involving the vector gauge fields W_μ^a and the gauge coupling constant g characterising the strength of the interaction. These vector fields transform under local gauge transformations as

$$W_\mu^a \to W_\mu^a + \frac{1}{g}\partial_\mu \alpha^a(x^\mu) + f_{abc} W_\mu^b \alpha^c(x^\mu), \tag{2.6}$$

and represent the spin-1 gauge bosons. Finally, a kinetic term

$$\mathcal{L}_{\text{gauge}} = -\frac{1}{4} F^a_{\mu\nu} F^{a,\mu\nu}. \tag{2.7}$$

for the gauge fields has to be added to the Lagrangian density, which describes the propagation of free gauge fields and is expressed in terms of the field strength tensor

$$F^a_{\mu\nu} = \partial_\mu W^a_\nu - \partial_\nu W^a_\mu + g f_{abc} W^b_\mu W^c_\nu. \tag{2.8}$$

Based on this formalism, the interactions of the particles and their fundamental multiplets are defined by the gauge symmetry group of the Standard Model

$$\mathrm{SU}(3)_C \times \mathrm{SU}(2)_L \times \mathrm{U}(1)_Y, \tag{2.9}$$

which is a product of three Lie groups, one for each interaction. Quantum chromodynamics, i.e. the strong interaction, is described by $\mathrm{SU}(3)_C$ and the unified electromagnetic and weak interactions by $\mathrm{SU}(2)_L \times \mathrm{U}(1)_Y$, where $\mathrm{U}(n)$ is the Lie group of unitary $n \times n$ matrices and $\mathrm{SU}(n)$ is a subgroup of $\mathrm{U}(n)$ consisting of unitary $n \times n$ matrices with determinant 1.

2.2 Quarks and the strong interaction

The first part of the gauge symmetry group of the Standard Model, the $\mathrm{SU}(3)_C$, belongs to the strong interaction. The index C refers to the associated charge that is called color and has three values, denoted red, green and blue, with corresponding anticolors for antiparticles. Color triplets $(q_r, q_g, q_b)^T$ for each of the six quarks form the fundamental representation of quantum chromodynamics. The six quarks are spin-$\frac{1}{2}$ fermions and called up (u), down (d), charm (c), strange (s), bottom (b) and top (t).

The $\mathrm{SU}(3)_C$ gauge group has eight generators T_a, which are given in the fundamental representation by $T_a = \frac{1}{2}\lambda_a$, where λ_a are the 3×3 Gell-Mann matrices. These generators are associated with eight gauge fields, the gluons, which carry color charges due to the non-Abelian nature of the $\mathrm{SU}(3)_C$ symmetry group. In non-Abelian gauge theories, the structure constants f_{abc} of Equation (2.4) are non-zero, leading to self-interactions of the gauge fields in Equation (2.7). As a consequence of the gluon self-interactions, the strong interaction becomes strong at low energies, leading to the phenomenon of confinement [12] of colored particles, quarks and gluons in color-neutral bound states, the hadrons. Hadrons are subdivided into baryons consisting of three quarks, and mesons composed of one quark and one antiquark. Confinement has an important implication for collider physics, namely that quarks and gluons produced in highly energetic collisions hadronise and form jets of hadrons. At high energies, the strong interaction becomes weak so that quarks and gluons behave like free particles inside the hadrons, an effect called asymptotic freedom [13, 14].

2.3 Leptons and the electroweak interaction

The second part of the Standard Model gauge group, $SU(2)_L \times U(1)_Y$, describes the electroweak interaction and is a direct product of the $SU(2)_L$ and $U(1)_Y$ Lie groups, with their associated charges being the third component of the weak isospin, $\vec{I}$, and the weak hypercharge, Y, respectively. The electric charge Q is related to these quantum numbers via the Gell-Mann-Nishijima relation [15–17]

$$Q = I_3 + \frac{Y}{2}. \tag{2.10}$$

Both the six quarks and the six leptons, spin-$\frac{1}{2}$ fermions, participate in the electroweak interactions. There are three electrically charged leptons, called electron (e), muon (μ) and tau (τ). Only the electron is stable, while the muon and the tau have lifetimes of $2.2 \cdot 10^{-6}$ s and $2.9 \cdot 10^{-13}$ s, respectively. Each charged lepton has an associated neutrino, ν_e, ν_μ, ν_τ, which is electrically neutral. Non-zero neutrino masses and neutrino oscillations [18] are not described by the Standard Model.

The left-handed fermion states form $SU(2)_L$ doublets with $I_3 = \pm\frac{1}{2}$, which is the fundamental representation of $SU(2)_L$, whereas right-handed fermions form singlets with $I_3 = 0$. The fermion singlets and doublets of the three generations of leptons and quarks are

$$\begin{aligned} &\begin{pmatrix} \nu_e \\ e \end{pmatrix}_L, \begin{pmatrix} \nu_\mu \\ \mu \end{pmatrix}_L, \begin{pmatrix} \nu_\tau \\ \tau \end{pmatrix}_L, \; e_R, \; \mu_R, \; \tau_R, \\ &\begin{pmatrix} u \\ d \end{pmatrix}_L, \begin{pmatrix} c \\ s \end{pmatrix}_L, \begin{pmatrix} t \\ b \end{pmatrix}_L, \; u_R, \; d_R, \; c_R, \; s_R, \; t_R, \; b_R. \end{aligned} \tag{2.11}$$

Table 2.1: Electroweak charge quantum numbers I_3, Y and Q for left- and right-handed fermion fields

	ν_L	ℓ_L	ℓ_R	u_L	d_L	u_R	d_R
I_3	+1/2	−1/2	0	+1/2	−1/2	0	0
Y	−1	−1	−2	+1/3	+1/3	+4/3	−2/3
Q	0	−1	−1	+2/3	−1/3	+2/3	−1/3

Right-handed neutrinos [19] are not included since the neutrinos are assumed to be massless in the Standard Model. Each generation has the same charge quantum numbers (see Table 2.1).

The $\mathrm{SU}(2)_L \times \mathrm{U}(1)_Y$ gauge group has four generators, the three weak isospin operators I_a, which are given in the fundamental representation by $I_a = \frac{1}{2}\sigma_a$ with the Pauli matrices σ_a, and the weak hypercharge Y. Each of them is associated with a gauge field, the three vector fields W^a_μ with I_a and the vector field B_μ with Y. Since the gauge group of the electroweak interaction is a product of $\mathrm{SU}(2)_L$ and $\mathrm{U}(1)_Y$, there are two independent gauge coupling constants, denoted by g_W and g_Y.

2.4 Electroweak symmetry breaking

So far, only massless particles have been considered. The local gauge symmetries require the gauge vector fields and the fermions to be massless. Adding mass terms to the Lagrangian density would break the local gauge invariance. Instead, particles acquire their masses through interactions with a complex scalar $\mathrm{SU}(2)_L$ doublet Φ [20–22], which is called the Higgs field and couples to the electroweak gauge fields via

$$\mathcal{L}_{\mathrm{Higgs}} = (D_\mu \Phi)^\dagger (D^\mu \Phi) - V(\Phi), \tag{2.12}$$

where D_μ is the covariant derivative for $\mathrm{SU}(2)_L$. Self-interactions of the Higgs field are described by its potential

$$V(\Phi) = -\mu^2 \Phi^\dagger \Phi + \frac{\lambda}{4}(\Phi^\dagger \Phi)^2, \tag{2.13}$$

with the mass parameter $\mu^2 < 0$ (in the electroweak symmetry breaking phase) and the self-interaction parameter $\lambda > 0$. The Lagrangian density of the Standard Model remains invariant under electroweak gauge transformations, whereas the ground state of the Higgs field, the vacuum, is not invariant due to its non-zero expectation value

$$|\langle\Phi\rangle| = \frac{\mu\sqrt{2}}{\sqrt{\lambda}} := \frac{v}{\sqrt{2}}, \tag{2.14}$$

i.e. the electroweak gauge symmetry is spontaneously broken. The vacuum expectation value is given by

$$v = (\sqrt{2}G_{\mathrm{F}})^{-\frac{1}{2}} \approx 246\,\mathrm{GeV}, \tag{2.15}$$

where G_{F} is the Fermi constant of the weak interaction, which is precisely determined from measurements of the muon lifetime [23]. The electrically neutral ground state of the Higgs field remains invariant under the transformations of the $\mathrm{U}(1)_Q$ gauge symmetry of the electromagnetic interaction, a subgroup of $\mathrm{SU}(2)_L \times \mathrm{U}(1)_Y$.

By choosing the unitary gauge [24, 25], three of the four degrees of freedom of the Higgs field are eliminated and transformed into the longitudinal polarisation states of the weak gauge fields, and the Higgs field can be parametrised by

$$\Phi(x) = \frac{1}{\sqrt{2}} \begin{pmatrix} 0 \\ v + h(x) \end{pmatrix}, \tag{2.16}$$

where h is a physical field describing a scalar neutral particle, the Higgs boson, with a mass $m_h = \mu\sqrt{2}$. In 2012, the Higgs boson was discovered by the ATLAS [1] and CMS [2] experiments at the Large Hadron Collider with a mass[2] of about 125 GeV [26].

The electroweak gauge fields W^a_μ and B_μ mix and form the mass eigenstates

$$W^\pm_\mu = \frac{1}{\sqrt{2}}(W^1_\mu \mp iW^2_\mu) \tag{2.17}$$

and

$$\begin{pmatrix} Z_\mu \\ A_\mu \end{pmatrix} = \begin{pmatrix} \cos\theta_W & \sin\theta_W \\ -\sin\theta_W & \cos\theta_W \end{pmatrix} \begin{pmatrix} W^3_\mu \\ B_\mu \end{pmatrix}, \tag{2.18}$$

[2]In this thesis, the masses of particles are given in units of energy by setting the speed of light c to 1.

where $W^{\pm}_{\mu}$ and Z_{μ} are the gauge boson fields mediating the weak interaction, A_{μ} is the photon field, the gauge boson of the electromagnetic interaction, and θ_W is the Weinberg angle. The masses of the weak gauge bosons are given in lowest order by

$$m_W = \frac{v}{2} g_W, \quad m_Z = \frac{v}{2}\sqrt{g_W^2 + g_Y^2}. \tag{2.19}$$

The Weinberg angle is related to these masses via

$$\cos\theta_W = \frac{m_W}{m_Z}. \tag{2.20}$$

Right-handed fermions are not charged under the $\mathrm{SU}(2)_L$ gauge group, i.e. $I_3 = 0$ as listed in Table 2.1. Consequently, the $W^{\pm}$ bosons couple only to left-handed fermions, meaning that the weak interaction maximally violates parity in contrast to the other three interactions. The Z boson couples to both helicity states of the fermions.

The electrically charged fermions acquire their masses through Yukawa interactions with the Higgs field described by

$$\mathcal{L}_{\text{Yukawa}} = -Y^{\ell}_{ij}\bar{L}^i_L \Phi \ell^j_R - Y^d_{ij}\bar{Q}^i_L \Phi d^j_R - Y^u_{ij}\bar{Q}^i_L \Phi^c u^j_R + \text{h.c.}, \tag{2.21}$$

with the generation indices i and j, the 3×3 Yukawa coupling matrices Y_{ij}, the $\mathrm{SU}(2)_L$ doublets $L^i_L = (\nu^i_L, \ell^i_L)^T$ and $Q^i_L = (u^i_L, d^i_L)^T$ and the charge-conjugate $\Phi^c = i\sigma_2\Phi$ of the Higgs field. The Yukawa coupling matrices are related to the fermion mass matrices via $M_{ij} = Y_{ij}\frac{v}{\sqrt{2}}$ and are in general non-diagonal. In such cases, the mass eigenstates are obtained by diagonalisation and are not identical to the $\mathrm{SU}(2)_L$ eigenstates. The resulting mixing matrix of the quark mass eigenstates is the Cabibbo-Kobayashi-Maskawa (CKM) matrix [27]. If neutrinos are massless, then there is no such mixing for the leptons.

2.5 The hierarchy problem

A theoretical problem of the Standard Model related to the electroweak symmetry breaking is the so-called hierarchy problem, which arises from the fact that gravity is so much weaker than the other forces. Thus, the energy scale of the electroweak symmetry breaking ($|\langle\Phi\rangle| \approx 174\,\text{GeV}$) is 17 orders of magnitude lower than that of quantum gravity, the Planck scale ($m_{\text{Pl}} \approx 10^{19}\,\text{GeV}$).

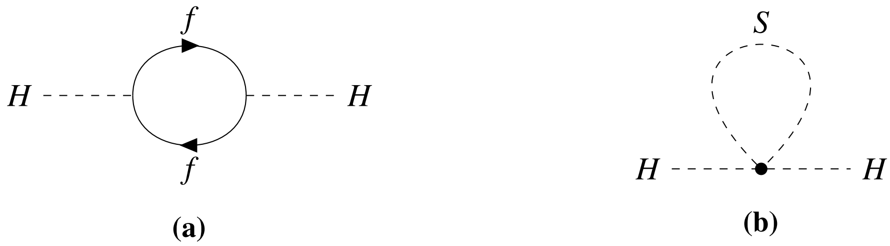

Figure 2.1: Feynman diagrams of loop corrections to the Higgs boson propagator with (a) fermions (f) and (b) scalar bosons (S).

While fermion masses are stabilised by chiral symmetries, the scalar Higgs boson receives quadratically divergent radiative loop corrections from all particles that couple to the Higgs boson, including potential undiscovered massive particles. The leading-order correction to the Higgs boson mass m_h due to fermion loops (see Figure 2.1a) is given by:

$$\Delta m_{h,f}^2 = -\frac{|\lambda_f|^2}{8\pi^2}(\Lambda^2 + \ldots), \tag{2.22}$$

where λ_f is the Yukawa coupling constant of the fermion to the Higgs field, which is proportional to the fermion mass, $\lambda_f = m_f v$. Λ is the cutoff in the fermion energies in the loop, i.e. the energy scale up to which the Standard Model is valid. If the Planck scale is assumed to be the cutoff energy, one would expect the Higgs mass in the range of the Planck mass in contrast to the observation. Without new physics beyond the Standard Model below m_{Pl}, it would be necessary to fine-tune the Higgs mass with extreme accuracy, which appears unnatural.

A very elegant solution is provided by supersymmetry [28–31], which predicts a new scalar boson for every fermionic degree of freedom of the Standard Model, leading to additional bosonic corrections to m_h (see Figure 2.1b),

$$\Delta m_{h,S}^2 = +\frac{\lambda_S}{16\pi^2}(\Lambda^2 + \ldots), \tag{2.23}$$

with opposite sign compared to the fermion terms in Equation (2.22). If supersymmetry were an exact symmetry, the corrections would cancel exactly and the Higgs mass would be stable to all orders of perturbation theory. A similar cancellation of corrections to m_h due to gauge boson loops occurs with their supersymmetric partners, fermions with spin $\frac{1}{2}$.

The fact that supersymmetry could solve the hierarchy problem is one of the main motivations to search for it using collider experiments such as ATLAS. There are other reasons that will be discussed in the next chapter along with the theoretical principles of supersymmetry.

Chapter 3

Supersymmetry

The predictions of the Standard Model have been tested in numerous experiments since the completion of its formulation in the 1970s and agree remarkably well with the measurements [32]. Some observations in nature, however, such as dark matter [33] or the baryon asymmetry [34] cannot be explained by the Standard Model. A promising answer to many of the open questions in particle physics is supersymmetry (SUSY) [35–40]. The energy scale at which supersymmetry might be realised is not known if it is a broken symmetry. At energies of up to a few TeV, supersymmetry [28–31] can solve the hierarchy problem of the Standard Model. Supersymmetric particles with masses of this size can be produced at the Large Hadron Collider, which is a strong motivation to search for supersymmetry with the ATLAS experiment.

The theoretical principles of a supersymmetric theory are explained in the next section. Afterwards the minimal supersymmetric extension of the Standard Model is described in Section 3.2.

3.1 Basic concepts

Supersymmetry[1] is a symmetry between fermions and bosons. Supersymmetric transformations are generated by fermionic spinor operators Q carrying a spin of $\frac{1}{2}$, which transform fermionic states into bosonic states and vice versa:

$$Q\,|\text{fermion}\rangle = |\text{boson}\rangle, \qquad Q\,|\text{boson}\rangle = |\text{fermion}\rangle. \tag{3.1}$$

[1] A comprehensive discussion of supersymmetry can be found in reference [41].

Symmetries of consistent quantum field theories have to fulfil the Haag-Lopuszanski-Sohnius theorem [42], which implies that Q and its Hermitian conjugate $Q^\dagger$ have to satisfy the following relations, the Super-Poincaré algebra:

$$\{Q_\alpha, Q^\dagger_{\dot\beta}\} = -2\sigma^\mu_{\alpha\dot\beta} P_\mu, \quad \{Q_\alpha, Q_\beta\} = \{Q^\dagger_{\dot\alpha}, Q^\dagger_{\dot\beta}\} = 0, \quad [Q_\alpha, P^\mu] = [Q^\dagger_{\dot\alpha}, P^\mu] = 0, \quad (3.2)$$

where α and β are left-handed and $\dot\alpha$ and $\dot\beta$ right-handed Weyl spinor indices and $P_\mu = -i\partial_\mu$ is the four-momentum operator, the generator of spacetime translations.

The fundamental representations of the supersymmetry algebra are called supermultiplets and contain equal numbers of fermionic and bosonic degrees of freedom, which are called superpartners of each other. In renormalisable supersymmetric theories that have only one operator Q and do not include gravity, there are only two types of supermultiplets. A Weyl fermion and two scalar bosons form a chiral supermultiplet, whereas a vector supermultiplet consists of a spin-1 vector boson and a Weyl fermion.

Supersymmetry can be given a geometrical interpretation by introducing the superspace, which extends the four spacetime coordinates x^μ by two complex, anti-commuting two-component spinors Θ^α and $\Theta^\dagger_{\dot\alpha}$, called Grassmann coordinates. Each supermultiplet is described by a single function of the superspace coordinates, the superfield $S(x, \Theta, \Theta^\dagger)$. The supersymmetry operators

$$Q_\alpha = i\frac{\partial}{\partial\Theta^\alpha} - (\sigma^\mu\Theta^\dagger)_\alpha\partial_\mu, \quad Q^\dagger_{\dot\alpha} = -i\frac{\partial}{\partial\Theta^{\dagger\dot\alpha}} + (\Theta\sigma^\mu)_{\dot\alpha}\partial_\mu \quad (3.3)$$

are differential operators acting on the superfields. Infinitesimal supersymmetric transformations of a superfield S are given by

$$\delta_\epsilon S = -i(\epsilon Q + \epsilon^\dagger Q^\dagger)S, \quad (3.4)$$

where ϵ is an complex, anti-commuting two-component Grassmann parameter. They can be interpreted as translations in superspace,

$$\begin{aligned} \Theta^\alpha &\to \Theta^\alpha + \epsilon^\alpha, \\ \Theta^\dagger_{\dot\alpha} &\to \Theta^\dagger_{\dot\alpha} + \epsilon^\dagger_{\dot\alpha}, \\ x^\mu &\to x^\mu + i\epsilon\sigma^\mu\Theta^\dagger + i\epsilon^\dagger\bar\sigma^\mu\Theta. \end{aligned} \quad (3.5)$$

The superfield of a chiral supermultiplet consisting of a complex scalar field ϕ and a Weyl fermion χ can be written as

$$\Phi = \phi(y) + \sqrt{2}\Theta\chi(y) + \Theta^2 F(y), \tag{3.6}$$

where F is a complex scalar field, called auxiliary field, and $y^\mu := x^\mu + i\Theta^\dagger\bar{\sigma}^\mu\Theta$. Auxiliary fields ensure that the numbers of bosonic and fermionic degrees of freedom of a supermultiplet match off-shell. Without them, the supersymmetry algebra would close only on-shell. Their equation of motion is $F = 0$, meaning that they do not propagate and that the particle content of the theory remains unchanged.

The superfield of a vector supermultiplet consisting of a vector field A_μ and a Weyl fermion λ can be written in the Wess-Zumino gauge as

$$V_{\text{WZ gauge}} = \Theta^\dagger\bar{\sigma}^\mu\Theta A_\mu + \Theta^\dagger\Theta^\dagger\Theta\lambda + \Theta\Theta\Theta^\dagger\lambda^\dagger + \frac{1}{2}\Theta\Theta\Theta^\dagger\Theta^\dagger D, \tag{3.7}$$

with the auxiliary field D.

To obtain a gauge-invariant supersymmetric theory, the gauge transformations of the Standard Model have to be generalised to supergauge transformations, under which chiral superfields Φ_i transform as

$$\Phi_i \longrightarrow (e^{2ig_a\Omega^a T^a})_i^j \Phi_j, \tag{3.8}$$

where g_a are the gauge couplings for the irreducible components of the Lie algebra, Ω^a are chiral superfields parametrising the transformation and T_a are the generators of the gauge group. Each generator is associated with a vector superfield V^a that involves the corresponding Standard Model gauge field. Analogous to the Standard Model, a gauge-invariant field strength

$$(\mathcal{W}^a_\beta)_{\text{WZ gauge}} = \lambda^a_\beta + \Theta_\beta D^a + \frac{i}{2}(\sigma^\mu\bar{\sigma}^\nu\Theta)_\beta F^a_{\mu\nu} + i\Theta\Theta(\sigma^\mu\nabla_\mu\lambda^{\dagger a})_\beta, \tag{3.9}$$

which is a chiral superfield, can be defined, where $F_{\mu\nu}$ is the field strength tensor from Equation (2.8),

$$\nabla_\mu\lambda^a = \partial_\mu\lambda^a + g f^{abc} A^b_\mu \lambda^c \tag{3.10}$$

is the covariant derivative with the structure constants f^{abc}, and λ^a and A^a_μ are the fermionic and vector constituents of the superfield V^a, respectively. Any integral of a superfield over the entire superspace is invariant under supersymmetric transformations of Equation (3.4), and therefore a supersymmetric Lagrangian density can be obtained by integrating superfields over the fermionic coordinates. For gauge-invariant supersymmetric theories, it has the form

$$\mathcal{L} = \int d^2\Theta d^2\Theta^\dagger \Phi^{*i} (e^{2g_a T^a V^a})_i^j \Phi_j + \left(\int d^2\Theta \left[W(\Phi_i) + \frac{1}{4} f \mathcal{W}^{a\alpha} \mathcal{W}_\alpha^a \right] + \text{c.c.} \right), \quad (3.11)$$

where W is the superpotential, a complex holomorphic function of the chiral superfields, and f is the so-called gauge kinetic function. In renormalisable theories, the superpotential

$$W = \frac{1}{2} M^{ij} \Phi_i \Phi_j + \frac{1}{6} y_{ijk} \Phi_i \Phi_j \Phi_k \quad (3.12)$$

is a cubic polynomial of the chiral superfields with the mass matrix M and the Yukawa couplings y, and the gauge kinetic function is a constant, $f = 1$.

3.2 The Minimal Supersymmetric Standard Model

Using the general principles of a supersymmetric theory discussed in the previous section, the Minimal Supersymmetric Standard Model (MSSM) [43, 44] can be formulated, which includes the smallest number of supersymmetric fields and additional Higgs fields required to obtain a supersymmetric extension of the Standard Model consistent with observations. It is based on a global supersymmetry with only one supersymmetric operator Q.

3.2.1 Supermultiplets and field content

Each particle of the MSSM belongs either to a chiral or a vector supermultiplet. Chiral supermultiplets, summarised in Table 3.1, contain the fermions of the Standard Model and new scalar bosons, which are their superpartners, called sfermions. The names of the sfermions are based on the corresponding Standard Model partners, but with an additional letter ‘s’ at the beginning of the name, e.g. selectron. Analogously, the symbols of supersymmetric particles have an additional tilde, e.g. $\tilde{e}$ for the selectron.

The generators of the Standard Model gauge groups commute with Q and $Q^\dagger$, which has two important implications for the sfermions. First, left-handed and right-handed fermions each get their own superpartners since they have different electroweak gauge

Table 3.1: Components of the chiral supermultiplets of the MSSM in the fundamental representations of the Standard Model gauge groups with the fermion generation index $i = 1, 2, 3$

Supermultiplet	Sfermions (spin-0)	Fermions (spin-$\frac{1}{2}$)
Q_i	$(\tilde{u}^i_L, \tilde{d}^i_L)^T$	$(u^i_L, d^i_L)^T$
$\bar{U}_i$	$\tilde{u}^{i*}_R$	$u^{i\dagger}_R$
$\bar{D}_i$	$\tilde{d}^{i*}_R$	$d^{i\dagger}_R$
L_i	$(\tilde{\nu}^i, \tilde{\ell}^i_L)^T$	$(\nu^i, \ell^i_L)^T$
$\bar{E}_i$	$\tilde{\ell}^{i*}_R$	$\ell^{i\dagger}_R$
Supermultiplet	Higgs fields (spin-0)	Higgsino fields (spin-$\frac{1}{2}$)
H_u	$(H^+_u, H^0_u)^T$	$(\tilde{H}^+_u, \tilde{H}^0_u)^T$
H_d	$(H^0_d, H^-_d)^T$	$(\tilde{H}^0_d, \tilde{H}^-_d)^T$

transformations. Even though these superpartners are scalar particles, they are called left-handed and right-handed sfermions. Secondly, the gauge interactions of the sfermions are the same as for their corresponding Standard Model partners. For example, left-handed sfermions couple to the W bosons, while right-handed sfermions do not.

Two complex $SU(2)_L$ doublets with weak hypercharges of $Y = +1/2$ and $Y = -1/2$, denoted by H_u and H_d, are needed in the MSSM to obtain the Yukawa couplings that generate the masses of the Standard Model up-type and down-type fermions, respectively. Their weak isospin components are denoted by $(H^+_u, H^0_u)^T$ and $(H^0_d, H^-_d)^T$ indicating the different electric charges. These Higgs fields are part of chiral supermultiplets together with their superpartners, which are spin-$\frac{1}{2}$ fermions and called Higgsinos.

Vector supermultiplets, summarised in Table 3.2, contain the gauge bosons and their superpartners called gauginos, which are spin-$\frac{1}{2}$ fermions. In contrast to the Standard Model fermions, left-handed and right-handed gauginos have the same gauge transformations. All gauginos have an ‘ino’ at the end of their name, e.g. gluino.

3.2.2 Supersymmetry breaking and the mass eigenstates

All particles of a supermultiplet must have the same mass, as the squared-mass operator $-P^2$ commutes with the operators Q and $Q^\dagger$ according to Equation (3.2). However,

Table 3.2: Components of the vector supermultiplets of the MSSM in the adjoint representations of the Standard Model gauge symmetries with the indices $a = 1, \ldots 8$ and $b = 1, 2, 3$

Supermultiplet	Gaugino	Gauge boson
G^a	$\tilde{g}^a$	g_μ^a
W^b	$\tilde{W}^b$	W_μ^b
B	$\tilde{B}$	B_μ

supersymmetric particles have not been observed yet, and therefore they have to be much heavier than their Standard Model partners. This means that supersymmetry must be a broken symmetry.

Analogous to the electroweak symmetry breaking, supersymmetry is expected to be spontaneously broken, i.e. the Lagrangian density of the theory is invariant under supersymmetric transformations but its vacuum state is not. Since it is not known which process of supersymmetry breaking is realised in nature, the origin of supersymmetry breaking is decoupled from the MSSM by adding terms to the Lagrangian density that break supersymmetry explicitly:

$$\mathcal{L}_{\mathrm{MSSM}} = \mathcal{L}_{\mathrm{SUSY}} + \mathcal{L}_{\cancel{\mathrm{SUSY}}}, \tag{3.13}$$

where $\mathcal{L}_{\mathrm{SUSY}}$ is invariant under supersymmetry and given by Equation (3.11), i.e. it contains all gauge and Yukawa interactions, while $\mathcal{L}_{\cancel{\mathrm{SUSY}}}$ breaks supersymmetry and includes the mass terms of supersymmetric particles. Consequently, $\mathcal{L}_{\mathrm{MSSM}}$ is an effective Lagrangian density that is only valid for energies below the supersymmetry breaking scale.

In the MSSM, so-called soft supersymmetry breaking [45] is assumed in which all parameters of $\mathcal{L}_{\cancel{\mathrm{SUSY}}}$ have a positive mass dimension to maintain the cancellation of the quadratically divergent radiative loop corrections to the masses of all scalar particles, in particular the Standard Model Higgs boson, to all orders in perturbation theory. The remaining corrections to the Higgs mass have the form

$$\Delta m_h^2 = m_{\mathrm{soft}}^2 \left[\frac{\lambda}{16\pi^2} \ln(\Lambda / m_{\mathrm{soft}}) + \ldots \right], \tag{3.14}$$

where m_{soft} is the largest mass of $\mathcal{L}_{\cancel{\text{SUSY}}}$ and λ is schematic for various dimensionless couplings. Assuming $\Lambda \sim m_{\text{Pl}}$ and $\lambda \sim 1$, it can be estimated from Equation (3.14) [46, 47] that m_{soft} should be at the TeV scale. Otherwise fine-tuning of the (Minimal Supersymmetric) Standard Model parameters is needed to stabilise the Higgs mass. This circumstance, referred to as naturalness, is one of the main motivations to search for supersymmetry at the Large Hadron Collider.

The most general soft supersymmetry breaking Lagrangian density conserving the gauge symmetries and R-parity (see Section 3.2.3) is given by

$$
\begin{aligned}
\mathcal{L}_{\cancel{\text{SUSY}}} = &-\frac{1}{2}\left(M_3\tilde{g}\tilde{g} + M_2\tilde{W}\tilde{W} + M_1\tilde{B}\tilde{B} + \text{c.c.}\right) \\
&-\left(\tilde{\bar{U}}\mathbf{a_U}\tilde{Q}H_u - \tilde{\bar{D}}\mathbf{a_D}\tilde{Q}H_d - \tilde{\bar{E}}\mathbf{a_E}\tilde{L}H_d + \text{c.c.}\right) \\
&-\tilde{Q}^\dagger\mathbf{m^2_Q}\tilde{Q} - \tilde{L}^\dagger\mathbf{m^2_L}\tilde{L} - \tilde{\bar{U}}\mathbf{m^2_{\bar{U}}}\tilde{\bar{U}}^\dagger - \tilde{\bar{D}}\mathbf{m^2_{\bar{D}}}\tilde{\bar{D}}^\dagger - \tilde{\bar{E}}\mathbf{m^2_{\bar{E}}}\tilde{\bar{E}}^\dagger \\
&- m^2_{H_u}H_u^*H_u - m^2_{H_d}H_d^*H_d - \left(bH_uH_d + \text{c.c.}\right).
\end{aligned}
\tag{3.15}
$$

The first line of Equation (3.15) consists of the gluino, wino and bino mass terms with masses $|M_3|$, $|M_2|$ and $|M_1|$, respectively. The second line contains couplings between three scalar particles parametrised by the coupling parameters $\mathbf{a_U}$, $\mathbf{a_D}$, $\mathbf{a_E}$, which are complex 3×3 matrices in family space. The mass terms for the squarks and sleptons with the complex Hermitian 3×3 matrices $\mathbf{m^2_Q}$, $\mathbf{m^2_L}$, $\mathbf{m^2_{\bar{U}}}$, $\mathbf{m^2_{\bar{D}}}$ in family space form the third line. Finally, there are supersymmetry breaking contributions to the Higgs potential with the mass parameters $m^2_{H_u}$, $m^2_{H_d}$ and b. The term bH_uH_d + c.c. is needed to allow for a non-zero vacuum expectation value of the Standard Model Higgs field. This means in particular that the breaking of the electroweak symmetry in the MSSM implies that supersymmetry must be broken. The values of the mass and coupling parameters of $\mathcal{L}_{\cancel{\text{SUSY}}}$ are not known, and thus $\mathcal{L}_{\cancel{\text{SUSY}}}$ significantly increases the number of parameters of the MSSM. There are 105 new parameters [48] in addition to the 19 parameters of the Standard Model.

The electroweak gauginos and the Higgsinos sharing the same quantum numbers in general mix to form new mass eigenstates. The neutral gauginos $\tilde{W}^0$ and $\tilde{B}^0$ mix with the neutral Higgsinos $\tilde{H}_u^0$ and $\tilde{H}_d^0$ to form the four neutralinos $\tilde{\chi}_1^0$, $\tilde{\chi}_2^0$, $\tilde{\chi}_3^0$, $\tilde{\chi}_4^0$. Their masses are obtained by diagonalising the mass matrix

$$\mathbf{M}_{\tilde{\chi}^0} = \begin{pmatrix} M_1 & 0 & -g_Y v_d/\sqrt{2} & g_Y v_u/\sqrt{2} \\ 0 & M_2 & g_W v_d/\sqrt{2} & -g_W v_u/\sqrt{2} \\ -g_Y v_d/\sqrt{2} & g_W v_d/\sqrt{2} & 0 & -\mu \\ g_Y v_u/\sqrt{2} & -g_W v_u/\sqrt{2} & -\mu & 0 \end{pmatrix}, \tag{3.16}$$

where v_u and v_d are the vacuum expectation values of the Higgs doublets H_u and H_d, respectively, and μ is a parameter of the superpotential (see Section 3.2.3). Adding v_u and v_d in quadrature yields the square of the vacuum expectation value $|\langle\Phi\rangle|$ of the Standard Model Higgs field (see Equation (2.14)):

$$v_u^2 + v_d^2 = |\langle\Phi\rangle|^2. \tag{3.17}$$

The charged gauginos $\tilde{W}^+$ and $\tilde{W}^-$ mix with the charged Higgsinos $\tilde{H}_u^+$ and $\tilde{H}_d^-$ to form the four charginos $\tilde{\chi}_1^\pm$, $\tilde{\chi}_2^\pm$. Diagonalising the mass matrix

$$\mathbf{M}_{\tilde{\chi}^\pm} = \begin{pmatrix} 0 & \mathbf{X}^\mathrm{T} \\ \mathbf{X} & 0 \end{pmatrix} \text{ with } \mathbf{X} = \begin{pmatrix} M_2 & g_W v_u \\ g_W v_d & \mu \end{pmatrix} \tag{3.18}$$

yields the masses of the charginos. The neutralinos and charginos are labelled in ascending mass order. The remaining gauginos, the gluinos, do not mix as there are no other supersymmetric particles sharing the same quantum numbers.

There is also a mixing between the two scalar superpartners of each electrically charged Standard Model fermion f, labelled $\tilde{f}_L$ and $\tilde{f}_R$, to form the mass eigenstates $\tilde{f}_1$ and $\tilde{f}_2$. The strength of the mixings depends on several parameters, including the masses of the Standard Model partners, which is why usually only third generation mixings are considered.

The two Higgs doublets H_u and H_d have eight degrees of freedom, of which three are needed to generate the $W^\pm$ and Z boson masses, as in the Standard Model, and the remaining five degrees of freedom correspond to five physical Higgs bosons. Four of them are scalar particles, namely the neutral Higgs boson h, its heavier version H and the two charged Higgs bosons H^+ and H^-. If the MSSM is to be consistent with the current experimental results, then h must be the Higgs boson observed by ATLAS and CMS. The fifth Higgs boson, A, is a pseudoscalar field, which changes sign under parity inversion.

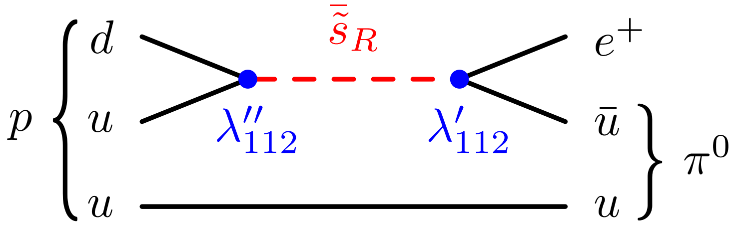

Figure 3.1: Example of a proton decay mediated by a virtual strange squark.

3.2.3 The superpotential and R-parity

The non-gauge interactions between the chiral superfields, which correspond to the chiral supermultiplets in Table 3.1, are described by the superpotential W whose general form is given by Equation (3.12). Writing down all possible renormalisable and gauge-invariant superpotential terms involving the chiral superfields of the MSSM yields

$$\begin{aligned} W = &(y_u^{ij} Q_i H_u \bar{U}_j + y_d^{ij} Q_i H_d \bar{D}_j + y_e^{ij} L_i H_d \bar{E}_j + \mu H_u H_d) + \\ &+ (\lambda^{ijk} L_i L_j \bar{E}_k + \lambda'^{ijk} L_i Q_j \bar{D}_k + \lambda''^{ijk} \bar{U}_i \bar{D}_j \bar{D}_k + \kappa^i L_i H_u), \end{aligned} \tag{3.19}$$

where i, j, k are generation indices, $\mathbf{y_u}$, $\mathbf{y_d}$, $\mathbf{y_e}$, λ, λ', λ'' yukawa couplings and μ and κ mass parameters.

The interactions associated with the coupling parameter λ'' violate the baryon number $B = \frac{1}{3}(N(q) - N(\bar{q}))$ conservation, while the remaining three interactions in the second line of Equation (3.19) violate the lepton number $L = N(\ell) - N(\bar{\ell})$ conservation. Simultaneous violation of lepton and baryon number conservation leads to rapid proton decay, for example into a lepton and a meson (see Figure 3.1). However, measurements at the Japanese water Čerenkov detector Super Kamiokande [49] set a lower limit of the proton lifetime of about 10^{34} years at 90% confidence level due to the non-observation of such a decay. There are comparable limits also for other decay modes [50].

To prevent rapid proton decay, a new conserved multiplicative quantum number called R-parity [51] is introduced in the MSSM,

$$P_\mathrm{R} = (-1)^{3(B-L)+2s}, \tag{3.20}$$

where s is the spin of the particle. All particles of the Standard Model together with the five Higgs bosons of the MSSM have $P_\mathrm{R} = +1$ while all supersymmetric particles have

$P_{\mathrm{R}} = -1$. R-parity conservation (RPC) forbids both interactions in the process in Figure 3.1 and has the following consequences for supersymmetry searches at collider experiments:

1. The lightest supersymmetric particle (LSP) with $P_{\mathrm{R}} = -1$ is stable, since it cannot decay into lighter Standard Model particles, which have $P_{\mathrm{R}} = +1$.
2. Mixing between Standard Model particles and their superpartners is not possible.
3. Supersymmetric particles can be produced only in even numbers (usually in pairs).
4. Supersymmetric particles, apart from the LSP, decay in cascades into final states which contain an odd number of LSPs (usually one).
5. The lepton number and baryon number violating terms in Equation (3.21) are forbidden, resulting in the superpotential

$$W_{\mathrm{MSSM}} = y_u^{ij} Q_i H_u \bar{U}_j + y_d^{ij} Q_i H_d \bar{D}_j + y_e^{ij} L_i H_d \bar{E}_j + \mu H_u H_d. \tag{3.21}$$

Since with R-parity conservation the LSP is stable and would have been produced in the early universe, it would be a good candidate for a dark matter particle if it is electrically neutral [52, 53]. Charged or colored LSPs are strongly disfavoured due to tight upper limits on the relic abundances of such particles [53]. The left-handed sneutrino has been ruled out as a dark matter candidate by direct dark matter searches [54]. Thus, the LSP is most likely the lightest neutralino. Two further candidates are possible in extensions of the MSSM, the right-handed sneutrino and the gravitino, which is the superpartner of the spin-2 graviton, the mediator of quantum gravity, in supergravity theories with local supersymmetry.

3.3 R-parity violation

While the simultaneous violation of the lepton and baryon number conservation is essentially excluded by the non-observation of the proton decay, the non-conservation of one of the two quantum numbers alone is much less constrained. In this case, **one** of the two terms

$$W_{\Delta L=\pm 1} = \kappa^i L_i H_u + \lambda^{ijk} L_i L_j \bar{E}_k + \lambda'^{ijk} L_i Q_j \bar{D}_k \tag{3.22}$$

or

$$W_{\Delta B=\pm 1} = \lambda''^{ijk} \bar{U}_i \bar{D}_j \bar{D}_k \tag{3.23}$$

may be included in the superpotential of the MSSM instead of forbidding them both by requiring R-parity conservation. An example is the conservation of baryon triality [55, 56].

The baryon triality is defined for particles with baryon number B and weak hypercharge Y as

$$Z_3^B = e^{2\pi i(B-2Y)/3}. \tag{3.24}$$

The symmetry requires that the product of the baryon trialities of the particles in any term in the Lagrangian density and the superpotential is equal to one. For each particle of the MSSM, Z_3^B is a cube root of unity. Consequently, the baryon triality is conserved in the MSSM. It implies baryon number conservation and violates the lepton number, i.e. it allows all terms of $W_{\Delta L=\pm 1}$ in Equation (3.22).

In total, there are 48 parameters in the superpotential terms of Equations (3.22) and (3.23), 45 of which are dimensionless Yukawa-type couplings, 9 λ^{ijk}, 27 λ'^{ijk} and 9 λ''^{ijk} couplings, while the remaining three are the dimensionful κ^i parameters. The number of independent λ' couplings is larger than the number of λ and λ'' couplings since gauge-invariance requires $\lambda^{ijk} = -\lambda^{jik}$ and $\lambda''^{ijk} = -\lambda''^{ikj}$.

Besides from the superpotential, R-parity violating (RPV) interactions[2] emerge also from the soft supersymmetry breaking terms

$$\begin{aligned}\mathcal{L}^{\text{RPV}}_{\cancel{\text{SUSY}}} =& \frac{1}{2} A^{ijk} \tilde{L}_i \tilde{L}_j \tilde{\bar{E}}_k + A'^{ijk} \tilde{L}_i \tilde{Q}_j \tilde{\bar{D}}_k + \frac{1}{2} A''^{ijk} \tilde{\bar{U}}_i \tilde{\bar{D}}_j \tilde{\bar{D}}_k \\ &+ b^i H_u \tilde{L}_i + (m_d^i)^2 H_d^* \tilde{L}_i + \text{c.c.}\,,\end{aligned} \tag{3.25}$$

which introduce 51 new parameters, 45 of them belonging to the A-terms that have the same antisymmetry properties as the corresponding superpotential couplings, while the remaining six parameters are the three b^i couplings and the three mass parameters m_d^i. Using a suitable superfield redefinition, three of the parameters κ^i, b^i and m_d^i can be eliminated resulting in a total of 96 independent RPV parameters.

The RPV terms of Equations (3.22), (3.23) and (3.25) are classified into bilinear and trilinear terms depending on the number of their chiral superfields, which are two and three, respectively. The bilinear terms describe mixings between sleptons and Higgs bosons carrying the same quantum numbers, the term $\kappa^i L_i H_u$ describes in addition the mixings between leptons and Higgsinos. Consequently, neutrinos can acquire masses by mixing with neutralinos, which means that RPV supersymmetry can explain the observed neutrino masses and neutrino flavour oscillations. Trilinear couplings describe the decays

[2] A broad overview of RPV supersymmetry can be found in reference [57].

Table 3.3: Upper bounds at 95% confidence level on the most constrained coupling for each class of RPV supersymmetry operators. The bounds are given for sfermion masses $m_{\tilde{f}}$ of 1 TeV and are typically proportional to $\frac{m_{\tilde{f}}}{100\,\mathrm{GeV}}$ [58].

Couplings	λ^{ijk}	λ'^{1jk}	λ'^{2jk}	λ'^{3jk}	λ''^{ijk}
Upper bound	0.49	0.09	0.59	1.1	0.5

of sfermions into two Standard Model fermions. The remaining part of this section focuses on trilinear couplings as only these are relevant for the search discussed in Chapter 5.

Lepton number and baryon number violating processes have not been observed yet, so that upper bounds can be placed on all RPV couplings. The constraints on trilinear couplings from μ, τ and meson decays etc. [58] are summarised in Table 3.3. These bounds depend on the masses of the sfermions and become weaker as the sfermion masses increase. For a sfermion with a mass of 1.0 TeV, the strongest upper bound is 0.09 on λ'^{1jk}. Many processes set bounds also on the product of two couplings, which can be significantly tighter than the bounds on single couplings. The lower limit on the proton lifetime, for example, requires $|\lambda'\lambda''^{*}| < \mathcal{O}(10^{-9})$ for all possible coupling combinations. Therefore, most RPV supersymmetric models considered in collider searches assume a single dominant coupling to evade these tight constraints.

The implications of RPC discussed in Section 3.2.3 are no longer valid for RPV models. Consequently, the LSP can be any supersymmetric particle and it decays into Standard Model particles. Another consequence of RPV is that supersymmetric particles do not have to be produced in pairs. If the trilinear couplings are smaller than $\mathcal{O}(10^{-1})$, however, the production of the supersymmetric particles is dominated by gauge interactions meaning that they are pair produced and decay in cascades to the LSP as in the case of RPC.

The lifetime of the LSP depends on the magnitude of the RPV couplings that mediate its decay. If these couplings are small, then the lifetime of the LSP can be of the order of ps to ns, so that its decay can be resolved as a secondary vertex in the inner tracking volume of the ATLAS detector. This is explained in more detail in Section 5.1 using a signal model where the LSP is the lightest neutralino.

Chapter 4

The ATLAS experiment

Since supersymmetry could answer many of the open questions in particle physics, it is important to search for it at collider experiments, where highly energetic particles are collided and the remnants of the collisions are studied with large detectors. Numerous experiments at past colliders, such as the Large Electron-Positron Collider (LEP) or the Tevatron, have tried to discover supersymmetry, but without success. In 2008, a new accelerator, the Large Hadron Collider (LHC) [59], was completed together with four main experiments, to probe particle physics at unprecedented energies. One of these experiments is ATLAS (**A** **T**oroidal **L**HC **A**pparatu**s**) [60], a multi-purpose detector designed to study the electroweak symmetry breaking and to search for physics beyond the Standard Model, especially supersymmetry.

The LHC and its performance are discussed in the next section. Section 4.2 explains the layout and functional principles of the ATLAS detector. Finally, the simulation and the reconstruction of collision events are described in Section 4.3 and 4.4, respectively.

4.1 The Large Hadron Collider

The LHC is the world's largest particle accelerator with a circumference of 26.7 km. It was built by the European Organisation for Nuclear Research (CERN) and lies beneath the France-Switzerland border near Geneva. The LHC was installed in the existing underground tunnel of its predecessor, LEP, whose depth varies between 50 m and 175 m with a mean of about 100 m. Two independent systems of 400 MHz radio frequency cavities accelerate the particles, which are kept on a circular orbit by superconducting magnets cooled with liquid helium down to 1.9 K. The particles are collimated into two counter-rotating beams that are brought to collision at four intersection points where the detectors are located. Most of the time, the LHC is operated with two proton beams, which are produced and pre-accelerated by a system of linear and circular accelerators shown in Figure 4.1 and then injected into the LHC ring. Heavy ions, lead usually, are also collided to study the quark-gluon plasma, a very hot and dense state of matter consisting of asymptotically free quarks and gluons. The analysis presented in Chapter 5 is performed on data from proton–proton collisions recorded in 2016, and therefore heavy ion collisions are not discussed further.

The LHC was designed to accelerate protons to energies of 7 TeV resulting in a centre-of-mass energy $\sqrt{s}$ of 14 TeV. Due to issues with the magnet system, however, the LHC has not been operated yet at its nominal energy. During the LHC Run 1 (2010–2012) $\sqrt{s}$ was 7 TeV in the first two years and 8 TeV in the third year. It was increased in the LHC Run 2 (2015–2018) to 13 TeV. For Run 3 scheduled to start in 2021, it is planned to reach the nominal energy.

The proton beams consist of bunches each filled with more than 10^{11} protons. The number of bunches per beam varies between the different data-taking periods and in 2016 it was most of the time 2076 or 2220. Each bunch has a length of about 1 ns and the spacing between two bunches is 25 ns leading to a crossing frequency of 40 MHz. The data recorded at the ATLAS detector for one bunch-crossing is usually referred to as an event.

The number of events per second produced in collisions at the LHC for a given process of interest is

$$\frac{dN}{dt} = \mathcal{L}\sigma, \tag{4.1}$$

where $\mathcal{L}$ is the instantaneous luminosity, a measure for how many collisions occur per unit time and area, and σ is the cross-section of the process in units of area, which describes the probability that this process occurs. The instantaneous luminosity $\mathcal{L}$ depends on the beam properties and is defined as:

$$\mathcal{L} = \frac{n_\mathrm{b} f_\mathrm{r} n_1 n_2}{2\pi \Sigma_x \Sigma_y}, \tag{4.2}$$

where n_1 and n_2 are the number of protons of the two beams, f_r is the revolution frequency of the LHC, n_b is the number of bunch pairs colliding in each revolution, and Σ_x and Σ_y are the horizontal and vertical convolved beam sizes.

The instantaneous luminosity at the ATLAS detector is measured using two luminometers [62], BCM (**B**eam **C**onditions **M**onitor) and LUCID-2 (**Lu**minosity Measurement

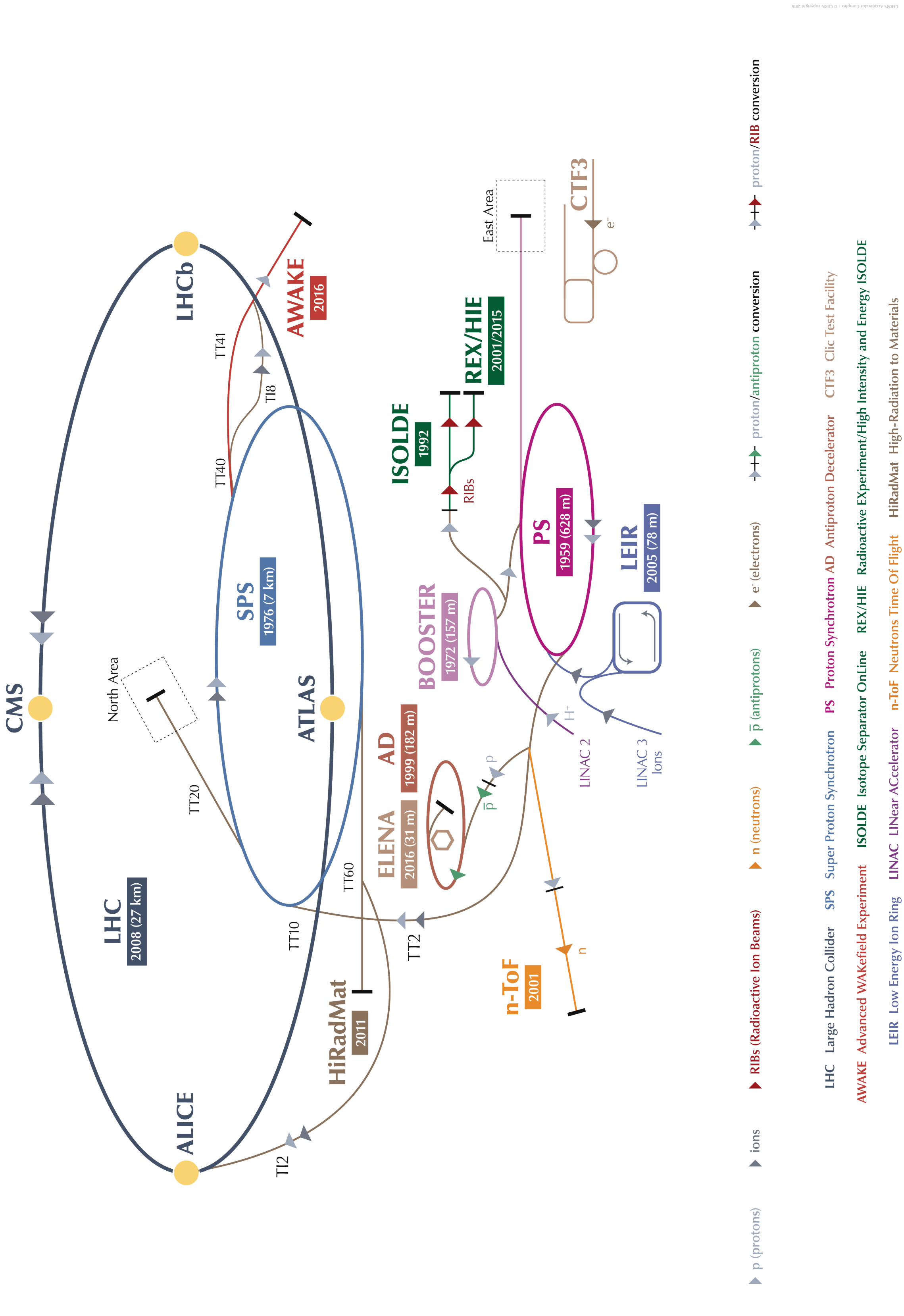

Figure 4.1: The accelerator complex of CERN [61].

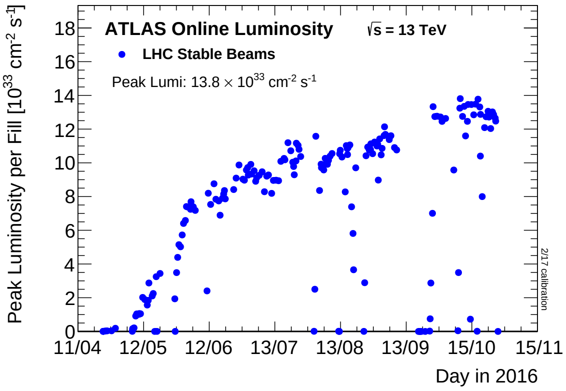

(a)

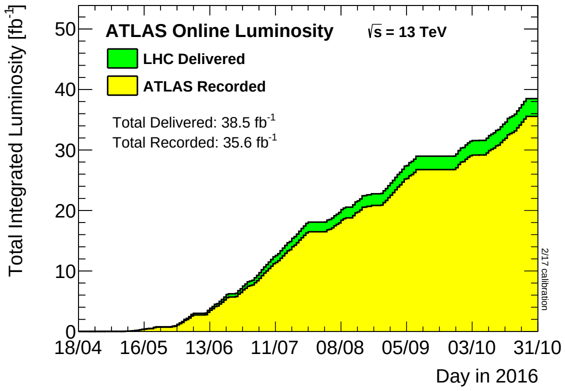

(b)

Figure 4.2: (a) Peak luminosity and (b) integrated luminosity of *pp* collisions at the ATLAS experiment in 2016 as function of time [64].

Using A **C**herenkov **I**ntegrating **D**etector) [63], supplemented by a method that counts the number of charged particles per bunch-crossing. To achieve a statistical precision at the percent level, the measured luminosity is averaged over the time of approximately one minute. This time interval is called a luminosity block in which the detector and luminosity conditions are assumed to be stable.

At the beginning of a physics run, the instantaneous luminosity is maximal, referred to as peak luminosity, and then it decreases over time as more and more protons are lost to collisions. Initially, the LHC was designed to achieve a peak luminosity of $1.0 \times 10^{34}\,\mathrm{cm}^{-2}\,\mathrm{s}^{-1}$, however, improvements of the beam sizes at the interaction points allowed the LHC to reach values of up to $1.4\times10^{34}\,\mathrm{cm}^{-2}\,\mathrm{s}^{-1}$ in 2016 as shown in Figure 4.2a and even values above $2.0 \times 10^{34}\,\mathrm{cm}^{-2}\,\mathrm{s}^{-1}$ in 2017 and 2018. The instantaneous luminosity summed over all luminosity blocks, called the integrated luminosity, is a measure for the amount of data collected and illustrated in Figure 4.2b for 2016. In total, the LHC delivered $38.5\,\mathrm{fb}^{-1}$ to the ATLAS experiment in 2016 of which $35.6\,\mathrm{fb}^{-1}$ (92.5%) were recorded. To be eligible for physics analyses, each data event has to pass quality criteria ensuring that all components of the detector were operational. In 2016, $32.8\,\mathrm{fb}^{-1}$ (92.1%) of the recorded data satisfied these criteria.

Due to the high proton density at the interaction points, there are multiple proton–proton collisions per bunch-crossing, an effect called pileup. Figure 4.3 shows that on average about 25 proton–proton collisions occurred per bunch-crossing in 2016. The vast majority of proton–proton collisions produce low energetic particles. At most one collision

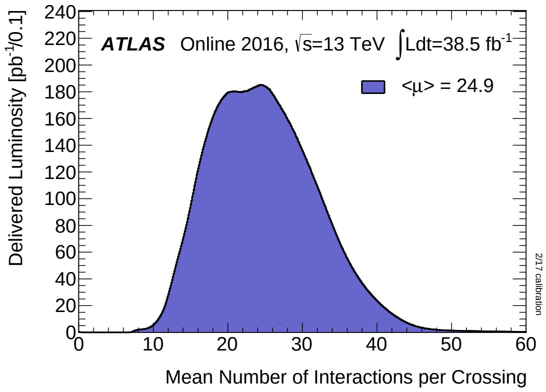

Figure 4.3: Integrated luminosity of *pp* collisions delivered to the ATLAS experiment in 2016 as a function of the mean number of interactions per bunch-crossing [64].

per bunch-crossing contains a collision with a large momentum transfer, also called a hard-scatter process. Hard-scatter processes produce copious numbers of jets as well as other particles (see Figure 4.4). New physics processes beyond the Standard Model such as supersymmetry are expected to produce heavy particles, and thus it is crucial to study these hard-scatter processes. This requires the capability to discriminate particles from the hard-scatter process and the pileup processes, meaning a sufficiently high detector resolution so that each particle track can be associated with the proton–proton collision from which it originated. The technology with which the ATLAS detector achieves this precision is explained in the next section.

4.2 The ATLAS detector

The ATLAS detector illustrated in Figure 4.5 has a length of 44 m, a diameter of 25 m and a total weight of about 7000 tons. It has a forward-backward symmetric cylindrical geometry and uses a right-handed coordinate system with its origin at the nominal interaction point in the centre of the detector and the z-axis along the beam direction. The xy plane is transverse to the beam direction with the x-axis pointing toward the centre of the LHC ring and the y-axis vertically upwards. Cylindrical coordinates r and ϕ are used in the transverse plane, where the radius $r = \sqrt{x^2 + y^2}$ denotes the transverse distance from the interaction point and the azimuthal angle ϕ is measured around the z-axis. The pseudorapidity $\eta = -\ln(\tan(\theta/2))$ is defined in terms of the polar angle θ measured with respect to the

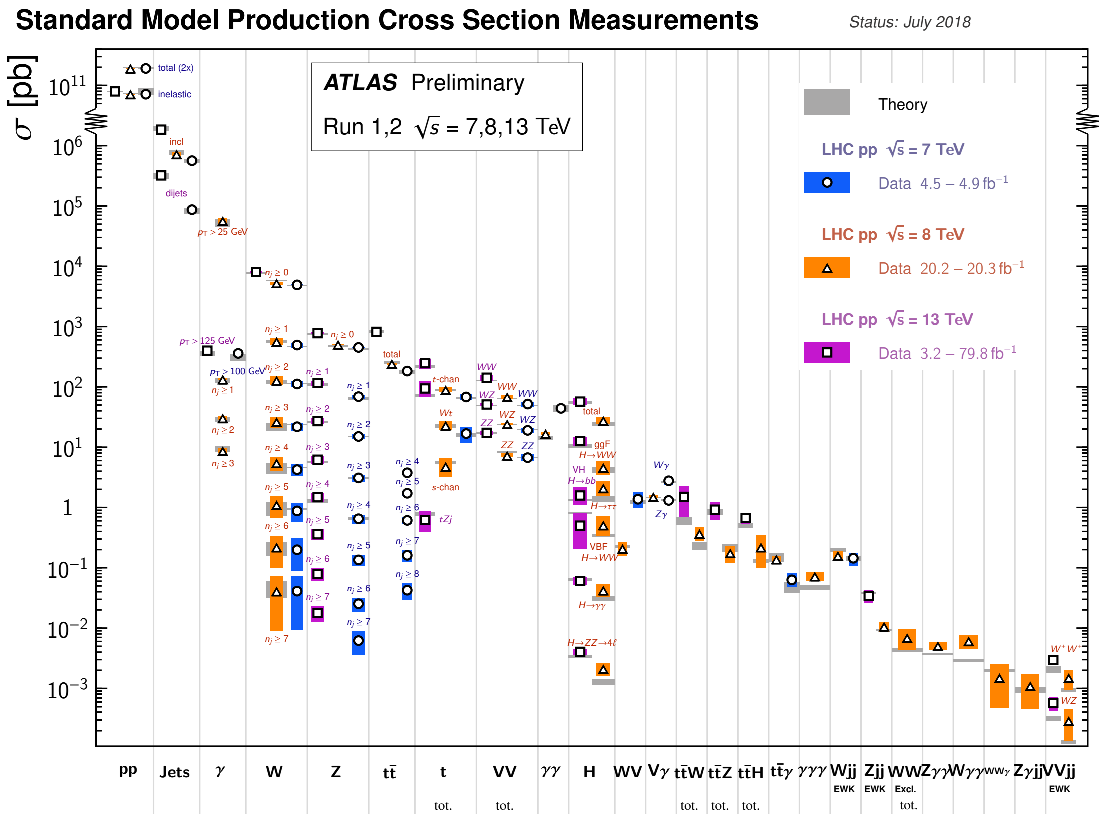

Figure 4.4: Summary of several Standard Model total and fiducial production cross-section measurements, corrected for leptonic branching fractions, compared to the corresponding theoretical expectations [64]. All theoretical expectations were calculated at the next-to-leading order or higher. The luminosity used for each measurement is indicated in the legend.

positive z-axis. Opening angles between two objects or cone sizes are often expressed in terms of $\Delta R = \sqrt{\Delta\eta^2 + \Delta\phi^2}$.

The detector system consists of three major subsystems: the inner detector, the calorimeters and the muon spectrometer. They are described in the following sections together with the trigger system, which decides what data are worth keeping. Further information about the ATLAS experiment can be found in reference [60].

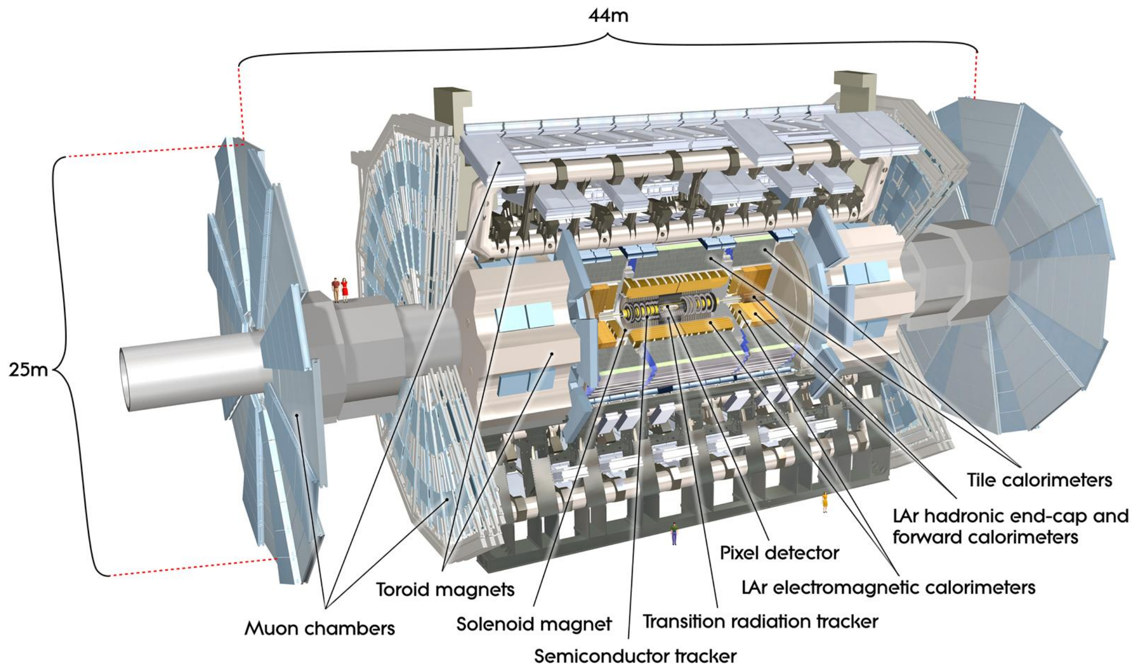

Figure 4.5: Cut-away view of the ATLAS detector [64].

4.2.1 The inner detector

The inner detector illustrated in Figure 4.6 encompasses the beam pipe, a 7.3 m long pipe with a diameter of 50 mm made in beryllium, and measures the paths of electrically charged particles. It consist of three independent tracking detectors, which are embedded in a 2 T axial magnetic field created by a solenoid that is 5.3 m long and 2.5 m in diameter. The solenoid coil is aligned with the beam pipe and surrounds all tracking detectors. The magnetic field deflects charged particles, and the curvature and direction of the deflection allows to measure their transverse momentum and the sign of their electric charge.

The innermost tracking detector is the **pixel detector**, which has the highest granularity and number of readout channels of all detectors in ATLAS. It is segmented into more than 86 million pixels each with a nominal size of 50 µm × 400 µm or 50 µm × 250 µm in the inner most layer. A hit is recorded in a pixel sensor when the electric charge deposited by a charged particle exceeds a certain threshold. Like most other detectors of ATLAS, the pixel detector is divided into a barrel and an end-cap part to cover $|\eta|$ values up to 2.5. The barrel contains four concentric layers that are parallel to the beam axis while

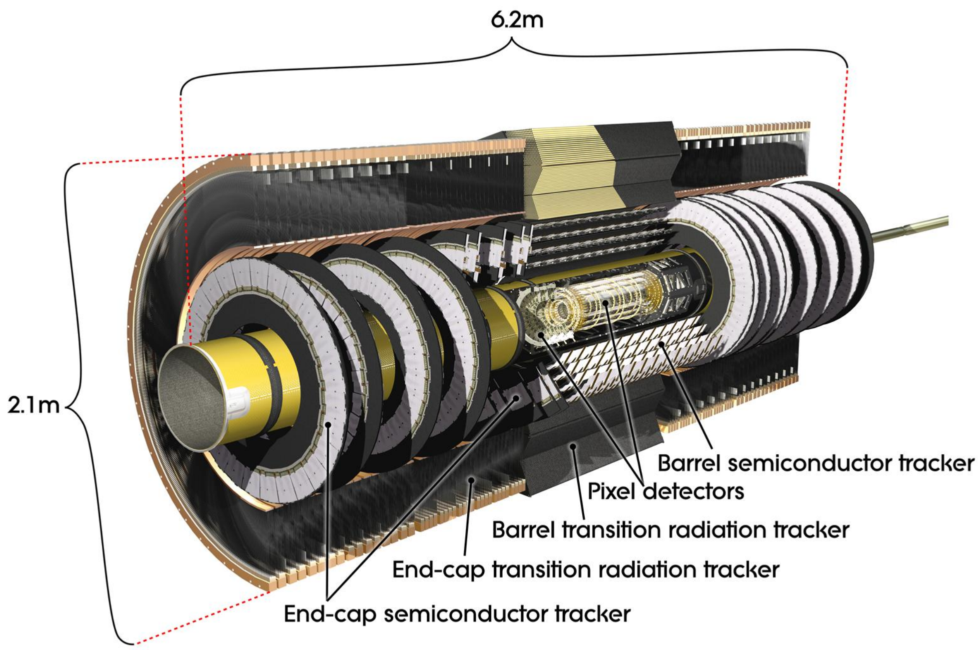

Figure 4.6: Cut-away view of the ATLAS inner detector [64].

the end-cap is made of three disks that are perpendicular to the beam axis. The positions and dimensions of the various parts of the pixel detector can be seen in Figure 4.7. The large number of pixels is necessary to achieve a high accuracy of the hit positions, 10 µm (r–ϕ) and 115 µm (z) in the barrel region and 10 µm (r–ϕ) and 115 µm (r) in the end-cap region, which allows a precise track reconstruction, so that the vast majority of vertices of proton–proton collisions can be resolved.

Next is the **semi-conductor tracker (SCT)**, while its layout and functional principle is very similar to the pixel detector, it is made of approximately 6.3 million silicon microstrips instead of pixels. Each SCT module consists of two pairs of single-sided sensors glued back-to-back and tilted by 40 mrad to allow for a two-dimensional position measurement. The two sensors of one side are wire-bonded leading to 126 mm long microstrips with a pitch of 80 µm in the barrel modules and 57–94 µm in the end-cap modules. The SCT barrel has four layers of rectangular modules, while radial strips of constant azimuth are used for the trapezoidal sensors in the eighteen end-cap disks. The accuracy of the hit positions are 17 µm (r–ϕ) and 580 µm (z) in the barrel region and 17 µm (r–ϕ) and 580 µm (r) in the end-cap region. The positions and dimensions of the barrel layers and of the

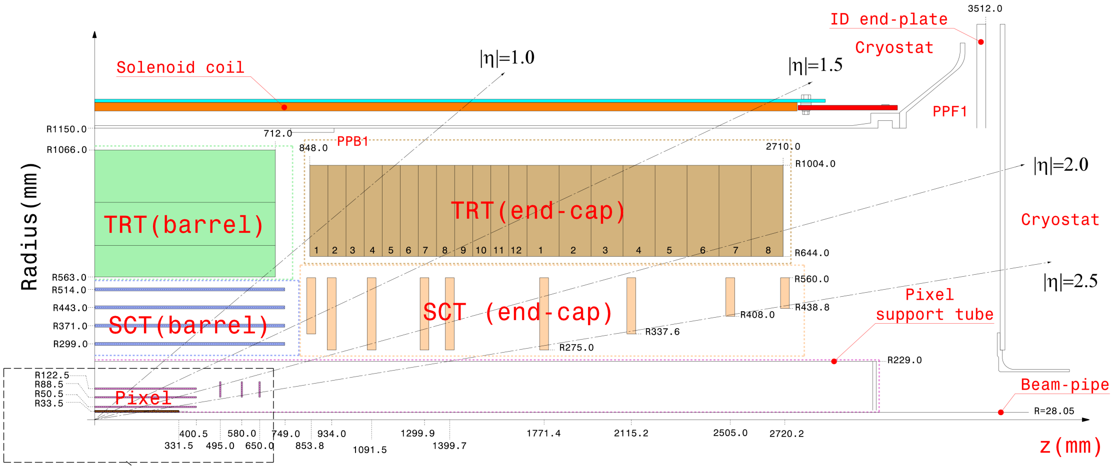

Figure 4.7: Schematic view of a quarter-section of the ATLAS inner detector that shows the main detector elements with their dimensions [64].

end-cap disks are illustrated in Figure 4.7. As with the pixel detector, the SCT detector covers $|\eta|$ values up to 2.5.

Finally, there is the **transition radiation tracker (TRT)** consisting of more than 300000 straw tubes that are 4 mm in diameter, have a 31 μm diameter gold-plated tungsten wire in the centre and are filled with a xenon-based gas mixture (70% Xe, 27% CO_2 and 3% O_2)[1]. The straw tubes serve two purposes, first they are classical drift tubes, where the incoming charged particle ionises gas atoms and the resulting electrons are accelerated in a radial electrical field towards the central anode, leading to the formation of an avalanche near the anode, whose signal is measured. Based on the drift time of the ionisation signal, the distance of the closest approach of the charged particle to the anode wire can be calculated, which is used to reconstruct the track. In addition, transition radiation, which is created by a relativistic charged particle passing through inhomogeneous media, is absorbed in the gas mixture yielding much larger signal amplitudes than for minimum-ionising charged particles[2]. The amount of transition radiation can be used to identify the type of the charged particle. The TRT covers $|\eta|$ values up to 2.0 and provides only r–ϕ information with an accuracy of about 130 μm per tube. In the barrel, the straw tubes are parallel to the beam axis and 144 cm long, while in the end-cap they are 37 cm

[1] During the last years, gas leaks appeared in parts of the TRT, and thus an argon-based gas mixture is used in the affected parts to reduce the operation costs.

[2] Particles whose mean energy loss rates through matter are close to the minimum.

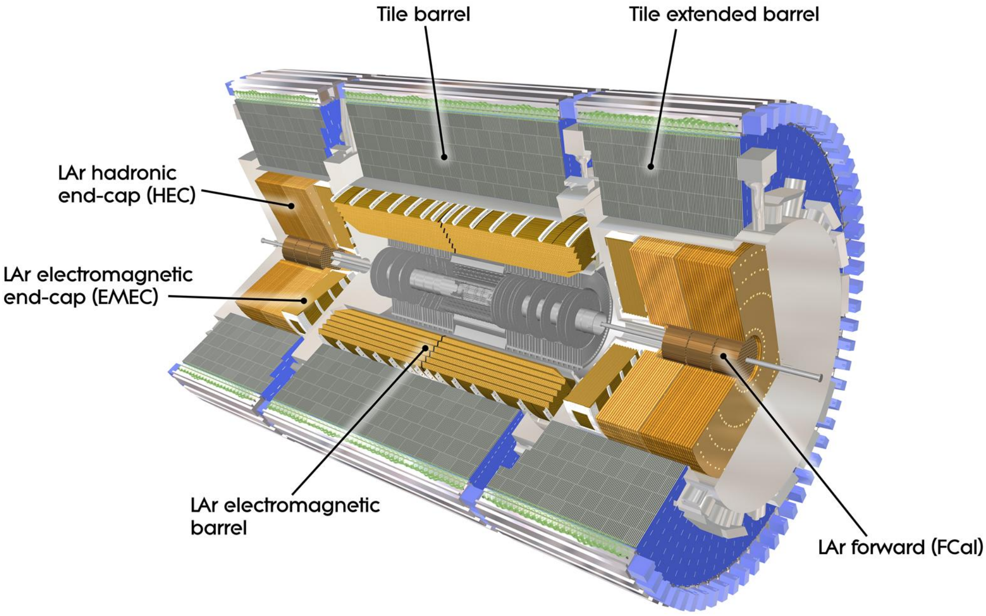

Figure 4.8: Cut-away view of the ATLAS calorimeter system [64].

long and arranged radially in wheels. Figure 4.7 shows the position of the TRT barrel and end-cap inside the inner detector.

4.2.2 The calorimeters

The inner detector is surrounded by calorimeters, which measure the energy of electromagnetically and strongly interacting particles. There are two calorimeters, the liquid argon (LAr) and the tile calorimeter (see Figure 4.8). Both are sampling calorimeters, where the incoming particles interact with a dense absorber material and lose their energy thereby and the resulting particle showers are measured with an active material such as a scintillator.

The inner part of the calorimeter system is the **LAr electromagnetic calorimeter**, whose main purpose is the precise energy measurement of electromagnetically interacting particles, in particular photons and electrons. It consists of lead absorber plates with an accordion geometry allowing for full ϕ coverage and liquid argon as active material. The barrel part of the electromagnetic calorimeter (EMB) covers $|\eta| < 1.475$ and is made of two identical half-barrels, centred around $z = 0$. The two end-caps consist of an inner wheel, the electromagnetic end-cap calorimeter (EMEC), covering $1.375 < |\eta| < 2.5$ and an outer wheel, the hadronic end-cap calorimeter (HEC), covering $2.5 < |\eta| < 3.2$. In contrast to the other LAr calorimeters, the latter uses flat copper plates as absorber. It absorbs strongly interacting particles, i.e. hadrons, to measure their energies together with the electromagnetic calorimeter. The transition region, $1.375 < |\eta| < 1.52$, between the EMB and the EMEC is referred to as the crack region of the LAr calorimeter. It contains a significant amount of inactive material required to perform service on the inner detector. The total thickness of the LAr electromagnetic calorimeter increases with $|\eta|$ from 22 to 33 radiation lengths[3] X_0 in the barrel and from 24 to 38 X_0 in the end-caps.

In the precision region $|\eta| < 2.5$, the LAr electromagnetic calorimeter is segmented into three layers (see Figure 4.9). In front of the first layer, there is the presampler, a thin liquid argon layer without absorber, whose purpose is to correct for the energy loss in the detector parts in front of the LAr calorimeter. The first layer has a very fine granularity of less than 0.01 in $\Delta\eta$ allowing a good separation of photons and π^0. Most of the particle energy is deposited in the second layer as it is much thicker than the other layers. It has a symmetric cell size of 0.025×0.025 in $\Delta\eta \times \Delta\phi$ to provide a good resolution of the η and ϕ measurement. Only particles with high energies reach the third layer and because of this, the cell size in $\Delta\eta$ can be doubled without the loss of resolution. This layout of the calorimeter modules results in an energy resolution of $\frac{10\%}{\sqrt{E/\text{GeV}}} \oplus 0.7\%$ [60].

To measure the energy of particles with $3.1 < |\eta| < 4.9$, there is a **LAr forward calorimeter (FCal)** placed between the beam pipe and the wheels of the HEC at a distance of approximately 4.7 m from the interaction point on each side of the detector. It consists of three modules, where the innermost module uses copper as absorber targeting electromagnetically interacting particles, while the other two modules use tungsten absorbers targeting strongly interacting particles.

The LAr calorimeter is surrounded by the hadronic **tile calorimeter (TileCal)**. It uses steel as absorber and scintillating plastic tiles as active material with a steel to scintillator ratio of 4.7 to 1. The barrel covers the region with $|\eta| < 1.0$ and is 5.8 m long, while the two extended barrels, one on each side of the barrel, cover $0.8 < |\eta| < 1.7$ and are 2.6 m long. Both the barrel and the extended barrels are divided in 64 wedge-shaped azimuthal modules arranged in three radial layers. Each layer is segmented into three-dimensional cells with a granularity in $\Delta\eta \times \Delta\phi$ of 0.1×0.1 in the first two layers and of 0.2×0.1 in

[3]The radiation length X_0 is both the mean distance over which a high-energy electron loses all but $1/e$ of its energy by bremsstrahlung, and $7/9$ of the mean free path for pair production by a high-energy photon.

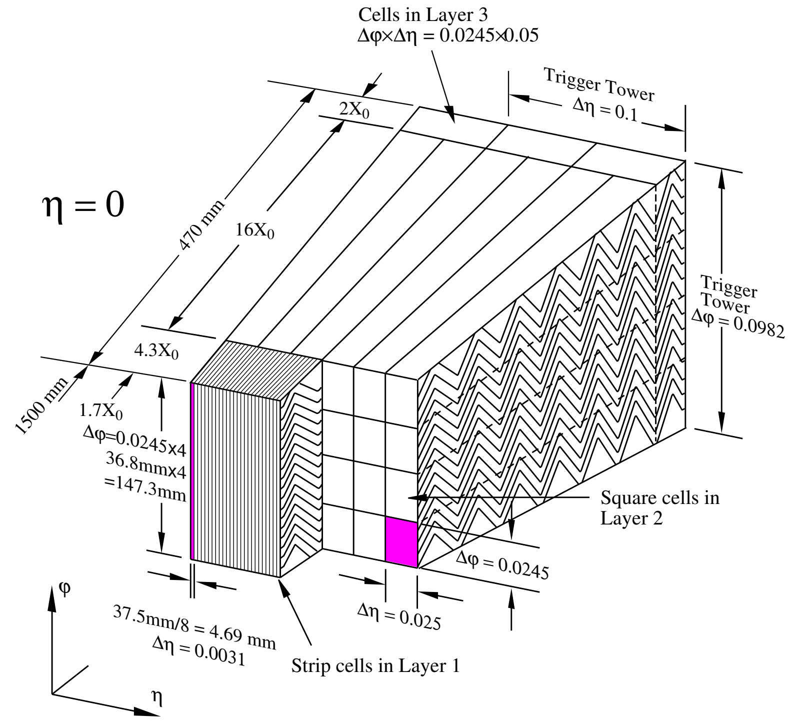

Figure 4.9: Sketch of a barrel module of the LAr calorimeter [64]. The granularity in η and ϕ of the cells of each of the three layers and of the trigger towers is also shown.

the last layer. The TileCal has a radial depth of more than 7 interaction lengths[4] λ. The energy resolution of the TileCal is approximately $\frac{50\%}{\sqrt{E/\mathrm{GeV}}} \oplus 3\%$ [60].

4.2.3 The muon spectrometer

The outermost part of the ATLAS detector is the muon spectrometer (see Figure 4.10). The purpose of this detector is to identify muons and to measure their transverse momentum precisely since their energies cannot be measured in the calorimeters due to their weak interactions with the calorimeter material.

Analogous to the inner detector, a magnetic field is used to bend the trajectories of the muons and their charge and transverse momentum is measured based on the curvature of their tracks. The magnetic field is created by three superconducting air-core toroid magnets, each consisting of eight coils and divided into a barrel toroid covering $|\eta| < 1.4$

[4]The nuclear interaction length λ is the mean path length required to reduce the numbers of relativistic hadrons by the factor $1/e$.

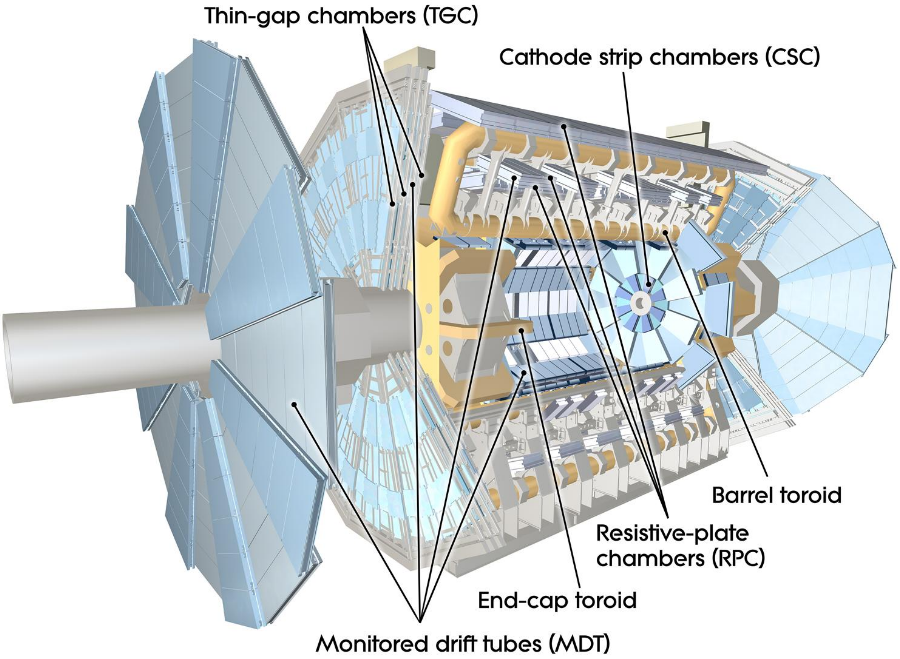

Figure 4.10: Cut-away view of the ATLAS muon spectrometer [64].

and two smaller end-cap toroids covering the range $1.6 < |\eta| < 2.7$. In the transition region $1.4 < |\eta| < 1.6$, the magnetic field originates from both the barrel and the end-cap toroids.

The muon spectrometer is made of many detector chambers that overlap in ϕ to achieve full coverage. The barrel consists of three concentric cylinders around the beam axis placed at radii of about 5 m, 7.5 m and 10 m. In the end-caps, the chambers are arranged in large wheels perpendicular to the beam axis placed at $|z|$ values of about 7 m, 11 m, 13 m and 21 m. Figure 4.11 illustrates the positions and envelopes of the chambers in the muon spectrometer. Around $|\eta| \approx 0$, there is a small gap in coverage to allow for services of the inner parts of the detector.

The muon spectrometer uses four different detector technologies, which can be classified into two types depending on their purpose. Precision tracking chambers measure the coordinate (η) in the track bending direction in the magnetic field, whereas the orthogonal coordinate (ϕ) is measured by the trigger chambers, which are used for the first-level muon triggers explained in the next section and allow for the identification of the bunch-crossing from which a triggered muon originated due to their high time resolution. The distribution of the four technologies inside the muon spectrometer can be seen in Figure 4.11.

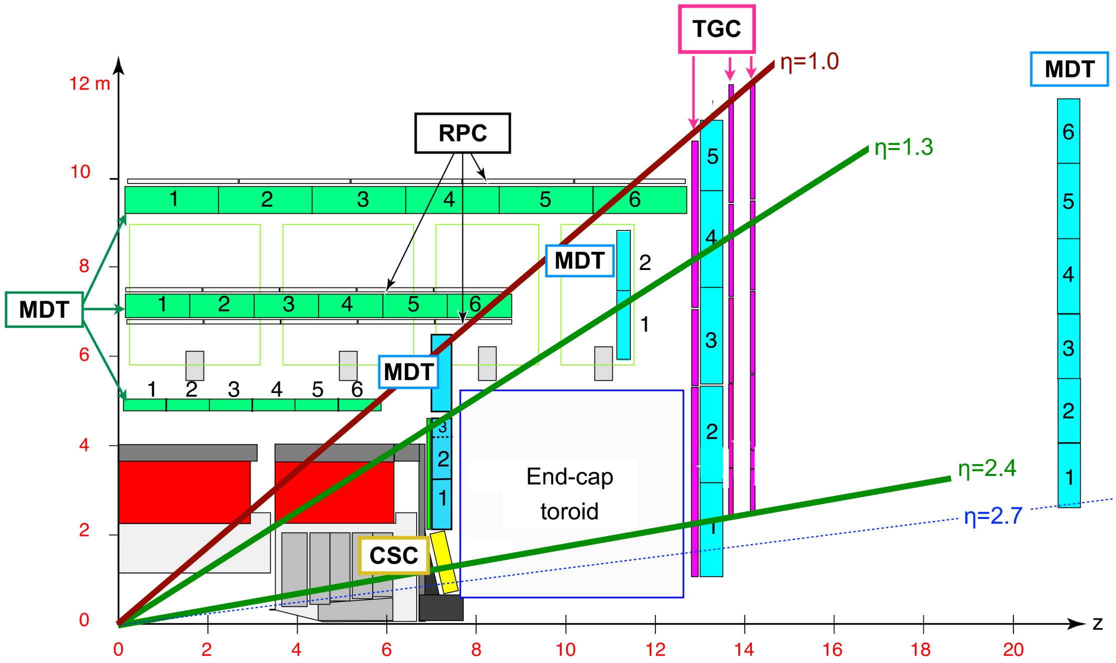

Figure 4.11: Cross-section of one quadrant of the muon spectrometer in a plane containing the beam axis [64].

Most of the muon precision tracking chambers are **monitored drift tube (MDT) chambers**. They cover the region $|\eta| < 2.7$ except for the region $|\eta| > 2.0$ in the innermost end-cap layer. Each MDT chamber contains two multilayers of three or four layers of 30 mm diameter drift tubes (see also Section 4.2.1), which contain a 50 µm diameter tungsten-rhenium wire in the centre and are filled with a gas mixture of 93% Ar and 7% CO_2 at 3 bar. The MDT chambers have an intrinsic spatial resolution of 35 µm.

The second type of precision tracking chambers are **cathode-strip chambers (CSCs)**. They are used in the innermost end-cap layer at $2.0 < |\eta| < 2.7$, where the counting rates are larger than 150 Hz cm^{-2} up to which MDT chambers can be efficiently operated. A CSC consists of an array of anode wires and orthogonal cathode strip planes and is filled with a gas mixture of 80% Ar and 20% CO_2. The CSCs measure the charge distributions induced by muons on the cathode strips in both coordinates. The cathode segmentation is much finer in the track bending direction in the magnetic field than in the orthogonal direction leading to intrinsic spatial resolutions of 40 µm and 5 mm, respectively.

In the region $|\eta| < 1.05$, **resistive-plate chambers (RPCs)** are used as trigger chambers. An RPC consists of two parallel high pressure laminate electrode-plates (“Bakelite”), between which a high voltage of about 5 kV is applied, separated by 2 mm and filled with a gas mixture of 94.7% $C_2H_2F_4$, 5% iso-C_4H_{10} and 0.3% SF_6. The RPCs measure avalanches in the thin-gap between the electrodes, which induce fast signals in the external crossed strip electrodes. The two inner RPC layers in the middle layer of the barrel are used for low-p_T triggers, while the outermost RPC layer in the outer layer of the barrel is used for high-p_T triggers in combination with the inner RPC layers. Each chamber consists of two layers of RPCs. Thus, there are six measurements of both coordinates for a muon track going though all three RPC layers. Three out of four hit coincidences are used for the low-p_T muon triggers and one out of two for the high-p_T triggers. The RPC chambers have a spatial resolution of about 10 mm in both coordinates and a time resolution of 1.5 ns.

Finally, **thin-gap chambers (TGCs)** are used as trigger chambers in the region $1.05 < |\eta| < 2.4$ and up to $|\eta| < 2.7$ for the measurement of the non-bending coordinate. Similar to CSCs, TGCs are multi-wire proportional chambers, but with a smaller anode-to-cathode distance of 1.4 mm compared to 2.5 mm and a different gas mixture of 55% CO_2 and 45% n-C_5H_{12}. The chambers are constructed as doublets or triplets of wire layers. Each chamber has two readout strip planes for the non-bending coordinate and two or three readout strip planes for the bending coordinate for doublet or triplet chambers, respectively. Coincidences of the hit measurements in the TGC chambers are used for the muon triggers. TGCs have a higher spatial resolution than the RPCs in both coordinates, 2 and 7 mm, respectively, but their time resolution of 4 ns is lower.

4.2.4 The trigger system

The system of detectors explained in the last sections has a total of about 100 million readout channels leading together with a collision frequency of 40 MHz to a data rate of about 60 TB/s, which cannot be stored within a reasonable budget. Thus, a system, the triggers, is needed that decides which events are stored and which events are discarded. The current trigger system of the ATLAS detector is illustrated in Figure 4.12 and consists of two major components.

The **first level (L1)** of the triggers is implemented on custom-made electronics and is part of the detector itself. It uses reduced-granularity information from a subset of the detectors, namely the RPCs, the TGCs and the calorimeters, to define region-of-interests (RoIs), which are signatures in the detector that exceed certain energy thresholds. The L1

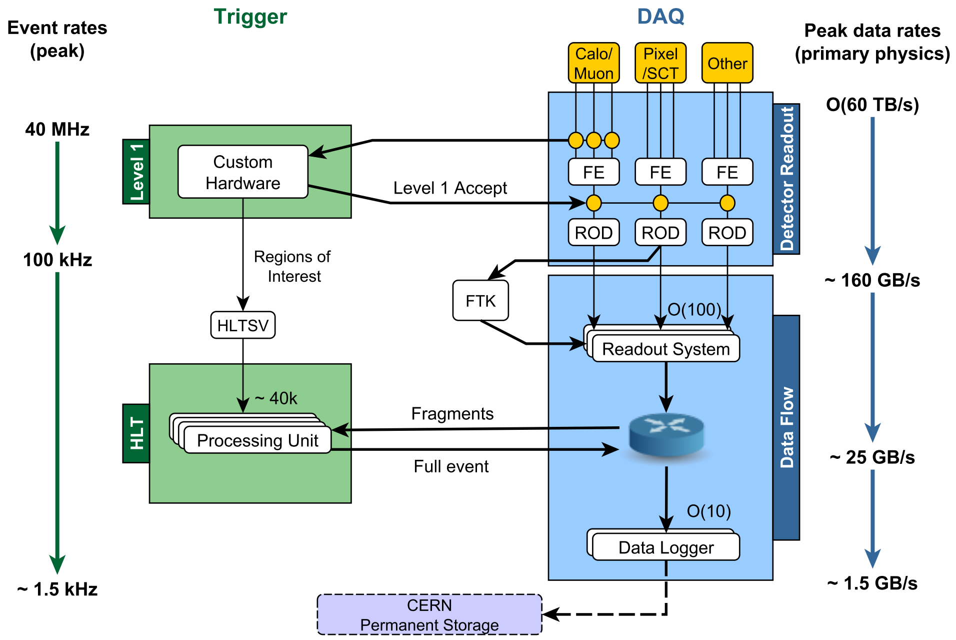

Figure 4.12: Functional diagram of the ATLAS trigger and data acquisition system showing expected peak rates and bandwidths through each component [64].

trigger makes a decision within 2.5 μs after the brunch-crossing and reduces the event rate to 100 kHz.

The RoIs of the L1 trigger are sent to the **high level trigger (HLT)** running on a dedicated computer farm outside of the detector. The HLT algorithms use the full granularity information of the muon and calorimeter chambers together with a reconstruction of the inner detector tracks to study the RoIs in more detail and to refine the trigger selection. They reduce the event rate to approximately 1.5 kHz with an average latency on the order of hundreds of ms. After an event is accepted by the HLT, it is written to disk and a full event reconstruction using the algorithms explained in Section 4.4 is run.

4.3 Simulation of collision events

Before a search for supersymmetry can be performed, the response of the detector to the supersymmetric process and background processes of the Standard Model has to be understood. Therefore, detailed simulations [65] are run consisting of the following steps:

1. Generation of proton–proton collision events for the process of interest.
2. Simulation of the detector response to the produced particles.
3. Reconstruction of the simulated events (see Section 4.4).

Many of these steps rely on the Monte Carlo (MC) method [66], a technique for numerical integration using random numbers, and often used to integrate probability density functions over a given parameter space.

The event generation process can be split into several independent steps. First, the hard process is simulated, in which the constituents, the partons, of the incoming protons interact to produce the outgoing particles (e.g. supersymmetric particles) according to the quantum mechanical matrix element of the hard process calculated in perturbation theory. The properties of the incoming partons are determined from parton distribution functions, which are probability densities for finding a given type of parton in a proton with a certain fraction of the longitudinal proton momentum at a certain energy scale. After that, particles are decayed whose lifetimes are shorter than the hadronisation time-scale such as the top quark. In the next step, parton showers are simulated which represent QCD corrections to the hard process due to gluon radiation. Parton showers originate from both initial-state radiation emitted by incoming partons and final-state radiation emitted by partons produced in the hard process. Subsequently, the interactions from partons not involved in the hard process are simulated, the so-called underlying event, which consists mainly of gluon-gluon scattering. Finally, the hadronisation of coloured particles is modelled, which cannot be described by perturbation theory as the strong interaction becomes strong at low energies. The event generator Pythia used later on in Chapter 5 describes the hadronisation via the string model [67], which is based on the observation that at large distances the gluon field lines are compressed to tube-like regions, called strings, whose fragmentations into hadrons are modelled by a linear potential. This last step of the event generation contains also the decays of the hadrons.

The detector response to the particles produced in the event generation step is simulated using the program Geant4 [68], in which the particle interactions with the detector components, passive materials and magnetic fields are described in detail using Monte

Carlo techniques. At this stage, expected signals of pileup collisions are added [69]. Finally, the algorithms described in the next section are used to reconstruct the simulated events.

4.4 Reconstruction of collision events

Both simulated and real data are reconstructed with the same algorithms, which use raw information from the detectors such as hits to build objects that can be used in a physics analysis. These objects include inner detector and muon spectrometer tracks, calorimeter clusters and particle objects such as electrons, photons, muons, hadronically decaying taus, and jets. Taus and jets are not relevant for the analysis presented in Chapter 5, and are therefore not discussed further.

This analysis relies on a reconstruction setup optimised for decays of long-lived particles and explained in the following. It is largely based on the standard reconstruction setup commonly used in ATLAS and differs in an additional tracking step, an algorithm to reconstruct secondary vertices and minor changes in the electron and muon reconstruction.

4.4.1 Reconstruction of inner detector tracks

First, the tracking algorithms are run to reconstruct the inner detector tracks, since they are used as input to reconstruct particle objects such as electrons and muons. Besides the standard tracking algorithm of ATLAS, an additional tracking algorithm [70], called large radius tracking, is performed that reconstructs tracks with large impact parameters.

Both tracking algorithms involve pattern recognition algorithms to identify measurements originating from the same charged particle, which are used in a fit to estimate the track of the particle. Each track is parametrised by five parameters: q/p, θ, ϕ, d_0 and z_0. These parameters are expressed with respect to the perigee, which is the point of the track's closest approach in the transverse plane to the measured beam line. The first parameter q/p is the charge divided by the momentum, while θ and ϕ define the direction of the momentum at the perigee. The transverse impact parameter d_0 is the signed transverse distance of the perigee to the beam line, i.e. the shortest transverse distance of the track to the beam line. The longitudinal impact parameter z_0 is the signed longitudinal distance of the perigee to the beamspot position.

4.4.1.1 The standard tracking

The standard tracking [71] consists of two independent steps, the inside-out and the outside-in tracking, which reconstruct tracks with a minimum p_T of 500 MeV. In the first step of the inside-out tracking, clusters of pixel and SCT hits are transformed into three-dimensional space points marking the points where the charged particles crossed the active detector material. Then, seeds are formed from sets of three space points and a combinatorial Kalman filter technique [72] is used to build track candidates by incorporating additional space points compatible with the preliminary track. Subsequently, an ambiguity solving is run to eliminate tracks from random hit combinations and track duplicates. Finally, if the track is within the TRT acceptance, then measurements in the TRT will be used to extend the track into the TRT, improving the momentum resolution.

The outside-in tracking starts with a segment finding in the TRT. Unlike the pixel or SCT modules, the straw tubes of the TRT do not contain information along the tube direction, and therefore three-dimensional space points cannot be formed. Instead, the pattern recognition has to be done in projective planes (r–ϕ in the barrel and r–z in the end-caps). Track segments from tracks with a p_T greater than 500 MeV appear as almost straight lines in the r–ϕ projection and rigorous straight lines in the z–ϕ projection, so called Hough transformations [73]. The segments found are then traced back into the silicon trackers to reconstruct the track.

4.4.1.2 The large radius tracking

The large radius tracking is an additional third tracking step. It runs after the standard tracking on unused hits and follows the same strategy as the standard inside-out tracking, but with relaxed selection criteria that are summarised in Table 4.1 and that allow the reconstruction of largely displaced tracks. Thus, it reconstructs tracks up to a $|d_0|$ value of 300 mm, which is a significant improvement over the 10 mm of the standard tracking. Tracks with even larger $|d_0|$ values cannot be reconstructed with a sufficient precision, since the associated particles do not leave enough hits in the SCT detector. In contrast to the standard tracking, the creation of track candidates is performed with a sequential Kalman filter approach. The rest of the inside-out tracking remains the same except for the relaxed selection criteria.

The large radius tracking reconstructs lepton tracks originating from decays of long-lived particles with efficiencies greater than 80%, 60% and 40% for decay radii of 100 mm,

Table 4.1: Main selection criteria differing between standard and large radius tracking [70]

	Standard	Large radius
Maximum $\|d_0\|$ [mm]	10	300
Maximum $\|z_0\|$ [mm]	250	1500
Maximum $\|\eta\|$	2.7	5
Maximum shared silicon modules	1	2
Seed extension	Combinatorial	Sequential

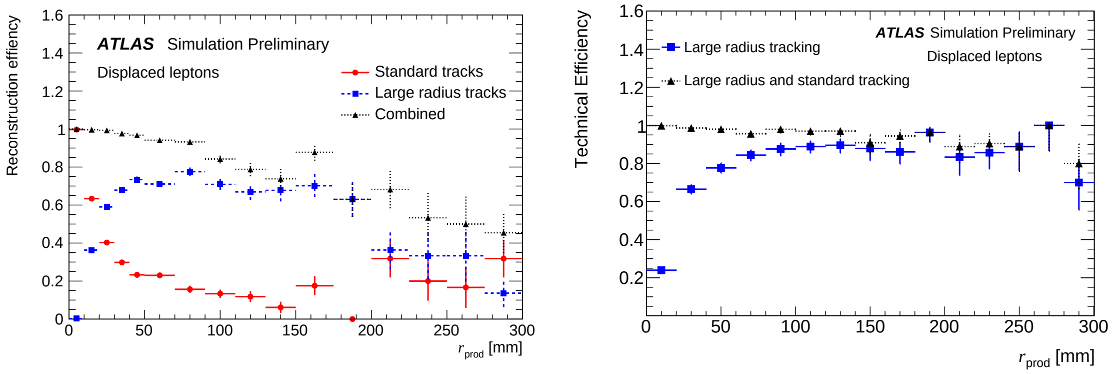

(a) **(b)**

Figure 4.13: (a) Reconstruction efficiency and (b) technical efficiency of tracks of displaced leptons produced by the decay of a long-lived signal particle [70]. The efficiencies are shown as a function of the transverse radius of production of the long-lived signal particle (r_{prod}). The technical efficiency is defined in the text.

200 mm and 300 mm, respectively (see Figure 4.13a). A "technical efficiency" is also defined, where only lepton tracks are considered, which can leave enough hits in the detector for geometrical reasons to be reconstructed by the tracking algorithms. The technical efficiency is depicted in Figure 4.13b and is greater than 80% for the entire range of decay radii, which shows that the loss of efficiency at large radii is not solely caused by the tracking algorithms, but mainly due to the non-hermeticity of the detector.

Table 4.2: Selection criteria applied to inner detector tracks in the displaced vertex reconstruction

Parameter	Requirement
p_T	> 1 GeV
$\lvert d_0 \rvert$	2–300 mm
$\lvert z_0 \rvert$	< 1500 mm
SCT hits	≥ 2
Pixel and TRT hits	TRT hits > 0 or pixel hits ≥ 2

4.4.2 Reconstruction of primary and secondary vertices

Primary vertices[5] are the proton–proton collisions of a bunch-crossing, including the pileup collisions. The primary vertex with the largest scalar sum of p_T of the associated tracks is referred to as the primary vertex (PV) and assumed to be the vertex of the hard scatter process. The transverse and longitudinal resolutions on the position of a primary vertex are about 20 µm and 30 µm, respectively. More details on the reconstruction of primary vertices and its performance can be found in Reference [74].

Secondary vertices, also called displaced vertices (DVs), originate from decays of long-lived particles and are located at a measurable distance from the primary vertex. They are reconstructed by a dedicated algorithm explained in the following. Only inner detector tracks satisfying the selection criteria of Table 4.2 are used to reconstruct displaced vertices. Most notably, tracks must have a $|d_0|$ of at least 2 mm, which implies that displaced vertices with a transverse radius of less than 2 mm are not reconstructed. Consequently, the track of a charged long-lived particle cannot be part of a displaced vertex due to its small $|d_0|$. The upper limit of the large radius tracking on the $|d_0|$ of 300 mm sets also an upper limit on the transverse radii of displaced vertices of the same value, meaning that displaced vertices are reconstructed up to the first SCT layer (see Figure 4.7).

The vertex reconstruction starts with the reconstruction of seed vertices made of two tracks. The vertex fit is performed for all possible two-track combinations of the selected tracks. Only seed vertices with a high fit quality are retained. To reduce the number of fake vertices, both tracks of a seed vertex are required to have no hits in pixel layers with a smaller radius than the radius of the seed vertex. Furthermore, they must have a hit in the

[5] A vertex is a point in space where multiple tracks meet.

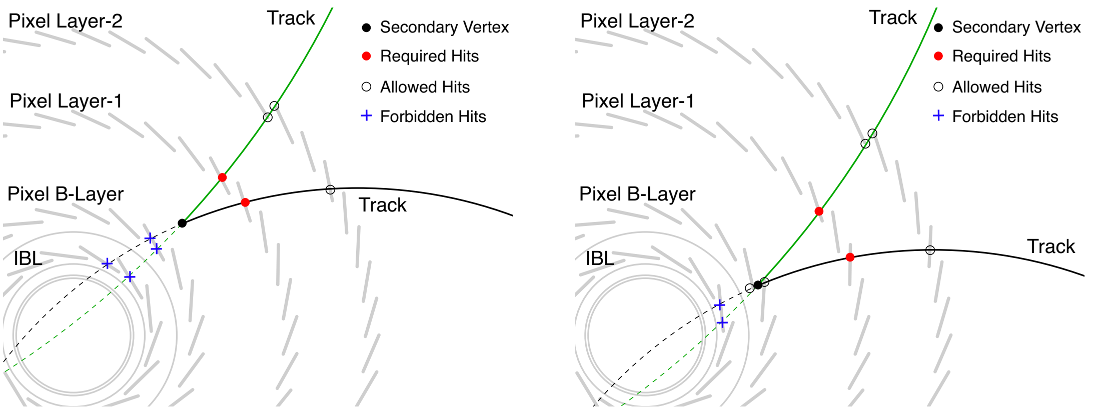

(a) **(b)**

Figure 4.14: Illustration of the fake rejection scheme for seed vertices located (a) between two pixel layers and (b) inside a pixel layer [64].

nearest pixel or SCT layer at larger radius. If the seed vertex is inside or close to a pixel layer, then no hit of that layer will be required or forbidden. This fake rejection scheme is illustrated in Figure 4.14. Additionally, the seed vertices have to be consistent with the decay of a particle originating from the primary vertex, by requiring

$$\frac{(\vec{r}_{\mathrm{DV}} - \vec{r}_{\mathrm{PV}}) \cdot \vec{p}_{\mathrm{DV}}}{|\vec{p}_{\mathrm{DV}}|} > -20, \tag{4.3}$$

where $\vec{r}_{\mathrm{DV}}$ and $\vec{r}_{\mathrm{PV}}$ are the positions of the displaced vertex and the primary vertex, respectively, and $\vec{p}_{\mathrm{DV}}$ is the momentum of the displaced vertex.

Displaced vertices with more than two tracks are reconstructed using the collection of seed vertices. In the beginning, a single track can be associated with multiple vertices. To resolve these ambiguities, an iterative process based on the incompatibility graph method [75] is used. For each track that is assigned to multiple vertices, the vertex V_1 with respect to which it has the largest χ^2 value[6] is identified. If this χ^2 value is larger than 6, the track is removed from V_1. Otherwise, the algorithm finds the vertex V_2 with the smallest d/σ_d, where d is the three-dimensional distance between the two vertices and σ_d its estimated uncertainty. If $d/\sigma_d < 3$, then the vertices V_1 and V_2 will be merged and refitted. If this is not the case, the track is removed from V_1. This procedure is repeated until no track is associated with more than one vertex. Finally, vertices separated by less than 1 mm are also merged and refitted.

[6]The χ^2 value is a measure for the goodness of a fit. The lower the value the better the fit.

4.4.3 Reconstruction and identification of electrons and photons

The reconstruction of electrons and photons is performed by a common algorithm [76] since photons and electrons have similar signals in the calorimeters. In the first step, seed clusters are formed in the electromagnetic part of the calorimeters with a transverse energy of at least 2.5 GeV by a sliding-window algorithm [77]. Next, inner detector tracks are searched for that can be matched to a seed cluster. They are refitted with a Gaussian-sum-filter technique [78, 79] to improve the track parameter resolution. If no track can be associated with a seed cluster, then it is reconstructed as an unconverted photon. Clusters that belong to a track with less than four hits in the pixel and SCT detectors, or to a track with no pixel hit and which is associated with a conversion vertex are reconstructed as converted photons, classified into single-track or double-track conversions depending on the number of associated tracks. Conversion vertices are reconstructed by a dedicated algorithm, which runs on pairs of tracks that are consistent with the assumption that they were produced by photon conversions, e.g. they are required to have a small opening angle. If the associated track is from the large radius tracking, then the cluster will be reconstructed both as photon and as electron. All remaining clusters are reconstructed as electrons only.

Both electron and photon candidates have to fulfil certain identification criteria to ensure that they are signal-like[7] objects and do not originate from background processes such as hadronic jets, for example. The electron identification makes use of about 20 discriminating variables based on calorimeter information such as shower shapes, track properties, track-cluster matching and information from the TRT. These variables are utilised in two different methods, a cut-based [80] and a likelihood-based method [81]. In the cut-based method, electrons have to pass cuts on each discriminating variable, while in the likelihood-based method signal and background probability density functions of the discriminating variables are used to calculate an overall probability for an electron candidate to be signal or background. Both methods have three working points, referred to, in order of increasing background rejection, as “loose”, “medium” and “tight”. The working points of the likelihood method had to be modified for the analysis described in Chapter 5 to achieve good identification efficiencies for largely displaced electrons. Thus, two discriminating variables related to the transverse impact parameter d_0 of the electron track and its uncertainty were dropped in the calculation of the likelihoods and explicit cuts on the minimum number of pixel hits were removed. The cut-based working points

[7] Signal objects originate from the process of interest such as the decay of a supersymmetric particle.

are later used only in cases, where the electrons have $|d_0|$ values of less than 10 mm, and thus no modifications of these working points were necessary.

The photon identification [82] is cut-based and uses information on the shower development in the electromagnetic calorimeter and the shower leakage fraction in the hadronic calorimeter. There are two working points, called “loose” and “tight”, labelling again the different amounts of background rejection. The loose working point is based on shower shapes in the second layer of the electromagnetic calorimeter and on the energy deposited in the hadronic calorimeter, while the tight working point adds information from the first layer of the electromagnetic calorimeter.

4.4.4 Reconstruction and identification of muons

The muon reconstruction [83] is first performed independently in the muon spectrometer and in the inner detector and then the information from both detectors is combined to obtain high quality muons. The reconstruction of muons in the inner detector is the same as for all charged particles and described in Section 4.4.1. In the muon spectrometer, the algorithm starts with the search for hit patterns inside each chamber to form segments. Subsequently, hits from multiple segments of different layers are fitted to obtain track candidates. Segments in the middle layer of the muon spectrometer are used as seeds and a combinatorial search for matching segments in the inner and outer layer is done. At least two matching segments are required to build a track candidate except for the transition region where a single high-quality segment can be used. Next, an overlap removal of track candidates that share segments is performed. Lastly, all hits of a track candidate are fitted to obtain the final track. During this step, hits with large contributions to the χ^2 value of the fit are removed and new hits consistent with the track trajectory are added. Only tracks are retained whose χ^2 value of the final fit satisfies the selection criteria.

By combining the information from multiple detectors, four different types of muons can be reconstructed. Compared to the standard reconstruction of muons, selection criteria on the transverse impact parameter d_0 and on the minimum number of pixel hits of inner detector tracks were removed to allow for the reconstruction of largely displaced muons. Combined muons are formed by matching an inner detector track to a muon spectrometer track. They are the main type of muons and have the highest quality among all types of muons. The other types are needed to fill gaps in the coverage of the muon spectrometer or the inner detector. The reconstruction of combined muons starts either with a muon spectrometer track or with an inner detector track and extrapolates the track to the other detector to find a matching track. A global refit of the hits associated with the two tracks is performed, where hits in the muon spectrometer can be added or removed to improve the fit quality. The second type of muons are segment-tagged muons consisting of an inner detector track matched to at least one segment in the MDT or CSC detectors. Similarly, inner detector tracks matched to an energy deposit in the calorimeters consistent with a minimum-ionising particle are called calo-tagged muons. Finally, extrapolated muons are built solely from muon spectrometer tracks and extrapolated to the centre of the detector to obtain the track impact parameters.

The muon identification [83] is cut-based and has three working points, referred to, in order of increasing background rejection, as “loose”, “medium” and “tight”. All muons except extrapolated muons have to pass quality criteria regarding their inner detector tracks. To achieve high identification efficiencies for largely displaced muons, the cut on the minimum number of pixel hits, applied by default, was removed. Thus, the inner detector tracks of muons are required to have at least five SCT hits and at least 10% of the TRT hits originally assigned to the track have to be used in the final fit. The TRT requirement is only applied to tracks with $0.1 < |\eta| < 1.9$, i.e. in the region of the TRT acceptance. In the medium and tight working points, additional quality criteria are applied to combined muons that include a minimum number of hits in the muon spectrometer and a good agreement of the momentum measurements in the inner detector and muon spectrometer.

Chapter 5

Search for displaced dilepton vertices

In this chapter, a model-independent search with the ATLAS experiment for long-lived particles with masses larger than 12 GeV decaying into oppositely charged ee, $e\mu$ or $\mu\mu$ pairs is presented. The analysis is based on data of proton–proton collisions at a centre-of-mass energy of 13 TeV recorded in 2016. It continues a previous ATLAS search [84, 85], which was performed on the 8 TeV data recorded in 2012. The search focuses on long-lived particles with lifetimes of the order of ps to ns, whose decays can be reconstructed in the inner detector as secondary vertices that are displaced from the primary proton–proton collision vertex. Since the Standard Model does not predict massive, long-lived particles decaying into leptons, the background is very small, which allows even a weak signal to be identified in the data. A supersymmetric signal model is used as benchmark model to study the sensitivity of the ATLAS detector to the decays of such long-lived particles.

5.1 The signal model

The supersymmetric signal model is illustrated in Figure 5.1. It is a simplified model, where only a small subset of the supersymmetric particle spectrum contributes to the production and decay processes. A pair of left- and right-handed squarks of the first two generations is produced via the strong interaction. The eight squarks are mass-degenerate. Each squark $\tilde{q}$ decays into its Standard Model partner q and the lightest neutralino $\tilde{\chi}_1^0$, which is the lightest supersymmetric particle and also the long-lived particle. All other sparticles are assumed to be decoupled, i.e. their masses are assumed to be so high in the simulation (here 450 TeV) that they cannot be produced at the LHC.

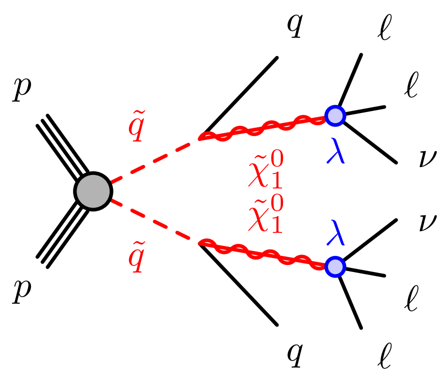

Figure 5.1: Supersymmetric signal model of squark-antisquark production, followed by the RPV decay of the long-lived neutralino $\tilde{\chi}_1^0$ into two charged leptons and a neutrino.

The $\tilde{\chi}_1^0$ is assumed to be a pure Bino, which decays via an RPV coupling, either λ_{121} or λ_{122}, to two charged leptons and a neutrino. As explained in Section 3.3, there are tight experimental constraints on combinations of RPV couplings, and thus the two couplings are studied independently. Both couplings belong to the lepton number violating part $W_{\Delta L=\pm 1}$ of the RPV superpotential in equation (3.22). Other λ couplings are not considered as they would lead to the production of taus, which decay with a branching ratio of about 65% to hadrons whose experimental signature, jets, is very different to electrons and muons and requires a dedicated search. The sensitivity to leptonic tau decays is rather low since the vertex reconstruction efficiency is reduced due to the non-negligible lifetime of the tau. Similarly, λ' or λ'' couplings are also not considered, since neutralino decays mediated by them always result in the production of hadrons.

The final states of the neutralino decays are classified according to the flavours of the charged leptons into three types: $ee\nu$, $e\mu\nu$ and $\mu\mu\nu$. The neutrino flavours are not distinguished, because neutrinos are not detected. For both couplings, the $\tilde{\chi}_1^0$ decays to two final states with equal branching ratio of 50%, namely $ee\nu$ and $e\mu\nu$ for λ_{121}, and $e\mu\nu$ and $\mu\mu\nu$ for λ_{122}.

As simplified models are not strictly tied to a fundamental supersymmetric theory, it is important to check that they are not already excluded by other experimental results. An important parameter of this signal model is the lifetime of the neutralino, which depends on the magnitude of the λ coupling. As discussed in Section 3.3, the λ couplings are constrained by various measurements. The λ_{121} and λ_{122} couplings have the same upper limit of $0.049 \cdot \frac{m(\tilde{f})}{100\,\text{GeV}}$ [58], where $m(\tilde{f})$ is the mass of a virtual sfermion, either a slepton

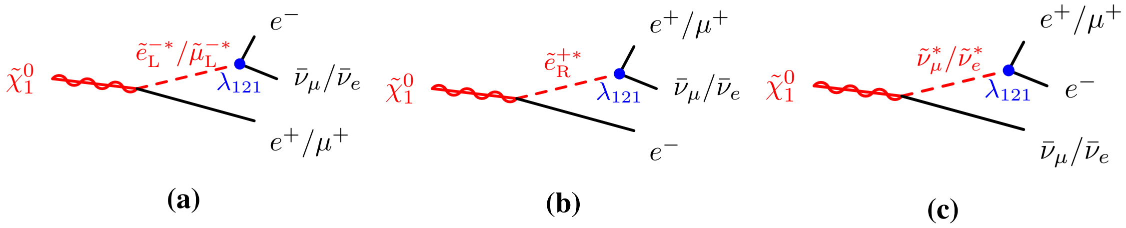

Figure 5.2: Diagrams of neutralino decays mediated by a λ_{121} coupling.

or a sneutrino, which mediates the neutralino decay as illustrated in Figure 5.2 for a λ_{121} coupling.

To verify that the chosen model is viable, the magnitudes of the λ couplings corresponding to the examined neutralino lifetimes and masses are estimated and compared to the upper limit. The lifetime of neutralino decays mediated by a single λ coupling is given by [57]

$$\tau \approx 10\,\text{ps} \cdot \left(\frac{m(\tilde{f})}{100\,\text{GeV}}\right)^4 \cdot \left(\frac{1\,\text{GeV}}{m(\tilde{\chi}_1^0)}\right)^5 \cdot \frac{1}{\lambda^2}. \tag{5.1}$$

Masses of the sleptons and sneutrinos have to be assumed for the estimation. Their current mass limits, set by LHC experiments, are less than 1 TeV. Thus, a common mass of 1 TeV has been chosen. Neutralino lifetimes below 0.3 ps and masses below 50 GeV have not been considered in the interpretations of this model (see Section 5.3.2). With these assumptions, Equation (5.1) yields $\lambda \approx 0.03$, which is much below the upper limit of 0.49 and therefore consistent with the current experimental constraints.

5.1.1 Simulated signal samples

The sensitivity of the ATLAS detector to this signal model is studied using MC simulations performed with the procedure described in Section 4.3. Each signal MC sample consists of twenty thousand events generated using MadGraph5_aMC@NLO 2.2.3 [86] for the calculation of the matrix element of the supersymmetric process and Pythia 8.210 [87] for the remaining steps of the event generation. The free parameters of the generators, e.g. regarding the underlying event and the hadronisation, were adjusted according to the A14 tune [88]. For the parton distribution functions (PDFs), the NNPDF23LO tune [89] was used.

Table 5.1: Properties of the signal MC samples. The cross-sections are computed at approximate NNLO+NNLL accuracy as described in the text assuming eight mass-degenerate squarks.

$m(\tilde{q})$ [GeV]	$m(\tilde{\chi}_1^0)$ [GeV]	$c\tau$ of $\tilde{\chi}_1^0$ [mm]	Cross-section [fb]	N_{Events}
700	50 500	10, 30, 100, 300 or 1000	630 ± 55	$2 \cdot 10^4$
1600	50 1300	10, 30, 100, 300 or 1000	1.15 ± 0.20	$2 \cdot 10^4$

Five different neutralino lifetimes ($c\tau$)[1] in the range from 10 to 1000 mm were simulated, each for four combinations of sparticle masses (see Table 5.1). A reweighting technique explained in Section 5.3.2 is used to interpolate the signal efficiencies between the simulated lifetime values. The four combinations of sparticle masses consist of two squark masses and a very small and a very large neutralino mass to evaluate the impact of the neutralino mass on the signal efficiency. Instead of performing each simulation two times, for $\lambda_{121} \neq 0$ and for $\lambda_{122} \neq 0$, a sample with neutralino decays into all three final states was produced with equal branching ratios of $1/3$. Each event is then reweighted so that the branching ratios of the LSP decay correspond to the λ coupling under consideration.

Table 5.1 contains also the cross-sections of the signal MC samples, which are calculated to approximate next-to-next-to-leading order in the strong coupling constant, adding the resummation of soft gluon emission at next-to-next-to-leading-logarithmic accuracy (approximate NNLO+NNLL) [90–97]. The nominal cross-section and the uncertainty are derived using the PDF4LHC15_mc PDF set, following the recommendations of Reference [98].

All signal MC samples were processed using the custom reconstruction setup described in Section 4.4. A few samples with $m(\tilde{q}) = 700\,\text{GeV}$ were also processed with the standard ATLAS reconstruction algorithms to study the signal efficiency of the filters, which are discussed in Section 5.2.1, used to preselect the data.

[1]In this thesis, lifetimes are expressed in units of length by multiplying them with the speed of light.

5.1.2 Signal distributions

The properties of the signal model have been studied using generated events without detector simulation. This allows for the investigation of the selection criteria before the simulation and the reconstruction of a large number of signal events is performed. The values of observables (such as the transverse momentum p_{T} of a lepton) predicted at the generator-level are often referred to as true values.

Since the neutralino masses considered are much larger than the masses of electrons and muons, the kinematic properties of electrons and muons produced in the neutralino decay are equal. In the following, the neutralino decay mode $\mu\mu\nu$ is used as an example. Figure 5.3 shows four kinematic observables of the muon pairs in the final state for a squark mass of 700 GeV and two different neutralino masses. If the mass difference between the squark and the neutralino is small, most of the squark energy ends up as kinetic energy of the leptons. Thus, the p_{T} distributions of the leading and subleading leptons are shifted to larger values as the neutralino mass increases. For $m(\tilde{\chi}_1^0) = 50\,\mathrm{GeV}$, 42% of the subleading leptons have a p_{T} greater than 50 GeV, while this fraction increases to 78% for $m(\tilde{\chi}_1^0) = 500\,\mathrm{GeV}$.

If the mass difference is large, then the neutralino has on average a higher kinetic energy leading to a boost of the leptons in the direction of the neutralino momentum, which reduces the average opening angle ΔR between the two charged leptons from 2.1 for $m(\tilde{\chi}_1^0) = 500\,\mathrm{GeV}$ to 0.5 for $m(\tilde{\chi}_1^0) = 50\,\mathrm{GeV}$. The invariant mass of the dilepton pair has a broad distribution with endpoint given by the neutralino mass.

The locations of the neutralino decays in the detector are shown in Figures 5.4a to 5.4d. Neutralinos with a longer lifetime travel further such that, for example, none of the 500 GeV neutralinos with lifetime of 10 mm decay at radii greater than 200 mm, while 66% do for $c\tau = 1000\,\mathrm{mm}$. The distributions of both the transverse and longitudinal decay positions have a maximum close to zero for all lifetimes and decrease towards larger decay lengths. The travelled distance depends on the lifetime of the neutralino in the lab frame, given by $\gamma c\tau$ according to special relativity, where γ is the Lorentz factor[2]. As the mass of the neutralino decreases, its kinetic energy increases on average, leading to an increase in γ, which means that lighter neutralinos travel longer distances than heavy neutralinos.

The distributions of the transverse impact parameter d_0 of the leptons are shown in Figures 5.4e and 5.4f. They peak at zero for all neutralino lifetimes, with the peak

[2] $\gamma = 1/\sqrt{1 - v^2/c^2}$, where v is the speed of the particle and c is the speed of light.

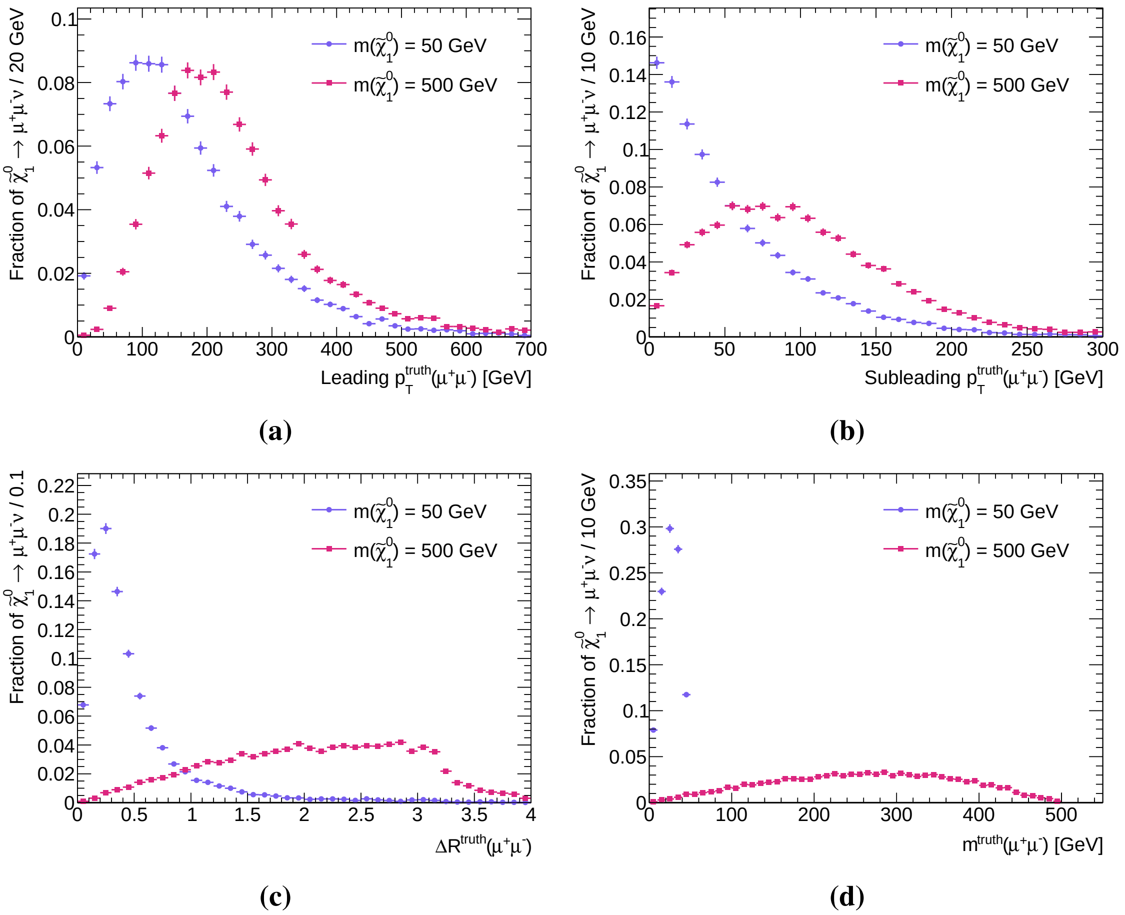

Figure 5.3: Generated kinematic observables of muon pairs produced in $\tilde{\chi}_1^0$ decays to $\mu^+\mu^-\nu$ with $c\tau = 100$ mm for $m(\tilde{q}) = 700$ GeV and two values of $m(\tilde{\chi}_1^0)$.

height decreasing with the lifetime. The distributions broaden significantly as the lifetime increases. Due to the maximum at $|d_0| \approx 0$, a non-negligible fraction of the leptons from a LSP decay is rejected by the $|d_0|$ cut of 2 mm applied in the reconstruction of displaced vertices (see Section 4.4.2) even for long lifetimes. When the lifetime increases, the average $|d_0|$ increases as well, so that for long lifetimes many leptons have $|d_0| > 10$ mm, whose tracks can only be reconstructed by the large radius tracking. For a 500 GeV neutralino with $c\tau = 1000$ mm, 90% of the leptons have $|d_0| > 10$ mm and 32% have $|d_0| > 300$ mm, which means that in this example the standard tracking can only reconstruct up to 10% of the lepton tracks, while up to 68% can be reconstructed if additionally the large radius tracking is performed, illustrating its great importance for long lifetimes.

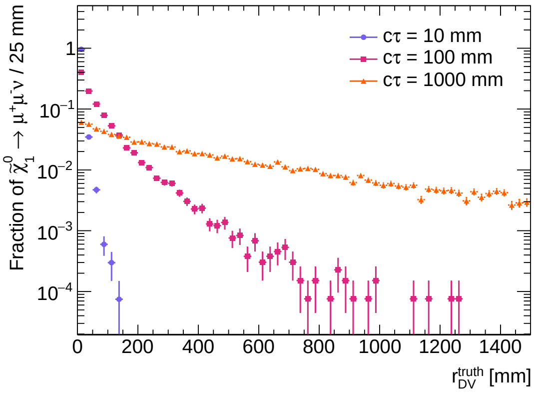

(a) $r_{\mathrm{DV}}^{\mathrm{truth}}$: $m(\tilde{\chi}_1^0) = 500\,\mathrm{GeV}$

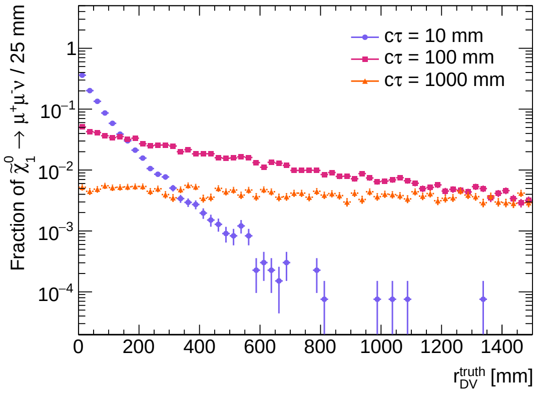

(b) $r_{\mathrm{DV}}^{\mathrm{truth}}$: $m(\tilde{\chi}_1^0) = 50\,\mathrm{GeV}$

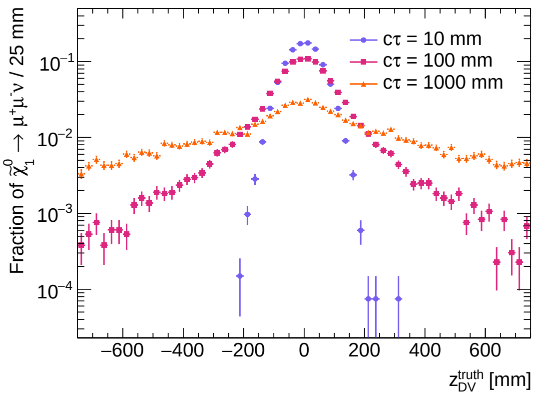

(c) $z_{\mathrm{DV}}^{\mathrm{truth}}$: $m(\tilde{\chi}_1^0) = 500\,\mathrm{GeV}$

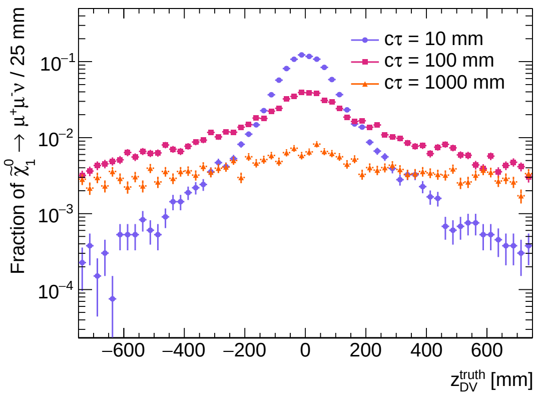

(d) $z_{\mathrm{DV}}^{\mathrm{truth}}$: $m(\tilde{\chi}_1^0) = 50\,\mathrm{GeV}$

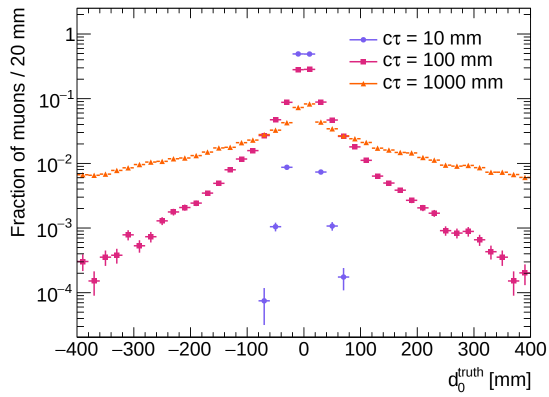

(e) d_0^{truth}: $m(\tilde{\chi}_1^0) = 500\,\mathrm{GeV}$

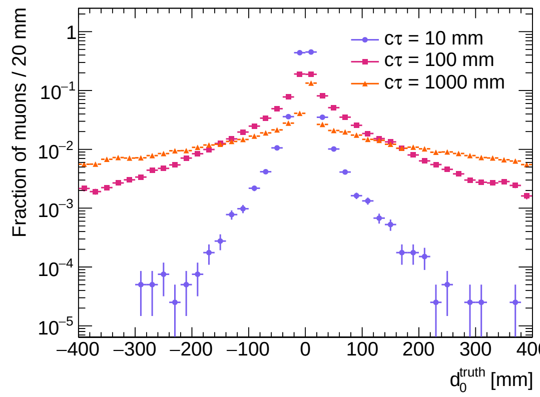

(f) d_0^{truth}: $m(\tilde{\chi}_1^0) = 50\,\mathrm{GeV}$

Figure 5.4: (top) Generated transverse radius $r_{\mathrm{DV}}^{\mathrm{truth}}$, (middle) z-position $z_{\mathrm{DV}}^{\mathrm{truth}}$ and (bottom) transverse impact parameter d_0^{truth} of the muons of $\tilde{\chi}_1^0$ decays to $\mu^+\mu^-\nu$ for $m(\tilde{q}) = 700\,\mathrm{GeV}$, two values of $m(\tilde{\chi}_1^0)$ and three different $\tilde{\chi}_1^0$ lifetimes ($c\tau$).

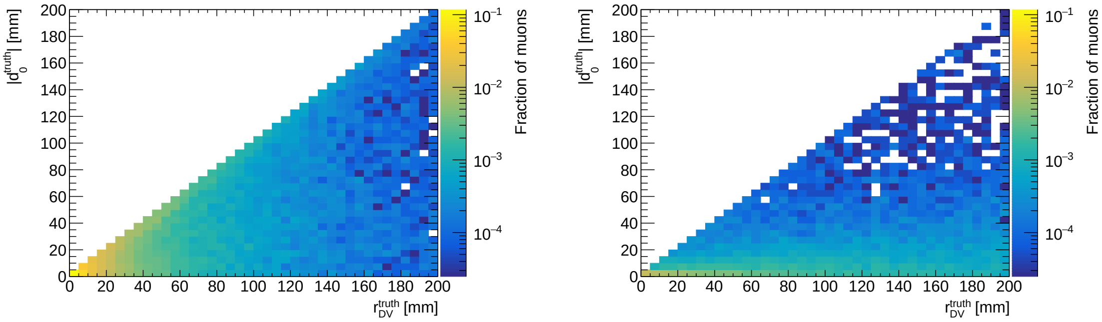

(a) $m(\tilde{\chi}_1^0) = 500\,\text{GeV}$ **(b)** $m(\tilde{\chi}_1^0) = 50\,\text{GeV}$

Figure 5.5: The magnitude of the transverse impact parameter $|d_0^{\text{truth}}|$ of muons from $\tilde{\chi}_1^0$ decays to $\mu^+\mu^-\nu$ as a function of the transverse radius $r_{\text{DV}}^{\text{truth}}$ of the $\tilde{\chi}_1^0$ decay for $m(\tilde{q}) = 700\,\text{GeV}$, two values of $m(\tilde{\chi}_1^0)$ and $c\tau = 100\,\text{mm}$.

The lepton $|d_0|$ and the transverse radius r_{DV} of the neutralino decay are related[3] by

$$|d_0| \approx r_{\text{DV}} \cdot |\sin \Delta\phi|, \tag{5.2}$$

where $\Delta\phi$ is the azimuthal angle between the lepton momentum $\vec{p}$ and the vector $\vec{D}$ from the primary vertex to the neutralino decay vertex. Thus, $|d_0|$ is zero when $\vec{p}$ and $\vec{D}$ are parallel and $|d_0| = r_{\text{DV}}$ when they are orthogonal to each other. This means that $|d_0|$ cannot become larger than r_{DV}.

This relationship is illustrated in Figures 5.5a and 5.5b for a 500 GeV and a 50 GeV neutralino, respectively. For leptons from the decay of a massive neutralino, $|d_0|$ values close to the diagonal are preferred, while $|d_0|$ tends to be small for light neutralinos, even if they decay at large radii. The average $|d_0|$ of leptons from the decays of 500 GeV neutralinos increases much faster with r_{DV} than for 50 GeV neutralinos (see Figure 5.6). This is due to the fact that light neutralinos have on average a higher kinetic energy, and therefore cause a large Lorentz boost of the leptons in the direction of the neutralino momentum, which is parallel to $\vec{D}$, and thus $\Delta\phi$ and $|d_0|$ are reduced.

[3]The scattering of the leptons in the detector material is neglected here.

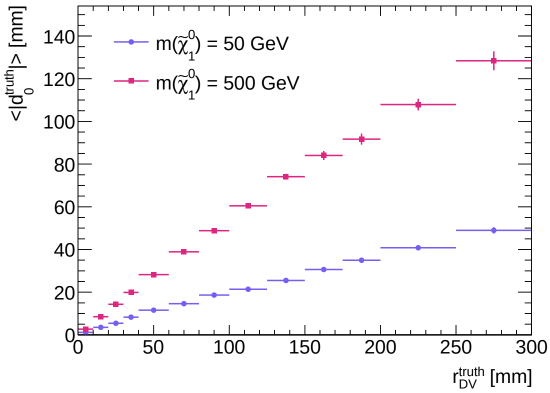

Figure 5.6: Average magnitude of the transverse impact parameter of muons from $\tilde{\chi}_1^0$ decays to $\mu^+\mu^-\nu$ as a function of the transverse radius of the $\tilde{\chi}_1^0$ decay for $m(\tilde{q}) = 700\,\text{GeV}$, two values of $m(\tilde{\chi}_1^0)$ and $c\tau = 100\,\text{mm}$.

5.2 Selection criteria

To search for the signal described in the previous section, a statistical analysis is performed in Section 5.7 that compares the expected number of events from background processes to the number of events observed in the data. An excess of events in the data that is statistically significant could be a hint for the existence of a signal. To maximise the statistical significance of a signal, only events are considered in the analysis that pass a set of selection criteria, called signal region, which are optimised for a high signal efficiency and a high background rejection.

The signal region of this search requires that an event satisfies the selection criteria described in Section 5.2.2 and that it has at least one displaced vertex candidate passing the selection criteria outlined in Section 5.2.3. To make the analysis as model-independent as possible, the kinematic cuts of the signal region are only applied to the secondary vertex candidates, while other objects in the event, such as jets, are not constrained.

5.2.1 Preselection

The algorithms used to improve the sensitivity to decays of long-lived particles, i.e. the large radius tracking and the displaced vertex reconstruction, are very CPU-intensive and cannot be run on all data events recorded in 2016. Thus, a few percent of the data events is preselected using a set of filters optimised for high signal efficiency and data rates that do

Table 5.2: Trigger criteria

Trigger	Symbol	p_T [GeV]	$\lvert\eta\rvert$
HLT_g140_loose	γ	> 140	< 2.47
HLT_2g50_loose	$\gamma\gamma$	> 50	< 2.47
HLT_mu60_0eta105_msonly	μ	> 60	< 1.05

not exceed the storage budget of the ATLAS experiment. The filters are employed on events reconstructed by the standard reconstruction setup of ATLAS. The preselected events are stored in a raw data format so that the reconstruction setup explained in Section 4.4 can be performed. Only these reprocessed events are used in the analysis.

Each filter requires the events to pass one of the triggers listed in Table 5.2. Only triggers that do not rely on inner detector information are used, such as photon triggers and a single muon trigger based only on muon spectrometer measurements. This is necessary because the electron and muon HLT algorithms use the standard tracking, which reconstructs tracks only up to $|d_0| = 10\,\mathrm{mm}$, and therefore have little sensitivity to leptons from displaced decay vertices.

Besides the trigger requirement, each filter applies also kinematic cuts to the reconstructed objects such as photons and muons. The p_T thresholds of the filters are slightly higher than the corresponding trigger thresholds to ensure that the lepton candidates are in the plateau regions of the triggers, where the trigger efficiency reaches the maximum and does not depend on p_T. Table 5.3 summarises the selection criteria of the filters. The filter definitions have been adopted from the previous analysis [84, 85] and adjusted to the higher centre-of-mass energy and luminosities to achieve data rates not exceeding the storage budget.

The filters selecting electron candidates of ee and $e\mu$ vertices, referred to as electron filters, involve either the single photon trigger `HLT_g140_loose` or the diphoton trigger `HLT_2g50_loose`. Photon triggers are sensitive to all energy deposits in the electromagnetic calorimeter and can therefore be triggered by electrons. Both photon triggers require the calorimeter clusters to pass the loose working point of the photon identification discussed in Section 4.4.3. Signal electrons are reconstructed as electrons if their associated track is reconstructed, otherwise as photons. This means in particular that signal electrons with $|d_0| > 10\,\mathrm{mm}$ can only be reconstructed as photons. Since the large radius tracking

Table 5.3: Filters used for the event preselection. Identification criteria are applied only to objects marked “loose”, which have to pass the loose working point of the cut-based identification algorithms.

Filter	Trigger	Object 1	p_T [GeV]	$\|\eta\|$	$\|d_0\|$ [mm]	Object 2	p_T [GeV]	$\|\eta\|$	$\|d_0\|$ [mm]
γ	γ	Photon (loose)	> 150	< 2.5	—	Photon (loose)	> 10	< 2.5	—
						or			
						Electron	> 10	< 2.5	> 2.0
						or			
						Muon	> 10	< 2.5	> 1.5
e	γ	Electron	> 150	< 2.5	> 2.0				
$\gamma\gamma$	$\gamma\gamma$	Photon (loose)	> 55	< 2.5	—	Photon (loose)	> 55	< 2.5	—
ee	$\gamma\gamma$	Electron	> 55	< 2.5	> 2.0	Electron	> 55	< 2.5	> 2.0
$e\gamma$ 1	$\gamma\gamma$	Electron	> 55	< 2.5	> 2.0	Photon (loose)	> 55	< 2.5	—
$e\gamma$ 2	$\gamma\gamma$	Electron (loose)	> 55	< 2.5	—	Photon (loose)	> 55	< 2.5	—
μ	μ	Muon ($\chi^2/n_{\mathrm{DoF}} < 5$)	> 62	< 1.07	> 1.5				
μ	μ	Muon ($\chi^2/n_{\mathrm{DoF}} \geq 5$)	> 62	< 1.07	—				

applied after preselection can recover the tracks of such signal electrons, the filters select not only reconstructed electrons but also photons to maximise the signal efficiency. The reconstructed electrons have to pass the $|d_0| > 2$ mm requirement of the displaced vertex reconstruction.

Muon candidates of $e\mu$ and $\mu\mu$ vertices are selected by a filter based on the `HLT_mu60_0eta105_msonly` trigger, which uses information from muon chambers only and is restricted to the barrel region $|\eta| < 1.05$, where RPC chambers are used as trigger chambers. Higher $|\eta|$ values, i.e. the end-caps, are not included in this trigger since the data rates would become too high. The muon filter employs a lower $|d_0|$ cut of 1.5 mm than the electron filters, because this cut value is sufficient to achieve acceptable data rates.

Signal MC studies showed that the standard ATLAS reconstruction algorithms reconstruct many muons with $|d_0| > 10$ mm as combined muons even though their inner detector tracks were not reconstructed. In such cases, another inner detector track was falsely matched to the muon spectrometer track of a signal muon, usually with a poor match quality. It is important to keep muons with poorly-matched tracks, as the large radius tracking applied after preselection can recover the correct tracks. Therefore, the muon filter must be highly efficient for signal muons that are reconstructed as combined muons with well-matched tracks, but also for those without.

To achieve this, muons with well-matched tracks have to be reliably distinguished from muons with poorly-matched tracks. For this purpose, the kinematic observables of inner detector tracks of combined muons have been studied in the signal MC samples. Figure 5.7a shows that there are two distinct populations: one of poorly-matched tracks, where p_T and $|d_0|$ of the inner detector track are much smaller than their true values, and one of well-matched tracks, where the true and reconstructed values agree well. In most cases, the falsely matched inner detector tracks are of low energy and not displaced, i.e. very different from the inner detector tracks of most signal leptons.

The two populations can also be seen in Figure 5.7b, where the χ^2/n_DoF value[4] of the track match is small for well-matched tracks, while it is uniformly distributed over a wide range for poorly-matched tracks. Further investigation revealed that a χ^2/n_DoF cut of 5 discriminates good and poor matches with very low misclassification probability. This is illustrated by Figure 5.8, which shows that the inner detector track p_T and the muon spectrometer track p_T agree within 10% for about 65% of the muons with

[4]The $\chi^2 = \sum_{i=1}^{k} \frac{(x_i - d_i)^2}{d_i}$ is a measure for the deviation of the values d_i of the fitted distribution to the observed values x_i for $n_\mathrm{DoF} = k - 1$ degrees of freedom.

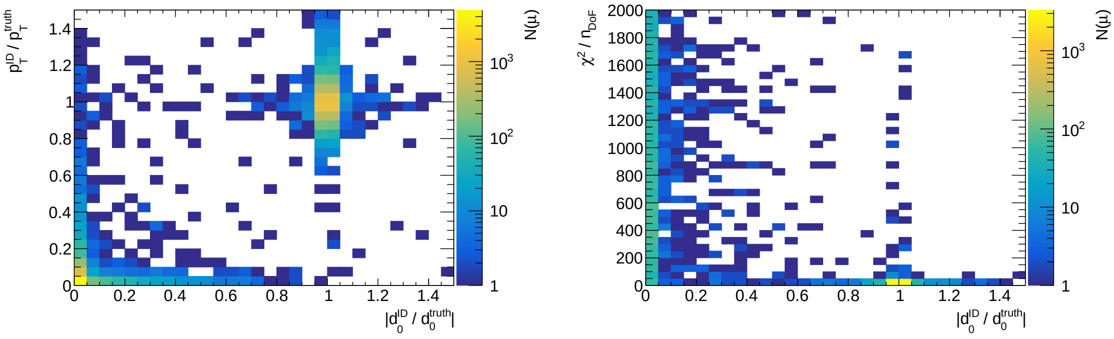

(a) **(b)**

Figure 5.7: (a) Ratio of the inner detector track p_T to the true p_T and (b) the χ^2/n_DoF value of the inner detector track to muon spectrometer track match for muons in the signal MC sample with $m(\tilde{q}) = 700\,\mathrm{GeV}$, $m(\tilde{\chi}_1^0) = 500\,\mathrm{GeV}$ and $c\tau = 100\,\mathrm{mm}$ processed by the standard ATLAS reconstruction, shown as a function of the absolute value of the ratio between the inner detector (ID) track d_0 and the true d_0.

$\chi^2/n_\mathrm{DoF} < 5$, while they can differ by up to two orders of magnitude for muons failing this requirement. Since the χ^2/n_DoF is modelled well in the simulations, as discussed at the end of Section 5.4.3.2, it is used in the muon filter to classify good and poor matches.

To achieve high selection efficiencies for signal muons with poorly-matched tracks, the d_0 cut of the muon filter is not applied to them. In addition, the p_T cut is applied to the muon spectrometer track for such muons, while it is applied to the combined track for muons with well-matched tracks. This is necessary to prevent the low p_T of the falsely matched inner detector track from causing the combined track to fail the p_T cut, even though the associated signal muon has a sufficiently high p_T.

The efficiencies of the filters have been studied in the signal MC samples, as shown in Figure 5.9 for two examples. If the neutralino has a mass of 500 GeV, then the total filter efficiency is expected to be greater than 60% in most cases and even 80% for neutralino decays to $e^+e^-\nu$. The efficiency drops significantly at low decay radii due to the d_0 requirements of the relevant filters. Figure 5.9a illustrates that the filters selecting reconstructed electrons are complementary to the filters selecting reconstructed photons. The former are more efficient at low decay radii, while the latter dominate for $r_\mathrm{DV}^\mathrm{truth} > 40\,\mathrm{mm}$ in this example. The total efficiency is significantly reduced for all decay modes if the $\tilde{\chi}_1^0$ mass is 50 GeV. This is mainly caused by lower trigger efficiencies, as the leptons have on average a lower p_T (see Figures 5.3a and 5.3b). Furthermore, the lepton pairs are produced in a narrow cone (see Figure 5.3c), which makes it harder for the reconstruction algorithms

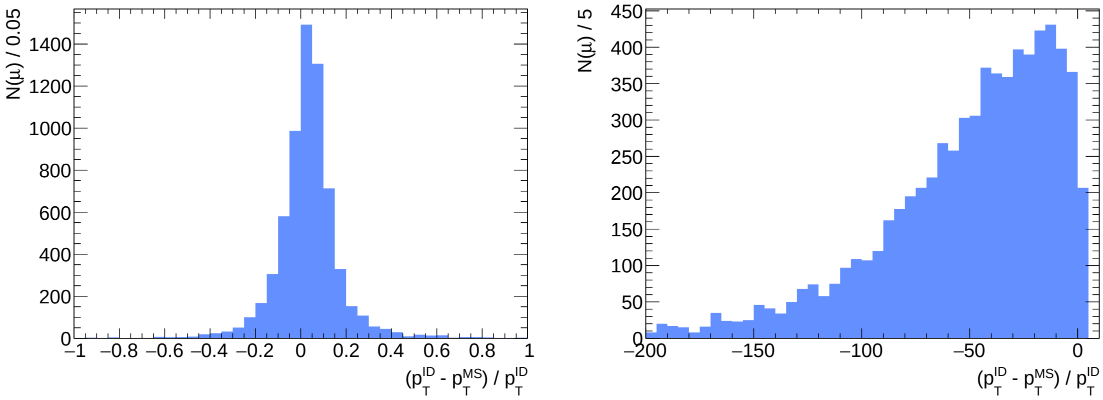

(a) $\chi^2/n_{\text{DoF}} < 5$ **(b)** $\chi^2/n_{\text{DoF}} > 5$

Figure 5.8: Relative difference between the inner detector (ID) and the muon spectrometer (MS) track p_{T} of muons with (a) a good and (b) a poor match quality in the signal MC sample with $m(\tilde{q}) = 700\,\text{GeV}$, $m(\tilde{\chi}_1^0) = 500\,\text{GeV}$ and $c\tau = 100\,\text{mm}$.

to identify the individual leptons. In addition, the total efficiency reaches its plateau at much larger decay radii since more leptons fail the d_0 requirements due to lower $|d_0|$ values on average for a given decay radius (see Figure 5.5b).

5.2.2 Event selection

Each event has to pass a set of criteria to ensure that all parts of the detector were functioning correctly. First, individual events are rejected if there were problems in one of the calorimeters, a recovery of the SCT detector or missing information after a restart of a detector component. This requirement is referred to as the "event cleaning". Secondly, events are only accepted if they are on the "Good Runs List" (GRL), which is used by all ATLAS analyses. For this analysis, additional luminosity blocks (corresponding to less than $0.1\,\text{fb}^{-1}$) had to be removed since the reconstruction setup of Section 4.4 could not be performed on few events of these blocks. It has been verified that these luminosity blocks do not contain any signal-like events.

Only events with a primary vertex within $|z| < 200\,\text{mm}$ are used. The standard deviation on the determination of the z-position of a primary vertex is usually $\sigma_z = 50\,\text{mm}$ [74]. Thus, this quality requirement is passed by more than 99.99% of the primary vertices. The events must pass at least one of the triggers listed in Table 5.2. Finally, events with a lepton pair that is back-to-back in $\eta\phi$-space are rejected to suppress the background from

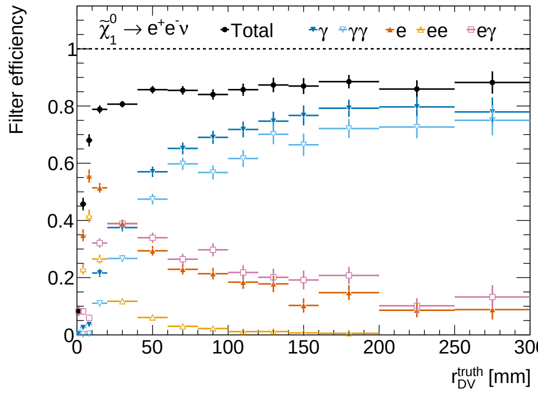

(a) $e^+e^-\nu$: $m(\tilde{\chi}_1^0) = 500\,\text{GeV}$

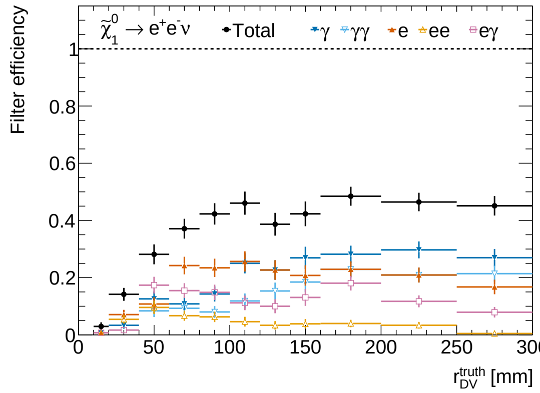

(b) $e^+e^-\nu$: $m(\tilde{\chi}_1^0) = 50\,\text{GeV}$

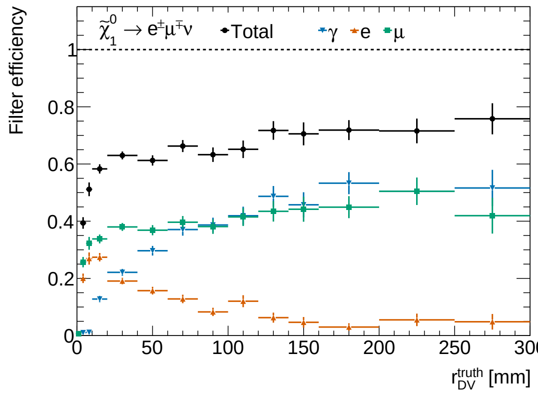

(c) $e^\pm\mu^\mp\nu$: $m(\tilde{\chi}_1^0) = 500\,\text{GeV}$

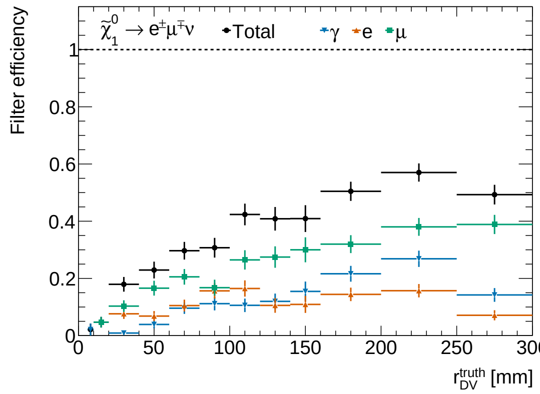

(d) $e^\pm\mu^\mp\nu$: $m(\tilde{\chi}_1^0) = 50\,\text{GeV}$

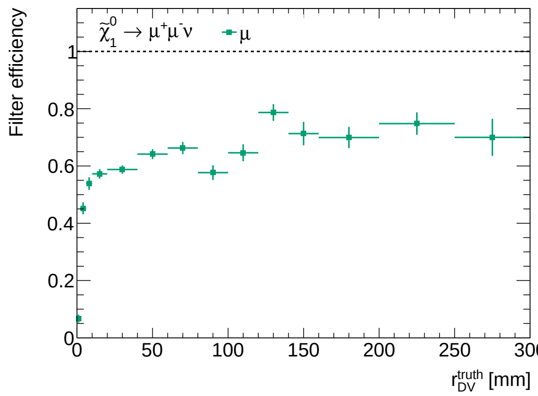

(e) $\mu^+\mu^-\nu$: $m(\tilde{\chi}_1^0) = 500\,\text{GeV}$

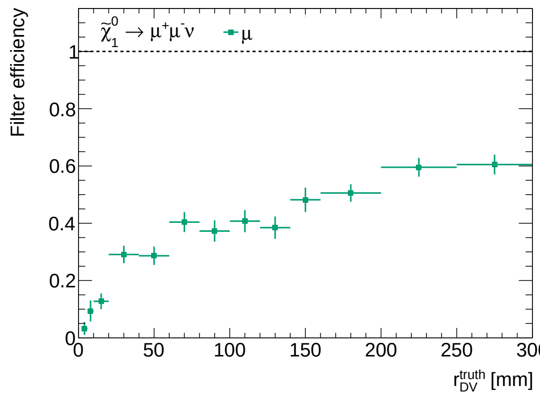

(f) $\mu^+\mu^-\nu$: $m(\tilde{\chi}_1^0) = 50\,\text{GeV}$

Figure 5.9: Filter efficiencies of $\tilde{\chi}_1^0$ decays to (top) $e^+e^-\nu$, (middle) $e^\pm\mu^\mp\nu$ and (bottom) $\mu^+\mu^-\nu$ as a function of the true transverse radius of the $\tilde{\chi}_1^0$ decay for $m(\tilde{q}) = 700\,\text{GeV}$, two values of $m(\tilde{\chi}_1^0)$ and $c\tau = 100\,\text{mm}$.

Table 5.4: Selection criteria for displaced dilepton vertex candidates

Vertex fit quality	$\chi^2/n_{\text{DoF}} < 5$
Transverse displacement	> 2 mm to all pp collisions
Vertex mass	> 12 GeV
Fiducial volume	$r < 300$ mm and $\|z\| < 300$ mm
Material veto	for ee and $e\mu$
Disabled pixel module veto	
Lepton kinematics	$p_{\text{T}} > 10$ GeV $\|\eta\| < 2.47$ (e) and $\|\eta\| < 2.5$ (μ)
Lepton identification	Modified loose working points
Overlap removal	
Number of leptons	≥ 2
Opposite charges	
Filter and trigger matching	

cosmic-ray muons by requiring $\Delta R_{\text{cosmic}} = \sqrt{(\eta_1 + \eta_2)^2 + (|\Delta\phi| - \pi)^2} > 0.01$ for all lepton pairs in the event, as discussed in Section 5.6.5.2. This veto is applied to all types of lepton pairs to cover also cases where the cosmic-ray muon is reconstructed as an electron.

5.2.3 Vertex selection

Events are finally selected if they have at least one displaced vertex fulfilling the following criteria (see Table 5.4). The vertex fit has to satisfy $\chi^2/n_{\text{DoF}} < 5$. A minimum transverse displacement of 2 mm with respect to all proton–proton collisions of the event is required to suppress the background from Standard Model processes. Pileup vertices are taken into account for the displacement calculation since it can happen that the hard-scatter process is misidentified as a pileup vertex. The displacement threshold matches the $|d_0|$ cut used in the reconstruction of secondary vertices. To eliminate contributions from low-mass dilepton processes, such as photon conversions, J/Ψ, Υ or other B hadron decays, the invariant mass[5] of a vertex has to be greater than 12 GeV, which is larger than the Υ mass taking into account the detector resolution.

[5]In the calculation of the vertex mass, the vertex tracks are assumed to be pions.

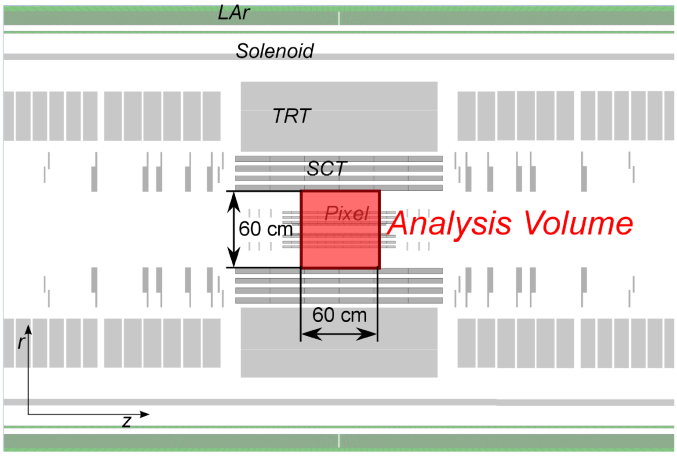

Figure 5.10: Detector volume in which displaced vertices are selected [85].

Furthermore, vertices have to be located inside a fiducial volume defined by $r < 300$ mm and $|z| < 300$ mm (see Figure 5.10). Thus, the fiducial volume covers a large fraction of the pixel barrel up to the first layer of the SCT detector. The radial limit cannot be increased because for $r > 300$ mm the number of measurements in the tracking detectors is too low to reconstruct the tracks (see Section 4.4.1.2). The cut on $|z|$ could be loosened, but the vertex reconstruction efficiency and accuracy decrease significantly close to the edge of the pixel barrel and even more beyond.

Vertices with at least one electron are vetoed if they are reconstructed inside a material-rich region, using a three-dimensional detector map, which was constructed for another search for displaced vertices [99] and is illustrated in Figure 5.11. The veto covers about 42% of the fiducial volume. It suppresses the background from photon conversions into electrons, which are significantly enhanced in regions with a high material density. It is not needed for $\mu\mu$ vertices, since photon conversions into a pair of muons are very rare due to the much larger mass of the muon, and since the probability for misidentifying hadronic interactions as $\mu\mu$ vertices is extremely small (see the discussion in Section 5.6.4).

A vertex candidate is rejected if it is located in front of a pixel module that was disabled during the data-taking in 2016, based on a three-dimensional map that was constructed for another search [99]. Without this veto, the vertex reconstruction efficiency would be overestimated in the simulations, because the simulated conditions of the pixel modules were defined before data-taking and lead to a mismodelling of the fake rejection explained in Section 4.4.2. The veto results in a small reduction of the fiducial volume by 2.3%.

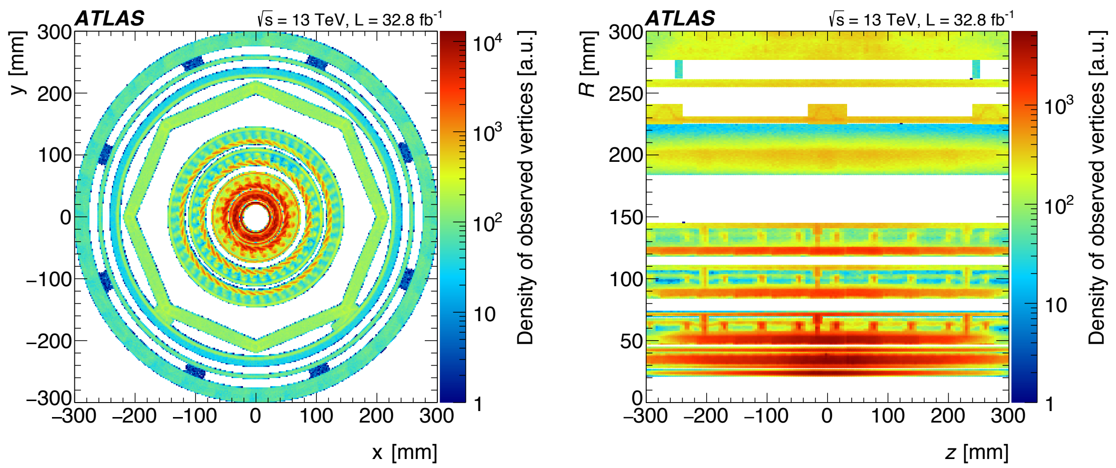

(a) **(b)**

Figure 5.11: Two-dimensional distributions of the observed vertex density in material-rich regions, projected in (a) the xy plane and (b) the zr plane [99]. The material-rich regions with $r < 150$ mm are the four pixel layers. The supporting structures of the pixel detector are located at $r > 180$ mm.

At least two light leptons, electrons and muons, have to belong to a vertex. Additional tracks are allowed and not further constrained. Both electrons and muons have to satisfy $p_\mathrm{T} > 10$ GeV. An overlap removal is applied to make sure that leptons from the same vertex do not share an inner detector track. Electrons have to fulfil $|\eta| < 2.47$ and are rejected if they are associated with an energy cluster in the calorimeter that does not pass standard quality criteria. The modified loose working point of the likelihood-based identification explained in Section 4.4.3 is applied to electrons. Only combined muons with $|\eta| < 2.5$ and that pass the modified loose working point of the muon identification described in Section 4.4.4 are accepted. Lepton pairs produced in the decay of a long-lived particle are usually oppositely charged, and therefore the vertex is required to have at least one positively and at least one negatively charged track.

The leptons of a vertex candidate have to pass at least one of the preselection filters of Table 5.3. This requirement is applied at the vertex-level and not at the event-level to ensure that the preselection is due to leptons of a displaced vertex and not due to other activity in the event. To pass a filter, the leptons have to be successfully matched to the corresponding trigger. Some of the filter criteria were originally applied to reconstructed photons, for which a different calibration than for electrons is used. Therefore, the kinematic cuts of the filters are applied not only to the electrons associated with the vertex, but also to the corresponding reconstructed photons.

The filter selection strongly constrains the kinematic properties of the two vertex leptons. The single photon, single electron and single muon filters require one lepton to be energetic, while the remaining filters require both leptons to have $p_T > 55$ GeV. Consequently, the general lepton p_T cut of 10 GeV is only relevant for vertices passing single particle filters only.

5.3 Signal efficiency

In this section, the efficiency of the selection criteria is evaluated using MC simulations. These studies are performed both for the output of the MC generators, the truth-level, and for reconstructed events after full detector simulation, referred to as reco-level.

5.3.1 Cutflows and reconstruction efficiencies

Representative cutflows are shown in Figure 5.12 for a 500 GeV neutralino and in Figure 5.13 for a 50 GeV neutralino. The bins show the fractions of neutralino decays passing the respective cut and all previous cuts. The second to fourth bin correspond to the event-level cuts discussed in Section 5.2.2. The data-quality requirements are not relevant for the simulations, and therefore not listed in these cutflows. All objects of an event are taken into account to verify whether an event-level cut is passed. Thus, it can happen that the neutralino decay under study fails the trigger matching requirement even though the event passes the trigger requirement, because the event was triggered by leptons of the second neutralino decay. For the trigger requirement at the truth-level, it is checked whether at least one electron or muon passes the p_T and η cuts of one of the triggers. The remaining cuts belong to the vertex-level selection explained in Section 5.2.3. Certain selection criteria do not apply at the truth-level, such as the fit quality or the overlap removal. The fifth bin of the reco-level cutflows requires that a reconstructed secondary vertex matches the neutralino decay under study. The subsequent cuts are then applied to this reconstructed vertex.

The event-level cuts have minor impact at the truth-level if the neutralino is massive, while for a light neutralino the trigger requirement rejects more than 10% of the events. Most of the selection inefficiency is due to the vertex-level cuts. For very low neutralino

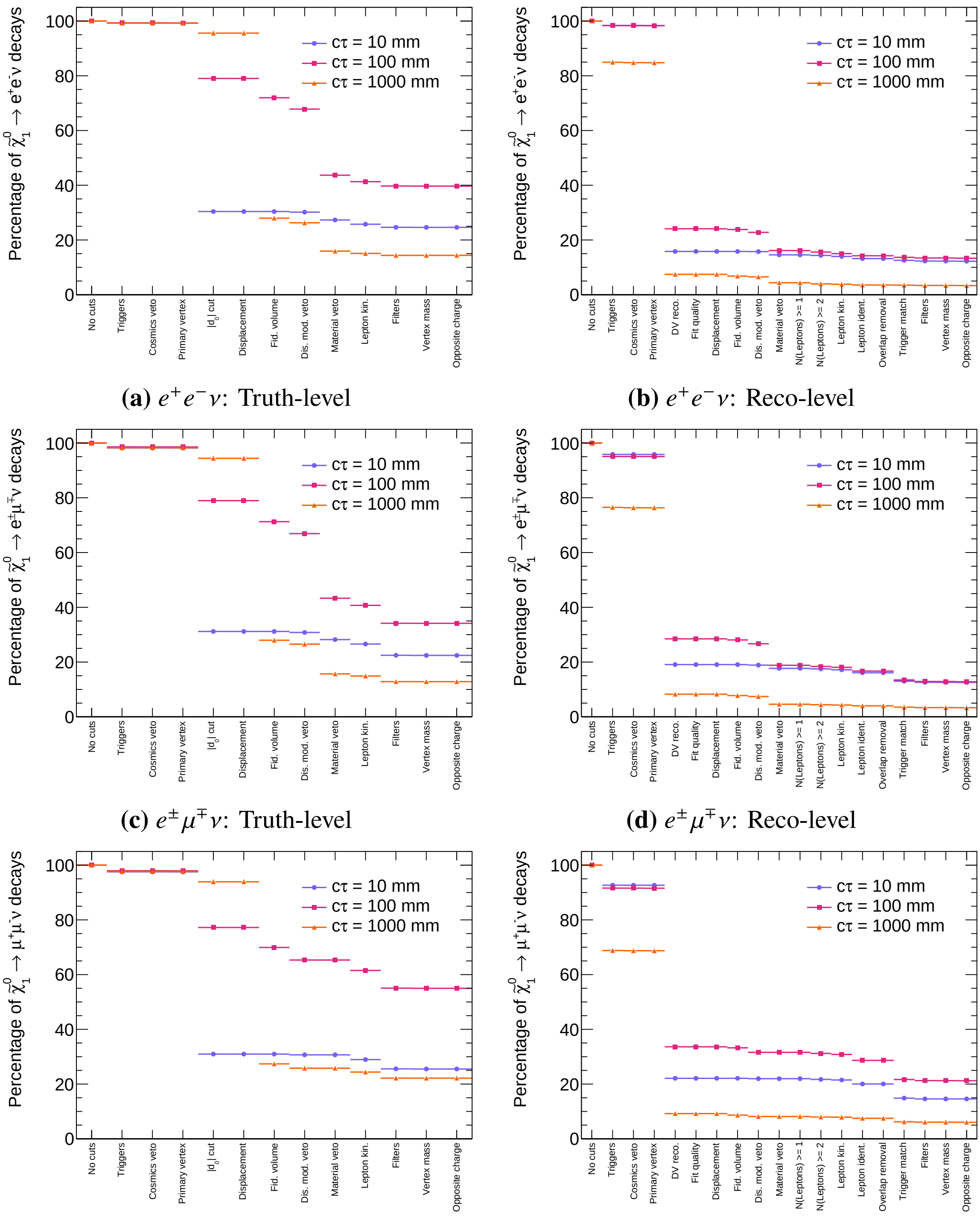

(a) $e^+e^-\nu$: Truth-level

(b) $e^+e^-\nu$: Reco-level

(c) $e^\pm\mu^\mp\nu$: Truth-level

(d) $e^\pm\mu^\mp\nu$: Reco-level

(e) $\mu^+\mu^-\nu$: Truth-level

(f) $\mu^+\mu^-\nu$: Reco-level

Figure 5.12: Fractions of $\tilde{\chi}_1^0$ decays to (top) $e^+e^-\nu$, (middle) $e^\pm\mu^\mp\nu$ and (bottom) $\mu^+\mu^-\nu$ passing sequentially the signal region cuts (left) at the truth-level and (right) at the reco-level for $m(\tilde{q}) = 700$ GeV, $m(\tilde{\chi}_1^0) = 500$ GeV and three $\tilde{\chi}_1^0$ lifetimes.

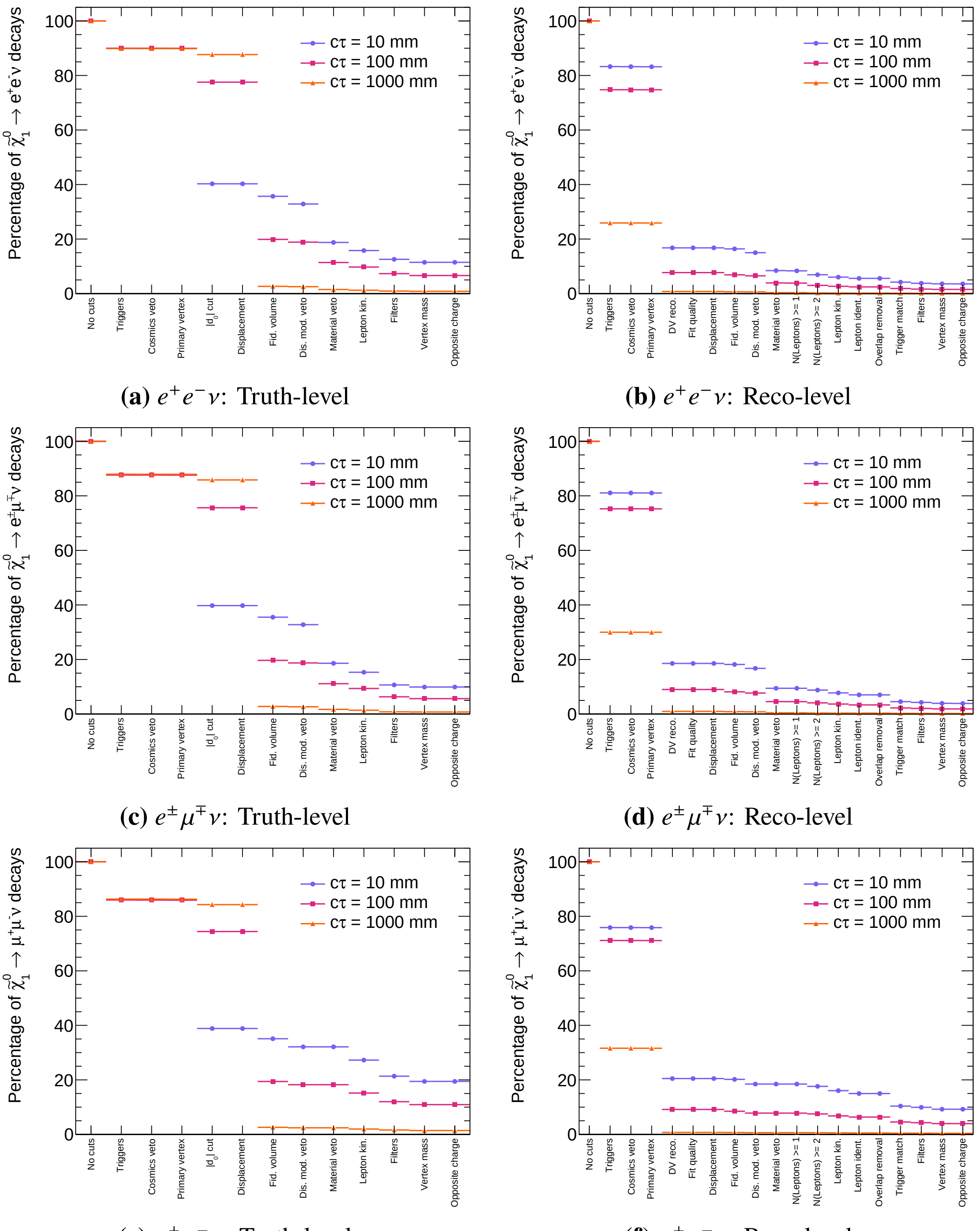

(a) $e^+e^-\nu$: Truth-level

(b) $e^+e^-\nu$: Reco-level

(c) $e^\pm\mu^\mp\nu$: Truth-level

(d) $e^\pm\mu^\mp\nu$: Reco-level

(e) $\mu^+\mu^-\nu$: Truth-level

(f) $\mu^+\mu^-\nu$: Reco-level

Figure 5.13: Fractions of $\tilde{\chi}_1^0$ decays to (top) $e^+e^-\nu$, (middle) $e^\pm\mu^\mp\nu$ and (bottom) $\mu^+\mu^-\nu$ passing sequentially the signal region cuts (left) at the truth-level and (right) at the reco-level for $m(\tilde{q}) = 700\,\text{GeV}$, $m(\tilde{\chi}_1^0) = 50\,\text{GeV}$ and three $\tilde{\chi}_1^0$ lifetimes.

lifetimes, the minimum $|d_0|$ requirement of 2 mm has the largest impact on the selection efficiency, while the fiducial volume cut is dominant for neutralinos with a very high lifetime. Decays into at least one electron have a reduced selection rate compared to decays into two muons because of the material veto, whose impact depends on the average flight distance of the neutralino. If the neutralino is heavy and has a short lifetime, then only few decays are rejected by the material veto as there is no material inside the beam pipe (radius of 25 mm). In all other cases, it can lead to a reduction of the selection efficiency of up to 42%. Depending on the signal MC sample, the kinematic requirements such as the filters or the vertex mass can be a non-negligible source of inefficiency.

In the reco-level cutflows, the trigger requirement rejects a significant fraction of the events if the neutralino has a long lifetime or low mass. In both cases, the flight distance of a neutralino can become so large that it decays inside the calorimeters or even the muon spectrometer. This can cause electrons to lose only a fraction of their energy in the electromagnetic calorimeter and muons to leave too few hits in the muon spectrometer to be reconstructed reducing the trigger efficiencies. For all signal MC samples, the reconstruction of displaced vertices (fifth bin) is one of the main sources of efficiency loss. At the reco-level, the fiducial volume cut has a much smaller impact than at the truth-level, since no vertices are reconstructed with $r > 300$ mm as already discussed, and therefore the impact of the fiducial volume cut is mostly hidden in the reconstruction efficiency of the vertices. Almost no vertices are rejected at the reco-level by the opposite charge requirement, which shows that a charge flip occurs very rarely. The impact of the remaining cuts follow similar patterns as at the truth-level.

Since the reconstruction of displaced vertices causes a large efficiency loss, it is studied in more detail. In the following, the total reconstruction efficiency is defined as the product of the tracking and vertexing efficiency. The tracking efficiency is the fraction of neutralino decays where both lepton tracks are reconstructed and each track is required to have at least one silicon hit[6]. Its dependence on the decay radius of the neutralino is shown for two neutralino masses in Figure 5.14. The tracking efficiency is maximal for low decay radii regardless of the neutralino mass. It is higher for $\mu\mu$ than for ee up to radii of 150 mm, where the trend reverses. For a heavy neutralino, the tracking efficiency has a maximum of 93–94% and decreases continuously with increasing radius, reaching values of 35–38% for radii between 250 and 300 mm. For a light neutralino, it has two plateaus separated by a

[6] In few cases, tracks are reconstructed based only on measurements from the TRT detector. Such tracks are not relevant for this analysis, and therefore not considered in this study as they would bias the results.

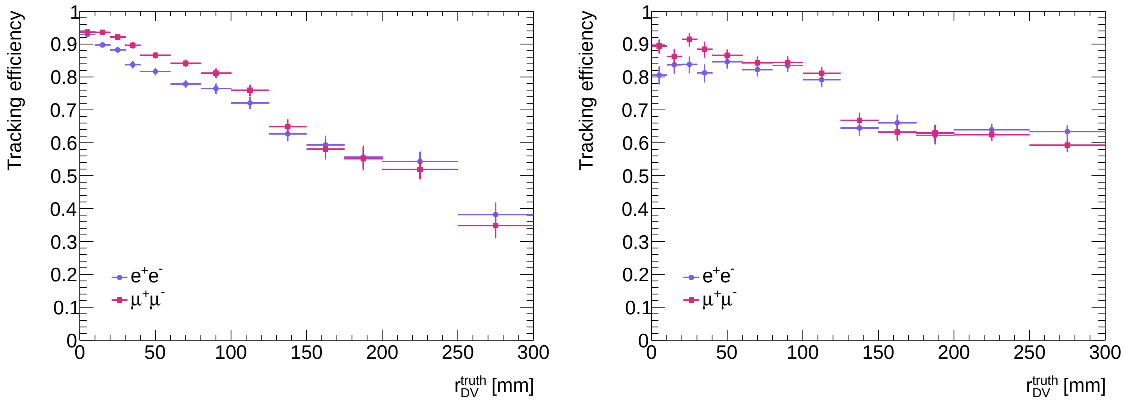

(a) $m(\tilde{\chi}_1^0) = 500\,\text{GeV}$ **(b)** $m(\tilde{\chi}_1^0) = 50\,\text{GeV}$

Figure 5.14: Tracking efficiency of $\tilde{\chi}_1^0$ decays to $e^+e^-\nu$ and $\mu^+\mu^-\nu$ as a function of the transverse radius of the $\tilde{\chi}_1^0$ decay for $m(\tilde{q}) = 700\,\text{GeV}$, two values of $m(\tilde{\chi}_1^0)$ and $c\tau = 100\,\text{mm}$. Neutralino decays outside the fiducial volume are not considered.

sudden drop at a radius of about 120 mm. The first plateau has efficiencies of 80–92%, while the efficiencies of the second plateau are 59–66%. This drop in efficiency can be explained by the fact that the leptons are produced outside the pixel barrel when the decay radius of the neutralino is greater than approximately 125 mm, so that their tracks have to be reconstructed using SCT measurements only, which reduces the probability that there are enough hits to reconstruct the track. There is also an efficiency drop at the same radius for a massive neutralino, but it is smaller. In general, the decline in tracking efficiency is much greater for a heavy neutralino, as the tracking efficiency deteriorates significantly with increasing magnitude of the transverse impact parameter d_0 (see Section 5.4.1), and as the $|d_0|$ is larger on average for a high neutralino mass (see Figure 5.6).

The second part of the reconstruction efficiency, the vertexing efficiency, is the probability that a vertex was found if both tracks were reconstructed and is shown in Figure 5.15 for the same signal MC samples as before. It is minimal for decay radii of less than 10 mm, as many tracks of such neutralino decays are rejected by the $|d_0| > 2\,\text{mm}$ requirement of the displaced vertex reconstruction. If the neutralino is light, the efficiency increases continuously until it reaches a plateau with values of 30–50% at a radius of about 40 mm. For a massive neutralino, the efficiency has a local maximum of 40% (ee) and 59% ($\mu\mu$) at radii between 10 and 20 mm, followed by a decrease in efficiency up to a radius of 40 mm, from where it remains almost constant up to a radius of 120 mm. After that, the efficiency increases up to a second maximum of 46% (ee) and 55% ($\mu\mu$) at a radius

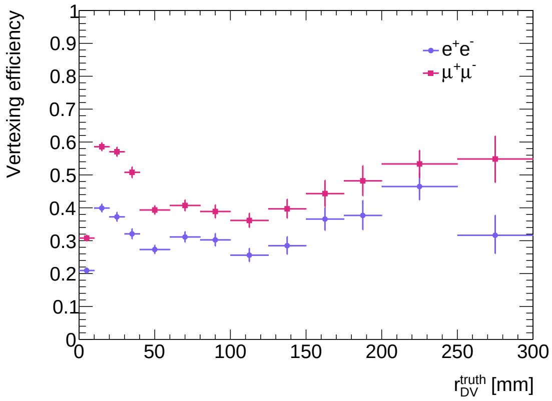

(a) $m(\tilde{\chi}_1^0) = 500\,\mathrm{GeV}$

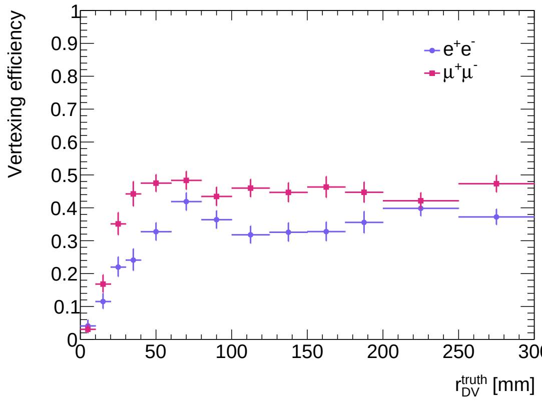

(b) $m(\tilde{\chi}_1^0) = 50\,\mathrm{GeV}$

Figure 5.15: Vertexing efficiency of $\tilde{\chi}_1^0$ decays to $e^+e^-\nu$ and $\mu^+\mu^-\nu$ as a function of the transverse radius of the $\tilde{\chi}_1^0$ decay for $m(\tilde{q}) = 700\,\mathrm{GeV}$, two values of $m(\tilde{\chi}_1^0)$ and $c\tau = 100\,\mathrm{mm}$. Neutralino decays outside the fiducial volume are not considered.

between 200 and 300 mm. In nearly all cases, the vertexing efficiency is greater for $\mu\mu$ than for ee, by up to 75%.

Figure 5.16 shows that the average uncertainty in the track impact parameter d_0 increases by about a factor of three at a decay radius of approximately 120 mm, where the last pixel layer is located (see Figure 4.7). A similar rise in uncertainty also occurs for the other four track parameters. As the track uncertainties increase, it becomes more likely that the tracks of a neutralino decay overlap within their uncertainties, which results in a lower χ^2/n_{DoF} value of the vertex fit, explaining why the vertexing efficiency for a massive neutralino improves at a radius of about 120 mm.

Not only the reconstruction efficiencies differ between ee and $\mu\mu$ vertices, but also the resolutions of the vertex observables. Figure 5.17 shows the relative differences between the reconstructed and true values of the transverse radius and mass of ee and $\mu\mu$ vertices in a signal MC sample. For 94% of the $\mu\mu$ vertices, the transverse radius agrees with its true value within 0.2%, while this is the case for 82% of the ee vertices. Thus, the displaced vertex position is determined with very high accuracy. The deviation of the reconstructed mass from the true mass is below 20% for 95% of the $\mu\mu$ vertices and symmetric around zero, while for ee vertices the reconstructed mass is smaller than the true mass in 88% of the cases, on average by 21%. The displaced vertex reconstruction uses the original inner detector tracks for electrons instead of the tracks refitted with Gaussian-sum-filter, which

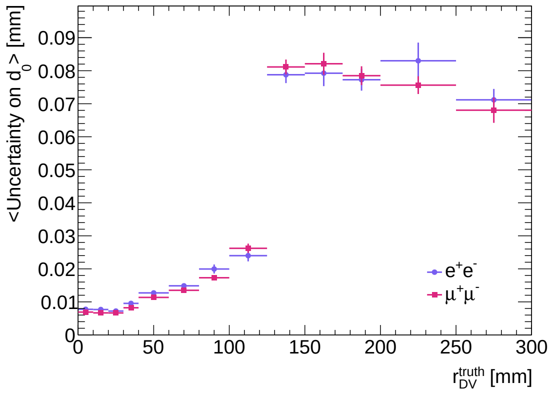

Figure 5.16: Average uncertainty in the transverse impact parameter of tracks of *ee* and $\mu\mu$ vertices as a function of the transverse radius of the $\tilde{\chi}_1^0$ decay for $m(\tilde{q}) = 700\,\text{GeV}$, $m(\tilde{\chi}_1^0) = 500\,\text{GeV}$ and $c\tau = 100\,\text{mm}$.

means that energy losses due to bremsstrahlung are not taken into account, which typically leads to smaller reconstructed masses of the *ee* vertices.

5.3.2 Lifetime reweighting and signal efficiency curves

So far, the signal efficiency has only been studied for specific values of the neutralino lifetime that have been simulated. Continuous interpolation between the discrete lifetime values is performed using the lifetime reweighting technique.

The probability density function of the neutralino lifetime t for a simulated mean lifetime τ_{MC} is given by an exponential:

$$P(t, \tau_{\text{MC}}) = \frac{1}{\tau_{\text{MC}}} \exp\left(-\frac{t}{\tau_{\text{MC}}}\right) . \tag{5.3}$$

The kinematics of an individual event and other details of the simulation do not depend on the lifetimes of the two neutralinos, but the probability of observing such an event depends on them. Thus, a sample with a different mean lifetime τ_{goal} can be emulated by applying the weight

$$w_{\text{Evt}} = w_{\text{LSP1}} \cdot w_{\text{LSP2}} \tag{5.4}$$

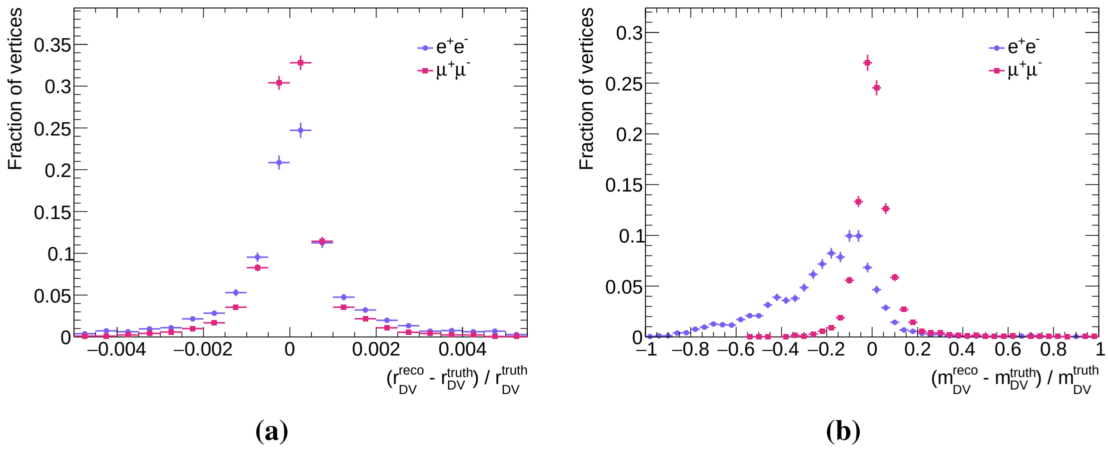

Figure 5.17: Relative difference between the reconstructed and the true value of (a) the transverse radius and (b) the vertex mass of ee and $\mu\mu$ vertices for $m(\tilde{q}) = 700\,\text{GeV}$, $m(\tilde{\chi}_1^0) = 500\,\text{GeV}$ and $c\tau = 100\,\text{mm}$.

to each event, where

$$w_{\text{LSP}} = \frac{P(t, \tau_{\text{goal}})}{P(t, \tau_{\text{MC}})} = \frac{\tau_{\text{MC}}}{\tau_{\text{goal}}} \exp\left(-\left(\frac{1}{\tau_{\text{goal}}} - \frac{1}{\tau_{\text{MC}}}\right) t\right) \tag{5.5}$$

is the weight for one of the two neutralinos of an event and given by the ratio of the probability density for τ_{goal} to that for τ_{MC}, evaluated at the lifetime t of the neutralino.

In practice, the lifetime reweighting can be used in various ways to obtain signal efficiency curves as a function of lifetime. For example, the five samples for the different neutralino lifetimes could be merged into a single large sample, which is reweighted accordingly. Several options were tested and the method that gave the best results is used in the analysis. Thus, the reweighing is performed independently for each of the five simulated lifetimes. In the end, a weighted mean of the five efficiency curves is calculated to obtain the final prediction of the signal efficiency. The so-called effective number of events

$$n_{\text{Eff}}(t) = \left(\sum w(t)\right)^2 / \left(\sum w(t)^2\right) \tag{5.6}$$

is used as weight in the computation of the mean. If all events have the same weight, then n_{Eff} is identical to the number of generated events. It is a measure for the number of events with equal weights that would have to be simulated to obtain the same relative statistical precision as in the weighted sample. A closure test of this lifetime reweighting procedure is presented in Appendix A.

The lifetime reweighting is used to study two types of efficiencies. Vertex-level efficiencies are the fraction of $\tilde{\chi}_1^0$ decays to one specific decay channel that pass the signal selection, while event-level efficiencies are the fraction of events that pass the signal selection. Thus, event-level efficiencies benefit from the fact that there are two neutralinos per event and are correlated with the vertex-level efficiencies by

$$\epsilon_{\mathrm{Evt}} = 1 - (1 - \bar{\epsilon}_{\mathrm{Vx}})^2 = 2\bar{\epsilon}_{\mathrm{Vx}} - \bar{\epsilon}_{\mathrm{Vx}}^2, \tag{5.7}$$

where $\bar{\epsilon}_{\mathrm{Vx}}$ is an average that takes into account the branching ratios of the $\tilde{\chi}_1^0$ decay. Consequently, event-level efficiencies can be up to two times higher than the vertex-level efficiencies.

The event-level efficiencies are used in Section 5.7 to derive upper limits on the cross-section of this signal model. The vertex-level efficiencies do not depend on the branching ratios of the neutralino and are therefore less model dependent. They can be used to reinterpret the results of this search in other models beyond the Standard Model that predict long-lived particles decaying to oppositely charged lepton pairs. The selection criteria explained in Section 5.2 were chosen to be as model-independent as possible to make a reinterpretation of the results possible.

Figure 5.18 shows the vertex-level efficiencies both at the truth-level and at the reco-level. The uncertainty bands on the truth-level efficiencies include only uncertainties from statistical fluctuations. Uncertainties at the reco-level efficiencies are much larger, and include all of the additional sources of systematic uncertainty discussed in Section 5.5. The truth-level efficiencies reach values up to 65% for $\mu^+\mu^-$ and up to 45% for the other two decay modes if the neutralino is massive, while these maxima are reduced to values of 20% and 10%, respectively, for a light neutralino. The full widths at half maximum of the truth-level efficiency curves span up to two orders of magnitude of the lifetime meaning that the selection criteria allow the analysis to be sensitive to a signal over a wide range of lifetimes. At the reco-level, the maxima are more than a factor of two lower due to the vertex reconstruction efficiency discussed in the previous section. Furthermore, if the $\tilde{\chi}_1^0$ is massive, the maxima are shifted towards shorter lifetimes compared to the truth-level and the curves also have a narrower width. This is likely explained by the fact that for longer lifetimes, more neutralinos decay close to the boundaries of the fiducial volume, where the tracking efficiencies are lower (see Figure 5.14).

The event-level efficiencies are shown in Figure 5.19 for $\tilde{\chi}_1^0$ decays mediated by a pure λ_{121} or λ_{122} coupling. Their shapes are very similar to the vertex-level efficiencies as explained by Equation (5.7), while the values are significantly higher. Thus, for a heavy neutralino, the event-level efficiencies can be as high as 80% at the truth-level and 40% at the reco-level, while for a light neutralino, the maximal values are 30% and 12%, respectively.

Not only the efficiencies themselves, but also the statistical uncertainties are larger for event-level efficiencies than for vertex-level efficiencies. In some cases, one of the two neutralinos receives a very small weight, resulting in a very small event weight, so that the event does not contribute much to the final result, increasing the statistical uncertainty. For the vertex-level efficiencies, each neutralino is evaluated independently, and thus the second neutralino of such cases can still fully contribute to the final result. The statistical uncertainties are shown in Appendix B along with other uncertainties for the reco-level efficiencies of Figures 5.18 and 5.19.

The number of signal events

$$N = \epsilon_{\mathrm{Evt}} \sigma L \tag{5.8}$$

expected in the signal region can be calculated using the event-level efficiencies at the reco-level, the cross-sections σ from the Table 5.1 and the integrated luminosity $L = 32.8\,\mathrm{fb}^{-1}$. Figure 5.20 illustrates that up to 6500 signal events are expected for eight mass-degenerate squarks with a mass of 700 GeV and up to 15 events for squarks with a mass of 1.6 TeV. Assuming that no event is observed in the data, the light squarks would be excluded at a confidence level of 95% for almost the entire lifetime space considered and even for the heavy squarks more than two orders of magnitude of the lifetime could be excluded if the neutralino mass is 1.3 TeV.

5.4 Lepton and trigger efficiencies

In the previous section, the signal efficiencies have been estimated using MC simulations. An important part of these are the lepton and trigger efficiencies. Both efficiencies are potentially mismodelled in the simulations, because they were produced prior to data taking and therefore the simulated detector conditions may not be identical to those of the data. In

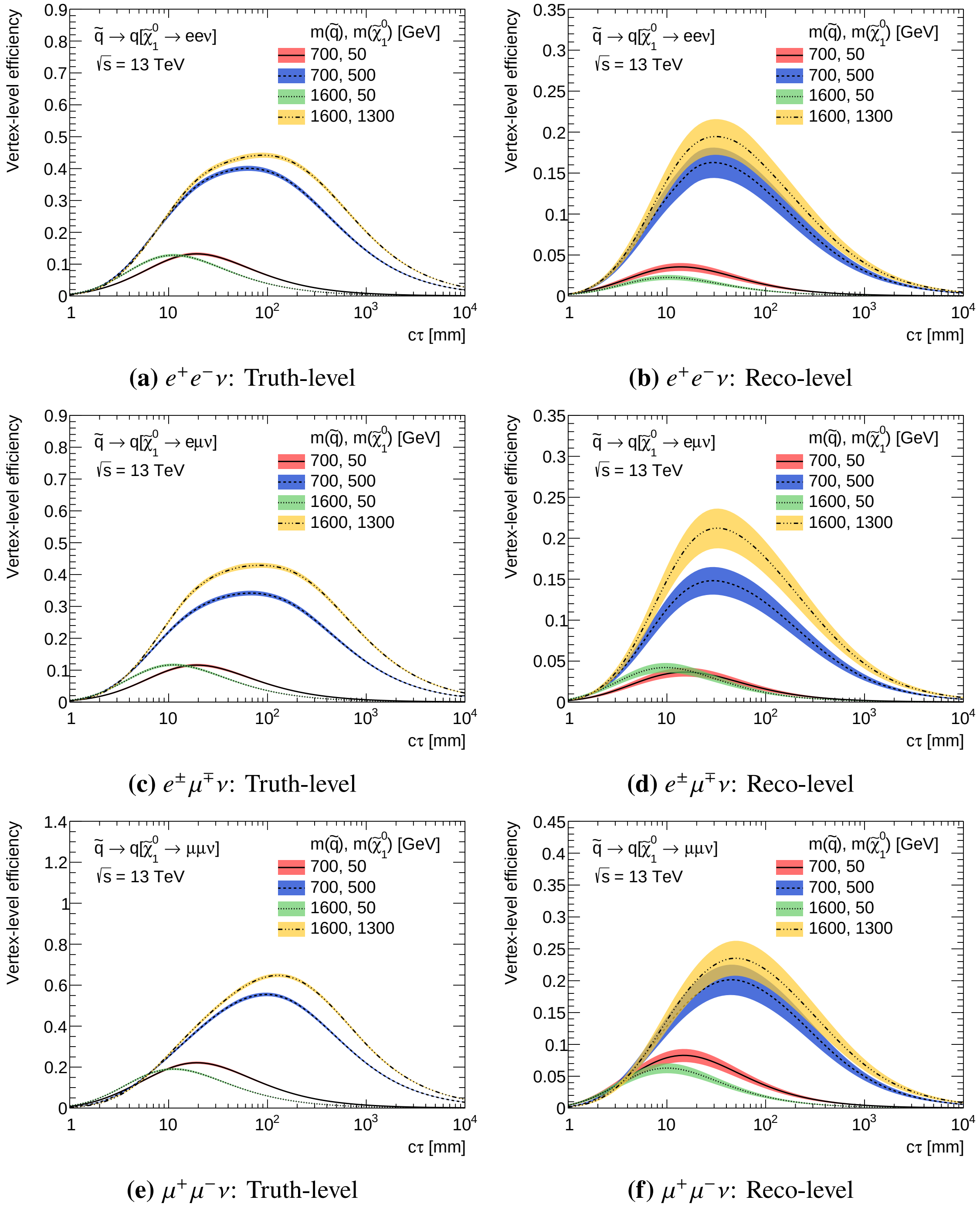

(a) $e^+e^-\nu$: Truth-level

(b) $e^+e^-\nu$: Reco-level

(c) $e^\pm\mu^\mp\nu$: Truth-level

(d) $e^\pm\mu^\mp\nu$: Reco-level

(e) $\mu^+\mu^-\nu$: Truth-level

(f) $\mu^+\mu^-\nu$: Reco-level

Figure 5.18: Fraction of $\tilde{\chi}_1^0$ decays to (top) $e^+e^-\nu$, (middle) $e^\pm\mu^\mp\nu$ and (bottom) $\mu^+\mu^-\nu$ passing the signal region criteria (left) at the truth-level and (right) at the reco-level as a function of the $\tilde{\chi}_1^0$ lifetime for four combinations of squark and neutralino masses.

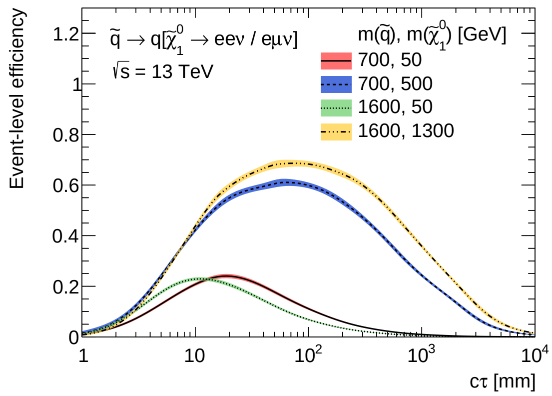

(a) λ_{121}: Truth-level

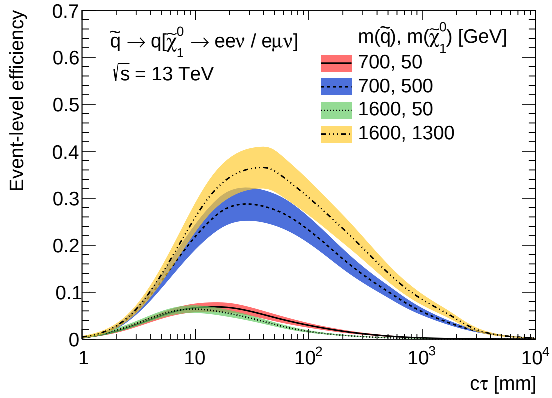

(b) λ_{121}: Reco-level

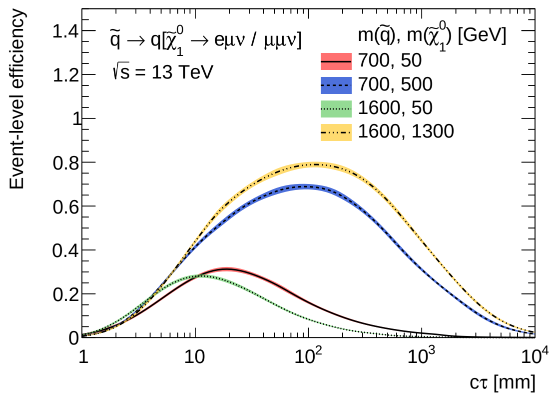

(c) λ_{122}: Truth-level

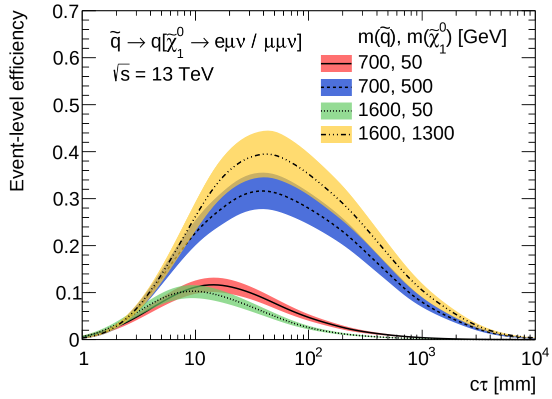

(d) λ_{122}: Reco-level

Figure 5.19: Fraction of events passing the signal region criteria (left) at the truth-level and (right) at the reco-level as a function of the $\tilde{\chi}_1^0$ lifetime for four combinations of squark and neutralino masses and $\tilde{\chi}_1^0$ decays mediated by (top) a λ_{121} or (bottom) a λ_{122} coupling.

addition, the models assumed in the simulations may not describe the data correctly, even if the detector conditions are the same. The standard procedure for correcting discrepancies between the simulations and data is to scale the simulated efficiencies to the data efficiencies using scale factors. The scale factors are determined by studying the efficiencies for a given Standard Model process both in the data and in simulations. For this purpose, the tag-and-probe method is usually performed on events in which a Z boson decays into an oppositely charged lepton pair, since this process has a large cross-section and provides a very clean signature. The Z boson has a very short lifetime of $2.6 \cdot 10^{-25}$ s, meaning that the leptons produced are not displaced. Therefore, the results of such tag-and-probe studies may not be relevant to this search.

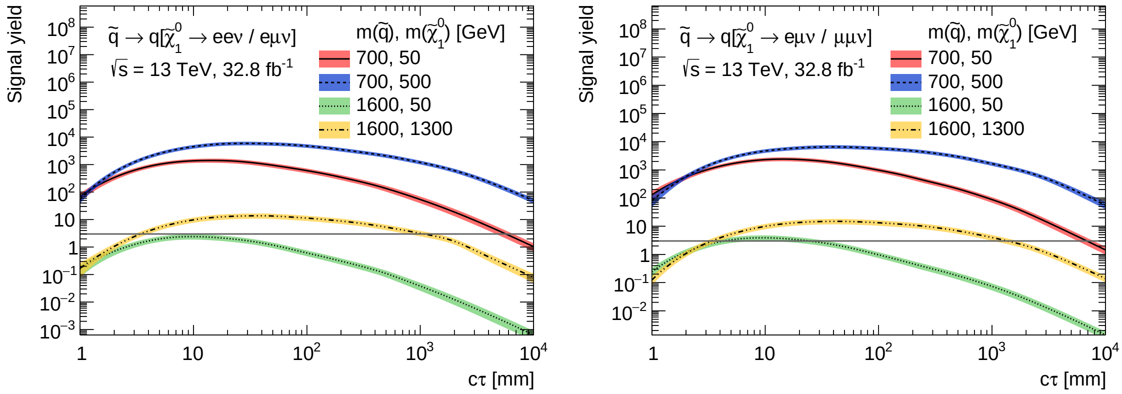

(a) λ_{121} **(b)** λ_{122}

Figure 5.20: Number of events passing the signal region criteria for four combinations of squark and neutralino masses and $\tilde{\chi}_1^0$ decays mediated by (a) a λ_{121} or (b) a λ_{122} coupling. The horizontal line shows the optimal exclusion limit at 95% confidence level of three events.

Instead, the efficiencies should be studied using processes that contain displaced leptons. There are only two sources of displaced leptons in the data, cosmic-ray muons and photon conversions. Unfortunately, cosmic-ray muons could not be used to study the efficiencies for muons. In 2016, there was only one cosmic run[7] where all subdetectors and magnets were operational, giving an insufficient data sample to perform a precise efficiency measurement. Furthermore, there are unavoidable differences in muon reconstruction between cosmic and standard ATLAS runs (including the signal MC) that make it difficult to compare the efficiencies measured in the cosmic data to those of signal MC samples. Photon conversions turned out to be impractical, as the electrons produced have a low p_{T} of a few GeV and there is a large background from hadronic processes with low masses, rendering it difficult to select photon conversions with sufficient purity.

Since it is not possible to measure the lepton and trigger efficiencies in the data with displaced leptons, it is important to examine whether tag-and-probe studies of Z+jets events could be used to correct the simulated efficiencies of displaced leptons. If these efficiencies do not depend on the displacement of the leptons, the scale factors calculated for prompt leptons can also be applied to displaced leptons. This dependence of the lepton and trigger efficiencies is therefore studied in the signal MC samples in Sections 5.4.1 and 5.4.2, respectively. It turns out that the lepton efficiencies strongly depend on the

[7] Special run with no beam, with the intention to record cosmic-ray muons.

displacement of the leptons, making a tag-and-probe study of them irrelevant. Since no way was found to measure them in the data, the lepton efficiencies predicted by simulations are used unmodified in the interpretations of this search. The studies of Section 5.4.1 also reveal that the tracking efficiency is the dominant part of the total lepton efficiency, and thus the systematic uncertainty in the tracking efficiency derived in Section 5.5.3 should be a good measure of an uncertainty in the lepton efficiency. In contrast, the trigger efficiencies show a negligible dependence, and therefore tag-and-probe studies of them are performed in Section 5.4.3.

5.4.1 Lepton efficiencies in signal MC samples

In the following, the dependences of the lepton efficiencies on the impact parameters of the leptons are investigated. The total lepton efficiency is divided into two independent parts to study the source of a potential efficiency loss. The first part is the tracking efficiency, which is the fraction of truth leptons produced in a $\tilde{\chi}_1^0$ decay that can be matched to a reconstructed inner detector track satisfying the selection criteria applied in the displaced vertex reconstruction (see Section 4.4.2). Tracks failing these criteria cannot be part of a displaced vertex, and are therefore irrelevant for the signal region. Finally, there is the identification efficiency, which is the fraction of truth-matched tracks that belong to a reconstructed lepton passing the modified loose working points of the lepton identification algorithms.

These two efficiencies are shown in Figure 5.21 for electrons and muons of a signal MC sample with a 500 GeV neutralino. The tracking efficiency decreases from values of up to 90% for low impact parameters to about 10% for $|d_0| = 250$ mm or $|z_0| = 500$ mm. There is a drop in efficiency by roughly 15% for $|d_0| > 10$ mm indicating that the large radius tracking is less efficient than the standard tracking. The muon identification efficiency shows only a very small dependence on the impact parameters and is greater than 90% in all cases, while the electron identification efficiency decreases constantly from 95% for very small $|d_0|$ to about 55% for $|d_0| > 230$ mm. The larger the $|d_0|$, the more likely it is that the lepton track has no pixel hit, and for $|d_0| \gtrapprox 125$ mm the tracks have no pixel hit, since the lepton is produced outside the active layers of the pixel detector. Figure 5.21d shows that the electron identification efficiency is noticeably reduced if the electron track has no pixel hit. The reason for this is that calorimeter clusters associated with such tracks are sometimes reconstructed as converted photons and not as electrons if the track is part

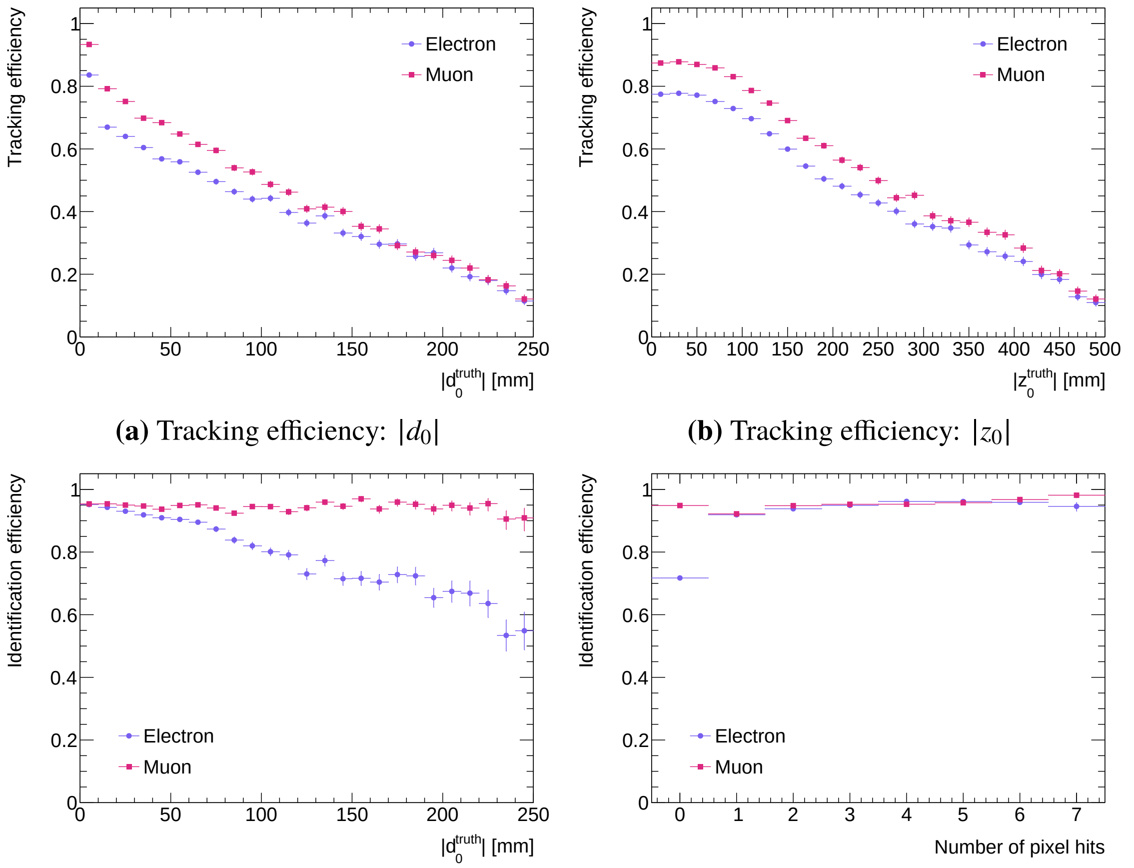

(a) Tracking efficiency: $|d_0|$

(b) Tracking efficiency: $|z_0|$

(c) Identification efficiency: $|d_0|$

(d) Identification efficiency: N(Pixel)

Figure 5.21: (top) Tracking and (bottom) lepton identification efficiencies as a function of the impact parameters at the truth-level and the number of pixel hits using all signal MC samples with $m(\tilde{q}) = 700\,\text{GeV}$ and $m(\tilde{\chi}_1^0) = 500\,\text{GeV}$. Only tracks passing the selection criteria of the displaced vertex reconstruction described in Section 4.4.2 are considered.

of a conversion vertex (see Section 4.4.3). This drop in efficiency for tracks with no pixel hit explains the decrease of the electron identification efficiency as the $|d_0|$ increases.

To illustrate the impact of a large Lorentz boost of the neutralino on these efficiencies, the same plots as before are shown in Figure 5.22 for a much lighter neutralino. The tracking efficiency is significantly reduced to values below 80% and decreases much faster in comparison to the low boost case, and therefore it reaches an efficiency as low as 10% already at $|d_0| \approx 100\,\text{mm}$ or $|z_0| \approx 200\,\text{mm}$. The Lorentz boost increases the average flight distance of the neutralino so that the leptons are produced at higher radii (see Figure 5.4b), which reduces the number of pixel hits, which in turn deteriorates the tracking efficiency.

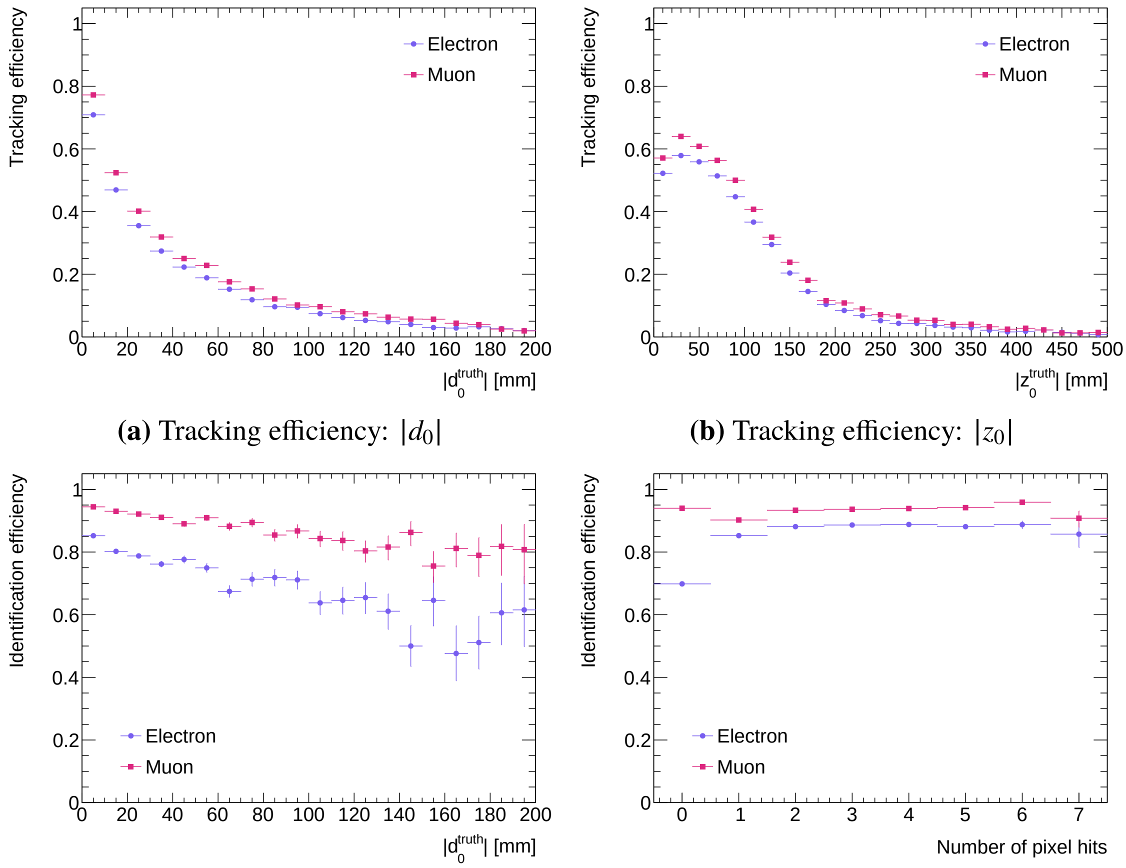

(a) Tracking efficiency: $|d_0|$ **(b)** Tracking efficiency: $|z_0|$

(c) Identification efficiency: $|d_0|$ **(d)** Identification efficiency: N(Pixel)

Figure 5.22: (top) Tracking and (bottom) lepton identification efficiencies as a function of the impact parameters at the truth-level and the number of pixel hits using all signal MC samples with $m(\tilde{q}) = 700\,\text{GeV}$ and $m(\tilde{\chi}_1^0) = 50\,\text{GeV}$. Only tracks passing the selection criteria of the displaced vertex reconstruction described in Section 4.4.2 are considered.

Both lepton identification efficiencies seem to decrease linearly as the magnitude of the transverse impact parameter increases. Thus, the muon identification efficiency decreases from 90% for a small $|d_0|$ to about 80% for $|d_0| = 200\,\text{mm}$, while the electron identification is for each bin in $|d_0|$ about 5–10% lower than the muon identification efficiency and decreases from 85% to 50% for $|d_0| = 160\,\text{mm}$. In contrast to the low boost case, the electron and muon identification efficiencies are not identical for tracks that have at least one pixel hit, instead the efficiency of electrons is always lower regardless of the number of pixel hits.

Summarising these studies, the tracking efficiency is the dominating source of efficiency loss for both electrons and muons and strongly depends on the displacement of the leptons and the boost of the neutralino. Also the lepton identification efficiencies show dependences on both quantities, especially for electrons. Consequently, these efficiencies cannot be studied in the data by performing a tag-and-probe study on prompt leptons from Z boson decays. As the tracking efficiency is the dominant contribution, its systematic uncertainty should be a good estimate of the systematic uncertainty in the total lepton efficiency. These studies also indicate that the dependences of the tracking efficiencies on the impact parameters of the leptons hardly differ between electrons and muons. Due to the latter and the fact that pion tracks should have similar properties to muon tracks because they have similar masses, pion tracks from K_S decays are used to derive a systematic uncertainty in the tracking efficiency. This study is discussed in Section 5.5 together with the other systematic uncertainties.

5.4.2 Trigger efficiencies in signal MC samples

In the following, the dependences of the trigger efficiencies on the impact parameters of the leptons are investigated. The trigger efficiency is defined as the fraction of reconstructed leptons that pass a given trigger. The leptons are required to fulfil the identification criteria of the signal selection discussed in Section 5.2.3. In addition, their p_T has to be in the plateau region of the trigger, using the p_T cuts derived in Section 5.4.3, and their η has to be within the acceptance region of the trigger. For these studies, signal MC samples are used where the neutralino has a high mass, because the leptons then have on average a high p_T, increasing the probability that they pass the p_T cuts, which in turn leads to a higher statistical precision of the trigger efficiencies.

The single photon trigger, `HLT_g140_loose`, has a high efficiency of about 98% for electrons with $p_\mathrm{T} > 148\,\mathrm{GeV}$ and $|\eta| < 2.47$. Figure 5.23 shows that the efficiency of this trigger remains nearly constant up to $|d_0| = 220\,\mathrm{mm}$ and $|z_0| = 320\,\mathrm{mm}$. This is expected because photons are reconstructed from energy deposits in the calorimeters without any constraints on their point of origin. For higher impact parameters, there seems to be a slight decrease of the efficiencies. The diphoton trigger efficiency has similar characteristics and is not shown here. Since their dependences on the impact parameters are negligible, the efficiencies of the two photon triggers can be measured in the data with a tag-and-probe study, which is discussed in the next section.

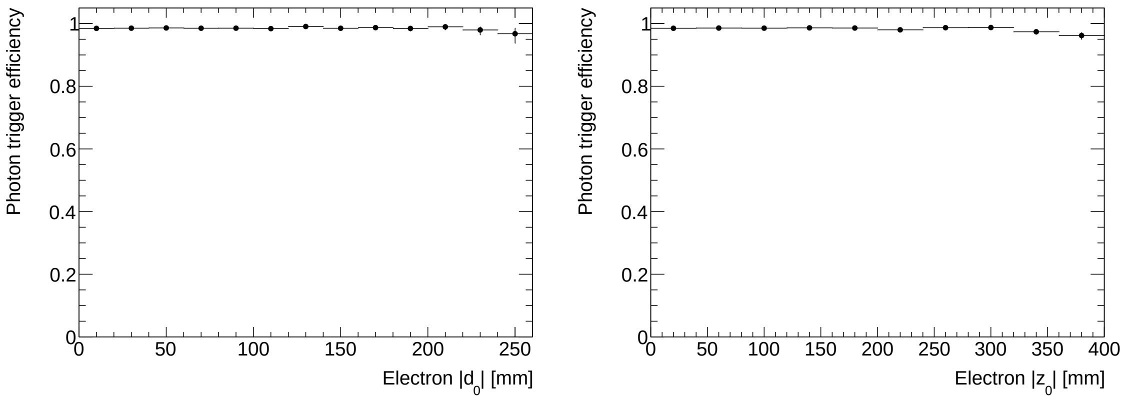

(a) **(b)**

Figure 5.23: Efficiency of the `HLT_g140_loose` trigger as a function of (a) the transverse and (b) the longitudinal impact parameter of selected electrons using all signal MC samples with $m(\tilde{q}) = 1.6\,\text{TeV}$ and $m(\tilde{\chi}_1^0) = 1.3\,\text{TeV}$. The selection criteria applied to electrons are explained in the text.

Finally, the single muon trigger, `HLT_mu60_0eta105_msonly`, is studied, whose efficiencies are illustrated in Figure 5.24. The muons of this study were required to have a $p_\text{T} > 62\,\text{GeV}$ and $|\eta| < 1.05$. The efficiency is stable at approximately 70% for $|d_0| < 120\,\text{mm}$ and $|z_0| < 160\,\text{mm}$, but drops for larger values of the impact parameters. The decline is more significant for the transverse impact parameter, where the efficiency reaches 37% for $|d_0| > 240\,\text{mm}$. This efficiency loss for large impact parameters has been investigated in more detail. As discussed in Section 4.2.4, each trigger in ATLAS consists of an L1 and an HLT part. The L1 trigger associated with the `HLT_mu60_0eta105_msonly` trigger is the `L1_MU20` trigger, which has a p_T threshold of 20 GeV. The efficiency of this L1 trigger was also studied and showed the same dependence on the impact parameters as the single muon trigger, while the pure HLT part had no dependence at all. Thus, the impact parameter dependence is due to the L1 trigger and likely caused by the requirement of the L1 muon triggers that the coincidences of hits in the RPC and TGC detectors have to point to the beam interaction region.

Due to the exponential decrease of the impact parameter distributions, as illustrated in Figure 5.4 for example, the performance of the triggers for low values is dominating the overall performance. Even for a lifetime of the neutralino as large as 1000 mm, the fraction of selected muons with $|d_0| > 120\,\text{mm}$ or $|z_0| > 160\,\text{mm}$ is only up to 15% and it decreases to less than 4% for a $c\tau$ of 100 mm. Furthermore, the trigger efficiency averaged

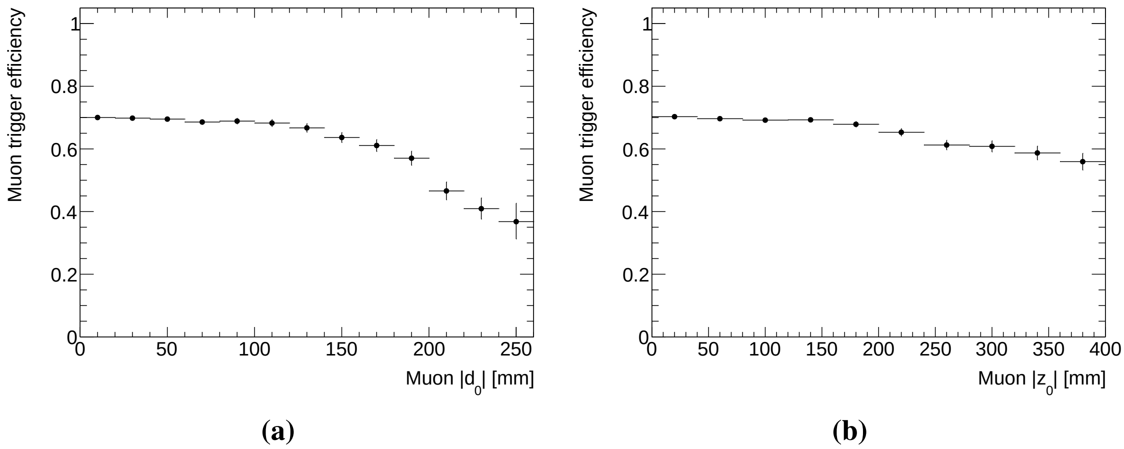

Figure 5.24: Efficiency of the `HLT_mu60_0eta105_msonly` trigger as a function of (a) the transverse and (b) the longitudinal impact parameter of selected muons using all signal MC samples with $m(\tilde{q}) = 1.6\,\text{TeV}$ and $m(\tilde{\chi}_1^0) = 1.3\,\text{TeV}$. The selection criteria applied to muons are explained in the text.

over all selected muons of one of the samples with $c\tau = 1000\,\text{mm}$ is in the range between 67% and 69% and is thus only a few percent smaller than the trigger efficiency for prompt muons. A potential mismodelling for high impact parameters is therefore neglected and the trigger efficiency of the muon trigger is measured using a tag-and-probe study, which is presented in the next section.

5.4.3 Tag-and-probe studies of trigger efficiencies

The studies of the previous section showed that the trigger efficiencies are constant over a sufficiently large range of displacements to allow measurements for prompt leptons to be applied also to displaced leptons. These measurements are done with a tag-and-probe method performed on leptons from the decay of a Z boson. In this method, a pair of leptons is selected, where the probe lepton has to satisfy loose selection criteria and the tag lepton is required to be isolated from hadronic activity and to pass tight identification criteria. Efficiencies are measured using the probe lepton, while the requirements on the tag lepton and on the invariant mass of the lepton pair ensure that lepton pairs are selected only from a specific process with a very low background. The events have to pass a single lepton trigger that includes the loosest possible selection criteria to maximise the statistical accuracy of the studies. It is required that this trigger is passed by the tag lepton, and thus the efficiency measurement of a second trigger is unbiased as it is performed on a different lepton, namely the probe. The decay of the Z boson to two leptons is an ideal candidate for a tag-and-probe measurement due to its large cross-section, 1.95 nb for each $Z \to e^+e^-$ and $Z \to \mu^+\mu^-$, and its high mass of 91.2 GeV, which allows to study the lepton p_{T} over a large range of values.

The main purpose of these measurements is the calculation of so-called scale factors, defined as the ratio between the data efficiency and the simulated efficiency, which are used to correct the simulated efficiencies such that they agree with the efficiencies observed in the data. This is necessary since parts of the detector become less efficient or have to be disabled during the data-taking reducing the efficiencies in the data. Thus, the signal efficiencies would be overestimated if no scale factors were applied. Such time-dependent effects cannot be incorporated into the simulations as the detector conditions are the same for all events of a MC sample and the final detector conditions are often not known at the time of production.

The tag-and-probe measurements are performed on the standard data of ATLAS and not on the data preselected for this analysis and reconstructed with the optimised setup for decays of long-lived particles. The reason is that the filters explained in Section 5.2.1 were optimised for high signal efficiencies and low data rates, and select therefore only tiny numbers of Z boson decays to leptons, which are not enough to perform these studies. Since the lifetime of the Z boson, $2.6 \cdot 10^{-25}$ s, is extremely short, all leptons from its decay have transverse impact parameters much smaller than 1 mm, and thus the missing large radius tracking has a negligible impact on the results.

The simulated Z boson samples are inclusive, i.e. they have no additional requirements on the kinematics of the leptons, and were produced with the generators Powheg [100] and Pythia 8.186 [87]. The parton distribution functions are modelled according to the CTEQ6L1 tune [101]. As the data, the simulated events are reconstructed with the standard setup of ATLAS. Separate samples with nearly 80 million events each, corresponding to an integrated luminosity of about 40 fb^{-1}, have been produced for $Z \to e^+e^-$ and $Z \to \mu^+\mu^-$.

5.4.3.1 Photon triggers

To measure the efficiencies of the photon triggers, the tag-and-probe method is performed on $Z \to e^+e^-$ events, which are required to pass the lowest p_{T} unprescaled electron trigger, `HLT_e26_lhtight_nod0_ivarloose`. The selection criteria of the tag and probe

Table 5.5: Selection criteria applied to tag and probe electrons in the photon trigger efficiency studies

Cut	Tag electron	Probe electron
p_{T} [GeV]	> 27	> 30
Trigger matched	`HLT_e26_lhtight_nod0_ivarloose`	—
$\lvert\eta\rvert$	< 1.37 or (1.52 to 2.47)	< 2.47
Identification	Tight	Modified loose
Track isolation	Yes	—
Jet veto	—	Yes

electrons are summarised in Table 5.5. The tag electron is required to pass the electron trigger and the tight working point of the likelihood-based identification. Furthermore, its track has to be isolated from hadronic interactivity by requiring $p_{\mathrm{T}}^{\mathrm{cone0.2}}/E_{\mathrm{T}} < 0.1$, where $p_{\mathrm{T}}^{\mathrm{cone0.2}}$ is the scalar sum of the transverse momentum of the tracks with $p_{\mathrm{T}} > 0.4\,\mathrm{GeV}$ in a cone of $\Delta R = 0.2$ around the tag electron, excluding the track of the tag electron itself, and E_{T} is the transverse energy of the tag electron. Each probe electron has to pass the modified loose working point of the likelihood-based identification and is not allowed to be reconstructed inside a hadronic jet with $p_{\mathrm{T}} > 20\,\mathrm{GeV}$ and cone size $\Delta R = 0.4$. Finally, the electron pair is required to have opposite charge, $|m(e^+e^-) - m(Z)| < 10\,\mathrm{GeV}$ and $\Delta R(\mathrm{tag}, \mathrm{probe}) > 0.4$. The ΔR cut ensures that the measurements of the tag and probe electrons are independent from each other.

The efficiencies of the diphoton trigger `HLT_2g50_loose` are measured by studying the single photon trigger `HLT_g50_loose`. Here, it is assumed that the probability that an electron pair passes the diphoton trigger is given by

$$P(\gamma\gamma|e_1e_2) = P(\gamma|e_1)\cdot P(\gamma|e_2), \tag{5.9}$$

where $P(\gamma|e)$ is the probability that the electron e passes the corresponding single photon trigger.

The invariant mass distributions of the tag-and-probe pairs are shown in Figure 5.25 for the two photon triggers, where each simulated distribution is normalised to the corresponding data distribution to allow for a comparison of the shapes. The scaling is necessary, since there are 30% more tag-and-probe pairs in the data than predicted by the

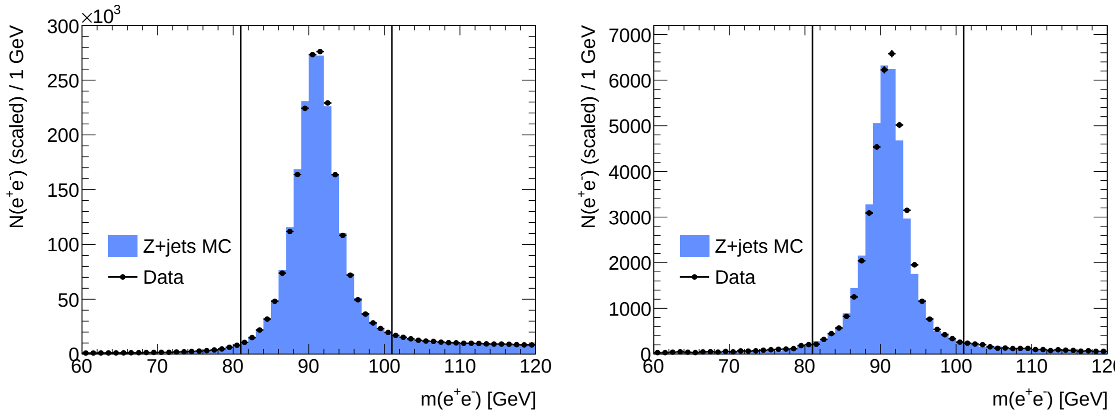

(a) `HLT_g50_loose` **(b)** `HLT_g140_loose`

Figure 5.25: Invariant mass of electron pairs used in the tag-and-probe study of the photon trigger efficiencies for the data and the Z+jets MC sample. Only pairs where the probe electron has (a) $p_{\mathrm{T}} > 55$ GeV and (b) $p_{\mathrm{T}} > 148$ GeV are considered. The data and simulated distributions are scaled to the same integral.

simulation for the `HLT_g140_loose` trigger, while the numbers agree within 0.3% for the `HLT_g50_loose` trigger. This discrepancy is caused by the fact that the simulation underestimates the number of high p_{T} probe leptons (see Figure 5.26). The scale factors used in the main analysis to correct the trigger efficiencies of the signal MC samples and derived below are not significantly affected by this p_{T} mismodelling because they are binned in p_{T}, as explained later. Furthermore, the remaining effects of this mismodelling are assessed with a systematic uncertainty, which is discussed in Section 5.5.1 and is less than one percent. After the scaling, the shapes of the distributions are in good agreement for both triggers, indicating that a background contamination is negligible. Thus, the trigger efficiencies are calculated without a background subtraction and are given by:

$$\epsilon = \frac{\text{Number of probes matched to trigger}}{\text{Number of probes}}. \tag{5.10}$$

The first row of Figure 5.27 shows the trigger efficiency for both triggers as a function of the probe p_{T}. The efficiency starts to rise significantly at about one GeV below the threshold of the respective trigger and reaches the plateau region after several GeV. Both the data and simulated efficiencies are not constant in the plateau region and grow with increasing p_{T}, with the data efficiency gradient being greater. Therefore, it is difficult to identify the exact beginning of the plateau regions of both triggers. Since only events

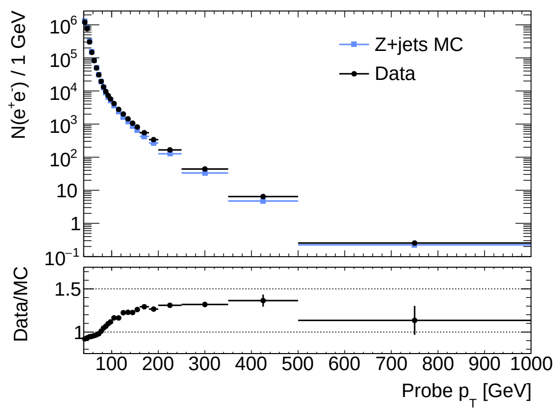

Figure 5.26: p_T of probe electrons used in the tag-and-probe study of the photon trigger efficiencies for the data and the Z+jets MC sample.

passing the filters of Table 5.3 are considered for the main analysis, their p_T cuts are used in the following to define the plateau regions, i.e. $p_\mathrm{T} > 55\,\mathrm{GeV}$ for `HLT_g50_loose` and $p_\mathrm{T} > 150\,\mathrm{GeV}$ for `HLT_g140_loose`. The second row of Figure 5.27 illustrates that there is also an η dependence of the photon trigger efficiencies. The data and simulated efficiencies agree within one percent in the barrel region, whereas in the crack region of the LAr calorimeter, $1.37 < |\eta| < 1.52$, the efficiencies are up to 19% lower in the data than in the simulation and also for $|\eta| > 2$ there is noticeable disagreement of up to 12%. The last row of this figure shows that within statistical uncertainties there is no $|z_0|$ dependence of the photon trigger efficiencies both in the data and in the simulation.

In the main analysis, the trigger efficiencies of the simulations are corrected using scale factors that are binned in p_T and η. A ϕ dependence of the scale factors was found to be negligible due to the azimuthal symmetry of the calorimeters. These scale factors are shown in the first row of Figure 5.28 and do not deviate by more than one percent from 1.0 in the barrel region for both triggers, while they can become as small as 0.8 in the crack region of the LAr calorimeter. The average scale factor is 0.98 for the `HLT_g50_loose` trigger and 0.99 for the `HLT_g140_loose` trigger. The second row of this figure illustrates that the statistical uncertainty in the scale factors can be up to 10% in the crack region, while it is often less than one percent in the barrel region.

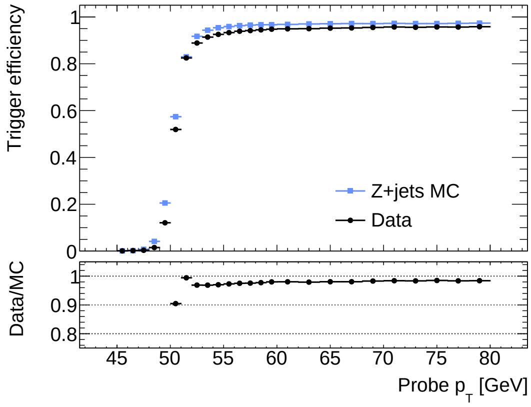

(a) p_T: `HLT_g50_loose`

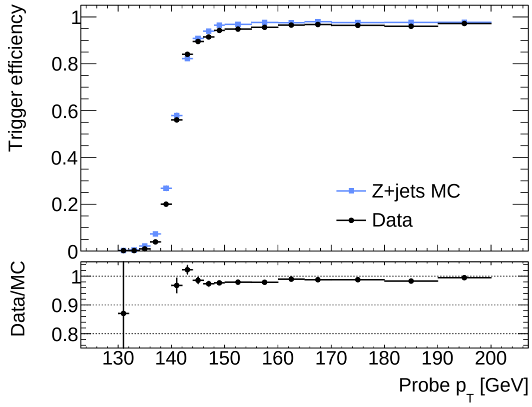

(b) p_T: `HLT_g140_loose`

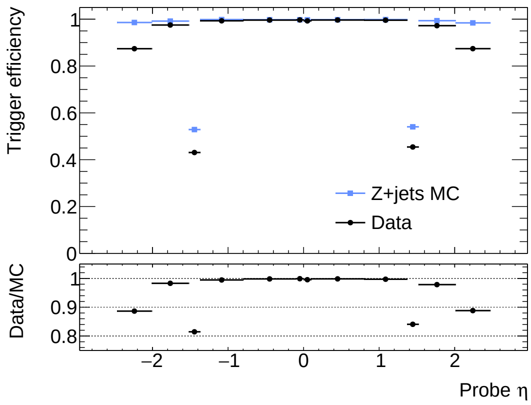

(c) η: `HLT_g50_loose`

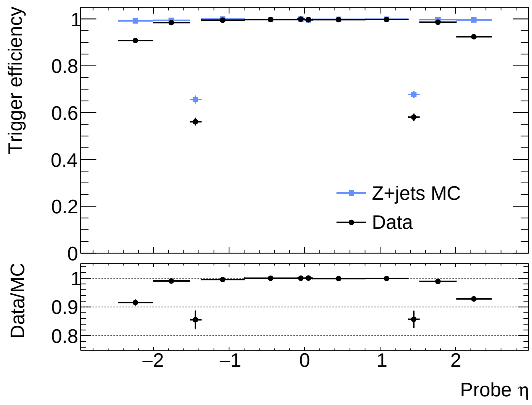

(d) η: `HLT_g140_loose`

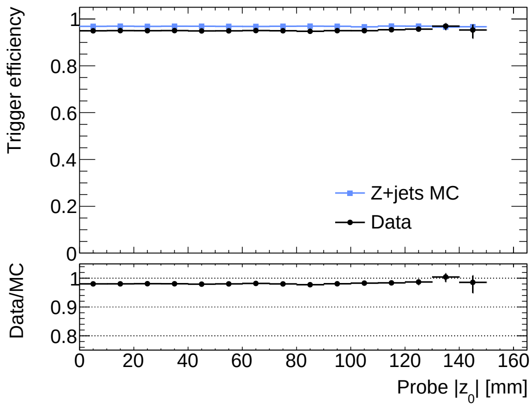

(e) $|z_0|$: `HLT_g50_loose`

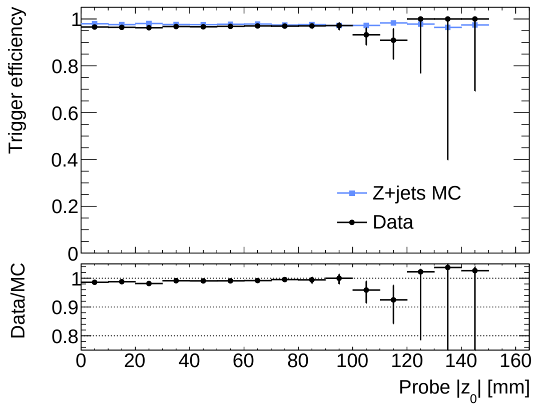

(f) $|z_0|$: `HLT_g140_loose`

Figure 5.27: Efficiencies of the `HLT_g50_loose` (left) and `HLT_g140_loose` (right) triggers as a function of (top) p_T, (middle) η and (bottom) $|z_0|$ of the probe electron for the data and the Z+jets MC sample. Only probe electrons with (left) $p_T > 55$ GeV and (right) $p_T > 148$ GeV are considered in the η and $|z_0|$ plots.

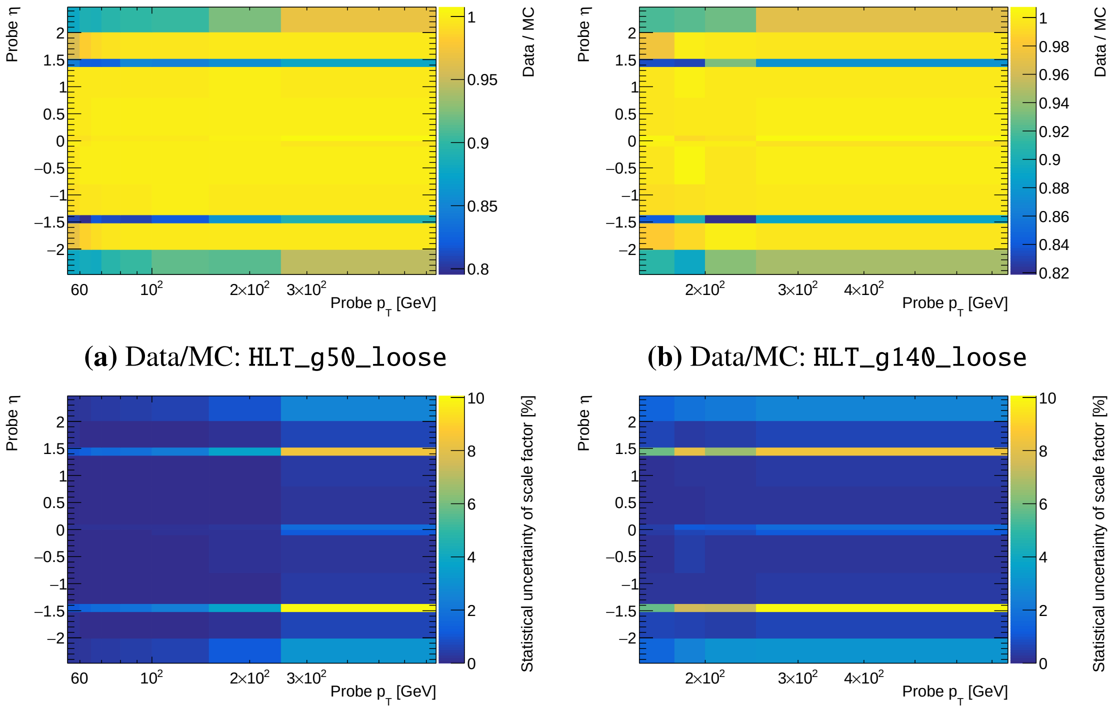

(a) Data/MC: `HLT_g50_loose` **(b)** Data/MC: `HLT_g140_loose`

(c) Stat. uncert.: `HLT_g50_loose` **(d)** Stat. uncert.: `HLT_g140_loose`

Figure 5.28: (top) Scale factors for (left) the `HLT_g50_loose` and (right) the `HLT_g140_loose` trigger and (bottom) their statistical uncertainties as a function of the probe p_{T} and η. Only probe electrons with (left) $p_{\mathrm{T}} > 55$ GeV and (right) $p_{\mathrm{T}} > 148$ GeV are considered.

5.4.3.2 Muon trigger

To measure the efficiencies of the muon trigger `HLT_mu60_0eta105_msonly`, the tag-and-probe method is performed on $Z \rightarrow \mu^+\mu^-$ events, which are required to pass the lowest p_{T} unprescaled muon trigger, `HLT_mu26_ivarmedium`. The selection criteria of the tag and probe muons are summarised in Table 5.6. Both tag and probe muons have to be combined muons. The tag muon is required to pass the `HLT_mu26_ivarmedium` trigger and the medium working point of the muon identification and to be isolated from hadronic interactivity by applying the loose working point of the muon isolation [83]. Its track has to be compatible with the assumption that it originates from the primary vertex by requiring that the transverse impact parameter normalised to its uncertainty is less than three and that the difference between the z-position of the perigee of the track and the z-position of the primary vertex times the sine of the track θ is less than 0.5 mm. All

Table 5.6: Selection criteria applied to tag and probe muons in the muon trigger efficiency studies

Cut	Tag muon	Probe muon
p_T [GeV]	> 28	> 30
Trigger matched	`HLT_mu26_ivarmedium`	—
$\lvert\eta\rvert$	< 2.4	< 1.05
Combined muon	Yes	Yes
Identification	Medium	Modified loose
Isolation	Loose	—
$\lvert d_0/\sigma_{d_0}\rvert$	< 3	—
$\Delta z_0 \sin\theta$ [mm]	< 0.5	—

probe muons have to pass the modified loose working point of the muon identification. Analogously to the electrons, the tag-and-probe pair is required to have opposite charge, $|m(\mu^+\mu^-) - m(Z)| < 10\,\mathrm{GeV}$ and $\Delta R(\mathrm{tag, probe}) > 0.4$.

The invariant mass distributions of the tag-and-probe pairs in the data and in the simulation agree well, as shown in Figure 5.29. This indicates a negligible background contamination and therefore, as for the photon triggers, the calculation of the trigger efficiencies is given by Equation (5.10). The p_T and $|z_0|$ dependences of the trigger efficiencies are shown in Figure 5.30. The muon trigger efficiency reaches its plateau at a p_T of 62 GeV, which in contrast to the plateaus of the photon triggers is very flat. Both the data and simulated efficiencies do not show any significant dependence on the $|z_0|$ within statistical uncertainties up to $|z_0| = 140\,\mathrm{mm}$.

Unlike the photon triggers, the performance of the muon trigger depends significantly on ϕ as illustrated in Figures 5.31a and 5.31b. This is caused by the fact that the muon spectrometer is segmented into hundreds of chambers, which differ in their efficiencies. Consequently, the scale factors used in the main analysis, depicted in Figure 5.31c, are binned both in η and ϕ. They are 0.88 on average and can be as low as 0.33 and 0.35 in two cases. This discrepancy between data and simulation of more than 10% is due to the fact that during data taking RPC chambers have been disabled or became less efficient over time. Despite the large number of bins, 112, the statistical uncertainties on the scale factors are usually only one to two percent and in few cases three to five percent.

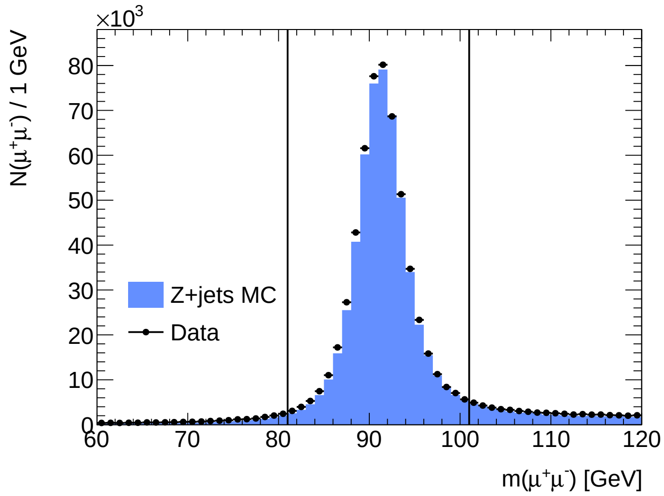

Figure 5.29: Invariant mass of muon pairs used in the tag-and-probe study of the `HLT_mu60_0eta105_msonly` trigger efficiencies for the data and the Z+jets MC sample. Only pairs with a probe muon $p_{\mathrm{T}} > 62\,\mathrm{GeV}$ are considered.

The fit quality χ^2/n_{DoF} of the inner detector track to muon spectrometer track match of a combined muon is used in the definition of the muon filter (see Section 5.2.1). The muon filter applies a cut value of 5.0 to distinguish between good and poor matches. As the selection criteria of the filter differ for muons with good and poor matches, the classification of the matches have to be modelled well in the simulations, otherwise the signal efficiency may be mismodelled. Ideally, the modelling quality of the χ^2/n_{DoF} should be evaluated using displaced muons such as cosmic-ray muons. Unfortunately, this is not possible due to the reasons mentioned in the beginning of Section 5.4, and thus probe muons from this tag-and-probe study are used instead. Figure 5.32 shows the simulated and the observed χ^2/n_{DoF} distribution for probe muons in the plateau region of the trigger. The tail of the simulated distribution is significantly mismodelled, however this has only a negligible impact on the overall agreement, as the peak at $\chi^2/n_{\mathrm{DoF}} < 1$ contains more than 97% of all probe muons. The fraction of good matches is greater than 99% and agrees within 0.2% between simulation and data. This shows that the modelling quality of the classification is very good for prompt muons.

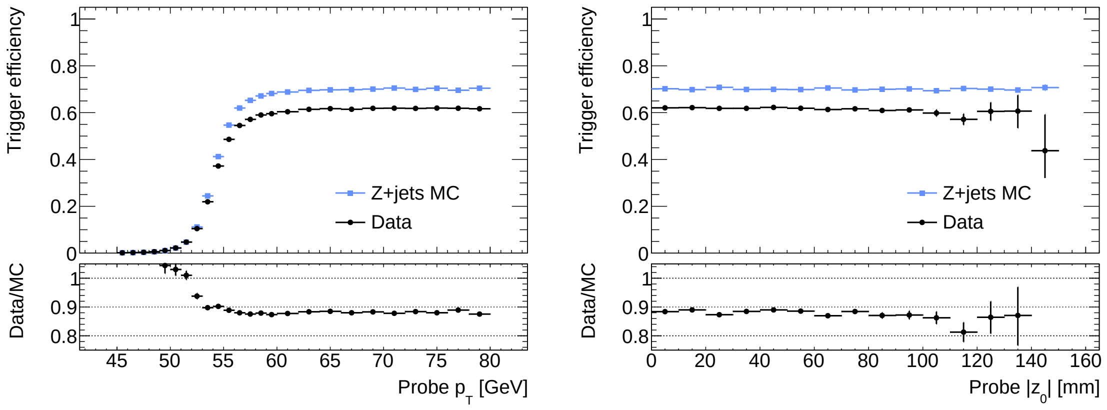

(a) p_{T} **(b)** $|z_0|$

Figure 5.30: Efficiencies of the `HLT_mu60_0eta105_msonly` trigger as a function of (a) p_{T} and (b) $|z_0|$ of the probe muon for the data and the Z+jets MC sample. Only probe muons with $p_{\mathrm{T}} > 62$ GeV are considered in the right plot.

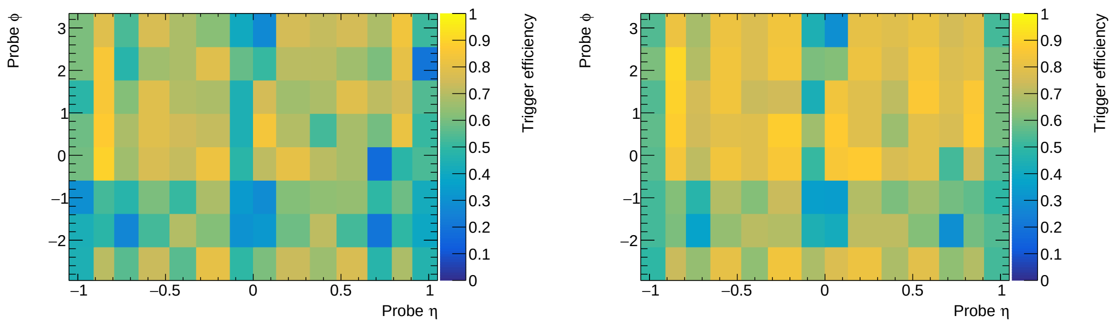

(a) Data **(b)** Z+jets MC

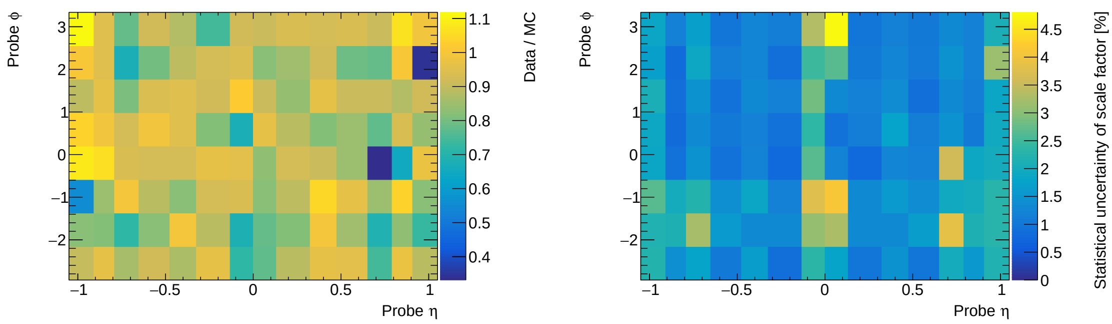

(c) Scale factor **(d)** Stat. uncert. of scale factor

Figure 5.31: Efficiencies of the `HLT_mu60_0eta105_msonly` trigger as a function of the probe η and ϕ for (a) the data and (b) the Z+jets MC sample and (c) the scale factor with (d) its statistical uncertainty. Only probe muons with $p_{\mathrm{T}} > 62$ GeV are considered.

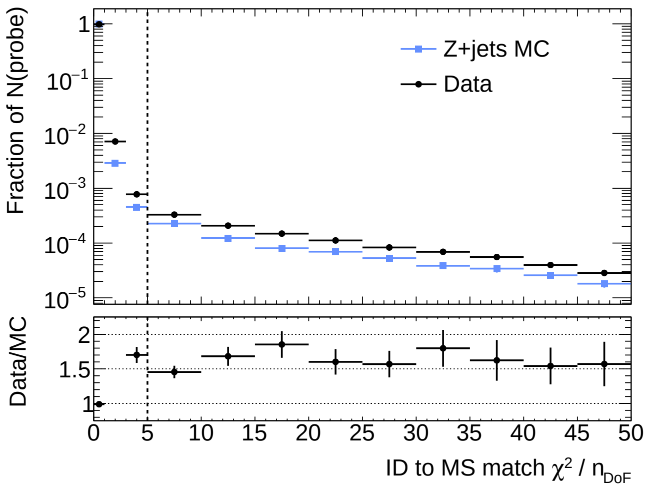

Figure 5.32: Fit quality of the inner detector track to muon spectrometer track match of probe muons with $p_\mathrm{T} > 62\,\mathrm{GeV}$ for the data and the Z+jets MC sample. The dotted line indicates the cut value of the muon filter discussed in Section 5.2.1.

5.5 Uncertainties in the signal yield

The number of signal events is calculated with Equation (5.8) and depends on the signal efficiency, the production cross-section and the integrated luminosity. Each of these three quantities is determined with an uncertainty. The uncertainty in the signal efficiency includes a statistical uncertainty due to the limited number of simulated signal events and three systematic uncertainties. One source of systematic uncertainty are the trigger scale factors, which are used to correct the trigger efficiencies of the signal MC samples. These scale factors are measured with an uncertainty discussed in Section 5.5.1. Another systematic uncertainty arises from the fact that the simulated events have to be reweighted so that their pileup distribution matches that of the data. This reweighting procedure and its uncertainties are explained in Section 5.5.2. The third source are the tracking and vertexing efficiencies, whose uncertainties are determined in Section 5.5.3 using K_S decays. The relative sizes of the four uncertainties in the signal efficiencies are shown in Appendix B for all signal MC samples as a function of the $\tilde{\chi}_1^0$ lifetime. The uncertainty in the production cross-sections of the signal process have already been discussed in Section 5.1.1. Finally, a symmetric uncertainty of 2.2% in the measured luminosity of 32.8 fb^{-1} is taken into account. It is derived, following a methodology similar to that detailed in Reference [62], and using the LUCID-2 detector for the baseline luminosity measurements [63], from calibration of the luminosity scale using x-y beam-separation scans.

5.5.1 Uncertainties in the trigger scale factors

The efficiencies of the three triggers used in the main analysis have been measured with tag-and-probe studies in the data and simulations as discussed in Section 5.4.3. Trigger scale factors are derived from these measurements, which are used to correct the trigger efficiencies in the signal MC samples. For each trigger scale factor, three systematic uncertainties are considered, whose size varies between the triggers. First, the systematic uncertainty due to the use of the tag-and-probe method is estimated by comparing the average tag-and-probe efficiency in the Z+jets MC sample with the average true efficiency, which is calculated using electrons and muons that can be matched at the truth-level to a Z boson decay and pass the probe selections of Tables 5.5 and 5.6, respectively.

Next, the uncertainty caused by the finite binning of the scale factors is evaluated with a closure test, in which the scale factors are applied to the trigger efficiencies of the probe leptons in the Z+jets MC sample and the resulting average trigger efficiency is compared to the average trigger efficiency in the data. This uncertainty is also a good measure for the impact of the p_{T} mismodelling of the Z+jets MC sample on the scale factors of the photon triggers. If the p_{T} binning of the scale factors were too coarse, then they would be affected by the mismodelling, leading to a significant discrepancy. However, this is not observed as the uncertainty is not larger than 0.3% for both photon triggers.

Finally, the impact of a remaining background contribution is estimated by performing the tag-and-probe method in the data with tightened selection criteria for the probe leptons, where they have to pass the same identification and isolation requirements as the tag leptons. The resulting average efficiency is compared to that determined using the standard selection criteria for the probe leptons. For the muon trigger, it was found that this uncertainty is completely negligible.

Adding the three systematic uncertainties in quadrature yields 3.5% for the `HLT_mu60_0eta105_msonly` trigger, 0.3% for the `HLT_g140_loose` trigger and 0.8% for the `HLT_2g50_loose` trigger. Thus, the total systematic uncertainty for both photon triggers is almost negligible.

5.5.2 Pileup reweighting

The amount of pileup is quantified using $\langle\mu\rangle$, which is the mean number of inelastic interactions per bunch-crossing and given by

$$\langle\mu\rangle = \frac{\langle L_{\mathrm{b}}\rangle \times \sigma_{\mathrm{inel}}}{f_{\mathrm{r}}}, \tag{5.11}$$

where $\langle L_{\mathrm{b}}\rangle$ is the mean instantaneous luminosity per bunch, σ_{inel} is the inelastic pp cross-section, which ATLAS takes to be 80 mb for $\sqrt{s} = 13\,\mathrm{TeV}$, and f_{r} is the LHC revolution frequency. All simulations used in this analysis assume the same distribution of $\langle\mu\rangle$, which is shown in Figure 5.33a. It has a broad maximum around $\langle\mu\rangle = 21$ and no entries for $\langle\mu\rangle > 40$. The data distribution illustrated in Figure 5.33b is shifted towards higher $\langle\mu\rangle$ and has therefore a larger average $\langle\mu\rangle$ of 24.5 compared to 21.0.

To correct these discrepancies, each simulated event of a particular MC sample is assigned a weight

$$w_{\mathrm{Pileup}} = \frac{L_i/L}{N_i/N}, \tag{5.12}$$

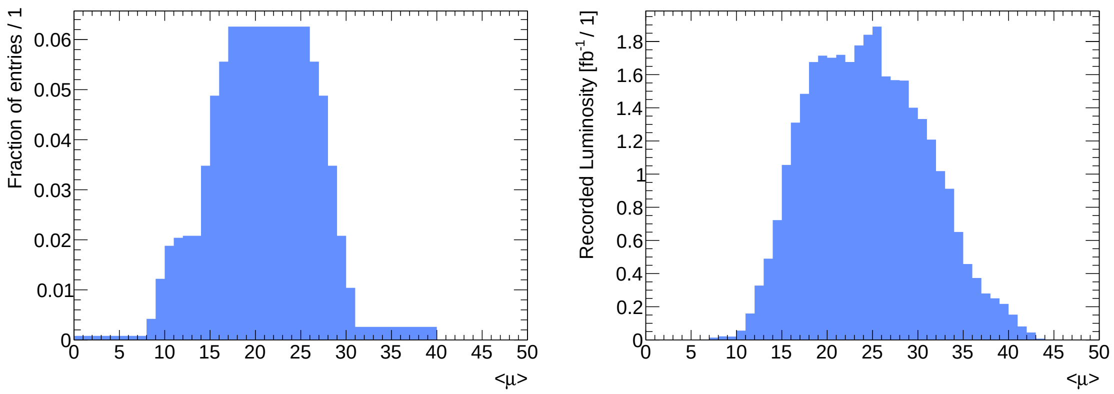

(a) Simulation **(b)** Data

Figure 5.33: Pileup distributions (a) assumed in the simulations and (b) observed in the data after applying the standard data quality requirements.

where L is the total integrated luminosity of the data of $32.8\,\mathrm{fb}^{-1}$, L_i is the integrated luminosity corresponding to the i^{th} bin in $\langle\mu\rangle$, N is the total sum of generator-weights over all events of that MC sample, and N_i is the sum of generator-weights over all events that have a $\langle\mu\rangle$ belonging to the i^{th} bin. This calculation uses the same binning in $\langle\mu\rangle$ as the histograms of Figure 5.33.

A small fraction of the data has a $\langle\mu\rangle$ larger than 40, which is not represented by the simulated distribution. To account for this and to not lose any data, the integrated luminosity of the unrepresented data is added to the integrated luminosity of the last bin in $\langle\mu\rangle$. Thus, simulated events with a $\langle\mu\rangle$ most similar to that of the unrepresented data receive increased weights.

The number of reconstructed primary vertices as a function of the actual μ of the event is different in the data and simulations, meaning that a given μ in the data corresponds most closely to some other value in the simulations, and thus $\langle\mu\rangle$ of the data is scaled before calculating the pileup weights to correct for this discrepancy. It is technically easier to scale the data since it has a continuous pileup distribution, in contrast to the simulations. The scale factors are measured with an uncertainty, and this uncertainty is propagated through to the observables such as the signal efficiency by recalculating the weights with different scale factors. The scale factors are $1/1.18$, $1/1.09$ and 1.0 for the down, nominal and up variation, respectively.

In general, the uncertainty in the signal efficiency due to the pileup reweighting procedure is a couple of percent. In very few cases, the uncertainty can be as large as 20% when the statistical uncertainties in the signal efficiencies are high.

5.5.3 Uncertainties in the tracking and vertexing efficiencies

In the following, a combined systematic uncertainty in the tracking and vertexing efficiencies is estimated using $K_S \to \pi^+\pi^-$ decays. An advantage of these decays is their long lifetime $c\tau$ of about 27 mm, which is within the range that is probed in this analysis. Furthermore, they are produced at a high rate allowing the efficiencies to be studied with a high statistical precision. On the other hand, the kaon mass of about 500 MeV is very low, so that the produced pions have on average a much lower p_T than the leptons of the signal process. Since there is no heavy long-lived particle in the Standard Model, it is not possible to study these efficiencies for large p_T in the data.

The track reconstruction used for this analysis consists of two independent steps as discussed in Section 4.4.1. First, the standard tracking of ATLAS is run, whose performance is well understood [102]. Most relevant to this analysis is the second tracking algorithm, the large radius tracking, which is required to reconstruct tracks with a transverse impact parameter in the range of 10 mm to 300 mm. Thus, only the performance of this tracking is studied in the following.

Displaced vertices are selected as K_S candidates if they have a mass in the range 350 MeV to 650 MeV and exactly two tracks that are oppositely charged. They have to pass the standard quality criteria of the signal region such as the material veto and the requirements on the fit quality and vertex position.

Ideally, the systematic uncertainty due to the large radius tracking would be determined by comparing the number of K_S candidates that have two tracks from the large radius tracking between data and simulation. However, this is not possible as only a few simulations of Standard Model processes were reconstructed using the large radius tracking and the displaced vertex reconstruction, and therefore the total number of K_S candidates observed in the data cannot be reproduced with the available simulations. Instead, the number of K_S

candidates reconstructed by the standard tracking is used to scale the simulations to the data. The uncertainty is derived using the ratio

$$\frac{N_{\mathrm{LRT}}^{\mathrm{Data}}/N_{\mathrm{Std}}^{\mathrm{Data}}}{N_{\mathrm{LRT}}^{\mathrm{MC}}/N_{\mathrm{Std}}^{\mathrm{MC}}}, \tag{5.13}$$

where N_{LRT} and N_{Std} are the number of K_{S} candidates reconstructed by the large radius tracking and the standard tracking only, respectively. This ratio has been studied as a function of the transverse radius of the K_{S} candidates. The largest discrepancy between data and simulation is found to be six percent including the statistical uncertainty.

A conservative value of 10% has been chosen for the combined systematic uncertainty in the tracking and vertexing efficiencies, which contains this discrepancy of six percent, as well as the maximal uncertainty of about two percent observed for the standard tracking [102] and an uncertainty of about one percent obtained by varying the parameters of the displaced vertex reconstruction [103].

5.6 Background estimation

In the following, the number of events from background processes that pass the selection criteria of the signal region are estimated. The background sources are divided into two categories: Collision backgrounds, which originate from proton–proton collisions, and non-collision backgrounds, which include cosmic-ray muons and beam-induced backgrounds. Both categories are studied in the following.

5.6.1 Study of top-antitop MC events

In the Standard Model, there is no long-lived particle with a mass greater than 12 GeV that decays into leptons. Therefore, the collision background is expected to be very small. To get a first impression of the possible types of contributions, a $t\bar{t}$ MC sample with a dilepton filter[8] is studied. This sample is generated with Sherpa 2.2.1 [104] and the parton distribution functions are modelled according to the NNPDF30NNLO tune [105]. It is reconstructed using the setup optimised for decays of long-lived particles described in Section 4.4 and consists of seven hundred thousand events corresponding to an integrated

[8]This filter selects only events in which both W bosons, produced by the decay of a top quark, decay leptonically.

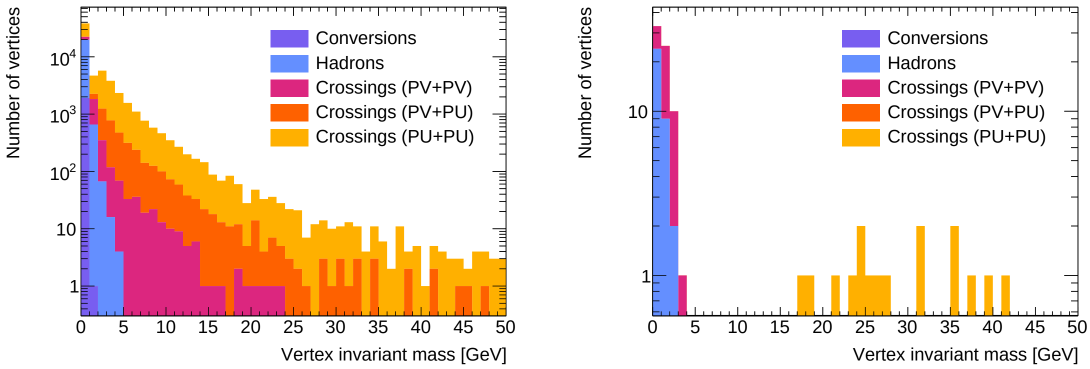

(a) $p_{\mathrm{T}} > 1\,\mathrm{GeV}$ **(b)** $p_{\mathrm{T}} > 10\,\mathrm{GeV}$

Figure 5.34: Invariant mass of displaced vertices with two tracks in the $t\bar{t}$ MC sample. A p_{T} cut (a) of 1 GeV and (b) of 10 GeV is applied to the vertex tracks.

luminosity of 8 fb^{-1}. The $t\bar{t}$ sample was chosen as it is contains many B-hadrons, which have a long lifetime of the order 10^{-12} s, and many high p_{T} leptons from W boson decays.

Figure 5.34 shows the invariant mass distributions of displaced vertices with two tracks categorised by their truth origin. If both tracks of a vertex originate from the same truth photon, then the vertex is classified as a conversion and if they have a hadron as a common ancestor, then the vertex is classified as a hadron. All other vertices belong to the category of random crossings, which is divided into three subcategories based on the number of truth matched tracks. Here, it is assumed that only tracks associated with the primary vertex (PV) can be matched to a truth particle, while there should be no truth match for tracks associated with pileup (PU) vertices.

Each displaced vertex has to satisfy basic selection criteria including the fit quality, displacement and fiducial volume. The vertex tracks are not required to be leptons as this would dramatically reduce the number of vertices impeding a meaningful study of the five vertex categories. Leptonic and non-leptonic vertices share many of their production processes, so that the general statements of this study also apply to leptonic vertices.

If a p_{T} cut of 1 GeV is applied to the vertex tracks, then a considerable fraction of the vertices with a mass of less than 1 GeV originates from conversions. Vertices from hadron decays have an exponentially decreasing mass spectrum with an endpoint near $m = 5\,\mathrm{GeV}$, which is the typical mass of a B-meson. Similarly, the mass spectrum of vertices from random crossings decreases with increasing mass, but less steeply. All vertices with a mass above 12 GeV are from random crossings, with crossings of pileup tracks dominating. A larger p_T cut of 10 GeV significantly reduces the number of vertices, so that for example not a single conversion vertex is observed. In this case, there seems to be a turn-on of the random crossings of pileup tracks around $m = 17\,\mathrm{GeV}$. In the limit of massless particles, the invariant mass of two particles is given by

$$m = \sqrt{2p_1p_2(1 - \cos\alpha)}, \tag{5.14}$$

where α is the angle between the momenta of the particles. As it is discussed in Section 5.6.3, opening angles around $\pi/2$ are favoured for random crossings, and therefore a turn-on around $\sqrt{2 \cdot 10\,\mathrm{GeV} \cdot 10\,\mathrm{GeV}} \approx 14\,\mathrm{GeV}$ is expected for a p_T cut of 10 GeV, which is consistent with the observed value.

Summarising this study, the dominating background contribution from collision processes seems to be the random crossing of unrelated tracks. However, a non-negligible contribution from the tails of the low-mass processes cannot be excluded due to the limited size of the MC sample and the fact that there are further Standard Model processes, such as $b\bar{b}$, which are relevant. Therefore, the contribution of low-mass processes is studied in the next section.

5.6.2 Low-mass processes

The study of the $t\bar{t}$ MC sample showed that there is a significant number of displaced vertices with low masses originating from photon conversions and hadron decays. In particular, B-hadrons could be a non-negligible background source since they have a lifetime of about 0.5 mm, which is only a factor of four lower than the displacement requirement in the signal region. An important example are B-meson decays into a J/Ψ and another meson, because the J/Ψ meson decays with a branching ratio of about 12% into a pair of oppositely charged leptons. Photon conversions can occur at any position in the detector, which can lead to large displacements of the lepton pair. They are, however, extremely suppressed by the mass and filter matching requirements. There are further processes that could produce low-mass displaced dileptons such as the Drell-Yan process [106] or resonances, e.g. J/Ψ or Υ. These processes have very small lifetimes of the order 10^{-20} s or lower, but their large cross-sections together with detector resolution effects could give rise to a non-negligible contribution.

It is not possible to thoroughly investigate these background sources using simulations as the number of MC samples reconstructed with the setup optimised for decays of long-lived particles is very small and the few available samples such as $t\bar{t}$ have an insufficient size. Thus, a dedicated control region is defined in the data by inverting the invariant mass cut. All selection criteria of the signal region are applied, with the exception of the trigger and filter matching, to enhance the number of events in this control region. The events are still required to pass at least one of the triggers used in the analysis.

No ee and no $e\mu$ vertices are observed in this control region, while eighteen $\mu\mu$ vertices pass the selection criteria, all of which have a mass below 5.4 GeV (see Figure 5.35a). There is a peak at a mass of 2.6 to 2.8 GeV, which is slightly lower than the mass of the J/Ψ meson of 3.1 GeV. It is assumed that these vertices originate from J/Ψ decays and their mass is misreconstructed due to detector resolution effects. To increase the size of the data sample, vertices with only one lepton are also studied, referred to as et and μt, where the non-leptonic tracks have to pass a p_{T} cut of 10 GeV. A single et vertex with a mass of about 0.5 GeV and 89 μt vertices are observed, their mass distribution is illustrated in Figure 5.35b. No μt vertex has a mass greater than 5.8 GeV, which agrees well with the end point of the mass distribution of the $\mu\mu$ vertices. There are multiple peaks, one near 0.5 GeV, which is the mass of a kaon, another one near 2 GeV likely due to semi-leptonically D-meson decays, a third one near the J/Ψ mass and a fourth peak at a mass of about 4 GeV, which is not associated with any hadron. Most of the low-mass μt and $\mu\mu$ vertices are located within the pixel barrel, i.e. they have $r \lesssim 120$ mm, and only 30% are reconstructed at larger radii.

To summarise these results, no leptonic vertex with a mass between 6 and 12 GeV is observed in the data. This is expected because only the Drell-Yan process and the Υ resonance can produce pairs of correlated leptons with an invariant mass in this range and both processes are extremely suppressed due to their very short lifetimes. There is also no evidence that the high mass tail of J/Ψ decays could be a non-negligible contribution. Another cross-check is performed in Section 5.6.3.3 using vertices not associated with any lepton, with the same result that no indication of a remaining contribution of these processes is found for masses between 6 and 12 GeV. The background from pairs of correlated leptons of the same low-mass process is therefore neglected. Leptons from low-mass processes, however, can randomly cross with leptons from other processes and form a high mass vertex. In the next section, the background from random crossings is estimated.

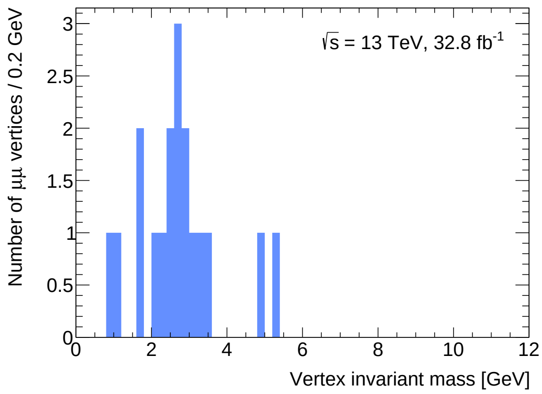

(a) $\mu\mu$: m

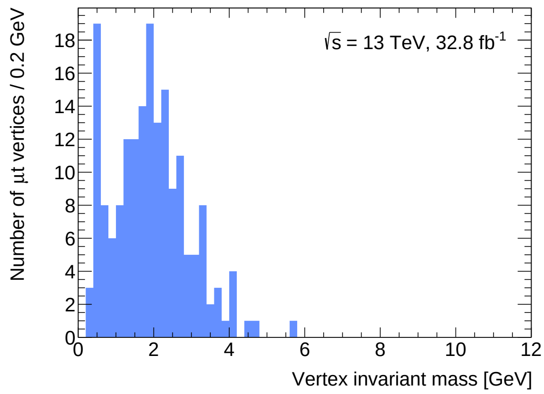

(b) μt: m

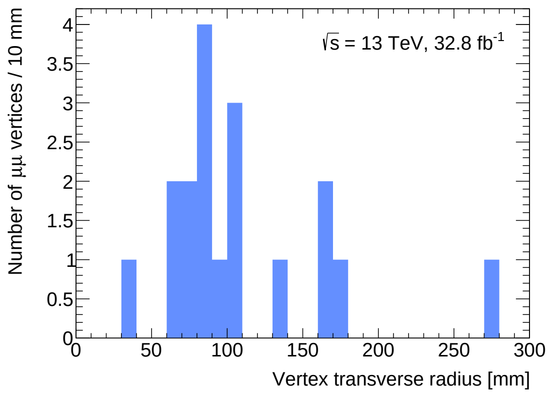

(c) $\mu\mu$: r

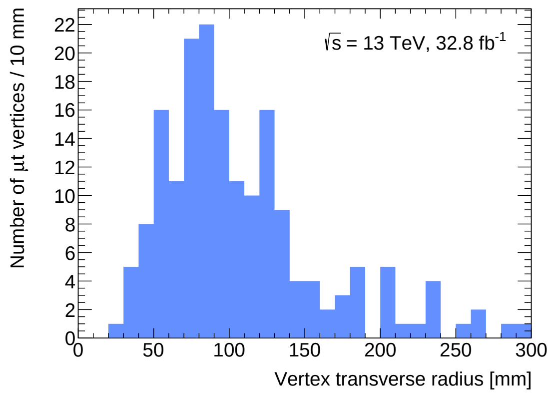

(d) μt: r

Figure 5.35: (top) Invariant mass and (bottom) transverse radius of (left) $\mu\mu$ and (right) μt vertices in the data that fail the mass cut.

5.6.3 Random crossings

5.6.3.1 Estimation procedure

The main background originating from pp collisions is due to random crossings of unrelated leptons, as indicated by the study of the $t\bar{t}$ MC sample. A data-driven technique referred to as event mixing is used, which combines leptons from different events to measure how often a pair would form a vertex. It consists of the following steps:

1. All leptons observed in the data that could be part of a signal vertex, i.e. they pass the track selection criteria of the displaced vertex reconstruction (see Section 4.4.2) and the standard kinematic cuts (e.g. $p_{\mathrm{T}} > 10\,\mathrm{GeV}$) as well as the identification criteria (see Section 5.2.3), are collected.

2. Pairs of leptons, referred to as seed pairs, are randomly sampled from the collection of leptons. Only seed pairs are selected that pass at least one of the filters used to preselect data events and the cosmic-ray veto.
3. For each seed pair, a set of primary vertices is randomly chosen from events that have at least one lepton candidate. This set is needed to evaluate the displacement cut and certain quality requirements applied in the displaced vertex reconstruction. In this step, the lepton tracks are moved to ensure that their impact parameters with respect to the new primary vertex match those with respect to the old primary vertex. Otherwise, leptons that originated from the primary vertex of their event could mistakenly be assigned to a pileup vertex of this set, leading to a mismodelling of the background.
4. The displaced vertex reconstruction is run on each seed pair. If a vertex is found that satisfies all criteria of the signal region discussed in Section 5.2.3, a background vertex consisting of the two leptons is recorded.
5. Finally, all vertices generated using this procedure are assigned a weight, which normalises the total estimate to the data.

Overall, this procedure is equivalent to multiplying the number of lepton pairs observed in the data, $N^{\text{obs}}_{\text{pairs}}$, by the probability that two leptons will form a displaced vertex by chance, p_{xing}:

$$N_{\text{vx}} = N^{\text{obs}}_{\text{pairs}} \times p_{\text{xing}}. \tag{5.15}$$

The lepton pairs used in the normalisation procedure have to pass the selection criteria mentioned in item 2 and to have an invariant mass greater than 6 GeV in order to remove any contamination from low-mass processes, which is particularly relevant for muon pairs.

Only random crossings of two leptons are estimated with this method, as this is the dominant contribution, while random crossings of more than two leptons or of two leptons with non-leptonic tracks are neglected, since the crossing probability for three or more particles is significantly lower than that for two particles. Similarly, random crossings of leptons with semileptonic vertices are neglected as no semileptonic vertex is observed in any of the events that contain a lepton pair passing the selection criteria.

The number of leptons and in particular the number of lepton pairs in the data is very low. The event mixing procedure and its simplicity are a result of this limitation. Thus, a flat average crossing probability is used since the size of the data sample does not allow it to be parametrised. Consequently, it is important to validate the procedure in simulations and in the data using non-leptonic vertices, which are much more abundant than leptonic vertices and allow to identify systematic deviations between the prediction and the observation.

5.6.3.2 Validation using MC simulation

The first test of the estimation procedure is performed on the $t\bar{t}$ MC sample discussed in Section 5.6.1. The vertex and track selection criteria are looser than in the signal region to reduce the statistical uncertainty when comparing the prediction with the observation. Thus, tracks forming a vertex candidate are required to have $p_{\mathrm{T}} > 5\,\mathrm{GeV}$, and no trigger or filter requirements are applied. In addition to the usual vertex selection criteria, the cosmic-ray veto is also applied at the vertex-level to be consistent with tests performed on data discussed in Section 5.6.3.3.

Not only the three dilepton types but also vertices containing one or two non-leptonic tracks are studied, resulting in six different types of vertices that can be tested, namely tt, et, μt, ee, $e\mu$ and $\mu\mu$. Vertices with at least one non-leptonic track are not required to have opposite charges to reduce the statistical uncertainty of prediction and observation even further, while opposite charges are required for dilepton vertices so that the selection criteria better match those of the signal region. Since the material veto is not applied to $\mu\mu$ vertices, it is important to test if a missing material veto causes any problems in the estimation procedure. The estimates for all six vertex types are therefore evaluated with and without the material veto. To obtain a precise prediction, millions of seed pairs are sampled for each estimate.

Table 5.7 summarises the event mixing predictions and the number of vertices found in the MC sample for all vertex types. The probability p_{xing} for a pair of tracks to form a vertex is of the order 10^{-4} for most vertex types. Only for the tt category, more than $\mathcal{O}(1)$ vertices are predicted and observed. Without the material veto, the number of tt vertices is overestimated by about 14%, while this discrepancy decreases to 11% when the material veto is applied. The event mixing predicts about 0.02 dilepton vertices in the entire $t\bar{t}$ MC sample, which is consistent with the observation of zero dilepton vertices. The material veto has almost no impact on the dilepton crossing probabilities, because in the $t\bar{t}$ MC sample most of the dilepton vertices from random crossings are located inside the beam pipe. The crossing probability is significantly lower for electron pairs than for $e\mu$ pairs, which in turn have a lower p_{xing} than muon pairs. This could be due to the fact that the displaced vertex reconstruction uses the original inner detector tracks for electrons

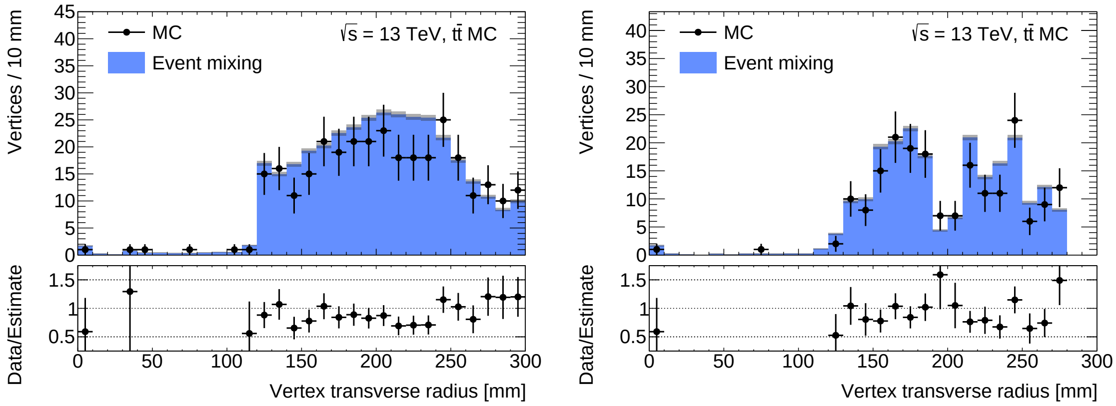

(a) No material veto **(b)** Material-rich regions vetoed

Figure 5.36: Comparison of the transverse radius of tt vertices in the $t\bar{t}$ MC sample with the expectation from the event mixing, (a) with and (b) without material veto. The bottom panel in each plot shows the ratio between the number of vertices found in the MC sample and the event mixing prediction. The error bars on the predictions are statistical only.

instead of the tracks refitted with a Gaussian-sum-filter, which take into account effects of bremsstrahlung. However, for technical reasons this could not be studied in detail.

Only the tt sample is large enough to compare the number of vertices found in the MC sample with the event mixing predictions as a function of different observables. Figure 5.36 shows that the large majority of vertices from random crossings have radii greater than 120 mm, i.e. they are located outside the pixel barrel. Even if the material veto is not applied, the number of vertices with radii smaller than 120 mm is negligible. The reason for this has already been discussed in Section 5.3.1, namely that the uncertainties in the track parameters increase significantly when the associated particle is produced outside the pixel detector, which in turn increases the probability that two tracks cross within their uncertainties.

The distributions of four further observables are shown in Figure 5.37, where the material veto is not applied to reduce the statistical uncertainties. The main characteristics of each distribution are correctly reproduced by the prediction. Perfect agreement in all details is not required, as these shapes are not used to discriminate signal from background. Both the mass and p_{T} distributions seem to follow an exponential curve with few entries for values greater than 100 GeV. The distribution of $\Delta\phi$ between the two vertex tracks is symmetric to $\Delta\phi = 0$ and has two maxima near $\Delta\phi = \pm\pi/2$. For the angle between the momentum and the displacement vectors, there is a continuous increase up to an angle

Table 5.7: Observed and predicted number of displaced vertices passing loosened selection criteria in the $t\bar{t}$ MC sample for six vertex types. The predicted number of vertices is obtained using Equation (5.15) and presented without an uncertainty estimate.

	tt	et	μt
$N_{\text{pairs}}^{\text{obs}}$	1.1×10^{6}	4093	4442
Without material veto			
Avg. p_{xing}	3.2×10^{-4}	2.1×10^{-4}	1.8×10^{-4}
Predicted vertices	353	0.85	0.80
Observed vertices	311	0	1
With material veto			
Avg. p_{xing}	2.0×10^{-4}	1.4×10^{-4}	1.4×10^{-4}
Predicted vertices	220	0.58	0.61
Observed vertices	198	0	1

	ee	$e\mu$	$\mu\mu$
$N_{\text{pairs}}^{\text{obs}}$	7	16	5
Without material veto			
Avg. p_{xing}	1.9×10^{-4}	5.0×10^{-4}	1.4×10^{-3}
Predicted vertices	1.3×10^{-3}	8.0×10^{-3}	7.2×10^{-3}
Observed vertices	0	0	0
With material veto			
Avg. p_{xing}	1.9×10^{-4}	5.0×10^{-4}	1.4×10^{-3}
Predicted vertices	1.3×10^{-3}	7.9×10^{-3}	7.2×10^{-3}
Observed vertices	0	0	0

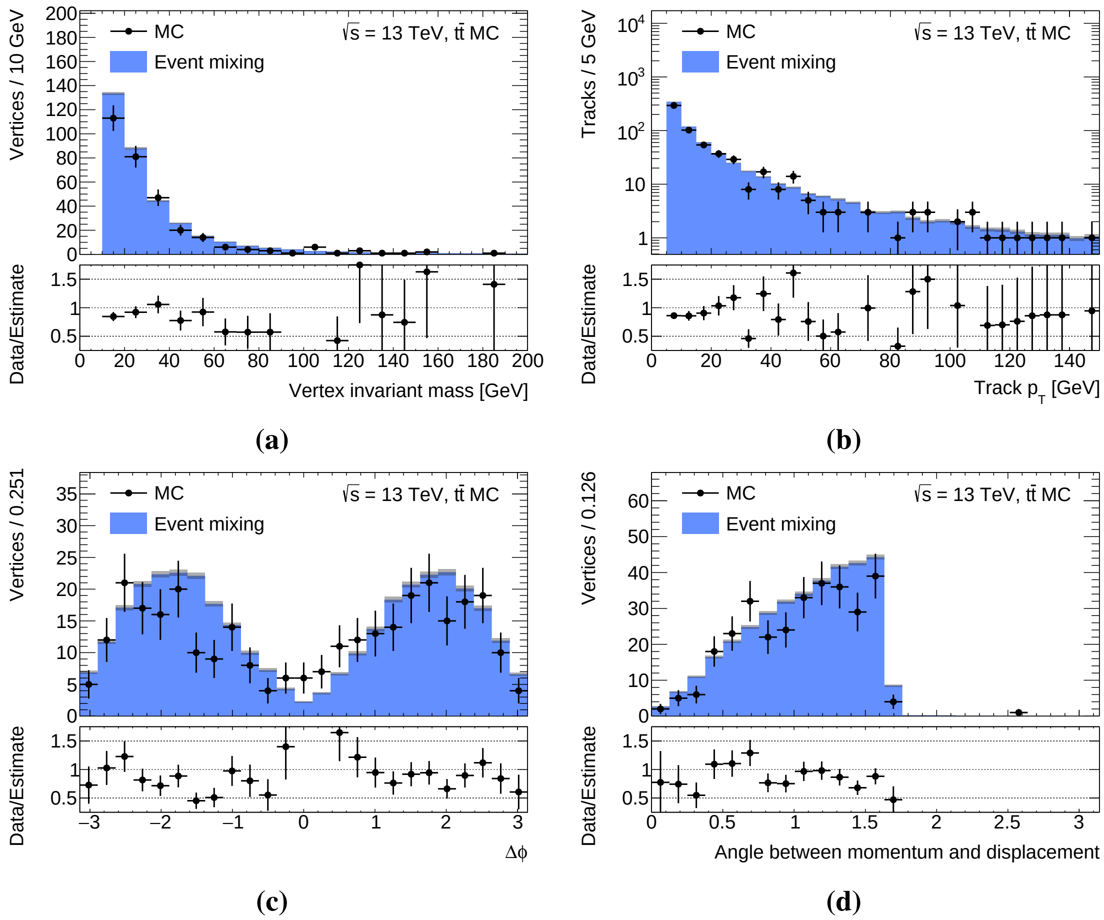

Figure 5.37: Comparison of four observables of tt vertices in the $t\bar{t}$ MC sample with the expectation from the event mixing. The material veto is not applied. The bottom panel in each plot shows the ratio between the number of vertices found in the MC sample and the event mixing prediction. The error bars on the predictions are statistical only.

of $\pi/2$, then there is a sharp drop caused by the requirement of Equation (4.3) applied in the displaced vertex reconstruction that the vertex has to be consistent with the decay of a particle originating from the primary vertex.

An additional test can be performed using non-leptonic tracks by studying whether their crossing probabilities depend on the origin of the tracks or not. The same classification scheme as in Section 5.6.1 is used, which means that tracks matched to a truth particle are assigned to the primary vertex (PV) and all other tracks to pileup (PU) vertices. Thus, three categories are considered, PV+PV, where both tracks originate from the primary vertex, PU+PU, where both tracks originate from pileup vertices, and PV+PU, where one

Table 5.8: Crossing probabilities of non-leptonic tracks in the $t\bar{t}$ MC sample. The uncertainties shown are statistical. For PV+PV, the upper limit at 95% confidence level on the crossing probability is given.

Type	$N_{\text{pairs}}^{\text{obs}}$	Observed vertices	Crossing probability [10^{-4}]
PU+PU	1.053×10^6	174	1.65 ± 0.13
PV+PU	144486	24	1.66 ± 0.34
PV+PV	17736	0	< 1.70

track is from the primary vertex and one from a pileup vertex. The crossing probability is calculated as the number of observed vertices passing the material veto divided by the number of track pairs in the sample. The results of this study are summarised in Table 5.8. The crossing probabilities for PV+PU and PU+PU are consistent within the statistical uncertainties. The crossing probability could not be calculated for PV+PV, because no vertex was found in this category. The upper limit at 95% confidence level on the PV+PV crossing probability is, however, consistent with the crossing probabilities of the other two categories. Consequently, there is no evidence that the crossing probability depends on the origin of the tracks.

5.6.3.3 Validation using data

Following the successful validation of the estimation technique on simulations, a further test is carried out using the collision data. To obtain a signal-depleted sample, vertices containing two leptons are not considered in this study. Therefore, only three out of the six categories are investigated: tt, et and μt. The tt sample contains significantly more events than the simulation studied so far, which allows to assess systematic differences between prediction and observation with a high precision.

Analogous to the signal region, each of the two tracks is required to have $p_{\mathrm{T}} > 10\,\mathrm{GeV}$. In addition to the usual vertex selection, the objects involved are required to pass the cosmic-ray veto[9]. It is applied to remove potential contamination from cosmic-ray muon events where the muon is not fully reconstructed. No triggers and filters are required to

[9]This is similar to the veto applied in the signal regions, but it is applied at the vertex-level to the tracks.

enlarge the size of the samples.[10] Furthermore, the requirement of opposite charges is not applied to further enhance the size of the samples, especially for the et and μt categories.

Each data run is processed independently so that the crossing probability can be studied as a function of the run conditions such as pileup. The total estimate is obtained by adding the estimates of all runs. To take into account the integrated luminosity of each run, the number of the randomly chosen seed pairs is proportional, a multiplier of one hundred is used, to the number of non-leptonic tracks in the tt category and to the number of leptons in the other two categories.

Table 5.9 summarises the predictions and observations for all three categories. The predicted crossing probabilities in the data agree within 30% to those in the $t\bar{t}$ MC sample for all three categories. As in the simulations, the number of non-leptonic vertices is significantly larger than that of the semileptonic vertices. The event mixing procedure overestimates the number of tt vertices by 20%, regardless of whether the material veto is applied or not, which indicates that the estimate works equally well for both cases. These overestimates are slightly larger than in the $t\bar{t}$ MC sample, where they are only 11–14%, but associated with much greater statistical uncertainties. For et vertices, the discrepancies increase to 35% if no material veto is applied and to 61% if it is applied. They become less significant when the statistical uncertainties on the number of observed vertices are taken into account, which are 24% and 33%, respectively.

In contrast to the other categories, the number of μt vertices are underestimated, namely by 9% if no material veto is applied and by 27% if it is applied. This is due to the fact that not all μt vertices originating from cosmic-ray muons are rejected by the cosmic-ray veto. In the signal region, the cosmic-ray veto is applied to combined muon tracks obtained from a global fit of the inner detector and muon spectrometer measurements, while in these studies it is applied to the inner detector tracks that are less precise. Thus, a tighter cosmic-ray veto of $\Delta R_{\mathrm{cosmic}} > 0.03$ would be necessary to reject this remaining contribution of cosmic-ray muons (see Figure 5.38).

By estimating the number of random crossings for vertex masses below the signal region cut of 12 GeV, a potential residual contribution of low-mass processes could be identified. Figure 5.39 shows the prediction and observation for tt vertices with a mass in the range of 6 to 12 GeV and the case that the material veto is not applied. Lower masses are not investigated since the seed pairs used in the estimation procedure are required to

[10]The reconstruction setup explained in Section 4.4 is applied also to events preselected for other ATLAS searches. If no preselection is required, then all events reconstructed using this setup can be used.

Table 5.9: Observed and predicted number of displaced vertices passing loosened selection criteria in the data for three vertex types. The predicted number of vertices is obtained using Equation (5.15) and presented without an uncertainty estimate as the statistical uncertainties are negligibly small in all cases.

	tt	et	μt
$N_{\text{pairs}}^{\text{obs}}$	1.1×10^{8}	119545	91044
Without material veto			
Avg. p_{xing}	2.6×10^{-4}	1.9×10^{-4}	2.3×10^{-4}
Predicted vertices	28543	22.9	21.1
Observed vertices	23795	17	23
With material veto			
Avg. p_{xing}	1.6×10^{-4}	1.2×10^{-4}	1.5×10^{-4}
Predicted vertices	17820	14.5	13.4
Observed vertices	14823	9	17

have a mass greater than 6 GeV, as mentioned in Section 5.6.3.1. In this mass range, 554 vertices are observed in the data, while the event mixing method predicts 615 vertices, i.e. it overestimates the data by 11%, which is less than the 20% for vertices with $m > 12$ GeV. Nevertheless, there seems to be no remaining contribution from low-mass processes, since the shapes of both distributions agree well within statistical uncertainties.

Since the estimation is performed separately for each data run, the crossing probability can be studied as a function of the amount of pileup, as shown in Figure 5.40a for tt vertices and no material veto. The expected crossing probability has a maximum value of 4.6×10^{-4} at low $\langle\mu\rangle$ and decreases approximately linearly to a minimal value of 1.4×10^{-4} at a very high $\langle\mu\rangle$ of about 35, i.e. there is a large dependence of p_{xing} on the amount of the pileup. The ratio between the predicted and the observed crossing probability is shown in Figure 5.40b. The latter probability is defined as the number of tt vertices divided by the number of tt pairs. The statistical uncertainties on the observed crossing probabilities are much larger than those on the expected crossing probabilities, which results in large uncertainties on the ratio. A fit of a linear function seems to indicate that the ratio is rather independent of $\langle\mu\rangle$ and that it decreases slightly when $\langle\mu\rangle$ increases. This would mean that the modelling quality of the event mixing does not depend significantly on the amount of

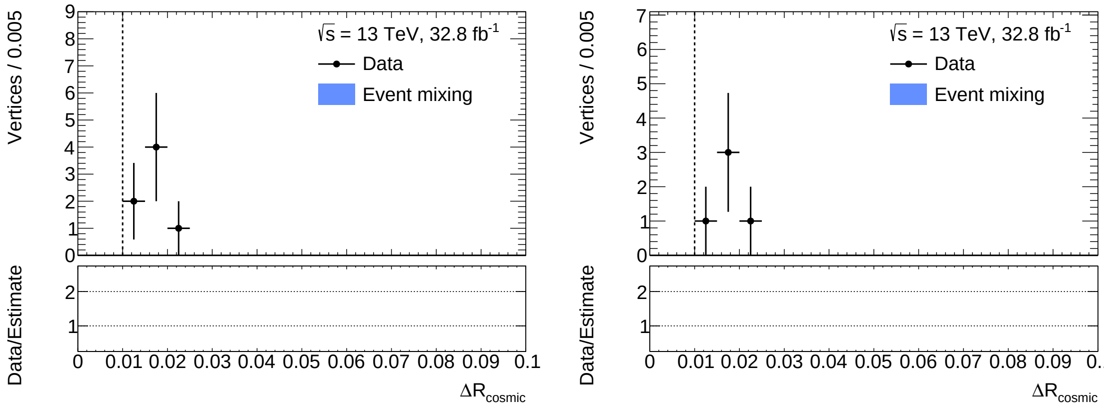

(a) No material veto **(b)** Material-rich regions vetoed

Figure 5.38: $\Delta R_{\mathrm{cosmic}}$ of μt vertices in the data. Only the region close to the signal region cut of 0.01 illustrated by a dashed line is shown. The event mixing method does not predict any vertices in this region. The bottom panel shows the ratio between the observation and the event mixing prediction. The estimated statistical uncertainties on the prediction are negligible.

pileup. However, the statistical uncertainties of the ratios are too large to make a conclusive statement.

Figure 5.41 shows a comparison of the predictions and observations for six observables of tt vertices, where the material veto is not applied. Most distributions have the same shape as in the $t\bar{t}$ MC sample (see Figures 5.36 and 5.37). Only the mass spectrum differs since it its maximum is shifted by 10 GeV to higher values. Three peaks can be seen in the d_0 distribution, which has not been shown before, a sharp maximum at $d_0 = 0$ and two broad maxima at about $d_0 = \pm 120$ mm. The latter two peaks are explained by the fact that most vertices from random crossings have $r > 120$ mm.

The tests on the data have shown that the predictions of the event mixing method correctly reproduce the characteristics of all distributions studied. There is also no evidence that a missing material veto causes any mismodelling of the predictions. The study of the tt sample consisting of several hundred million track pairs indicates that this method overestimates the number of random crossings by 20%, regardless of the kinematic properties of the track pair. Given the simplicity of the estimation procedure, it is a great achievement that such a non-standard background can be estimated with an accuracy of 20%.

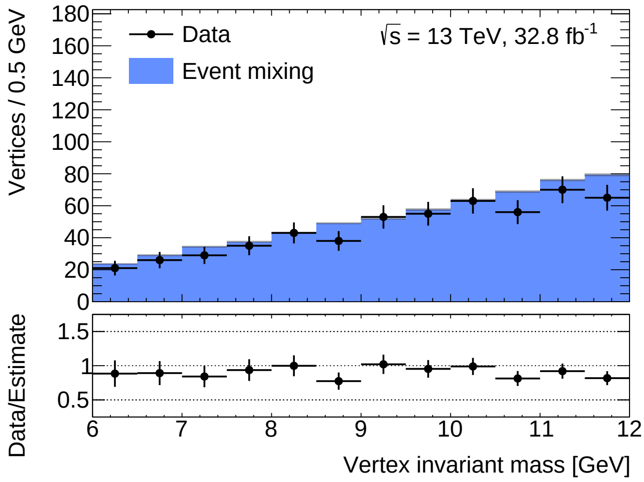

Figure 5.39: Comparison of the invariant mass of tt vertices that fail the mass cut in the data with the expectation from the event mixing. The material veto is not applied. The bottom panel shows the ratio between the observation and the event mixing prediction. The estimated statistical uncertainties on the prediction are negligible.

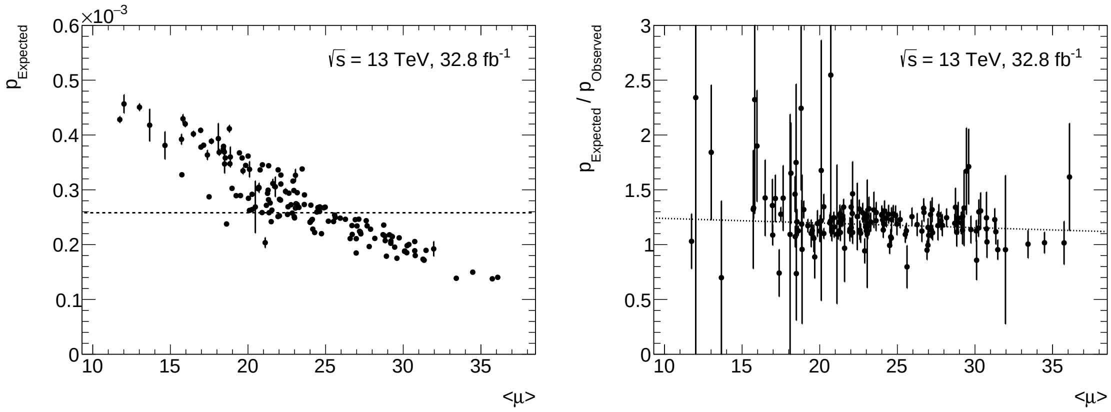

(a) p_{Expected} **(b)** $p_{\text{Expected}}/p_{\text{Observed}}$

Figure 5.40: (a) Expected crossing probability and (b) the ratio between the expected and the observed crossing probability of tt vertices as function of the mean number μ of collisions per bunch-crossing for each run of the data. The material veto is not applied. The dashed line shows the average crossing probability and the dotted line is a fit of a linear function.

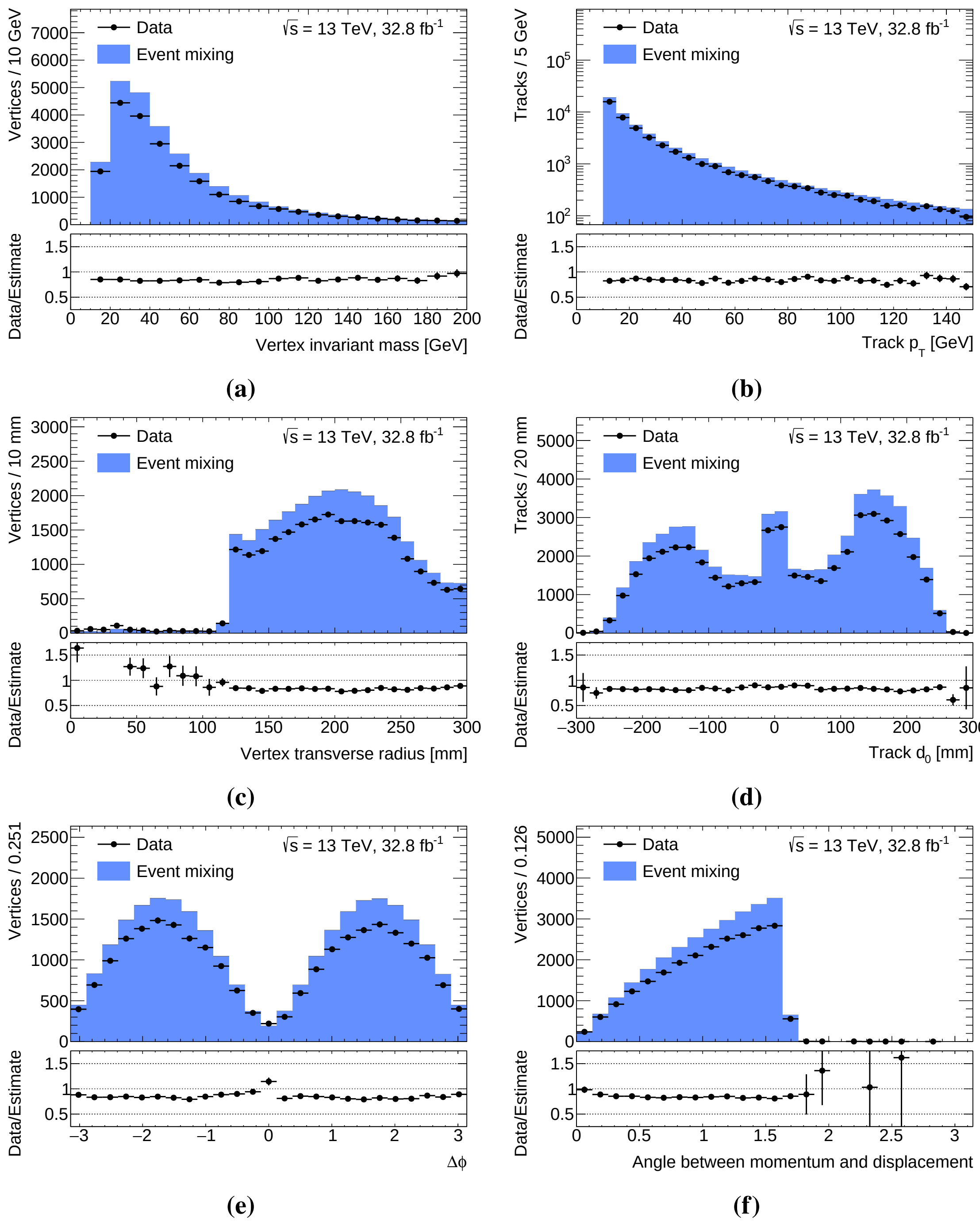

Figure 5.41: Comparison of six observables of tt vertices in the data with the expectation from the event mixing. The material veto is not applied. The bottom panel in each plot shows the ratio between the observation and the event mixing prediction. The estimated statistical uncertainties on the prediction are negligible.

5.6.3.4 Signal region estimate

To allow an estimation of the statistical uncertainty in the crossing probability, the event mixing estimate for each dilepton type is performed two hundred times on a randomly selected subset of seed pairs, which contains 2–3% of the possible seed pairs, and the variations in the crossing probabilities are measured. The spread of the results obtained from this procedure is shown in Figure 5.42. The mean of each p_{xing} distribution is used as the nominal crossing probability, while its uncertainty is taken as an estimate of the statistical uncertainty, which is less than 0.5% for all three dilepton types, and is therefore neglected hereafter. The distributions are well described by Gaussian functions, i.e. p_{xing} is normally distributed, suggesting that the subsets are rather independent of each other.

Table 5.10 summarises the crossing probabilities of lepton pairs and the expected number of displaced dilepton vertices from random crossings. The background in the signal region is calculated by adding the estimates for the three dilepton types, which yields

$$(2.39 \pm 0.53\ (\text{stat.}) \pm 1.53\ (\text{syst.})) \times 10^{-3} \tag{5.16}$$

events, assuming that there is no more than one random crossing per event. The possibility of two random crossings in the same event can be neglected as there are no events in the data with more than one lepton pair and the probability of two crossings in the same event is proportional to p^2_{xing}, which is less than 10^{-7} for all dilepton types. The statistical uncertainty of 22% arises from the normalisation to the number of dilepton events in the data. There are 21 events that contain a ee pair, whereas only half as many events are observed for each of the other two dilepton types. Both the kinematic requirements of the filters and the production processes differ for the three dilepton types, so it is not expected that the number of lepton pairs should be the same for all dilepton types.

The random crossing background has been estimated with an alternative method, which runs the displaced vertex reconstruction on events after one track has been randomly selected and flipped with respect to the beam spot, and then counts the number of displaced vertices that pass the selection criteria. More details on the track flipping method can be found in Reference [107]. The difference between the estimates obtained with the event mixing and the track flipping methods is used as a systematic uncertainty of 64%.

The crossing probability for muon pairs is more than a factor of two greater than that for $e\mu$ pairs. Almost 40% of the $\mu\mu$ vertices predicted by the event mixing method are located

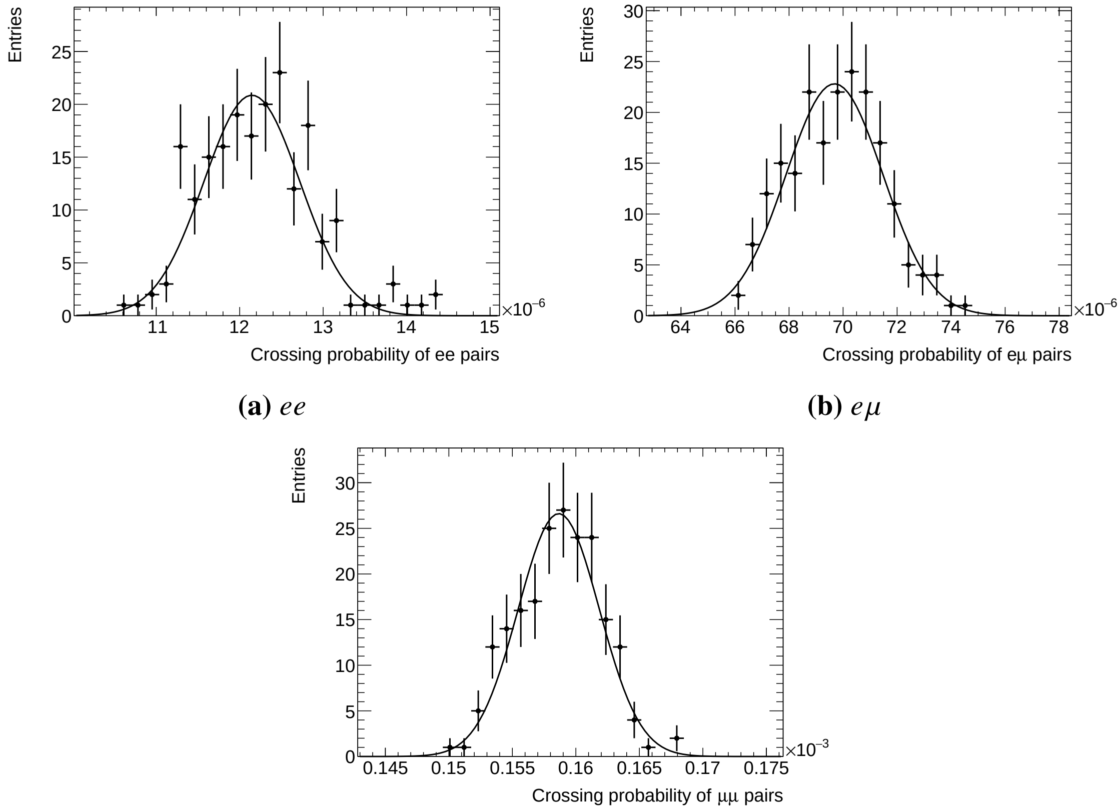

(a) ee **(b)** $e\mu$

(c) $\mu\mu$

Figure 5.42: Crossing probabilities of two hundred estimates for each dilepton type. A Gaussian function is fitted to each distribution, represented by the solid line.

inside a material-rich region, explaining a part of this discrepancy since the material veto is applied to $e\mu$ vertices but not to $\mu\mu$ vertices. This is contrary to the $t\bar{t}$ MC sample, where the dilepton crossing probabilities are not affected by the material veto as almost all dilepton vertices from random crossings are inside the beam pipe ($r < 25$ mm). For the data, the event mixing method predicts that most $\mu\mu$ vertices have $r > 120$ mm. More than 76% of the muons selected in the data have $\phi < 0$, which indicates that a significant fraction of them originates from cosmic-ray muons that are not rejected by the cosmic-ray veto, because the corresponding muon with $\phi > 0$ has not been reconstructed. Since there are no cosmic-ray muons in the $t\bar{t}$ MC sample, this could explain the different transverse radii of the $\mu\mu$ vertices. The crossing probability is minimal for ee pairs, an observation that has already been made in the $t\bar{t}$ MC sample.

Table 5.10: Event mixing results for the three dilepton types. The predicted number of vertices is obtained using Equation (5.15).

Type	$N^{\mathrm{obs}}_{\mathrm{pairs}}$	p_{xing} $[10^{-5}]$	N_{vx} $[10^{-4}]$
ee	21 ± 4.6 (stat.)	1.2	2.6 ± 0.6 (stat.)
$e\mu$	10 ± 3.2 (stat.)	7.0	7.0 ± 2.2 (stat.)
$\mu\mu$	9 ± 3.0 (stat.)	15.9	14.3 ± 4.8 (stat.)

Table 5.11: Estimated dilepton crossing probabilities for the nominal sample and the low-pileup and high-pileup subsamples. The statistical uncertainties are below 2%, and therefore not shown.

Type	p_{xing} $[10^{-5}]$		
	Low-pileup ($N_{\mathrm{PV}} \leq 12$)	Nominal ($\langle N_{\mathrm{PV}}\rangle = 14$)	High-pileup ($N_{\mathrm{PV}} \geq 16$)
ee	0.7	1.2	1.9
$e\mu$	6.4	7.0	7.3
$\mu\mu$	16.0	15.9	15.8

The dependence of the dilepton crossing probabilities on the amount of pileup is tested by performing the estimates on two disjoint subsamples, where the events have different amounts of pileup. The average number of primary vertices per event is 14.4 in the nominal sample. The low-pileup subsample is made of all events with $N_{\mathrm{PV}} \leq 12$, while the high-pileup subsample consists of all events with $N_{\mathrm{PV}} \geq 16$. Both subsamples contain about 30% of the events of the nominal sample. The dilepton crossing probabilities for these two subsamples are shown in Table 5.11 and compared to the nominal p_{xing}. The crossing probability of $\mu\mu$ pairs is nearly the same for all three samples. A variation of up to 8% is observed for $e\mu$ pairs, which is negligible compared to the systematic uncertainty of 64%. Large variations of up to 52% are found only for ee pairs, which contribute only 11% to the final estimate, so that the impact of this variation on the total systematic uncertainty can be neglected.

5.6.4 Material interactions

Another type of background are interactions of particles from pp collisions with detector material leading to the production of lepton pairs. One contribution originates from photons that interact with atomic nuclei and thereby convert into pairs of oppositely charged electrons. Photon conversions into muons are also possible, but they are significantly suppressed because the cross-section of photon conversions is inversely proportional to the square of the lepton mass [108] and the muon mass is more than two hundred times larger than the electron mass. The second relevant process involves the annihilation of a quark from a hadron with an antiquark from another hadron creating a virtual photon or Z boson which then decays into a pair of oppositely charged leptons, known as the Drell-Yan process [106], whose cross-section is the same for both electrons and muons. This contribution is dominated by charged pions interacting with the nucleons of atomic nuclei as charged pions have a lifetime of $2.6 \cdot 10^{-8}$ s and can reach therefore all layers of the pixel detector.

These two processes are studied using *ee* vertices by defining a control region in the data in which the material veto is inverted and the mass cut of 12 GeV is removed. The selection criteria of this control region are much looser than those of the signal region to enhance the number of its events. No triggers and filters are required as in the studies in Section 5.6.3.3. In addition, the opposite charge requirement and the p_T cut of 10 GeV are not applied. Each track is still required to have a minimum p_T of 1 GeV, which is ensured by the track selection of the displaced vertex reconstruction.

In total, 123 *ee* vertices are found in this control region. All but one are oppositely charged, which is consistent with the assumption that they originate from one of the two processes. Distributions of several observables of these vertices are shown in Figure 5.43. All but five of the vertices have a mass between 200 and 400 MeV, which is a strong indication that they were produced by photon conversions. In principal, *ee* vertices from photon conversions should have a mass of zero, since photons are massless particles, but in the calculation of the vertex mass all tracks are assumed to be pions, so that the vertex mass is shifted to values of about $2 \cdot m_\pi \approx 280$ MeV. The majority of tracks has a p_T of less than 5 GeV. No vertex of this control region has a mass of more than 8 GeV or passes a p_T cut of 10 GeV. The electron pairs are highly collimated, as their $|\Delta\Phi|$ values indicate, which are smaller than 0.15. Most vertices are produced at very large radii of $r > 180$ mm in the supporting structures of the pixel detector. Nevertheless, the magnitudes of the transverse impact parameters of their tracks are predominantly less than 10 mm, caused by a small angle between the momentum and the displacement of the vertex.

None of these *ee* vertices would pass the signal region criteria if the material veto were not applied to *ee* vertices. Only five of them seem not to have been produced by

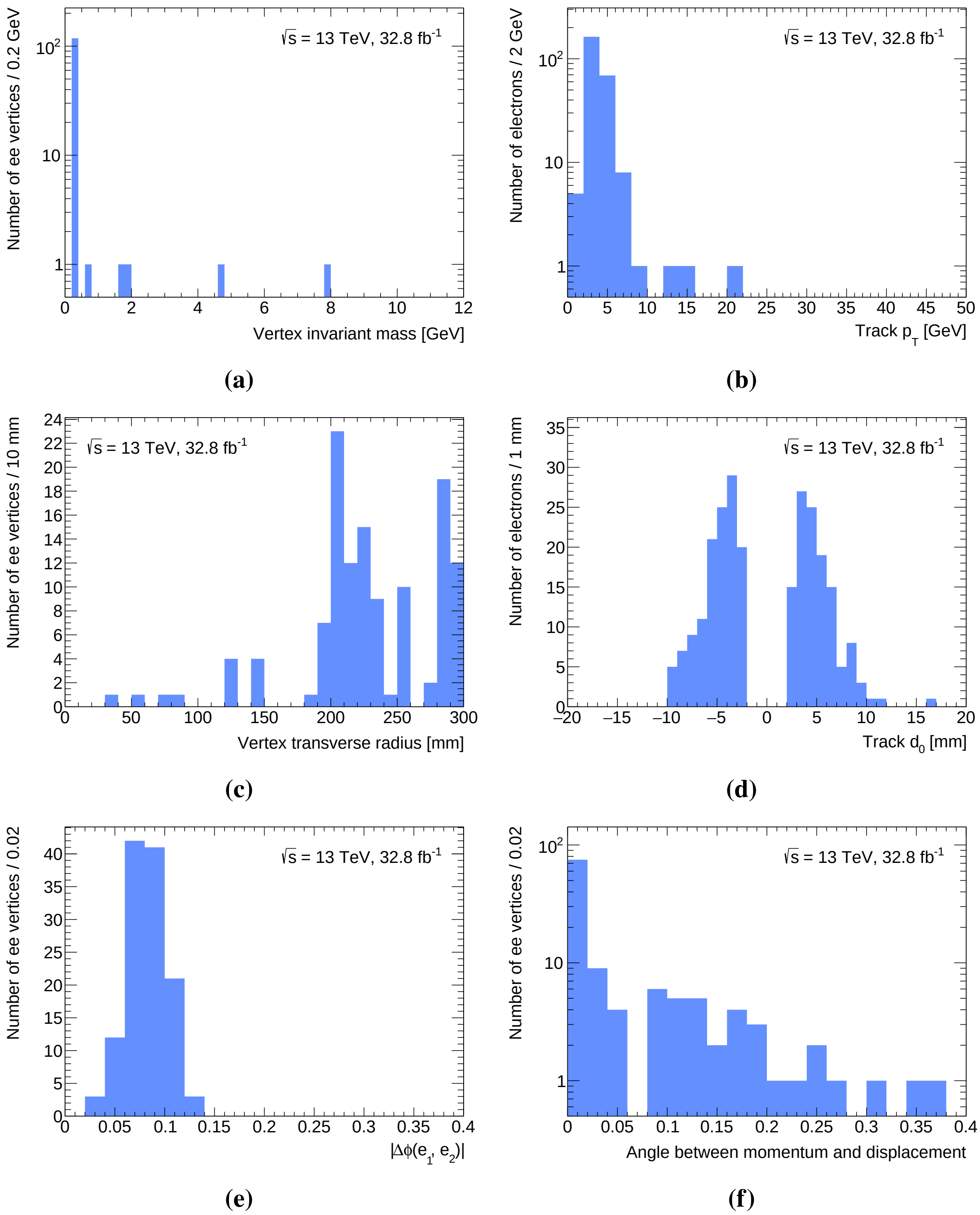

Figure 5.43: Six observables of *ee* vertices in the data that fail the material veto and pass loosened selection criteria.

Table 5.12: Properties of *ee* vertices with $m_{\mathrm{DV}} > 0.5\,\mathrm{GeV}$ in the data that fail the material veto and pass loosened selection criteria.

m_{DV} [GeV]	$N(e)$	$N(\text{tracks})$	$p_{\mathrm{T}}^{\text{leading } e}$ [GeV]	$p_{\mathrm{T}}^{\text{subleading } e}$ [GeV]	$q_{e,1} \cdot q_{e,2}$
0.76	2	2	14	4.4	−1
1.7	2	2	20	8.1	−1
1.9	2	4	13	4.2	−1
4.7	2	2	3.3	1.4	+1
8.0	2	3	4.7	3.8	−1

photon conversions and could have been produced by Drell-Yan processes, their properties are listed in Table 5.12. The electron pair of one of these five vertices is not oppositely charged, which is not consistent with the assumption that it was produced by a Drell-Yan process. It is possible that this vertex originates from a misconstruction, as it is unlikely to have been generated by a random crossing due to the small $|\Delta\Phi|$ of the electron pair. The remaining four vertices have masses of up to 8 GeV and no track with $p_{\mathrm{T}} > 20\,\mathrm{GeV}$, which means that they significantly fail the filter matching requirements. Consequently, there is no indication that lepton pairs from Drell-Yan processes could be a non-negligible source of background. This is consistent with the observation that no $\mu\mu$ vertex with a mass between 6 and 12 GeV is found in the data (see Section 5.6.2).

Consequently, the application of a material veto seems not be necessary for highly energetic displaced dilepton vertices. Nevertheless, the material veto is applied in the signal region to vertices containing at least one electron to reject remaining contributions from photon conversions and non-leptonic material interactions that are misidentified as dilepton vertices. The latter occurs much more frequently for electrons than for muons, because the number of hadrons interacting with the electromagnetic calorimeter is significantly higher than the number of hadrons traversing the barrel of the muon spectrometer. The misidentification rate, however, is so low even for *ee* vertices that it was not possible to estimate it.

5.6.5 Non-collision backgrounds

In the previous sections, the background originating from proton–proton collisions was studied. In addition, there are non-collision backgrounds, which include beam-induced backgrounds and particles from external sources such as cosmic-ray muons.

5.6.5.1 Beam-induced backgrounds

Beam-induced backgrounds [109] are due to the loss of protons, which can occur at any position in the LHC ring. Inelastic interactions of the protons, for example with the residual gas in the beam-pipe, lead to the production of secondary particles such as leptons. There is a dedicated shielding of the ATLAS detector to absorb these secondary particles, but it cannot stop high-energy muons that are capable of penetrating a large amount of material. Such muons traverse the detector in a direction almost parallel to the beam pipe because they are highly boosted along the direction of the proton momentum. Therefore, they cannot pass the muon trigger, which requires the muon to traverse the muon spectrometer barrel from the inside to the outside. This means that a $\mu\mu$ vertex passing the selection criteria of the signal region and consists only of beam-induced muons is not possible. A single beam-induced muon, however, could become part of a displaced vertex passing the signal region if it crosses another lepton by chance, but this is already covered by the estimate presented in Section 5.6.3.4.

5.6.5.2 Events with single cosmic-ray muons

Of the external sources, only muons from cosmic-rays are energetic enough to pass the selection criteria of this search. Cosmic-rays are high-energy particles that originate from galactic sources such as supernovae and consist mainly of protons and helium nuclei. In the atmosphere of the earth, they collide with atoms and molecules, primarily oxygen and nitrogen, producing a shower of secondary particles. A cosmic-ray shower often contains charged mesons such as pions and kaons, which can decay into muons. Even though muons have only a lifetime of about $2.2 \cdot 10^{-6}$ s, highly energetic cosmic-ray muons can reach the surface of the earth due to the relativistic time dilation. Since the ATLAS detector is only 100 m underground, it is not particularly strongly shielded against cosmic-ray muons. At this depth, the rate of cosmic-ray muons with $p_{\mathrm{T}} > 20\,\mathrm{GeV}$ is about $1\,\mathrm{s}^{-1}\mathrm{m}^{-2}$ [110].

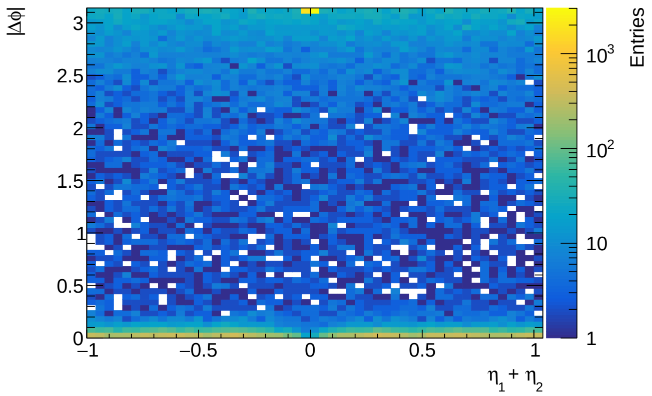

Figure 5.44: $|\Delta\phi|$ vs. $\eta_1 + \eta_2$ of muon pairs in the events selected by the muon filter.

Cosmic-ray muons traverse the entire ATLAS detector from top to bottom, producing hits in the tracking detectors along a straight trajectory that extends across the entire inner detector. The track reconstruction algorithms assume that all particles originate from proton–proton collisions, and thus the track of a cosmic-ray muon is split near the beamline into two tracks, which are almost perfectly back-to-back in the $\eta\phi$-space. Consequently, a cosmic-ray muon is sometimes reconstructed as a back-to-back muon pair, which is oppositely charged as the two muons point in opposite directions. This does not occur very frequently, since the cosmic-ray muon traverses the upper half of the muon spectrometer in the opposite direction than a collision muon, resulting in low reconstruction efficiencies of the associated muon spectrometer track. Muon pairs that are back-to-back in the $\eta\phi$-space have $|\Delta\phi| \approx \pi$ and $\eta_1 + \eta_2 \approx 0$. Figure 5.44 shows the two-dimensional distribution of these variables for muon pairs in the events selected by the muon filter. The peak in the top centre illustrates that about 7‰ of the muon pairs are back-to-back.

A significant number of these back-to-back muon pairs are reconstructed as displaced vertices that pass the entire signal selection, which would constitute a large background. Therefore, events that have at least one lepton pair with

$$\Delta R_{\mathrm{cosmic}} = \sqrt{(|\Delta\phi| - \pi)^2 + (\eta_1 + \eta_2)^2} < 0.01 \tag{5.17}$$

are vetoed in the signal region to suppress the background from cosmic-ray muons. The veto is applied to any type of lepton pair to cover cases where the cosmic-ray muon is reconstructed as an electron. The cut value was chosen so that the size of the remaining background can be estimated with a simple method and remains small.

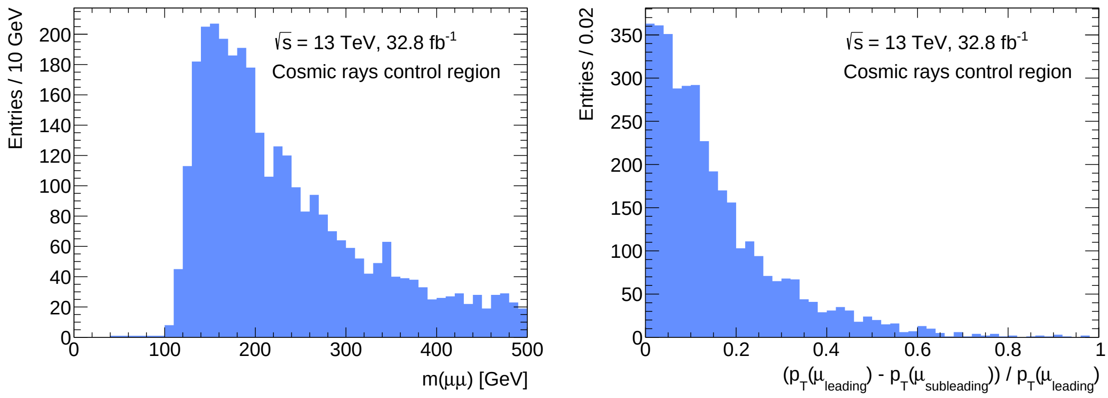

(a) **(b)**

Figure 5.45: (a) Invariant mass and (b) the relative difference in p_T of muon pairs in the events of the cosmic-rays control region.

A cosmic-rays control region is defined in the collision data by selecting events that pass the muon filter and have at least one muon pair with $\Delta R_\mathrm{cosmic} < 0.04$. Muon pairs forming a vertex and passing the cosmic-ray veto are not selected to keep the signal region blind. All event-level cuts of Section 5.2.2 are applied except the cosmic-ray veto. Each of the two muons has to pass the usual selection criteria described in Section 5.2.3 and the track selection criteria of the displaced vertex reconstruction as detailed in Section 4.4.2. Furthermore, the muon pair has to satisfy the muon filter requirements including a successful match to the muon trigger.

Figure 5.45a shows that more than 97% of the muon pairs in this control region have an invariant mass that is greater than 120 GeV, meaning that a negligible fraction of them fails the 12 GeV mass cut of the signal region. Using Equation (5.14) and taking into account the p_T cut of 62 GeV of the muon filter, a peak near $\sqrt{2 \cdot (62\,\mathrm{GeV})^2 \cdot (1 - \cos\pi)} = 124\,\mathrm{GeV}$ is expected, assuming that both muons have the same p_T. The peak is observed at a p_T between 140 and 150 GeV, which is close to the roughly estimated value. In about 74% of the cases, the p_T values of the two muons agree within 20% (see Figure 5.45b), which is expected since the two muons originate from the same cosmic-ray muon and should have therefore a very similar p_T.

The study of this control region indicates the presence of events with more than one cosmic-ray muon, which are further investigated in Section 5.6.5.3. The inner detector tracks of two muons that originate from the same cosmic-ray muon have consistent impact parameters, meaning that they satisfy the relations $d_0^1 \approx -d_0^2$ and $z_0^1 \approx z_0^2$. All muon pairs

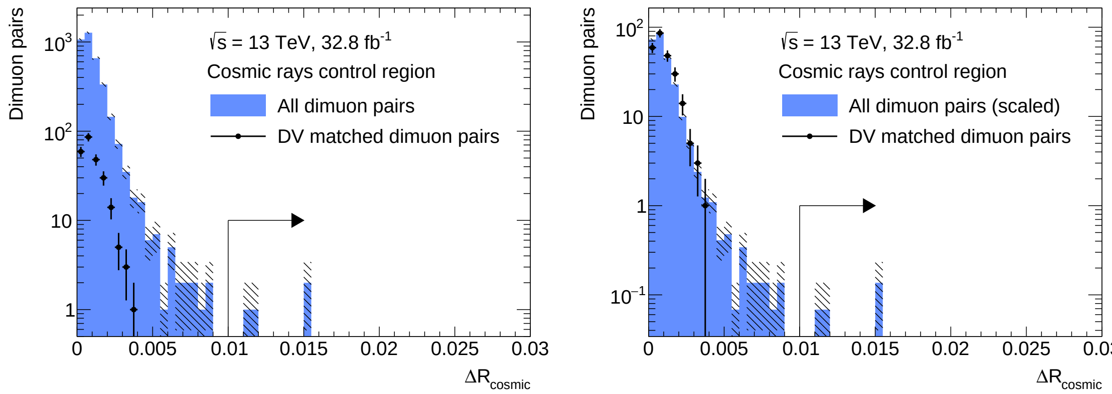

(a) Unscaled **(b)** Scaled

Figure 5.46: ΔR_{cosmic} of muon pairs in the events of the cosmic-rays control region. The distribution of all muon pairs is shown by the filled area, while the dots indicate the subset forming a displaced vertex. The arrow shows the cut on ΔR_{cosmic} applied in the signal region.

in this control region are required to have $|d_0^1 + d_0^2| < 2\,\text{mm}$ and $|z_0^1 - z_0^2| < 25\,\text{mm}$ to reject the contributions from events with multiple cosmic-ray muons. The cut values have been chosen based on the observations presented in Section 5.6.5.3.

In total, 3646 muon pairs satisfying all those criteria are found, their ΔR_{cosmic} distribution is shown in Figure 5.46a. Of these muon pairs, 246 (about 7%) form a displaced vertex that passes all of the signal region criteria except the cosmic-ray veto. The ΔR_{cosmic} distribution of the $\mu\mu$ vertices ends near $\Delta R_{\text{cosmic}} = 0.004$. To estimate the size of this background, the distribution of all muon pairs is used to extrapolate the vertex distribution to the signal region. This is done by normalizing the pair distribution to the vertex distribution using the integrals of the two distributions for $\Delta R_{\text{cosmic}} < 0.004$. All distributions, before and after normalisation, are shown in Figures 5.46a and 5.46b.

With this method, the cosmic-rays background is estimated to be

$$0.27 \pm 0.14\,(\text{stat.}) \pm 0.10\,(\text{syst.}). \tag{5.18}$$

The statistical uncertainty is given by the Poisson error on the number of muon pairs ($N = 4$) that do not form a vertex and pass the cosmic-ray veto, while the systematic uncertainty is estimated by alternatively using the first three bins ($\Delta R_{\text{cosmic}} < 0.0015$) for the normalisation and evaluating the difference of the integrals of the two distributions for

$0.0015 < \Delta R_{\text{cosmic}} < 0.004$. This background is about two orders of magnitude larger than the random crossing background, and therefore the dominant source of background for this analysis.

Another source of background due to single cosmic-ray muons results from the random crossings of these with leptons from collision processes. This contribution, however, is already covered by the estimate presented in Section 5.6.3.4.

5.6.5.3 Events with multiple cosmic-ray muons

In rare cases, two muons produced in the same cosmic-ray shower, referred to as dicosmics, traverse the ATLAS detector during a bunch-crossing. If one of these muons is reconstructed as a back-to-back muon pair, then the event is rejected by the cosmic-ray veto. However, it can happen that only the two muons that have a negative ϕ are reconstructed due to the low reconstruction efficiencies of cosmic-ray muons in the upper half of the detector. In this case, the event is not rejected and both muons could randomly cross and form a vertex. If the crossing probability of dicosmics is similar to collision muons, then this contribution is already covered by the random crossing estimate discussed in Section 5.6.3.1. To check whether this is the case, dicosmics are studied in the following.

As already mentioned in the previous section, muon pairs that originate from the same cosmic-ray muon have consistent impact parameters. Thus, dicosmic events can be identified by searching for muon pairs in the cosmic-rays control region that have inconsistent impact parameters. Figures 5.47a and 5.47b show that all muon pairs observed in this control region have $z_0^1 \approx z_0^2$ and $d_0^1 \approx -d_0^2$, apart from one and two outliers, respectively. These outliers belong to two muon pairs, for which the origin of the tracks is separated by several centimetres (see Figure 5.47c), and this difference is not covered by the uncertainty in the measured track parameters (see Figure 5.47d).

To study these two muon pairs in more detail, event displays have been produced, which are shown in Figures 5.48 and 5.49. The first event is a good example of a dicosmic event, since it contains two back-to-back muon pairs that are close in space. In the second event, only three muons were reconstructed, but the reconstructed segments in the muon spectrometer are consistent with the assumption that they originate from a pair of cosmic-ray muons. In none of these dicosmic events, the cosmic-ray muons randomly cross and form a vertex.

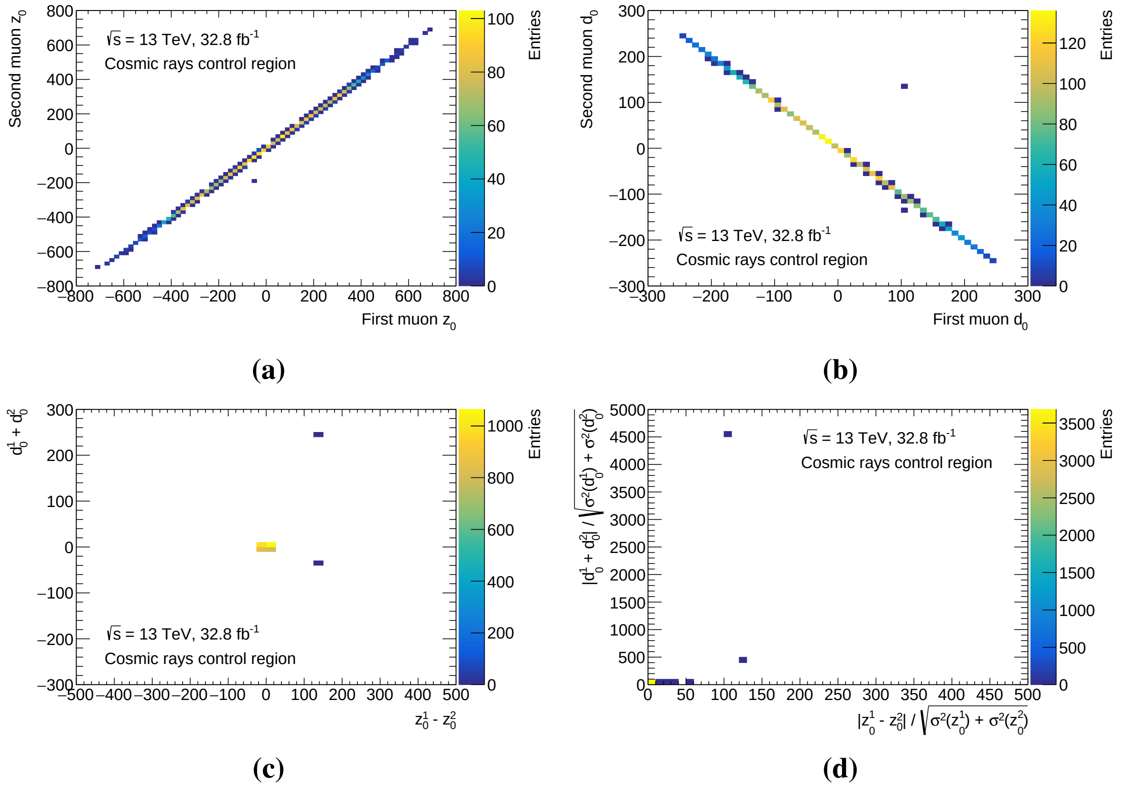

Figure 5.47: (a) Longitudinal and (b) transverse impact parameters, (c) magnitudes of the sum of transverse impact parameters and the difference of longitudinal impact parameters of muon pairs in the events of the cosmic-rays control region and (d) the corresponding significances.

The fact that only two dicosmic events are found in the data shows that they are very rare. The associated background is therefore negligible compared to the contribution from single cosmic-ray muons, except if the crossing probabilities of dicosmics are at least two orders of magnitude larger than those of collision muons. As indicated by the event displays, dicosmics seem to be close in space, which could lead to an increased crossing probability.

Unfortunately, it is not possible to study the random crossing probabilities of dicosmics directly as they are not very abundant. In an attempt to increase the size of the dicosmics sample, events were selected that have two muons with negative ϕ that are each back-to-back to an inner detector track, which has consistent track impact parameters. However, only the two already known dicosmic events passed this selection.

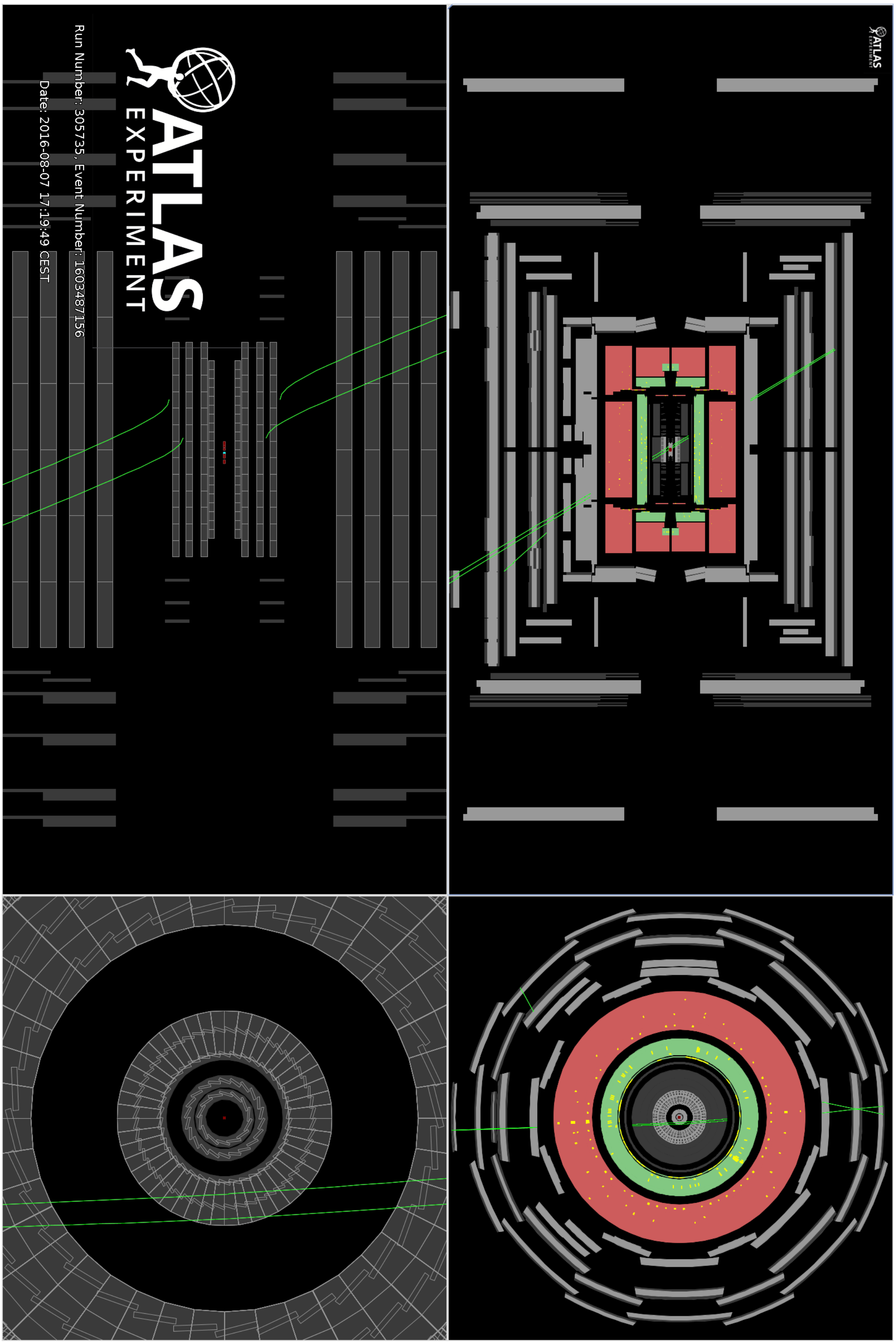

Figure 5.48: Event displays of a dicosmic event recorded in August 2016. For reasons of clarity, inner detector tracks not associated with cosmic-ray muons are not displayed.

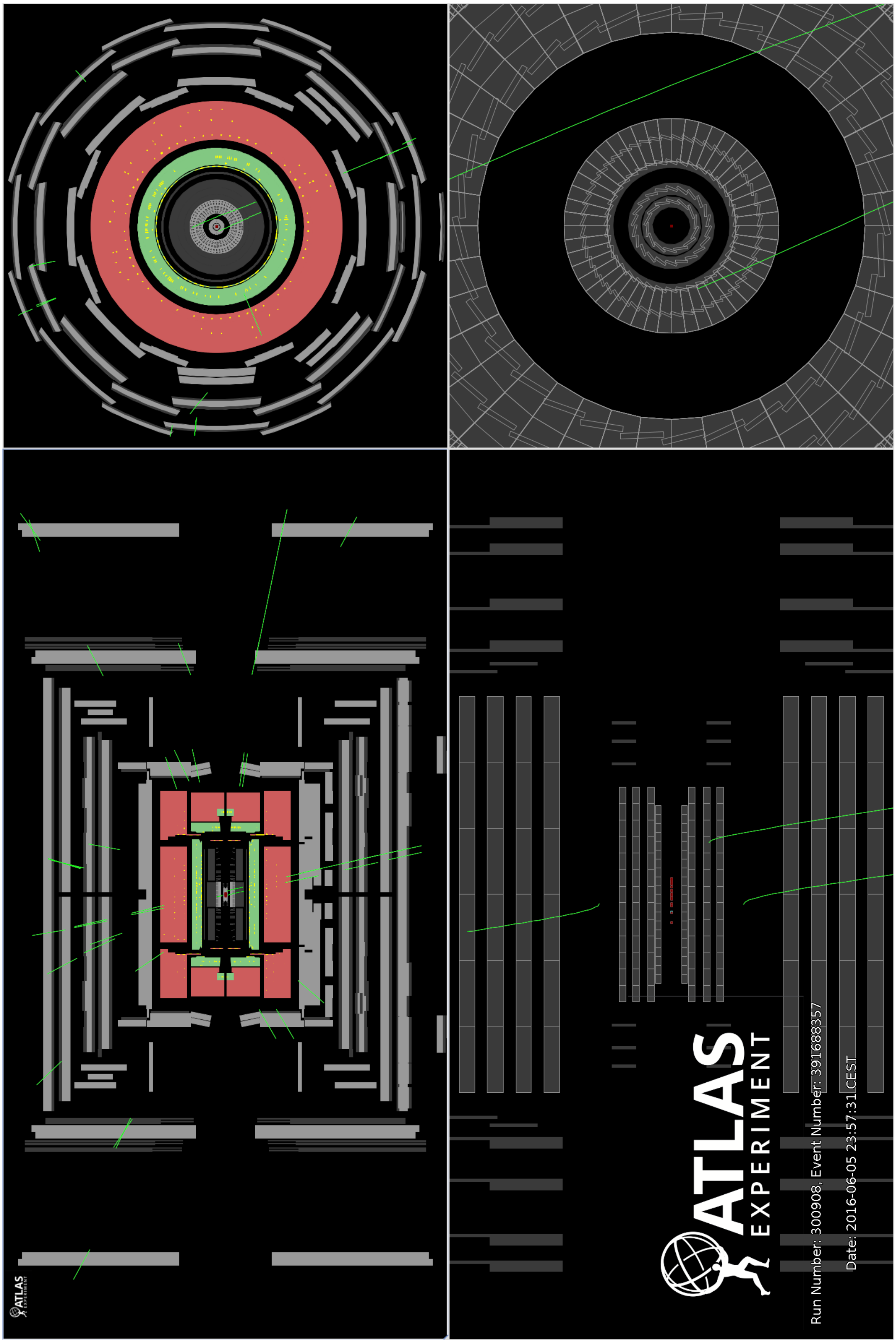

Figure 5.49: Event displays of a dicosmic event recorded in June 2016. For reasons of clarity, inner detector tracks not associated with cosmic-ray muons are not displayed.

Instead, the estimation procedure for random crossings explained in Section 5.6.3.1 is performed on muons from events that fail the cosmic-ray veto. The procedure is exactly the same as for the signal region estimate, except that a different collection of muons is used. The crossing probability of cosmic-ray muons of 1.52×10^{-4} is four percent smaller than that of collision muons (1.59×10^{-4}). The statistical uncertainties on the crossing probabilities are below one percent and cannot explain this minor discrepancy. Since the crossing probabilities of cosmic-ray muons and collisions muons do not differ significantly, there is no indication that the random crossing of dicosmics is not covered by the estimate discussed in Section 5.6.3.4.

5.6.6 Final background estimate

Both collision and non-collision backgrounds have been studied in the previous sections. The collision background is dominated by random crossings of lepton tracks and is of the order of 10^{-3} events. The non-collision background is two orders of magnitude larger and originates from cosmic-ray muons reconstructed as back-to-back muon pairs. Thus, the random crossing background can be neglected and the number of background events expected in the signal region is given by:

$$N_{\mathrm{SR}}^{\mathrm{bkg}} = 0.27 \pm 0.14\ (\mathrm{stat.}) \pm 0.10\ (\mathrm{syst.}). \tag{5.19}$$

5.7 Results

5.7.1 Signal region observation

In the following, the selection criteria of the signal region are applied to the data events and the observation is compared with the background expectation. The cutflows in Figure 5.50 show the number of events in the data as a function of the signal region cuts for each dilepton type separately. The value of the first bin in each cutflow, 82.06 million events, is the total number of events of the data sample that was reconstructed with the setup optimised for decays of long-lived particles. The second to sixth bin are the event-level cuts of Section 5.2.2. Of these, only the trigger requirement has a significant impact on the number of accepted events. Here, it should be noted that the data sample consists of events preselected for multiple ATLAS searches that use different triggers, and therefore only about 1/3 of the events pass one of the triggers of this search. The seventh bin requires the presence of at least one displaced vertex candidate, which is the case for about 38% of the events that pass all event-level cuts. All subsequent cuts, which are described in Section 5.2.3, are applied to displaced vertex candidates in the event. For the ee and $e\mu$ channels, the material veto reduces the number of events by 53%, which is more than the fraction (40%) of the fiducial volume covered by it, which could be due to the enhanced production of non-leptonic vertices in the material-rich regions. The two cuts requiring at least one or two leptons can only be passed by leptons whose flavours match the dilepton type of the cutflow. Only for the $\mu\mu$ channel, there are events that have a displaced vertex with two leptons passing the identification criteria and the overlap removal. These eighteen events belong to the low-mass control region discussed in Section 5.6.2, i.e. the corresponding vertices all have a mass of less than 12 GeV.

For all three channels, no event is observed in the last bin, i.e. the signal region. This observation is consistent with the background expectation of 0.27 ± 0.17 events.

5.7.2 Statistical methods

Since there is no indication of a signal in the data, upper limits on the production cross-section of the signal model are set. They are computed using the HistFitter [111] framework, which employs a Frequentist method to perform the hypothesis tests based on a profile likelihood ratio test statistic [112].

As first step of the procedure, a statistical model is defined to describe the data. The likelihood L is given by the product of a Poisson distribution ($\mathrm{Pois}(N|\nu) = \frac{\nu^N}{N!}e^{-\nu}$) for the number of events in the signal region and of multiple Gaussian distributions with unit width ($\mathrm{Gaus}(\Theta) = \frac{1}{\sqrt{2\pi}}e^{-\frac{1}{2}\theta^2}$) to take into account the systematic uncertainties:

$$L(\mu, \vec{\Theta}|N_{\mathrm{SR}}, \vec{\Theta}^0) = \mathrm{Pois}(N_{\mathrm{SR}}|\nu = b(\vec{\Theta}) + \mu s(\vec{\Theta})) \times \prod_{j \in \mathcal{S}} \mathrm{Gaus}(\Theta_j^0 - \Theta_j), \tag{5.20}$$

where N_{SR} is the number of events observed in the signal region, ν the mean of the Poisson distribution, b and s the numbers of background and signal events, μ the signal strength, $\mathcal{S}$ the set of systematic uncertainties, Θ_i the nuisance parameters for the systematic uncertainties and Θ_i^0 are the central values around which Θ_i can be varied. The signal strength $\mu \geq 0$ is a scale factor of the signal, with the background-only hypothesis corresponding to $\mu = 0$ and the nominal signal+background hypothesis to $\mu = 1$.

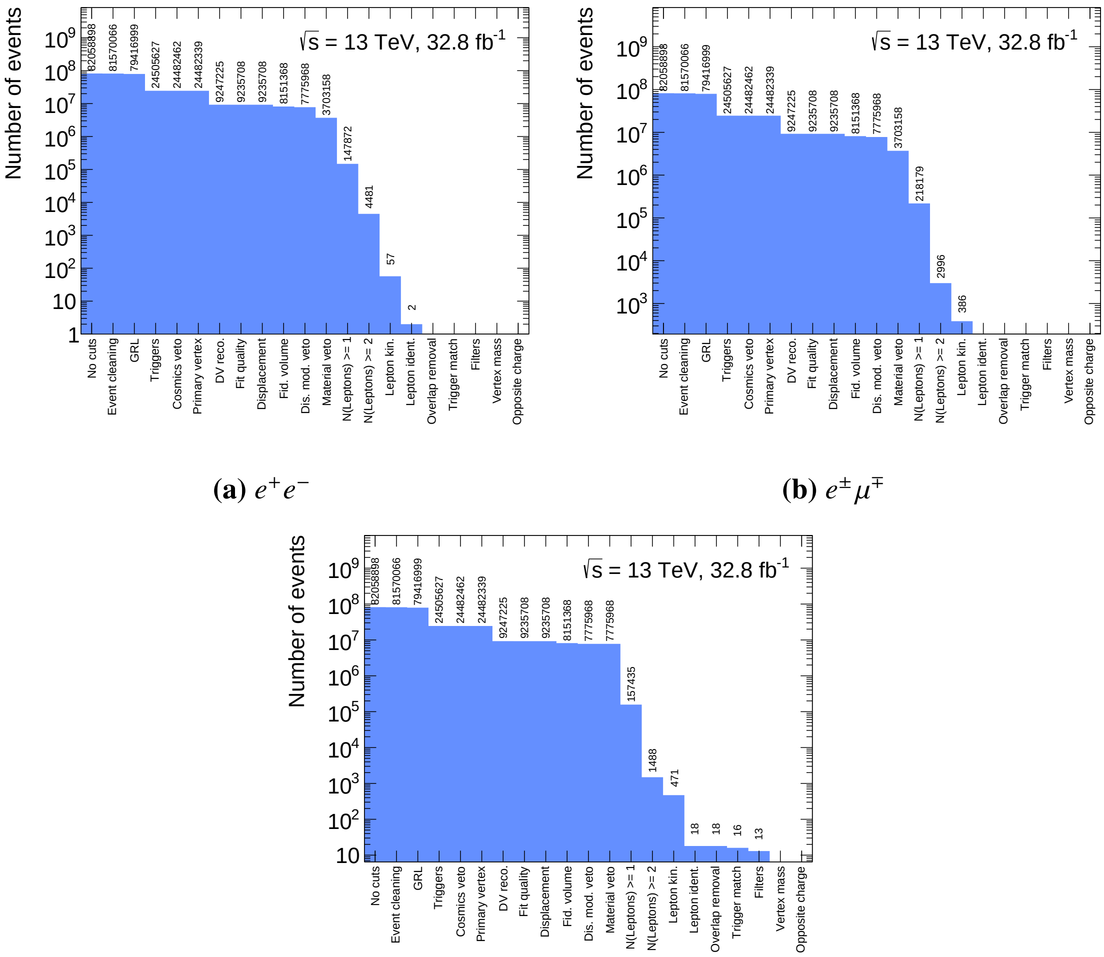

(a) e^+e^-

(b) $e^\pm\mu^\mp$

(c) $\mu^+\mu^-$

Figure 5.50: Number of events observed in the data passing sequentially the signal region cuts for the three dilepton channels. Entries in the last bin pass the signal region criteria.

The hypothesis tests are performed by evaluating the agreement of the signal hypotheses differing in μ with the data using the one-sided profile likelihood ratio test statistic

$$q_\mu = \begin{cases} -2\ln\frac{L(\mu,\hat{\hat{\vec{\Theta}}})}{L(\hat{\mu},\hat{\vec{\Theta}})}, & \hat{\mu} \le \mu, \\ 0, & \hat{\mu} > \mu, \end{cases} \tag{5.21}$$

which is based on a profile likelihood ratio, where the numerator, $L(\mu, \hat{\hat{\vec{\Theta}}})$, is the maximum of the likelihood for a given μ and the denominator, $L(\hat{\mu}, \hat{\vec{\Theta}})$, the overall maximum of the likelihood. The probability density function $f(q_\mu|\mu, \vec{\Theta})$ of the test statistic is obtained by performing several thousand pseudo-experiments in which N_{SR} and Θ_i^0 are randomly generated according to the distribution derived from Equation (5.20) for given μ and $\vec{\Theta}$.

The agreement between the data and a signal hypothesis is quantified based on the p-value of the test statistic distribution, which is the probability of obtaining data that is at least as incompatible with the signal hypothesis as the observed data:

$$p_{\mu,\vec{\Theta}} = \int_{q_{\mu,\mathrm{obs}}}^{\infty} f(q_\mu|\mu, \vec{\Theta})dq_\mu, \tag{5.22}$$

where $q_{\mu,\mathrm{obs}}$ is the value of the test statistic for the observed data. Consequently, the p-value depends on the nuisance parameters $\vec{\Theta}$, so that for each signal hypothesis there is a set of p-values. The decision as to whether a signal hypothesis is rejected is based on the largest p-value, the so-called supremum p-value

$$p_\mu^{\mathrm{sup}} = \sup_{\vec{\Theta}} p_{\mu,\vec{\Theta}}. \tag{5.23}$$

However, it is computationally not feasible to calculate the p-values for all $\vec{\Theta}$. The p-value becomes large when there is good agreement between data and signal hypothesis, and therefore the values of $\vec{\Theta}$ leading to the supremum p-value can be estimated by fitting them based on the observed data and the given μ, i.e. by determining $\hat{\hat{\vec{\Theta}}}$. This is often referred to as profiling the nuisance parameters. As a result, the p-value is calculated according to the equation

$$p_\mu = \int_{q_{\mu,\mathrm{obs}}}^{\infty} f(q_\mu|\mu, \hat{\hat{\vec{\Theta}}}(\mu, \mathrm{obs}))dq_\mu. \tag{5.24}$$

The CL_s value [113] of a signal hypothesis is given by

$$CL_s = \frac{p_\mu}{p_{\mu=0}}. \tag{5.25}$$

The upper limit μ^{95} on the signal strength at 95% confidence level (CL) is defined as the signal strength μ for which the CL_s value is 0.05. The CL_s values of the hypothesis tests are linearly interpolated to calculate μ^{95}. The 95% CL upper limit on the cross-section is defined as the product of the signal cross-section and μ^{95}.

The procedure discussed above describes how the observed upper limit is derived. The expected upper limit is computed with the same procedure with two exceptions. First, pseudo data is used instead of real data to determine the lower limit of the integral in Equation (5.24). The pseudo data is generated assuming the background-only hypothesis. To make the expectation the most compatible assessment for the actual observation, the nuisance parameters are profiled based on the observed data and not the pseudo data. Secondly, the calculation of the upper limit is repeated with different pseudo data, resulting in a distribution of the upper limit. The median of this distribution is used as the expected upper limit, and the 16th and 84th percentiles are used to determine the $\pm 1\sigma$ variations of the expected upper limit.

5.7.3 Exclusion limits

Figure 5.51 shows the upper limits on the signal production cross-section as a function of the neutralino $c\tau$ for various choices of signal parameters. The observed limits are consistent with the expected limits within the $\pm 1\sigma$ uncertainties. For a squark mass of 700 GeV, the upper limits are in almost all cases smaller than the predicted cross-section, meaning that these signal hypotheses are excluded at 95% confidence level. Only 50 GeV neutralinos with a $c\tau$ larger than 6 m are not excluded in that case. If the squark mass is 1.6 TeV, lifetimes of a 1.3 TeV neutralino in the range of 3 mm to 1 m are excluded, while the lifetime of a 50 GeV neutralino can only be constrained if it decays via a λ_{122} coupling, where $c\tau$ values between 4 and 30 mm are excluded. The better sensitivity to neutralino decays mediated by a λ_{122} coupling is caused by the fact that no material veto is needed for $\mu\mu$ vertices.

Model-independent upper limits on the visible cross-section, which is the production cross-section times the signal efficiency, and on the visible number of signal events are

Table 5.13: Model-independent upper limits at 95% confidence level on the visible cross-section $\langle\epsilon\sigma\rangle^{95}_{\mathrm{obs}}$ and on the visible number of signal events s^{95}_{obs} and its expectation s^{95}_{exp} with $\pm 1\sigma$ variations

	$\langle\epsilon\sigma\rangle^{95}_{\mathrm{obs}}$ [fb]	s^{95}_{obs}	s^{95}_{exp}
Upper limit	0.09	3.0	$3.0^{+0.6}_{-0.0}$

shown in Table 5.13. Signal models that predict at least three events in the signal region are excluded at 95% confidence level.

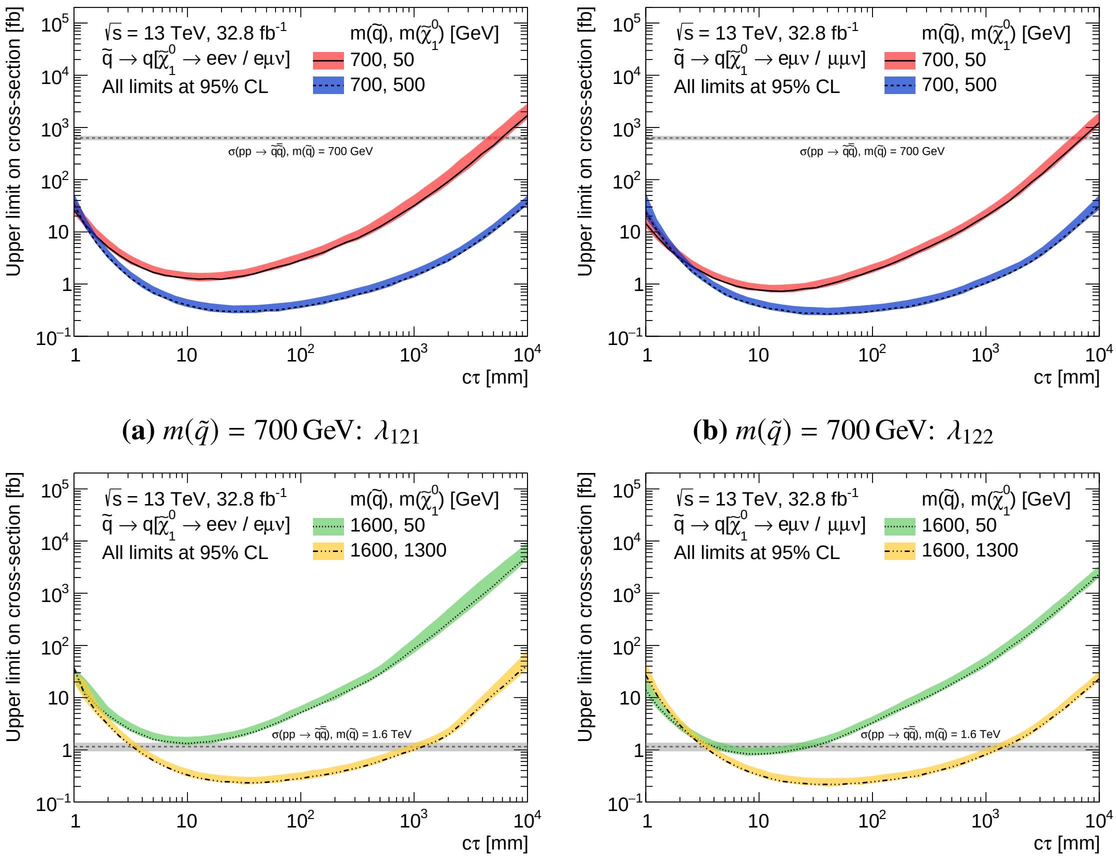

(a) $m(\tilde{q})$ = 700 GeV: λ_{121}

(b) $m(\tilde{q})$ = 700 GeV: λ_{122}

(c) $m(\tilde{q})$ = 1.6 TeV: λ_{121}

(d) $m(\tilde{q})$ = 1.6 TeV: λ_{122}

Figure 5.51: Observed upper limits at 95% confidence level (CL) on the squark-antisquark production cross-section as a function of the $\tilde{\chi}^0_1$ lifetime ($c\tau$) for four combinations of squark and neutralino masses and $\tilde{\chi}^0_1$ decays mediated by (left) a λ_{121} or (right) a λ_{122} coupling. The shaded bands around the observed limits indicate the $\pm 1\sigma$ variations in the expected limit, while the horizontal bands show the expected cross-sections and their uncertainties.

5.7.4 Comparison with the results of the previous search

Previously the ATLAS collaboration searched for displaced dilepton vertices in the inner detector of ATLAS at $\sqrt{s}$ = 8 TeV [84, 85]. The Run-1 search considered a simplified supersymmetic model, in which a pair of gluinos is produced via the strong interaction. Each gluino decays into two quarks of the first two generations and the lightest neutralino, which is the long-lived particle and decays via an RPV coupling, either λ_{121} or λ_{122}, to two charged leptons and a neutrino. No events were observed in the signal region of the Run-1 search. Figure 5.52 shows the upper limits on the gluino pair production cross-section set by the Run-1 search.

The main difference between the Run-1 and Run-2 signal models is that the gluino in the Run-1 model decays into three particles and the squark in the Run-2 model into two. When considering the same masses, the neutralino has on average a higher kinetic energy in the Run-2 model, since it receives a larger fraction of the mass difference between it and the next-to-lightest supersymmetric particle (NLSP) as kinetic energy. The kinematic properties of the lepton pair from a neutralino decay are similar in both models if the kinetic energy of the neutralino is small compared to its mass, i.e. if the NLSP-neutralino mass difference is small and the neutralino is massive. Thus, the cross-section limits of both searches are compared under this assumption. Figure 5.53 shows the upper limits for the signal MC sample of each search where the sparticle masses are largest. For most neutralino lifetimes, the limits of the Run-2 search are significantly better, mostly due to the 62% higher integrated luminosity. This is particularly the case for low lifetimes, which is caused by the factor of two smaller displacement cut of the Run-2 search. The improvement is higher for neutralino decays mediated by a λ_{122} coupling, since the Run-2 search does not apply the material veto to $\mu\mu$ vertices, while the Run-1 search did. Only for $c\tau$ values larger than 4 m, the Run-2 limits become worse than the Run-1 limits.

The Run-2 search significantly benefits from the increased production cross-sections of squarks and gluinos due to the higher centre-of-mass energy of 13 TeV. The cross-section for the production of a 1.6 TeV squark-antisquark pair at $\sqrt{s}$ = 13 TeV is more than 50 times larger than at $\sqrt{s}$ = 8 TeV. Thus, the Run-1 search is not at all sensitive to a 1.6 TeV squark, while the Run-2 search excludes more than two orders of magnitude in neutralino lifetime for such a squark if the neutralino mass is 1.3 TeV.

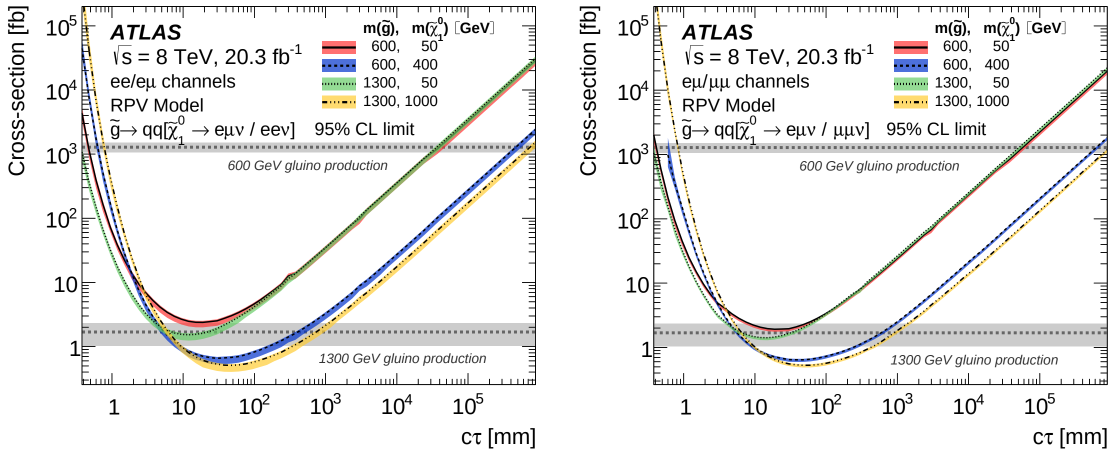

(a) λ_{121} **(b)** λ_{122}

Figure 5.52: Observed upper limits at 95% confidence level (CL) of the Run-1 search on the gluino pair production cross-section as a function of the $\tilde{\chi}_1^0$ lifetime ($c\tau$) for four combinations of gluino and neutralino masses and $\tilde{\chi}_1^0$ decays mediated by (a) a λ_{121} or (b) a λ_{122} coupling [84]. The shaded bands around the observed limits indicate the $\pm 1\sigma$ variations in the expected limit, while the horizontal bands show the expected cross-sections and their uncertainties.

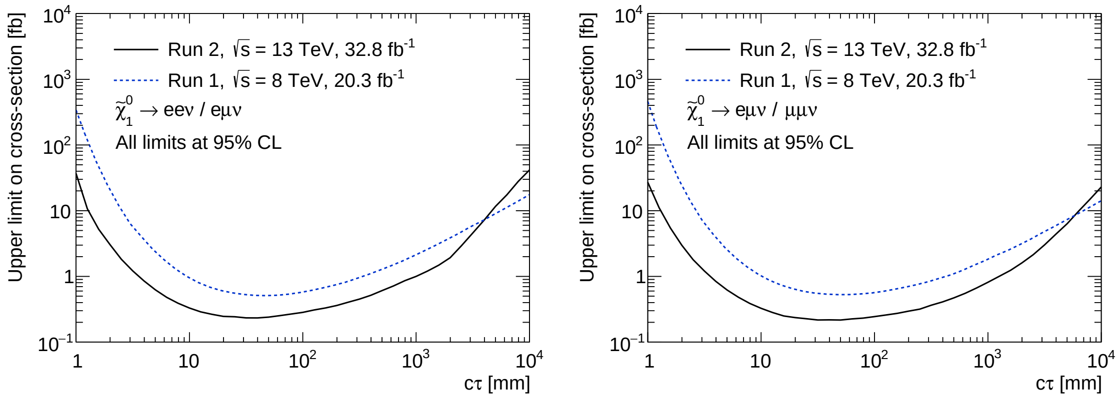

(a) λ_{121} **(b)** λ_{122}

Figure 5.53: Comparison of the observed upper limits at 95% confidence level between the Run-1 and the Run-2 search for $\tilde{\chi}_1^0$ decays mediated by (a) a λ_{121} or (b) a λ_{122} coupling. The Run-1 limits for $m(\tilde{g}) = 1.3$ TeV and $m(\tilde{\chi}_1^0) = 1.0$ TeV are shown and the Run-2 limits for $m(\tilde{q}) = 1.6$ TeV and $m(\tilde{\chi}_1^0) = 1.3$ TeV.

Chapter 6

Summary

In this thesis, a search for new long-lived particles with masses larger than 12 GeV decaying into oppositely charged ee, $e\mu$ or $\mu\mu$ pairs is presented. The search is based on data of proton–proton collisions at a centre-of-mass energy of 13 TeV collected by the ATLAS experiment at the Large Hadron Collider in 2016, corresponding to an integrated luminosity of 32.8 fb^{-1}. The lepton pairs are required to form a common vertex within the ATLAS inner detector, which is displaced from the primary collision vertex.

To improve the sensitivity to decays of long-lived particles, two dedicated algorithms have been developed. The first is an additional track reconstruction algorithm, which runs after the standard ATLAS track reconstruction on unused measurements of the tracking detectors and reconstructs tracks with large impact parameters. The second reconstructs displaced vertices from tracks of both tracking algorithms. As these algorithms are CPU-intensive and significantly increase the storage size of a recorded collision event, they could only be run on a preselected subset of the data. The events are preselected based on two photon triggers, which are sensitive to calorimeter deposits of electrons, and a muon trigger using only information from the muon spectrometer. These triggers do not require the leptons to be produced close to the primary collision vertex, and are therefore very efficient for displaced leptons. They have high p_{T} thresholds of 50 to 140 GeV, leading to a high p_{T} of at least one of the two leptons of a displaced dilepton vertex.

Since the Standard Model does not predict massive, long-lived particles decaying into leptons, the background is very small and dominated by cosmic-ray muons that are reconstructed as displaced vertices of back-to-back dimuons. A dedicated veto is used to reject back-to-back lepton pairs, resulting in a background expectation of 0.27 ± 0.17 events from pp collision data. Other backgrounds, such as random crossings of leptons, were found to be negligible.

No events with displaced dilepton vertices have been observed, which is in agreement with the background expectation. The result is interpreted in a simplified supersymmetric model where the lightest neutralino, produced via squark-antisquark production, decays via an R-parity violating coupling, either λ_{121} or λ_{122}, to $\ell^+\ell'^-\nu$ ($\ell = e, \mu$). For both couplings, the $\tilde{\chi}_1^0$ decays to two final states with equal branching ratio of 50%, namely $ee\nu$ and $e\mu\nu$ for λ_{121}, and $e\mu\nu$ and $\mu\mu\nu$ for λ_{122}. Upper limits on the production cross-section have been derived for specific squark and neutralino masses and for neutralino lifetimes ($c\tau$) between 1 mm and 10 m. For a 700 GeV squark and neutralino masses between 50 and 500 GeV, neutralino lifetimes between 1 mm and 6 m are excluded at 95% confidence level. If the squark mass is 1.6 TeV and the neutralino mass is 1.3 TeV, the excluded $c\tau$ range is 3 mm to 1 m. For a 50 GeV neutralino, no lifetime can be constrained for the λ_{121} decay, while lifetimes between 4 and 30 mm are excluded for the λ_{122} decay.

The search is the successor of an ATLAS search for displaced dilepton vertices at $\sqrt{s} = 8$ TeV [84, 85] and features a substantially improved sensitivity to masses of supersymmetic particles larger than 1 TeV, since the cross-sections of the production processes are significantly enhanced by the larger $\sqrt{s}$ of 13 TeV and the integrated luminosity is 62% larger. The relaxation of certain selection criteria has further improved sensitivity. The displacement cut has been reduced by a factor of two leading to higher signal efficiencies for long-lived particles with lifetimes of a few mm. The sensitivity to $\mu\mu$ vertices has been greatly improved by selecting them not only in material-free regions, but also in material-rich regions.

Appendix A

Closure test of the lifetime reweighting

The lifetime reweighting discussed in Section 5.3.2 allows to study the signal efficiencies as a continuous function of the neutralino lifetime in the range of 1 mm to 10 m. To verify that the efficiencies obtained from this procedure are valid, they are compared to the efficiencies calculated without the lifetime reweighting for the five simulated lifetimes. This closure test is performed only for the reco-level efficiencies as they are used to derive the limits presented in Section 5.7. Figures A.1 to A.5 show that there is a good agreement within the uncertainties in most cases, meaning that the reweighting procedure works well both for vertex-level and event-level efficiencies.

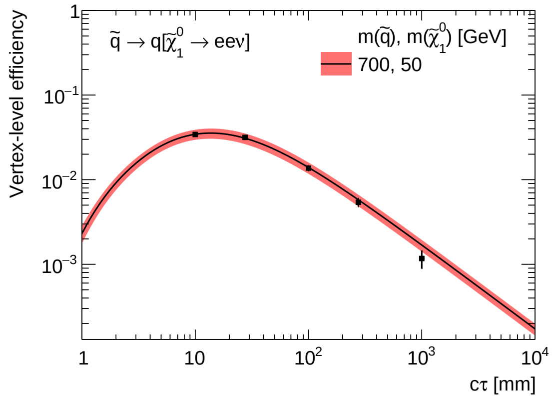

(a) $m(\tilde{q}) = 700\,\text{GeV}$, $m(\tilde{\chi}_1^0) = 50\,\text{GeV}$

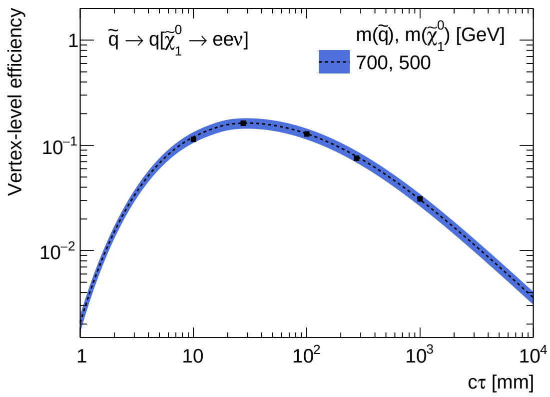

(b) $m(\tilde{q}) = 700\,\text{GeV}$, $m(\tilde{\chi}_1^0) = 500\,\text{GeV}$

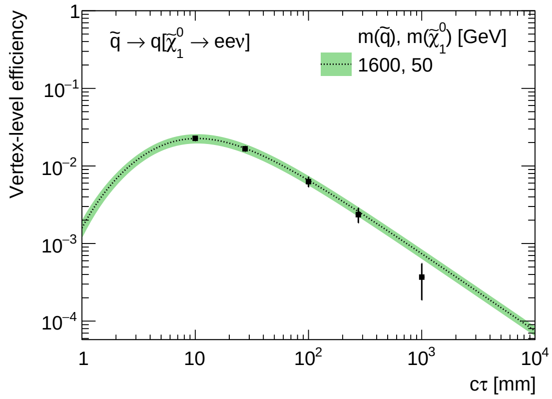

(c) $m(\tilde{q}) = 1.6\,\text{TeV}$, $m(\tilde{\chi}_1^0) = 50\,\text{GeV}$

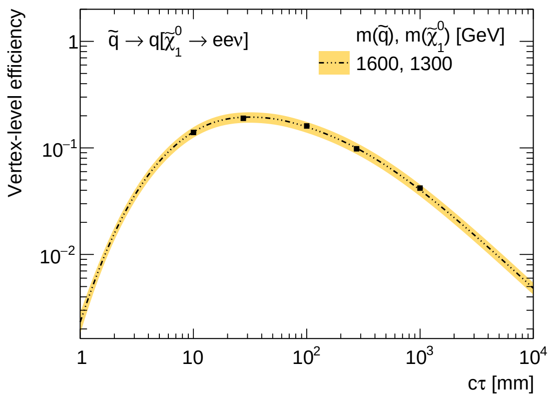

(d) $m(\tilde{q}) = 1.6\,\text{TeV}$, $m(\tilde{\chi}_1^0) = 1.3\,\text{TeV}$

Figure A.1: Vertex-level efficiencies at the reco-level obtained with the lifetime reweighting for $\tilde{\chi}_1^0$ decays to $e^+e^-\nu$ and four combinations of squark and neutralino masses. The squares show the efficiencies calculated without the lifetime reweighting for each of the five simulated lifetimes.

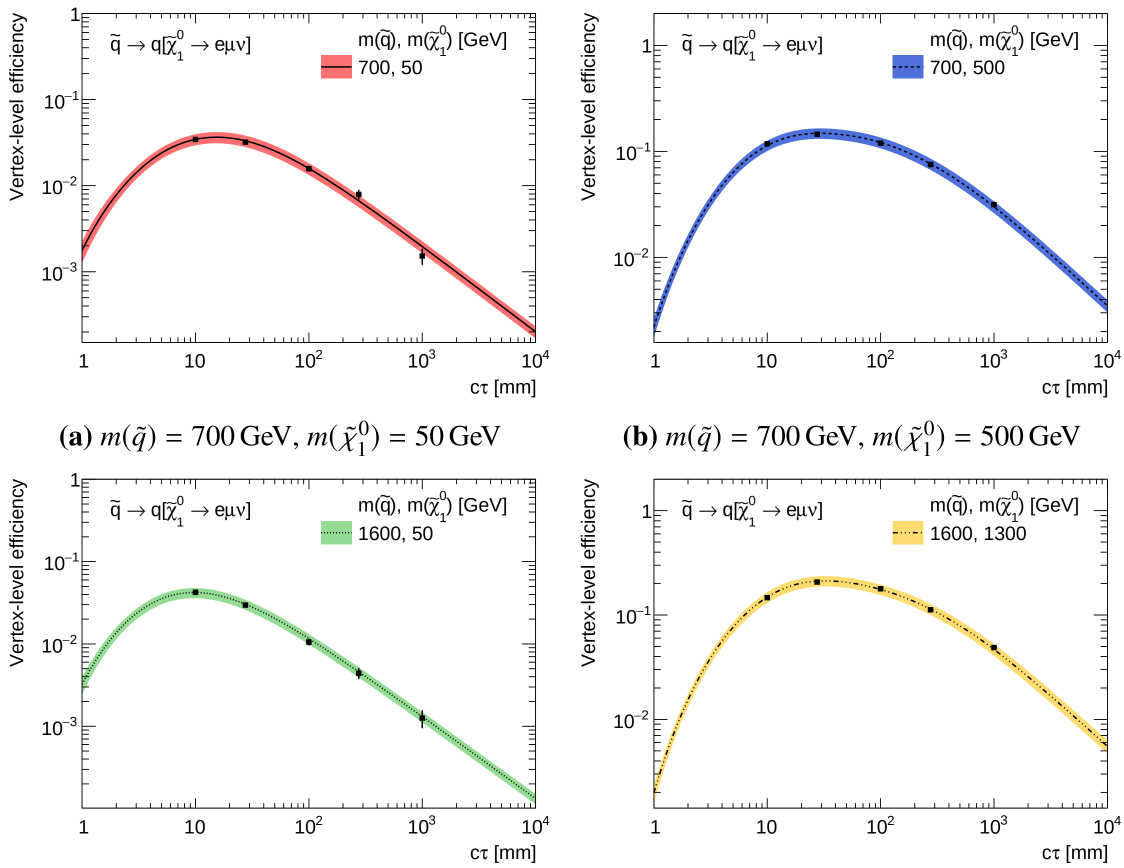

(a) $m(\tilde{q})$ = 700 GeV, $m(\tilde{\chi}_1^0)$ = 50 GeV

(b) $m(\tilde{q})$ = 700 GeV, $m(\tilde{\chi}_1^0)$ = 500 GeV

(c) $m(\tilde{q})$ = 1.6 TeV, $m(\tilde{\chi}_1^0)$ = 50 GeV

(d) $m(\tilde{q})$ = 1.6 TeV, $m(\tilde{\chi}_1^0)$ = 1.3 TeV

Figure A.2: Vertex-level efficiencies at the reco-level obtained with the lifetime reweighting for $\tilde{\chi}_1^0$ decays to $e^{\pm}\mu^{\mp}\nu$ and four combinations of squark and neutralino masses. The squares show the efficiencies calculated without the lifetime reweighting for each of the five simulated lifetimes.

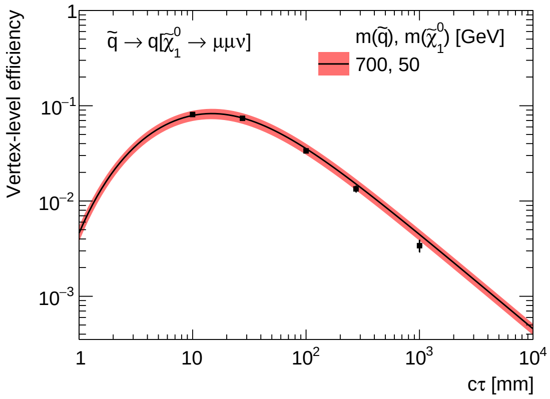

(a) $m(\tilde{q}) = 700\,\text{GeV}$, $m(\tilde{\chi}_1^0) = 50\,\text{GeV}$

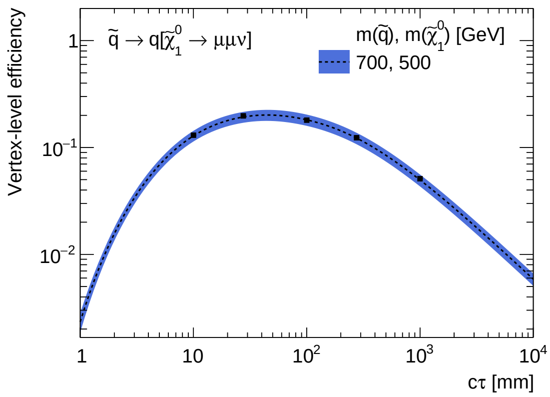

(b) $m(\tilde{q}) = 700\,\text{GeV}$, $m(\tilde{\chi}_1^0) = 500\,\text{GeV}$

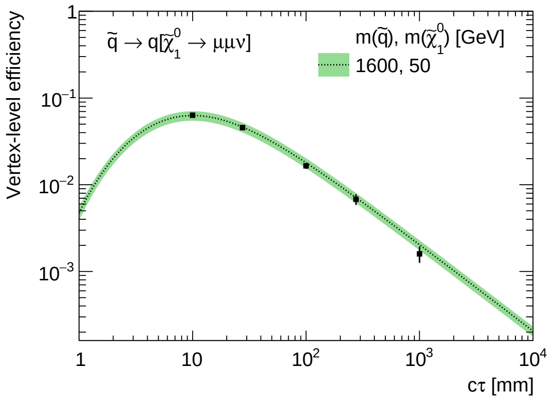

(c) $m(\tilde{q}) = 1.6\,\text{TeV}$, $m(\tilde{\chi}_1^0) = 50\,\text{GeV}$

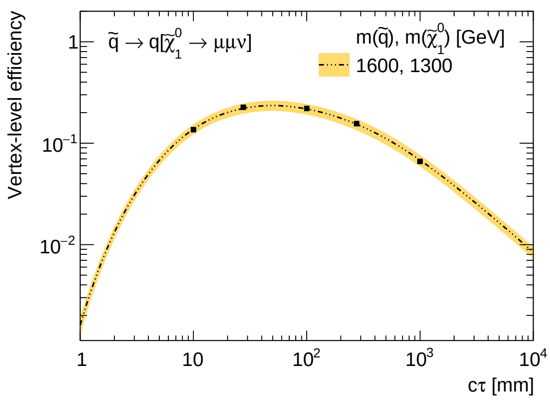

(d) $m(\tilde{q}) = 1.6\,\text{TeV}$, $m(\tilde{\chi}_1^0) = 1.3\,\text{TeV}$

Figure A.3: Vertex-level efficiencies at the reco-level obtained with the lifetime reweighting for $\tilde{\chi}_1^0$ decays to $\mu^+\mu^-\nu$ and four combinations of squark and neutralino masses. The squares show the efficiencies calculated without the lifetime reweighting for each of the five simulated lifetimes.

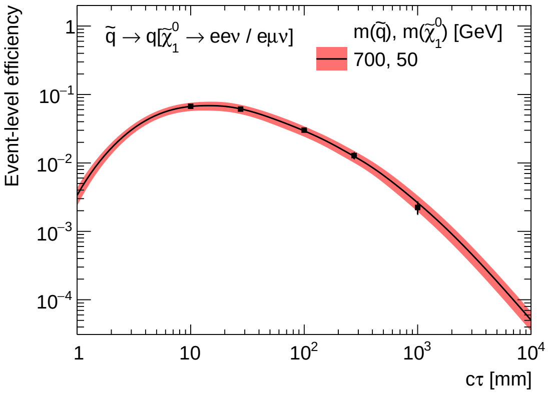

(a) $m(\tilde{q})$ = 700 GeV, $m(\tilde{\chi}_1^0)$ = 50 GeV

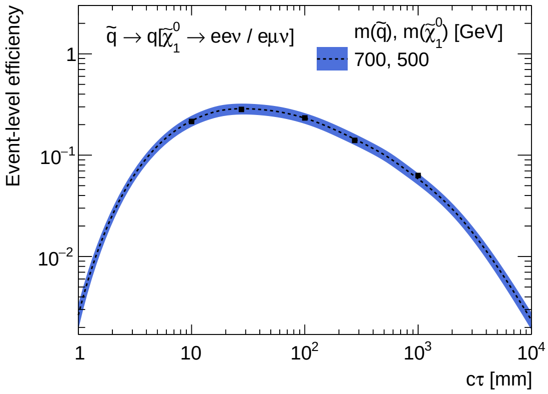

(b) $m(\tilde{q})$ = 700 GeV, $m(\tilde{\chi}_1^0)$ = 500 GeV

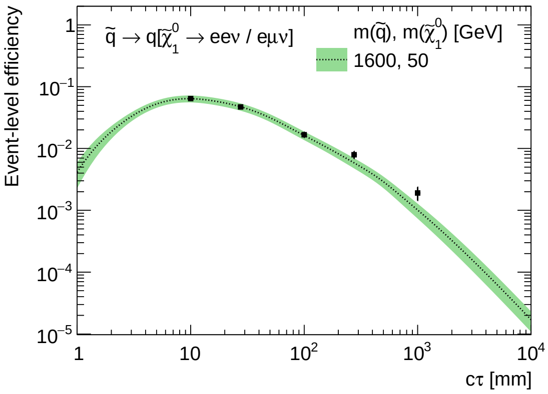

(c) $m(\tilde{q})$ = 1.6 TeV, $m(\tilde{\chi}_1^0)$ = 50 GeV

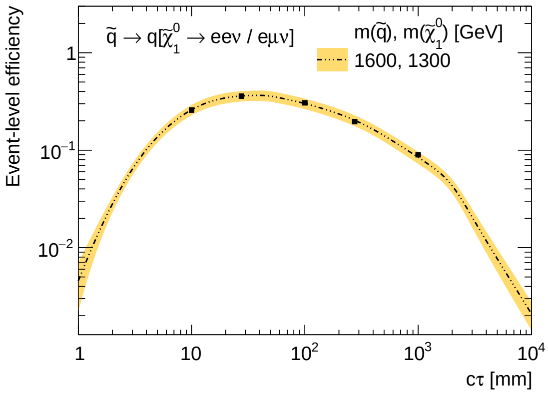

(d) $m(\tilde{q})$ = 1.6 TeV, $m(\tilde{\chi}_1^0)$ = 1.3 TeV

Figure A.4: Event-level efficiencies at the reco-level obtained with the lifetime reweighting for $\tilde{\chi}_1^0$ decays mediated by a λ_{121} coupling and four combinations of squark and neutralino masses. The squares show the efficiencies calculated without the lifetime reweighting for each of the five simulated lifetimes.

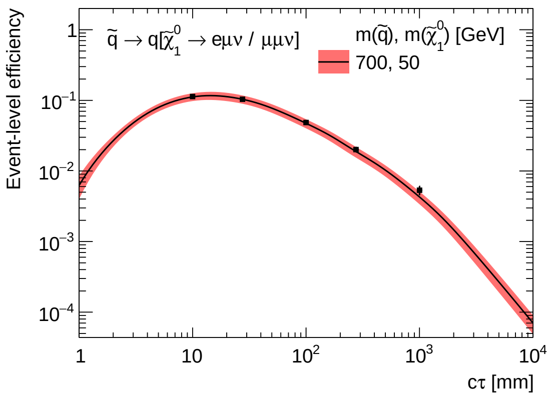

(a) $m(\tilde{q})$ = 700 GeV, $m(\tilde{\chi}_1^0)$ = 50 GeV

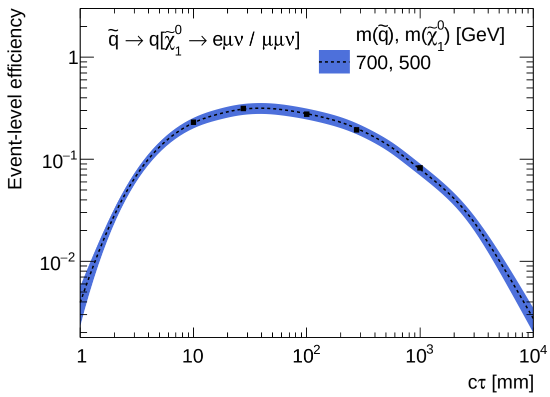

(b) $m(\tilde{q})$ = 700 GeV, $m(\tilde{\chi}_1^0)$ = 500 GeV

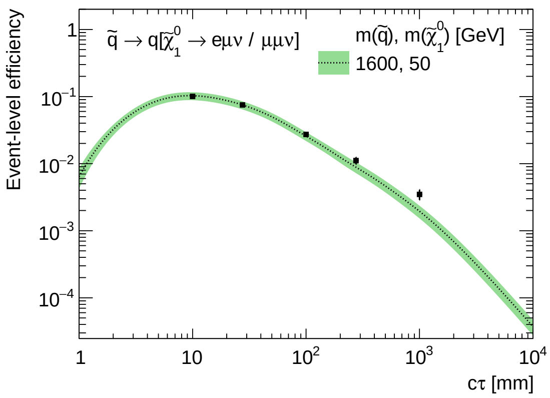

(c) $m(\tilde{q})$ = 1.6 TeV, $m(\tilde{\chi}_1^0)$ = 50 GeV

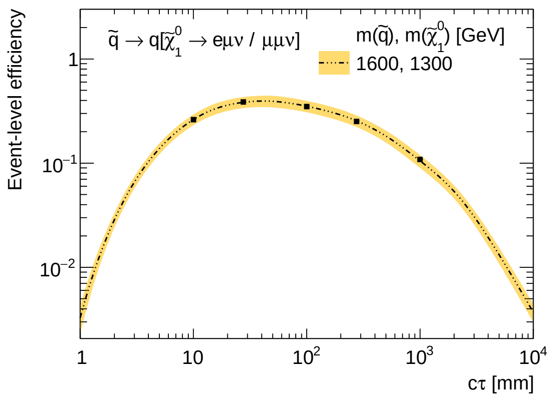

(d) $m(\tilde{q})$ = 1.6 TeV, $m(\tilde{\chi}_1^0)$ = 1300 GeV

Figure A.5: Event-level efficiencies at the reco-level obtained with the lifetime reweighting for $\tilde{\chi}_1^0$ decays mediated by a λ_{122} coupling and four combinations of squark and neutralino masses. The squares show the efficiencies calculated without the lifetime reweighting for each of the five simulated lifetimes.

Appendix B

Uncertainties on the signal efficiencies

In Section 5.5 three systematic uncertainties in the reco-level signal efficiencies have been discussed, namely an uncertainty in the measured trigger scale factors, another one from reweighting the events to obtain the pileup distribution observed in the data, and finally a flat uncertainty of 10% in the tracking and vertex reconstruction efficiencies. In addition, there is also a statistical uncertainty due to the limited number of simulated events.

Figures B.1 to B.5 show the relative sizes of these uncertainties and the total uncertainty. The total uncertainty on the vertex-level efficiencies is usually 12 to 16%, except for very short lifetimes of less than 3 mm, where it can be as large as 28% due to an increased statistical uncertainty. The uncertainty on the reconstruction efficiencies is usually the largest component, in some cases the statistical uncertainty or the pileup uncertainty are similar or even slightly larger. The general trends are similar for the event-level efficiencies except that the statistical uncertainties are significantly enhanced at short and long lifetimes, and thus the total uncertainty can become as large as 52%.

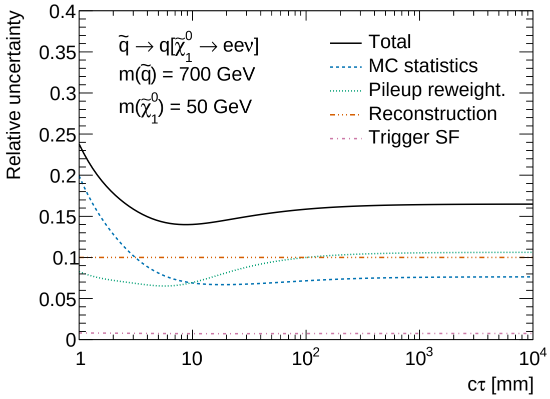

(a) $m(\tilde{q}) = 700\,\text{GeV}$, $m(\tilde{\chi}_1^0) = 50\,\text{GeV}$

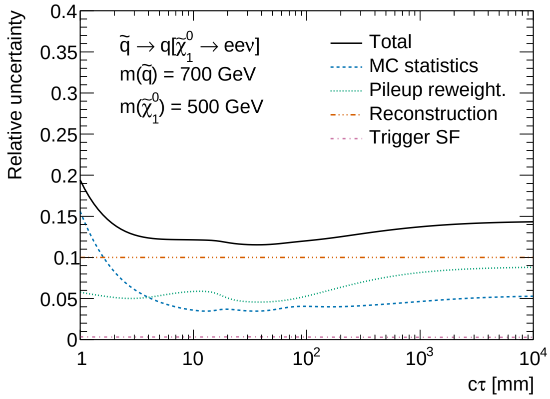

(b) $m(\tilde{q}) = 700\,\text{GeV}$, $m(\tilde{\chi}_1^0) = 500\,\text{GeV}$

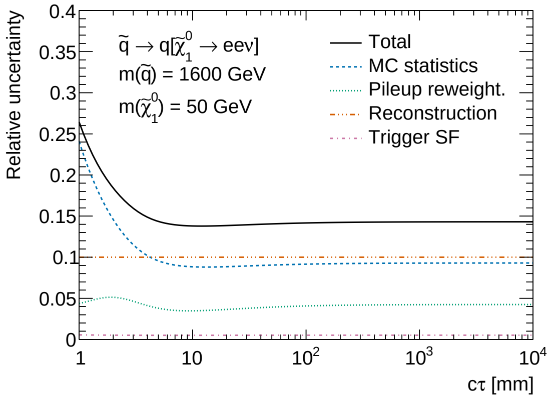

(c) $m(\tilde{q}) = 1.6\,\text{TeV}$, $m(\tilde{\chi}_1^0) = 50\,\text{GeV}$

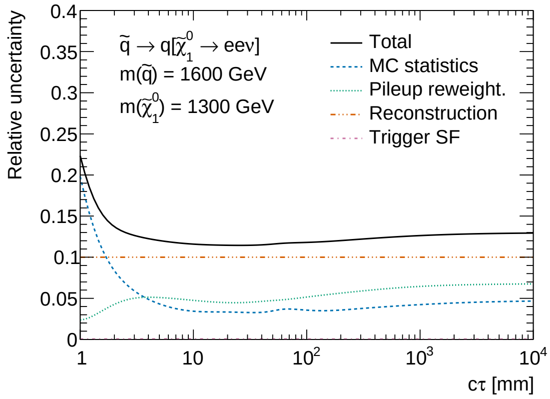

(d) $m(\tilde{q}) = 1.6\,\text{TeV}$, $m(\tilde{\chi}_1^0) = 1.3\,\text{TeV}$

Figure B.1: Relative sizes of the four uncertainties and the total uncertainty in the vertex-level efficiencies at the reco-level as a function of the $\tilde{\chi}_1^0$ lifetime for $\tilde{\chi}_1^0$ decays to $e^+e^-\nu$ and four combinations of squark and neutralino masses.

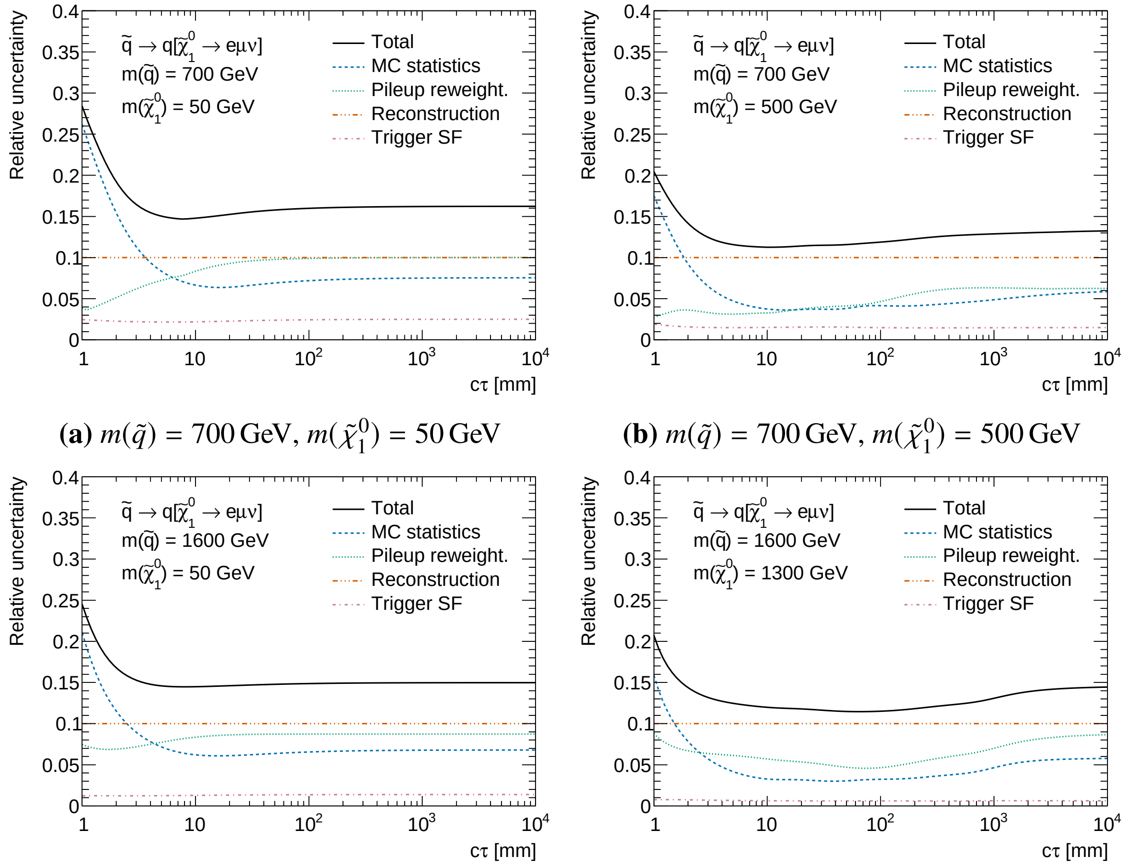

(a) $m(\tilde{q})$ = 700 GeV, $m(\tilde{\chi}_1^0)$ = 50 GeV

(b) $m(\tilde{q})$ = 700 GeV, $m(\tilde{\chi}_1^0)$ = 500 GeV

(c) $m(\tilde{q})$ = 1.6 TeV, $m(\tilde{\chi}_1^0)$ = 50 GeV

(d) $m(\tilde{q})$ = 1.6 TeV, $m(\tilde{\chi}_1^0)$ = 1.3 TeV

Figure B.2: Relative sizes of the four uncertainties and the total uncertainty in the vertex-level efficiencies at the reco-level as a function of the $\tilde{\chi}_1^0$ lifetime for $\tilde{\chi}_1^0$ decays to $e^{\pm}\mu^{\mp}\nu$ and four combinations of squark and neutralino masses.

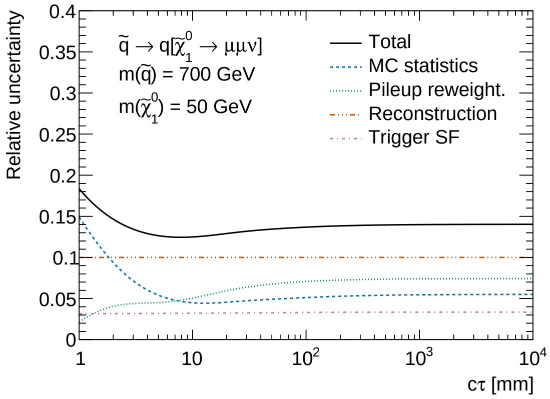

(a) $m(\tilde{q}) = 700\,\mathrm{GeV}$, $m(\tilde{\chi}_1^0) = 50\,\mathrm{GeV}$

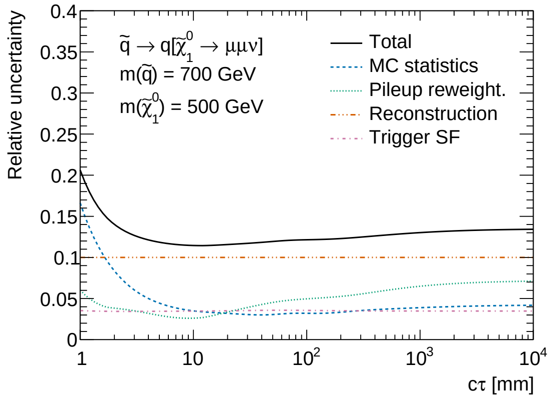

(b) $m(\tilde{q}) = 700\,\mathrm{GeV}$, $m(\tilde{\chi}_1^0) = 500\,\mathrm{GeV}$

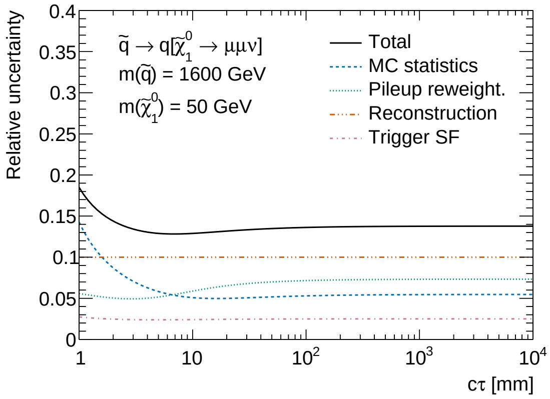

(c) $m(\tilde{q}) = 1.6\,\mathrm{TeV}$, $m(\tilde{\chi}_1^0) = 50\,\mathrm{GeV}$

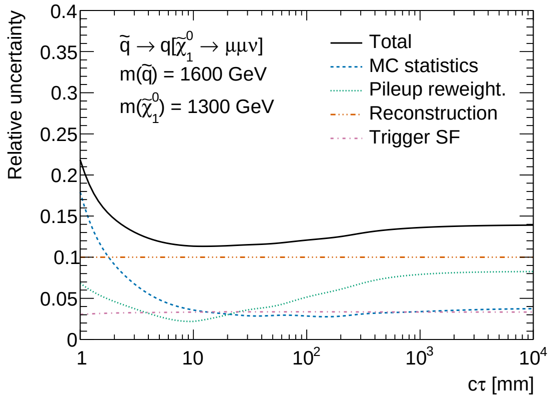

(d) $m(\tilde{q}) = 1.6\,\mathrm{TeV}$, $m(\tilde{\chi}_1^0) = 1.3\,\mathrm{TeV}$

Figure B.3: Relative sizes of the four uncertainties and the total uncertainty in the vertex-level efficiencies at the reco-level as a function of the $\tilde{\chi}_1^0$ lifetime for $\tilde{\chi}_1^0$ decays to $\mu^+\mu^-\nu$ and four combinations of squark and neutralino masses.

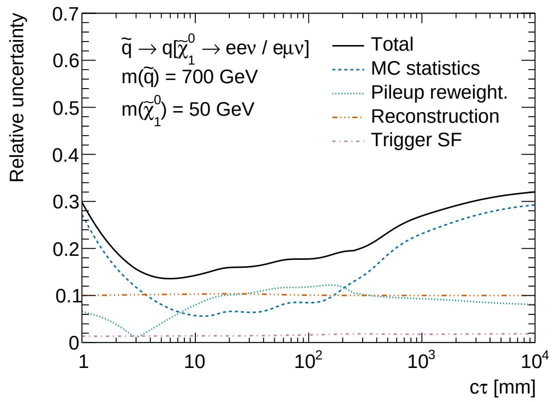

(a) $m(\tilde{q})$ = 700 GeV, $m(\tilde{\chi}_1^0)$ = 50 GeV

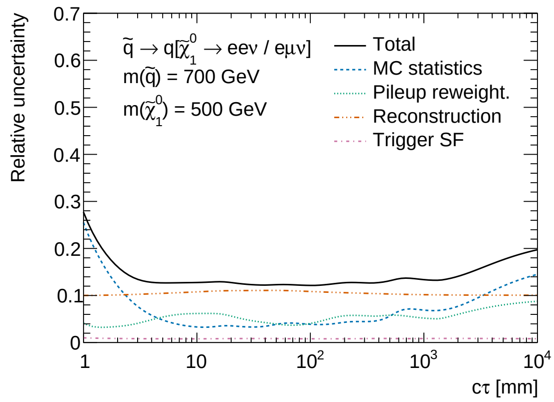

(b) $m(\tilde{q})$ = 700 GeV, $m(\tilde{\chi}_1^0)$ = 500 GeV

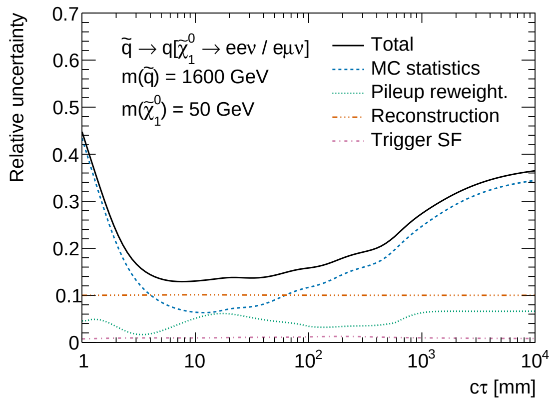

(c) $m(\tilde{q})$ = 1.6 TeV, $m(\tilde{\chi}_1^0)$ = 50 GeV

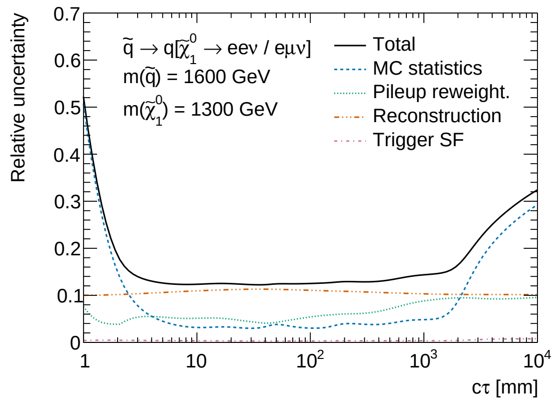

(d) $m(\tilde{q})$ = 1.6 TeV, $m(\tilde{\chi}_1^0)$ = 1.3 TeV

Figure B.4: Relative sizes of the four uncertainties and the total uncertainty in the event-level efficiencies at the reco-level as a function of the $\tilde{\chi}_1^0$ lifetime for $\tilde{\chi}_1^0$ decays mediated by a λ_{121} coupling and four combinations of squark and neutralino masses.

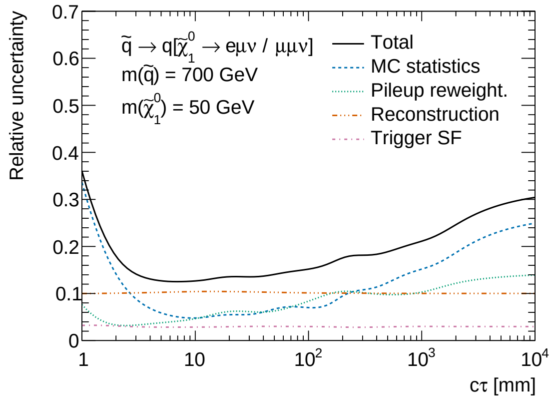

(a) $m(\tilde{q}) = 700\,\mathrm{GeV}$, $m(\tilde{\chi}_1^0) = 50\,\mathrm{GeV}$

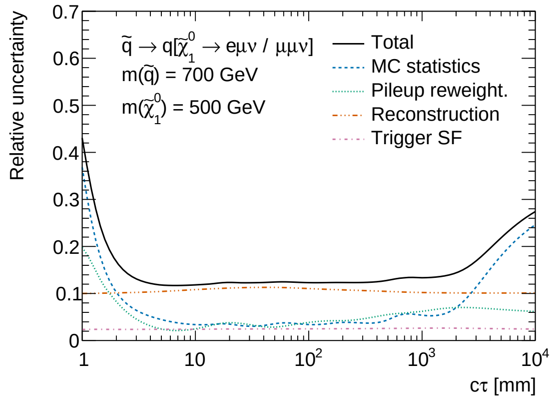

(b) $m(\tilde{q}) = 700\,\mathrm{GeV}$, $m(\tilde{\chi}_1^0) = 500\,\mathrm{GeV}$

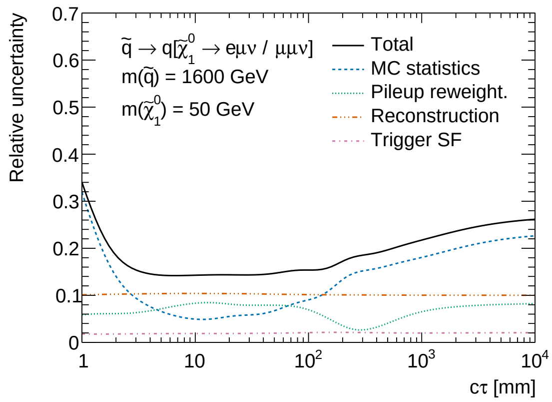

(c) $m(\tilde{q}) = 1.6\,\mathrm{TeV}$, $m(\tilde{\chi}_1^0) = 50\,\mathrm{GeV}$

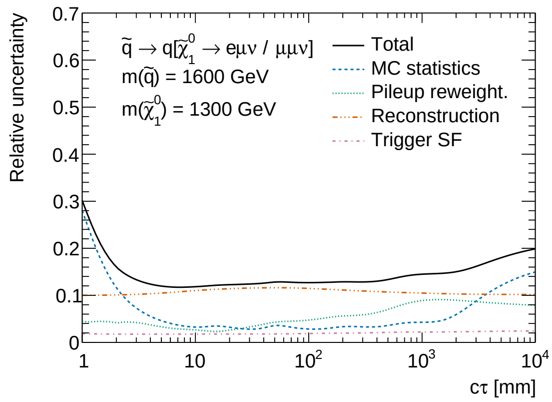

(d) $m(\tilde{q}) = 1.6\,\mathrm{TeV}$, $m(\tilde{\chi}_1^0) = 1300\,\mathrm{GeV}$

Figure B.5: Relative sizes of the four uncertainties and the total uncertainty in the event-level efficiencies at the reco-level as a function of the $\tilde{\chi}_1^0$ lifetime for $\tilde{\chi}_1^0$ decays mediated by a λ_{122} coupling and four combinations of squark and neutralino masses.

Bibliography

[1] ATLAS Collaboration, *Observation of a new particle in the search for the Standard Model Higgs boson with the ATLAS detector at the LHC*, Phys. Lett. B **716** (2012) 1, arXiv: `1207.7214 [hep-ex]`.

[2] CMS Collaboration, *Observation of a new boson at a mass of 125 GeV with the CMS experiment at the LHC*, Phys. Lett. B **716** (2012) 30, arXiv: `1207.7235 [hep-ex]`.

[3] Planck Collaboration, *Planck 2018 results. VI. Cosmological parameters*, Submitted to A&A (2018), arXiv: `1807.06209 [astro-ph.CO]`.

[4] W. Hollik, *Quantum field theory and the Standard Model*, Lectures given at the 17th European School of High-Energy Physics, Bautzen, Germany (2009), arXiv: `1012.3883 [hep-ph]`.

[5] S. Weinberg, *The making of the Standard Model*, Eur. Phys. J. C **34** (2004) 5, arXiv: `hep-ph/0401010 [hep-ph]`.

[6] S. L. Glashow, *Partial symmetries of weak interactions*, Nucl. Phys. **22** (1961) 579.

[7] S. Weinberg, *A model of leptons*, Phys. Rev. Lett. **19** (1967) 1264.

[8] A. Salam, *Weak and electromagnetic interactions*, Proceedings of the 8th Nobel Symposium, Lerum, Sweden (1968) 367.

[9] H. Fritzsch and M. Gell-Mann, *Current algebra: Quarks and what else?*, Proceedings of the 16th International Conference on High-Energy Physics, Batavia, Illinois (1972) 135, arXiv: `hep-ph/0208010 [hep-ph]`.

[10] H. Fritzsch, M. Gell-Mann, and H. Leutwyler, *Advantages of the color octet gluon picture*, Phys. Lett. B **47** (1973) 365.

[11] A. Einstein, *Die Grundlage der allgemeinen Relativitätstheorie*, Ann. Phys. **354** (1916) 769.

[12] K. G. Wilson, *Confinement of quarks*, Phys. Rev. D **10** (1974) 2445.

[13] D. J. Gross and F. Wilczek, *Ultraviolet behavior of non-abelian gauge theories*, Phys. Rev. Lett. **30** (1973) 1343.

[14] H. D. Politzer, *Reliable perturbative results for strong interactions?*, Phys. Rev. Lett. **30** (1973) 1346.

[15] T. Nakano and K. Nishijima, *Charge independence for V-particles*, Prog. Theor. Phys. **10** (1953) 581.

[16] K. Nishijima, *Charge independence theory of V-particles*, Prog. Theor. Phys. **13** (1955) 285.

[17] M. Gell-Mann, *The interpretation of the new particles as displaced charge multiplets*, Nuovo Cim. **4** (1956) 848.

[18] G. Bellini, L. Ludhova, G. Ranucci, and F. L. Villante, *Neutrino oscillations*, Adv. High Energy Phys. **2014** (2014) 191960, arXiv: `1310.7858 [hep-ph]`.

[19] M. Drewes, *The phenomenology of right-handed neutrinos*, Int. J. Mod. Phys. E **22** (2013) 1330019, arXiv: `1303.6912 [hep-ph]`.

[20] F. Englert and R. Brout, *Broken symmetry and the mass of gauge vector mesons*, Phys. Rev. Lett. **13** (1964) 321.

[21] P. W. Higgs, *Broken symmetries and the masses of gauge bosons*, Phys. Rev. Lett. **13** (1964) 508.

[22] G. S. Guralnik, C. R. Hagen, and T. W. B. Kibble, *Global conservation laws and massless particles*, Phys. Rev. Lett. **13** (1964) 585.

[23] MuLan Collaboration, *Improved measurement of the positive muon lifetime and determination of the Fermi constant*, Phys. Rev. Lett. **99** (2007) 032001, arXiv: `0704.1981 [hep-ex]`.

[24] S. Weinberg, *Physical processes in a convergent theory of the weak and electromagnetic interactions*, Phys. Rev. Lett. **27** (1971) 1688.

[25] S. Weinberg, *General theory of broken local symmetries*, Phys. Rev. D **7** (1973) 1068.

[26] ATLAS and CMS Collaborations, *Combined measurement of the Higgs boson mass in pp collisions at $\sqrt{s} = 7$ and 8 TeV with the ATLAS and CMS experiments*, Phys. Rev. Lett. **114** (2015) 191803, arXiv: 1503.07589 [hep-ex].

[27] M. Kobayashi and T. Maskawa, *CP violation in the renormalizable theory of weak interaction*, Prog. Theor. Phys. **49** (1973) 652.

[28] N. Sakai, *Naturalness in supersymmetric GUTs*, Z. Phys. C **11** (1981) 153.

[29] S. Dimopoulos, S. Raby, and F. Wilczek, *Supersymmetry and the scale of unification*, Phys. Rev. D **24** (1981) 1681.

[30] L. E. Ibanez and G. G. Ross, *Low-energy predictions in supersymmetric Grand Unified Theories*, Phys. Lett. B **105** (1981) 439.

[31] S. Dimopoulos and H. Georgi, *Softly broken supersymmetry and SU(5)*, Nucl. Phys. B **193** (1981) 150.

[32] Gfitter Group, *The global electroweak fit at NNLO and prospects for the LHC and ILC*, Eur. Phys. J. C **74** (2014) 3046, arXiv: 1407.3792 [hep-ph].

[33] K. Garrett and G. Duda, *Dark matter: A primer*, Adv. Astron. **2011** (2011) 968283, arXiv: 1006.2483 [hep-ph].

[34] L. Canetti, M. Drewes, and M. Shaposhnikov, *Matter and antimatter in the universe*, New J. Phys. **14** (2012) 095012, arXiv: 1204.4186 [hep-ph].

[35] Yu. A. Golfand and E. P. Likhtman, *Extension of the algebra of Poincaré group generators and violation of p invariance*, JETP Lett. **13** (1971) 323, [Pisma Zh. Eksp. Teor. Fiz. **13** (1971) 452].

[36] D. V. Volkov and V. P. Akulov, *Is the neutrino a Goldstone particle?*, Phys. Lett. B **46** (1973) 109.

[37] J. Wess and B. Zumino, *Supergauge transformations in four-dimensions*, Nucl. Phys. B **70** (1974) 39.

[38] J. Wess and B. Zumino,
Supergauge invariant extension of quantum electrodynamics,
Nucl. Phys. B **78** (1974) 1.

[39] S. Ferrara and B. Zumino, *Supergauge invariant Yang-Mills theories*,
Nucl. Phys. B **79** (1974) 413.

[40] A. Salam and J. A. Strathdee, *Supersymmetry and non-abelian gauges*,
Phys. Lett. B **51** (1974) 353.

[41] S. P. Martin, *A supersymmetry primer*,
Adv. Ser. Direct. High Energy Phys. **18** (1998) 1, arXiv: `hep-ph/9709356`.

[42] R. Haag, J. T. Lopuszanski, and M. Sohnius,
All possible generators of supersymmetries of the S-matrix,
Nucl. Phys. B **88** (1975) 257.

[43] P. Fayet, *Supersymmetry and weak, electromagnetic and strong interactions*,
Phys. Lett. B **64** (1976) 159.

[44] P. Fayet, *Spontaneously broken supersymmetric theories of weak, electromagnetic and strong interactions*, Phys. Lett. B **69** (1977) 489.

[45] L. Girardello and M. T. Grisaru, *Soft breaking of supersymmetry*,
Nucl. Phys. B **194** (1982) 65.

[46] R. Barbieri and G. F. Giudice, *Upper bounds on supersymmetric particle masses*,
Nucl. Phys. B **306** (1988) 63.

[47] B. de Carlos and J. A. Casas, *One loop analysis of the electroweak breaking in supersymmetric models and the fine tuning problem*, Phys. Lett. B **309** (1993) 320,
arXiv: `hep-ph/9303291`.

[48] S. Dimopoulos and D. W. Sutter, *The supersymmetric flavor problem*,
Nucl. Phys. B **452** (1995) 496, arXiv: `hep-ph/9504415 [hep-ph]`.

[49] Super-Kamiokande Collaboration,
Search for proton decay via $p \to e^+\pi^0$ and $p \to \mu^+\pi^0$ in 0.31 megaton·years exposure of the Super-Kamiokande water Cherenkov detector,
Phys. Rev. D **95** (2017) 012004, arXiv: `1610.03597 [hep-ex]`.

[50] Particle Data Group, *Review of particle physics*, Phys. Rev. D **98** (2018) 030001.

[51] G. R. Farrar and P. Fayet, *Phenomenology of the production, decay, and detection of new hadronic states associated with supersymmetry*, Phys. Lett. B **76** (1978) 575.

[52] H. Goldberg, *Constraint on the photino mass from cosmology*, Phys. Rev. Lett. **50** (1983) 1419, Erratum: Phys. Rev. Lett. **103** (2009) 099905.

[53] J. R. Ellis, J. S. Hagelin, D. V. Nanopoulos, K. A. Olive, and M. Srednicki, *Supersymmetric relics from the Big Bang*, Nucl. Phys. B **238** (1984) 453.

[54] T. Falk, K. A. Olive, and M. Srednicki, *Heavy sneutrinos as dark matter*, Phys. Lett. B **339** (1994) 248, arXiv: `hep-ph/9409270 [hep-ph]`.

[55] L. E. Ibanez and G. G. Ross, *Discrete gauge symmetry anomalies*, Phys. Lett. B **260** (1991) 291.

[56] L. E. Ibanez and G. G. Ross, *Discrete gauge symmetries and the origin of baryon and lepton number conservation in supersymmetric versions of the Standard Model*, Nucl. Phys. B **368** (1992) 3.

[57] R. Barbier et al., *R-parity violating supersymmetry*, Phys. Rept. **420** (2005) 1, arXiv: `hep-ph/0406039 [hep-ph]`.

[58] D. Dercks, H. Dreiner, M. E. Krauss, T. Opferkuch, and A. Reinert, *R-parity violation at the LHC*, Eur. Phys. J. C **77** (2017) 856, arXiv: `1706.09418 [hep-ph]`.

[59] L. Evans and P. Bryant, *LHC machine*, JINST **3** (2008) S08001.

[60] ATLAS Collaboration, *The ATLAS experiment at the CERN Large Hadron Collider*, JINST **3** (2008) S08003.

[61] CERN.

[62] ATLAS Collaboration, *Luminosity determination in pp collisions at $\sqrt{s} = 8$ TeV using the ATLAS detector at the LHC*, Eur. Phys. J. C **76** (2016) 653, arXiv: `1608.03953 [hep-ex]`.

[63] G. Avoni et al., *The new LUCID-2 detector for luminosity measurement and monitoring in ATLAS*, JINST **13** (2018) P07017.

[64] ATLAS Collaboration.

[65] ATLAS Collaboration, *The ATLAS simulation infrastructure*, Eur. Phys. J. C **70** (2010) 823, arXiv: `1005.4568 [physics.ins-det]`.

[66] N. Metropolis and S. M. Ulam, *The Monte Carlo method*, J. Amer. Stat. Assoc. **44** (1949) 335.

[67] B. Andersson, G. Gustafson, G. Ingelman, and T. Sjostrand, *Parton fragmentation and string dynamics*, Phys. Rept. **97** (1983) 31.

[68] GEANT4 Collaboration, *GEANT4: A simulation toolkit*, Nucl. Instrum. Meth. A **506** (2003) 250.

[69] T. Novak, *ATLAS pile-up and overlay simulation*, Talk given at the 3rd LPCC Detector Simulation Workshop (2017), URL: `https://cds.cern.ch/record/2270396`.

[70] ATLAS Collaboration, *Performance of the reconstruction of large impact parameter tracks in the ATLAS inner detector*, ATL-PHYS-PUB-2017-014, 2017, URL: `https://cds.cern.ch/record/2275635`.

[71] T. Cornelissen, M. Elsing, S. Fleischmann, W. Liebig, and E. Moyse, *Concepts, design and implementation of the ATLAS new tracking*, ATL-SOFT-PUB-2007-007, 2007, URL: `https://cds.cern.ch/record/1020106`.

[72] R. Frühwirth, *Application of Kalman filtering to track and vertex fitting*, Nucl. Instrum. Meth. A **262** (1987) 444.

[73] J. Illingworth and J. Kittler, *A survey of the Hough transform*, Comp. Vis. Graph. Image Proc. **44** (1988) 87.

[74] ATLAS Collaboration, *Reconstruction of primary vertices at the ATLAS experiment in run 1 proton–proton collisions at the LHC*, Eur. Phys. J. C **77** (2017) 332, arXiv: `1611.10235 [physics.ins-det]`.

[75] S. R. Das, *On a new approach for finding all the modified cut-sets in an incompatibility graph*, IEEE Trans. Comput. **22** (1973) 187.

[76] ATLAS Collaboration, *Electron and photon energy calibration with the ATLAS detector using LHC run 1 data*, Eur. Phys. J. C **74** (2014) 3071, arXiv: 1407.5063 [hep-ex].

[77] W. Lampl et al., *Calorimeter clustering algorithms: Description and performance*, ATL-LARG-PUB-2008-002, 2008, URL: https://cds.cern.ch/record/1099735.

[78] R. Frühwirth, *A Gaussian-mixture approximation of the Bethe-Heitler model of electron energy loss by bremsstrahlung*, Comput. Phys. Commun. **154** (2003) 131.

[79] ATLAS Collaboration, *Improved electron reconstruction in ATLAS using the Gaussian Sum Filter-based model for bremsstrahlung*, ATLAS-CONF-2012-047, 2012, URL: https://cds.cern.ch/record/1449796.

[80] ATLAS Collaboration, *Electron reconstruction and identification efficiency measurements with the ATLAS detector using the 2011 LHC proton–proton collision data*, Eur. Phys. J. C **74** (2014) 2941, arXiv: 1404.2240 [hep-ex].

[81] ATLAS Collaboration, *Electron efficiency measurements with the ATLAS detector using the 2015 LHC proton–proton collision data*, ATLAS-CONF-2016-024, 2016, URL: https://cds.cern.ch/record/2157687.

[82] ATLAS Collaboration, *Measurement of the photon identification efficiencies with the ATLAS detector using LHC run-1 data*, Eur. Phys. J. C **76** (2016) 666, arXiv: 1606.01813 [hep-ex].

[83] ATLAS Collaboration, *Muon reconstruction performance of the ATLAS detector in proton–proton collision data at $\sqrt{s}$ = 13 TeV*, Eur. Phys. J. C **76** (2016) 292, arXiv: 1603.05598 [hep-ex].

[84] ATLAS Collaboration, *Search for massive, long-lived particles using multitrack displaced vertices or displaced lepton pairs in pp collisions at $\sqrt{s}$ = 8 TeV with the ATLAS detector*, Phys. Rev. D **92** (2015) 072004, arXiv: 1504.05162 [hep-ex].

[85] M. E. Goblirsch-Kolb, *Searches for R-parity violating supersymmetry in multilepton final states with the ATLAS detector*, CERN-THESIS-2015-095, 2015, URL: https://cds.cern.ch/record/2035968.

[86] J. Alwall et al., *The automated computation of tree-level and next-to-leading order differential cross sections, and their matching to parton shower simulations*, JHEP **07** (2014) 079, arXiv: 1405.0301 [hep-ph].

[87] T. Sjöstrand et al., *An introduction to PYTHIA 8.2*, Comput. Phys. Commun. **191** (2015) 159, arXiv: 1410.3012 [hep-ph].

[88] ATLAS Collaboration, *ATLAS run 1 PYTHIA 8 tunes*, ATL-PHYS-PUB-2014-021, 2014, URL: https://cds.cern.ch/record/1966419.

[89] R. D. Ball et al., *Parton distributions with LHC data*, Nucl. Phys. B **867** (2013) 244, arXiv: 1207.1303 [hep-ph].

[90] W. Beenakker, C. Borschensky, M. Krmer, A. Kulesza, and E. Laenen, *NNLL-fast: predictions for coloured supersymmetric particle production at the LHC with threshold and Coulomb resummation*, JHEP **12** (2016) 133, arXiv: 1607.07741 [hep-ph].

[91] W. Beenakker et al., *NNLL resummation for squark and gluino production at the LHC*, JHEP **12** (2014) 023, arXiv: 1404.3134 [hep-ph].

[92] W. Beenakker et al., *Towards NNLL resummation: hard matching coefficients for squark and gluino hadroproduction*, JHEP **10** (2013) 120, arXiv: 1304.6354 [hep-ph].

[93] W. Beenakker et al., *NNLL resummation for squark-antisquark pair production at the LHC*, JHEP **01** (2012) 076, arXiv: 1110.2446 [hep-ph].

[94] W. Beenakker et al., *Soft-gluon resummation for squark and gluino hadroproduction*, JHEP **12** (2009) 041, arXiv: 0909.4418 [hep-ph].

[95] A. Kulesza and L. Motyka, *Soft gluon resummation for the production of gluino-gluino and squark-antisquark pairs at the LHC*, Phys. Rev. D **80** (2009) 095004, arXiv: 0905.4749 [hep-ph].

[96] A. Kulesza and L. Motyka, *Threshold resummation for squark-antisquark and gluino-pair production at the LHC*, Phys. Rev. Lett. **102** (2009) 111802, arXiv: `0807.2405 [hep-ph]`.

[97] W. Beenakker, R. Hopker, M. Spira, and P. Zerwas, *Squark and gluino production at hadron colliders*, Nucl. Phys. B **492** (1997) 51, arXiv: `hep-ph/9610490`.

[98] J. Butterworth et al., *PDF4LHC recommendations for LHC Run II*, J. Phys. G **43** (2016) 023001, arXiv: `1510.03865 [hep-ph]`.

[99] ATLAS Collaboration, *Search for long-lived, massive particles in events with displaced vertices and missing transverse momentum in $\sqrt{s} = 13$ TeV pp collisions with the ATLAS detector*, Phys. Rev. D **97** (2018) 052012, arXiv: `1710.04901 [hep-ex]`.

[100] S. Alioli, P. Nason, C. Oleari, and E. Re, *A general framework for implementing NLO calculations in shower Monte Carlo programs: the POWHEG BOX*, JHEP **06** (2010) 043, arXiv: `1002.2581 [hep-ph]`.

[101] J. Pumplin et al., *New generation of parton distributions with uncertainties from global QCD analysis*, JHEP **07** (2002) 012, arXiv: `hep-ph/0201195 [hep-ph]`.

[102] ATLAS Collaboration, *Early inner detector tracking performance in the 2015 data at $\sqrt{s} = 13$ TeV*, ATL-PHYS-PUB-2015-051, 2015, URL: `https://cds.cern.ch/record/2110140`.

[103] ATLAS Collaboration, *A measurement of material in the ATLAS tracker using secondary hadronic interactions in 7 TeV pp collisions*, JINST **11** (2016) P11020, arXiv: `1609.04305 [hep-ex]`.

[104] T. Gleisberg et al., *Event generation with SHERPA 1.1*, JHEP **02** (2009) 007, arXiv: `0811.4622 [hep-ph]`.

[105] NNPDF Collaboration, *Parton distributions for the LHC run II*, JHEP **04** (2015) 040, arXiv: `1410.8849 [hep-ph]`.

[106] S. D. Drell and T.-M. Yan, *Massive lepton pair production in hadron-hadron collisions at high-energies*, Phys. Rev. Lett. **25** (1970) 316, Erratum: Phys. Rev. Lett. **25** (1970) 902.

[107] S. Che, *Search for long-lived resonance decaying to a dilepton pair in pp collisions at $\sqrt{s} = 13$ TeV with the ATLAS detector*, CERN-THESIS-2018-117, 2018, URL: `https://cds.cern.ch/record/2634838`.

[108] H. Burkhardt, S. R. Kelner, and R. P. Kokoulin, *Monte Carlo generator for muon pair production*, CERN-SL-2002-016-AP. CLIC-Note-511, 2002, URL: `https://cds.cern.ch/record/558831`.

[109] ATLAS Collaboration, *Characterisation and mitigation of beam-induced backgrounds observed in the ATLAS detector during the 2011 proton–proton run*, JINST **8** (2013) P07004, arXiv: `1303.0223 [hep-ex]`.

[110] E. Hill, *The cosmic muon flux in the ATLAS detector at the Large Hadron Collider*, CERN-THESIS-2011-118, 2011, URL: `https://cds.cern.ch/record/1389902`.

[111] M. Baak et al., *HistFitter software framework for statistical data analysis*, Eur. Phys. J. C **75** (2015) 153, arXiv: `1410.1280 [hep-ex]`.

[112] G. Cowan, K. Cranmer, E. Gross, and O. Vitells, *Asymptotic formulae for likelihood-based tests of new physics*, Eur. Phys. J. C **71** (2011) 1554, Erratum: Eur. Phys. J. C **73** (2013) 2501, arXiv: `1007.1727 [physics.data-an]`.

[113] A. L. Read, *Presentation of search results: The CL(s) technique*, J. Phys. G **28** (2002) 2693.

List of Figures

List of Tables